Continuous synthesis of iron oxide nanoparticles for biomedical applications

---

Dissertation

zur Erlangung des akademischen Grades „Doktor der Naturwissenschaften“

dem Fachbereich Chemie, Pharmazie und Geowissenschaften

der

Johannes-Gutenberg-Universität Mainz

vorgelegt von

Abdulkader Baki

Mainz 2021

Dekan:

1. Berichterstatter:

2. Berichterstatter:

Tag der mündlichen Prüfung:

Eidesstattliche Erklärung

Die vorliegende Dissertation wurde in der Zeit von Dezember 2016 bis Dezember 2021 unter der Betreuung von Herrn Prof. Dr. Michael Maskos am Institut für Physikalische Chemie der Johannes-Gutenberg-Universität Mainz in Kooperation mit der Abteilung Nanopartikeltechnologien am Fraunhofer-Institut für Mikrotechnik und Mikrosysteme IMM, Mainz angefertigt.

Hiermit versichere ich, dass diese Arbeit selbständig von mir verfasst wurde und ich ausschließlich die angegebenen Quellen und Hilfsmittel verwendet habe. Alle Stellen, die im Wortlaut oder dem Sinn gemäß anderen Arbeiten entnommen wurden, sind durch Angabe der Quellen kenntlich gemacht.

Die Arbeit ist in gleicher oder ähnlicher Form weder veröffentlicht noch einer Prüfungsbehörde vorgelegt worden.

Mainz, den 20.12.2021 _____

Abdulkader Baki

„Knowledge in the migrations land is a homeland“
averroes

Diese Arbeit ist meinen Eltern Abdulhadi und Elham Baki gewidmet

Abstract

Within the exciting area of nanotechnology, magnetic nanoparticles constitute an important subclass of smart materials with a huge number of applications in industry, life science, and medicine. Controlled synthesis approaches and reliable characterization of the magnetic nanoparticles are key factors for the development of novel magnetic nanoparticle systems. Numerous synthesis routes for batch production of magnetic nanoparticles have been established each exhibiting specific advantages and disadvantages. Quite often, batch-to-batch variations and broad size distributions of the resulting magnetic nanoparticles lead to a reduced performance in the envisaged applications. An alternative approach provides the continuous micromixer synthesis of magnetic nanoparticles with promising higher reproducibility and scalability compared to conventional methods. In this approach, spatial and temporal separation between nucleation and growth of the particles, beneficial high heat and mass transfer, and the capability to separately control reaction parameters such as temperature and residence time can be achieved. Due to their huge magnetic moments, single core magnetic nanoparticles with core sizes larger than 20 nm are of particular interest for several biomedical applications. However, to synthesize magnetic nanoparticles of these sizes that remain stable in physiological environment, is very challenging due to the strong interparticle interactions. Even though great efforts of numerous researchers have been made, stably dispersed single-core magnetic nanoparticles with average core sizes above 20 nm are so far not accessible neither by conventional batch methods nor by continuous synthesis approaches.

In this work, the continuous micromixer synthesis of magnetic single core iron oxide nanoparticles with core diameters up to 40 nm stably dispersed in aqueous environment has been established. The synthesis route relies on modifications of the synthesis method by Sugimoto and Matijević, where ferrous hydroxide is precipitated and then oxidized to obtain magnetic nanoparticles. The influence of the two main parameters in micromixer synthesis, the reaction temperature and the residence time,

was thoroughly characterized. To avoid agglomeration or further oxidation, the magnetic nanoparticles were stabilized with tannic acid. Additional protein coating of the nanoparticle surface with bovine serum albumin was successfully achieved to further improve their stability in physiological environments.

The resulting physicochemical and magnetic properties as well as the reproducibility of continuous micromixer synthesis in comparison to conventional batch synthesis were determined. To this end, core and hydrodynamic sizes, size distribution, and particle morphology were investigated by transmission electron microscopy and differential centrifugal sedimentation. The crystal structure of MNP was studied using X-ray diffraction. To study the changes in particle surface, zeta potential measurements and gel electrophoresis were carried out. AC-susceptibility measurements of the linear magnetic susceptibility, reflecting changes in the hydrodynamic properties of the MNP systems were investigated. The colloidal stability and changes in the magnetic and physicochemical properties of the synthesized magnetic nanoparticles were analysed in the presence of physiological NaCl concentrations.

The capability of the micromixer synthesized magnetic nanoparticles as tracer for magnetic particle imaging was determined by magnetic particle spectroscopy measurements. Nuclear magnetic resonance relaxivity measurements were carried out to assess the performance of the magnetic nanoparticles as contrast agent in magnetic resonance imaging. Finally, the heat generation capacity of the magnetic nanoparticles in magnetic fluid hyperthermia as a therapeutic approach for cancer treatment was determined by AC magnetic loss measurements.

Contents

1 Introduction

With his famous lecture entitled *"There's Plenty of Room at the Bottom"* at the California institute of technology on the Annual Meeting of the American Physical Society in 1959, Richard Feynman changed our ideas about microscopic materials. His innovative talk about the ability to chemically manipulate atoms has opened the door to a beautiful huge world of "dwarf" particles, the world of *nanotechnology* [1].

The US National Nanotechnology Initiative (NNI) defined *nanotechnology* as the manipulation of matter at length scales of 1 to 100 nm (1 nm = 10^{-9} m) [2]. Nanotechnology has a broad range of applications and is used at present for countless purposes such as catalysts [3,4], batteries [5] textiles [6], cosmetics [7] and biomedicine [8–11]. Thus, it already became an integral and indispensable part of our everyday life.

Nanoparticles (NP), an important subclass of nanotechnology, drew significant attention when researchers realized the influence of minimizing the sizes of objects on their optical, physical, and chemical material properties [12]. In this size range, NP exhibit different properties compared to their bulk counterparts, which is mainly attributed to the increased surface area to volume ratio and the small diameter of the NP. In a dispersed medium, surface atoms, which constitute the largest part of NP, are directly in contact with different ions and molecules of the medium and consequently, are influencing the NP properties and performance. For example, plasmonic NP, such as gold-NP, with different sizes and shapes show various characteristic colours arising from their surface plasmon resonance modes. This property can be utilized in imaging applications [13–16]. Besides size, NP are characterized by chemical composition, structure, and their shape. Therefore, NP engineering requires a well understanding of these factors for the development of novel applications and for risk assessment related to their use.

Nanomedicine as an interdisciplinary part of medicine utilizes nanotechnology to contribute in medical applications at a molecular level [17]. NP have a fraction of the size compared to human cells, which typically ranges from 5 μm to 150 μm (Figure 1).

Thus, NP can be transported within the bloodstream and are able to penetrate biological barriers through phagocytosis or pinocytosis. Hence, NP are considered as powerful tools with promising potential in medical applications such as drug delivery [18–21], imaging [22,23], vaccines [24–26], biomolecule detection [27], antimicrobial agents [28], or dental treatment [29]. Moreover, coating or surface functionalization enable to equip the NP additionally with specific targeting moieties, for instant ligands binding to tumour cell surface markers. Surface modifications are also used to prevent unwanted protein adsorption (opsonization) or particle agglomeration or aggregation that would lead to severe side effects if administered to the human body. [30].

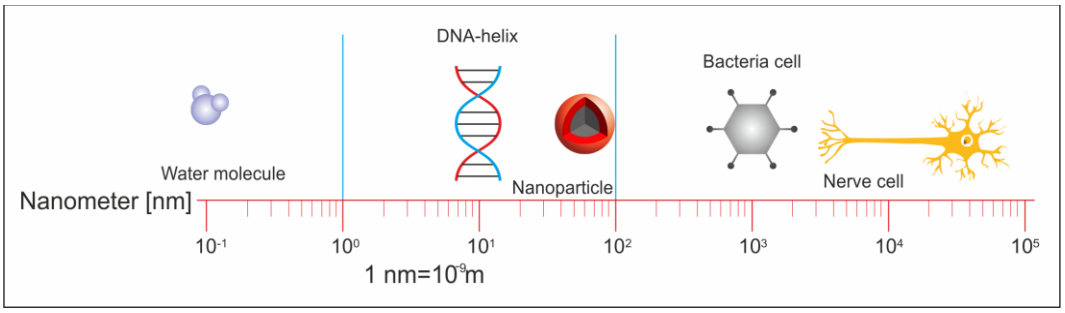

Figure 1. Nanotechnology refers to materials with sizes ranging from 1 to 100 nanometres. Nanoparticles as a subclass in this size range are objects with dimensions typically larger than DNA but smaller than cells making them interesting for biomedical applications (adopted from [31]).

Due to their specific properties, magnetic nanoparticles (MNP) have been intensively investigated for biomedical applications in the last decades. MNP can be oriented and manipulated by using an external magnetic field. Especially, their magnetic properties differ from the corresponding bulk material and are strongly size-dependent. As a consequence, MNP show superparamagnetic behaviour, e.g. by continuously flipping the direction of the magnetic moments under the influence of thermal energy. After a certain time, the MNP sample will show a zero net magnetization (vanishing magnetic remanence) without an applied magnetic field. Note, that superparamagnetism therefore is depending on the observation (measurement) time and temperature.

MNP composed of iron oxide are biodegradable and biocompatible and therefore preferable candidates for in vivo applications; in diagnosis as contrast agents for

magnetic resonance imaging (MRI) or magnetic particle imaging (MPI), as well as in therapeutic applications as drug delivery vehicles or hyperthermia agents. In combination, iron oxide based MNP can integrate diagnostic imaging capability and therapeutic drugs into one multifunctional nanocarrier, for which the term theranostics emerged, recently [32–34]. One example of theranostic application is cancer treatment. At present, cancer is one of the leading causes of death worldwide and is characterized by uncontrolled growth of cells as well as their spread into healthy tissues [35,36]. Additionally, symptoms usually appear only after the disease reached advanced stages. Treatment forms involve surgery, chemotherapy, and radiation therapy. These methods are accompanied by undesirable and often painful side effects as well as damage of healthy tissue due to insufficient tumour specificity. Therefore, improving cancer treatment opportunities by minimizing unwanted side effects is essential. MNP are potentially capable to deliver, accumulate and release pharmaceutical drugs into tumour tissue controlled by applying external magnetic fields. Additionally, MNP can increase the efficiency of radiotherapy by producing reactive oxygen species [37]. Therefore, MNP are promising candidates for cancer treatment.

An example of MNP-based drug in biomedical applications is ferumoxytol that was approved in 2009 by the US food and drug administration (FDA) for anemia treatment for patients with chronic kidney disease [38].

In general, uniformity in the MNP characteristics such as form, size, and magnetic behaviour facilitates their clinical translation since predictions of their biological fate and efficacy become more reliable. However, every biomedical application requires a specific adjustment of the underlying MNP characteristics to improve their performance and guarantee a safe implementation. Hence, researchers have been focusing on developing robust, effective, tuneable, and highly reproducible synthesis routes to manufacture MNP with defined properties. Precise control of reaction parameters such as temperature, educts, mixing ratios, solvents and surface ligands play a key role in process development. Additionally, modern synthesis approaches

need to incorporate preserving environmental resources and minimize row materials and energy consumption without generating undesirable chemical by-products during the entire synthesis process [39]. Moreover, using organic solvents and toxic educts for the synthesis can be harmful to the human body and is therefore inappropriate for medical applications.

Up to now, numerous conventional batch synthesis routes for MNP production have been developed such as co-precipitation [40,41], sol-gel [42,43], micro-emulsion [44,45], and thermal decomposition [46,47]. Although co-precipitation is the most common used synthesis approach, it has some limitations such as addressable size range, broad size distribution and large batch-to-batch variation of the resulting MNP. Therefore, novel and advanced synthetic routes to overcome these drawbacks are still demanded. Continuous manufacturing approaches for NP synthesis promises significant advantages compared to conventional batch synthesis such as improved control over reaction parameters, enhanced reproducibility, the possibility to automate the entire production process and to scale-up the product [48,49].

The properties of synthesized MNP are generally characterized by structural, physicochemical, and magnetic measurements to assure their quality and to verify their potential for different applications. The most common measurement techniques used for characterization are: Transmission Electron Microscopy (TEM) that is an effective tool using an electron beam resolving single NP to determine core size, size distribution, and morphology with high resolution. Dynamic Light Scattering (DLS) and Differential Centrifugal Sedimentation (DCS) are two ensemble methods employed to measure the average hydrodynamic size and size distribution of NP. Magnetic properties can be measured by Magnetic Particle Spectroscopy (MPS), which detects the non-linear dynamic magnetic response of MNP exposed to an alternating magnetic field and AC-Susceptibility (ACS) to determine the linear dynamic magnetic susceptibility. Nuclear Magnetic Resonance (NMR) is used to measure the relaxivity of MNP from which their capability as contrast agent in MRI is assessed. By static DC

Magnetization (DCM) measurements, magnetic properties of the MNP such as the saturation magnetization can be extracted.

2 Theoretical background

2.1 Magnetic Nanoparticles

2.1.1 Classification of magnetic behaviour of materials

All matter is "magnetic" which denotes a property that is caused by quantum exchange interactions between the electronic orbitals and spins in the atoms constituting a material. Therefore, materials can be classified according to their reaction when exposed to an external magnetic field [50]. In *diamagnetic* materials, the electrons are arranged in pairs so that there is no exchange interaction between the atomic magnetic moments. Thus, diamagnetic materials have zero net magnetic moment exhibiting no magnetic properties in the absence of an external magnetic field. An applied magnetic field induces an additional angular momentum of the electrons and thereby leads to a weak magnetization opposite to the field direction resulting in a negative linear susceptibility $\chi_{dia}<0$ of the diamagnetic material. All materials exhibit diamagnetic properties.

Paramagnetic materials show no exchange interaction between atomic magnetic moments, and therefore, as in diamagnetic materials, the net magnetic moment is zero in the absence of an external magnetic field. However, due to unpaired electrons, paramagnetic materials exhibit a positive net magnetic moment in a magnetic field leading to a positive linear susceptibility $\chi_{para}>0$. If present (i.e., an electronic configuration with unpaired electrons such as in radicals, transition metals lanthanoids), the paramagnetic susceptibility dominates the always existing but much weaker diamagnetism.

In *ferromagnetic* materials like iron, nickel, or cobalt, permanent atomic magnetic dipole moments are existing even in the absence of an external magnetic field. The moments are coupled with each other forming large areas of parallel arrangement as a consequence of strong negative exchange interactions in the electronic configuration. Again, ferromagnetism dominates the diamagnetic behaviour in a material and shows

hysteresis behaviour in an external magnetic field. *Antiferromagnetic* materials are similar to ferromagnetic materials, but exhibit a positive exchange interaction. In such materials, the application of a magnetic field aligns neighbouring atomic moments into antiparallel directions, thus resulting in a zero net magnetization. Special cases of antiferromagnetic materials are *ferrimagnetic* materials such as the iron oxides magnetite Fe_3O_4 and maghemite γ-Fe_2O_3 where moments of different size are arranged antiparallel leading to a residual non-zero net magnetic moment in a magnetic field.

2.1.2 Size-dependent magnetic behaviour of MNP

So far, the magnetic classification was related to general bulk materials. Additional interesting magnetic behaviour arises in magnetic nanoparticles, where the size of the objects is reduced down to about 1 to 100 nm. These nanoparticles exhibit *superparamagnetic* behaviour. In an individual nanoparticle, all atomic dipole moments are coupled by exchange interactions either in parallel (nanoparticle made of ferromagnetic material) or antiparallel (when using ferrimagnetic or antiferromagnetic materials) configuration as in the corresponding bulk material. In the absence of a magnetic field, thermal fluctuations permanently flip the individual magnetic moments of an ensemble of MNP into random directions so that after a ceratin time of relaxation no longer a net magnetization is observed. Superparamagnetic MNP show no remanence or hysteresis behaviour in contrast to their corresponding ferro- or ferrimagnetic bulk materials [51]. Due to exchange coupling of typically 10^2 to 10^4 atomic moments in an MNP, superparamagnetic materials possess much higher susceptibilities than paramagnetic materials. Applying an increasing external magnetic field continuously magnetizes (by orienting the MNP moments towards the field direction) a superparamagnetic material until saturation magnetization M_S (all moments pointing into field direction) is reached (Figure 2).

Commonly used magnetic nanoparticles are iron oxide nanoparticles (ferrites) like maghemite γ-Fe_2O_3 or magnetite Fe_3O_4, metallic nanoparticles like Fe or Co, or alloy nanoparticles such as Fe-Pt or Co-Pt alloys.

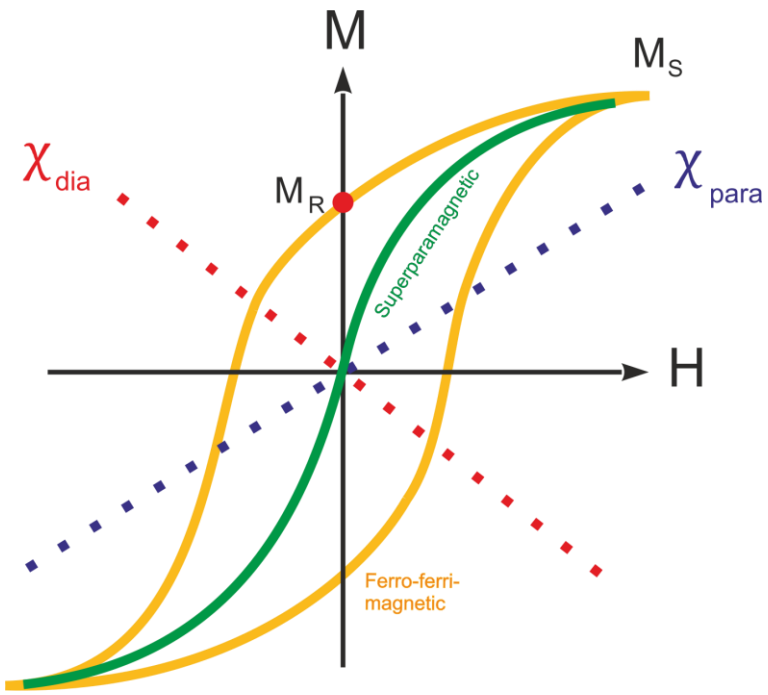

Figure 2. Classification of materials: In a magnetic field *H*, materials behave magnetically different. Diamagnetic materials exhibit a linear negative (dashed red line), paramagnetic materials a linear positive susceptibility $\chi = M/H$ (dashed blue line). Ferro- and ferrimagnetic materials show a non-linear magnetization curve (yellow line) with saturation at M_s and hysteresis, while MNP in a superparamagnetic state, a non-linear magnetization curve (green line) with saturation at M_s but without hysteresis is present.

Changing the direction of the MNP moments as a reaction of an applied magnetic field requires a certain time. Accordingly, when switching off an external magnetic field, the net magnetization of an MNP sample is decaying within a characteristic time interval (needed for the magnetic moments to reach an equilibrium random distribution). For this relaxation effect two mechanisms are responsible, the Néel and the Brownian relaxation. For Néel relaxation, the directions of the magnetic moments are reorienting by surmounting the energy barriers given by the specific crystal structure (Figure 3). The corresponding time constant is given by the Néel relaxation time τ_N (Equation 1):

$$\tau_N = \tau_0 \exp\left(\frac{KV_c}{k_B T}\right) \qquad (1)$$

where τ_0 ($\approx 10^{-9}$ s) is a characteristic relaxation time for thermal fluctuations, also called attempt time, K the effective anisotropy constant including crystal, strain and shape anisotropy contribution for the MNP, V_c: the volume of the magnetic core, k_B the Boltzmann constant, and T the temperature.

MNP in suspension can undergo a second relaxation mechanism, the Brownian motion, here the magnetic moment is reorienting by rotation of the whole MNP (Figure 3). The corresponding Brownian relaxation time is given by (Equation 2):

$$\tau_B = \frac{3\eta V_{hyd}}{k_B T} \qquad (2)$$

where η denotes the viscosity of the carrier liquid, and V_{hyd}: the hydrodynamic volume.

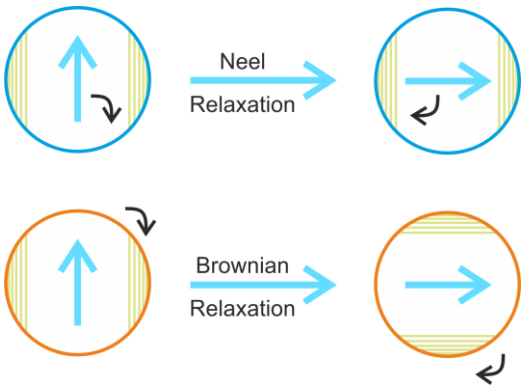

Figure 3. The two relaxation mechanisms for reorientation of the magnetic moment of an MNP, Néel and Brownian process.

If both competing relaxation mechanisms are present, the faster relaxation is dominating and therefore an effective relaxation time is observed that can be described by (Equation 3):

$$\frac{1}{\tau_{eff}} = \frac{1}{\tau_N} + \frac{1}{\tau_B} \qquad (3)$$

Since the Néel relaxation time exponentially increases with increasing particle core volume V_c (Equation 1), the Brownian relaxation time becomes dominant for larger MNP [52] as shown in (Figure 4). For the chosen parameters the transition from Néel to Brownian relaxation being the dominating relaxation mechanism occurs at a particle diameter of about d_c=7.5 nm.

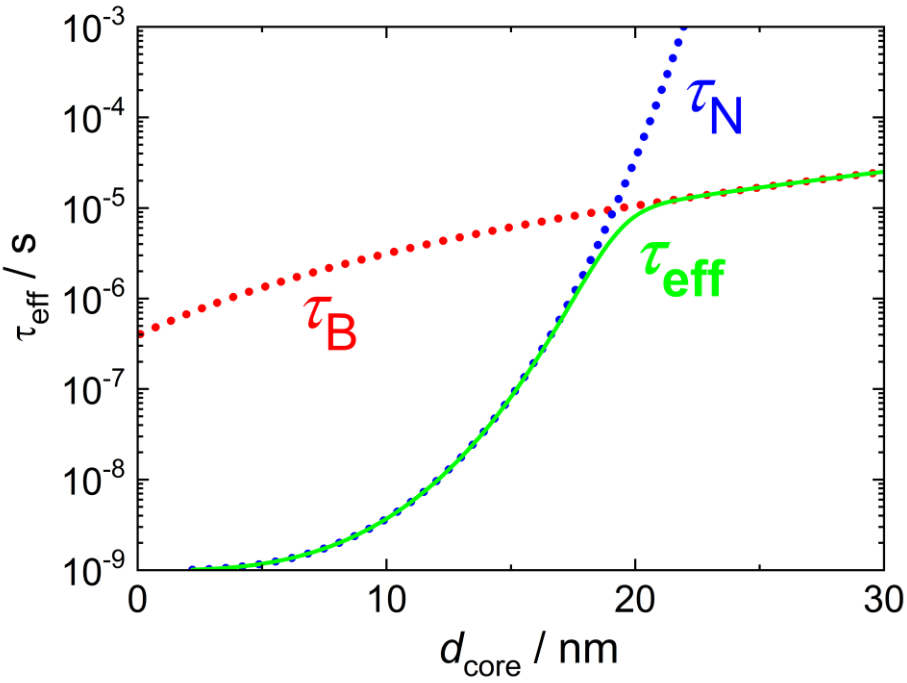

Figure 4. Effective relaxation time τ_{eff} as a function of particle diameter for Néel and Brownian relaxation. For the calculation, an effective anisotropy constant K= 10^4 J/m^3, the viscosity of water η=1 mP·s, and room temperature T=298 K were assumed and for simplicity, V_c=V_{hyd} e.g., a vanishing shell layer of the MNP.

2.1.3 Iron oxide

Iron oxides are composed of iron and oxygen at different stoichiometries and crystalline structures. The most-common iron oxide structures are magnetite (Fe_3O_4), maghemite (γ-Fe_2O_3), and hematite (α-Fe_2O_3).

Magnetite has an inverse spinel crystal structure Fe^{3+} $[Fe^{2+}Fe^{3+}]O^{2-}{}_4$ with a face-centred cubic (fcc) unit cell. Tetrahedral sites are occupied only by (Fe^{3+}), whereas octahedral sites are distributed between (Fe^{2+}) and (Fe^{3+}). (O^{2-}) ions are forming a regular cubic close packing. Maghemite has a defect spinel structure $0.75Fe^{3+}$ $[Fe^{3+}{}_{5/3}\square_{1/3}]O^{2-}{}_4$ (□:

vacant site) and can be formed from magnetite via oxidation resulting in Fe^{3+} sites, only. Both, magnetite and maghemite are ferrimagnetic materials [53]. Values for bulk saturation magnetization of magnetite and maghemite are listed in Table 1. [54].

Table 1. Magnetic properties of iron oxides in the bulk state [55].

Iron oxide	M_S(T = 5 K) $Am^2/kg(Fe)$	M_S(T = 300 K) $Am^2/kg(Fe)$
Fe_3O_4	98.0	92.0
γ-Fe_2O_3	84.0	78.0

2.1.4 Biomedical applications of MNP

Living organisms are made up of cells with typical sizes of 5-150 μm. However, these cells contain much smaller components such as proteins that have typical dimensions of several nanometres (about 5 nm). Therefore, MNP are a powerful tool to investigate cells and cellular processes. Numerous other medical applications are relying on using nanoparticles including (see Figure 1 in publication: *Bioengineering*, paper No.1):

1- Magnetic cell tracking [56–58].
2- Drug delivery [59–61].
3- Gene therapy [62,63].
4- Magnetic fluid hyperthermia [64–66].
5- Bio-magnetic imaging (as a contrast medium) [67–71].
6- Nanorobotics and magnetic actuation [72–74].

In this work, the performance of continuously synthesized MNP for medical applications was evaluated and optimized for the following three applications: MRI, MPI and magnetic hyperthermia. Further details and state of the art for these methods are discussed in publication: (*Bioengineering*, paper No. 1). The evaluation of the MNP synthesized in this work for medical applications are shown in publication: (*Nanoscale*

advances, paper No. 2). In the following three paragraphs (2.1.4.1 – 3), the general principle of these applications of MNP are shortly summarized.

2.1.4.1 Magnetic Resonance Imaging

Magnetic Resonance Imaging (MRI) is a common imaging modality to visualize living organisms without using ionizing radiation. This non-invasive technique provides detailed information about the structure and function of living tissues with a sub-millimetre spatial resolution [75].

MRI relies on the nuclear magnetic resonance (NMR) of protons which have an advantageous high abundance in living tissues. The signals are detected after applying radiofrequency pulses for excitation of the protons. Tissues can be differentiated depending on their proton content. To enhance imaging contrast between similar tissues like muscles and blood vessels, or to detect tissue damage, MNP as contrast agents can be utilized [76]. Contrast agents are capable to shorten the T_1 (longitudinal) and T_2 (or transverse) relaxation time of surrounding water protons. The signal intensity of T_1-weighted images appears brighter and is known as positive contrast. On the other hand, T_2-weighted images appear darker and are known as negative contrast. In both approaches, the contrast agents lead to a higher image resolution [77–79].

The biodistribution of contrast agents is a crucial factor for medical applications. Commonly used gadolinium-based contrast agents are rapidly eliminated from the blood circulation by renal excretion [80]. In contrast, iron oxide based MNP have lower toxicity and the biodistribution depends on their size and surface modification. Because they are accumulated in reticuloendothelial system (RES) organs, liver and spleen, iron oxide based MNP are advantageous to be used for MRI visualization of these organs. Feridex and Resovist are examples of iron oxide-based MNP that have been approved by the FDA for liver imaging [30].

2.1.4.2 Magnetic Particle Imaging

Magnetic Particle Imaging (MPI) is a quantitative tomographic imaging technology that was first introduced in 2005 by Gleich and Weizenecker [81]. MPI is using MNP as tracers and is characterized by a high spatial (less than 1 millimetre); excellent temporal resolution (few milliseconds) and a good sensitivity (ng) for MNP detection. After successful proof of principle demonstration by imaging a beating mouse heart [82,83], MPI presently is under development for human application with a high potential for diagnostic vascular or perfusion imaging, imaging-guided vascular interventions, or cancer detection [84].

MPI relies on the detection of the non-linear dynamic magnetization of MNP exposed to a sinusoidally oscillating magnetic excitation field. For spatial encoding, additional magnetic field gradients are used that create a field-free region (depending on the device architecture called *field-free-point* or *field-free-line*) from which the MNP response is recorded by receiving coils. Only within this spatially constrained region, the dynamic magnetic magnetization response of MNP is occurring, while at all other regions the MNP are saturated (Figure 5). By moving the field-free region through the field of view (FOV) of the sample, signals from the MNP are acquired from which an image of their distribution can be reconstructed by solving an inverse problem. For the image reconstruction an additional calibration measurement for each MNP type is required, where a point-like reference sample of known MNP content is positioned by a robot at numerous defined positions in the FOV and the corresponding MNP dynamic magnetization response is recorded. This process is called system-function measurement and can last up to several days depending on the chosen voxel resolution and averaging. In contrast, measuring a sample is very fast, since the excitation fields and the field-free space movement is operated at kHz frequencies, a scan of the whole FOV can be achieved within about 20 ms [81,83,85].

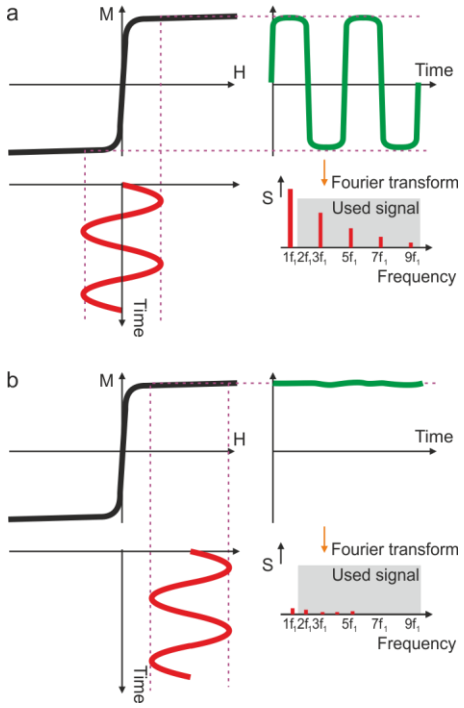

Figure 5. General mechanism of MPI, a: In the field-free region (no magnetic gradient field), the MNP exhibit a dynamic magnetization response to the basic sinusoidally magnetic excitation field at a frequency of about 25 kHz (red curve). Due to the non-linear magnetization of the MNP a distorted magnetization response is resulting (green curve) which after Fourier Transform leads to the characteristic MPI spectra (red bars). b: If an additional gradient field is applied (e.g.., everywhere outside the field-free region, nearly no response (green curve) is observed since the MNP magnetization is saturated. Accordingly, no MPI spectra become visible after Fourier Transform (red bars), (adopted from [81]).

MPI detects solely the MNP. Therefore, the resulted MP images are background-free and do not provide any anatomical information. A combination of MPI with MRI data could be a promising hybrid MPI/MRI modality for a high-resolution 3D images with molecular tracking of MNP [86].

2.1.4.3 Magnetic fluid hyperthermia

Hyperthermia is an established method to treat diseases by exposure of locally affected organs or the whole human body to elevated temperatures. Already in ancient times, Egyptians used heating power to treat breast cancer by fire drills (hot blades and sticks). This method was also known in China and India [87]. Much younger is magnetic fluid hyperthermia, an approach to fight tumour cells by increasing their temperature using MNP heating up in an external oscillating magnetic field. Since

cancer cells are more sensitive to temperature than normal cells, cancer cells will undergo apoptosis or necrosis, e.g., their cell death followed by a series of metabolic cascades [88–90]. MNP are advantageous to reach organs such as the brain that cannot be reached easily by conventional heating methods. The heating mechanism can be attributed to the Néel und Brownian relaxation of the MNP (as described in section 2.1.2) that occur if they are exposed to an alternating magnetic field [91,92]. The energy transformation from magnetic into thermal energy can be characterized by the specific absorption rate (SAR) of MNP in units of W/g and is given by (Equation 4) [93]:

$$SAR = C \left(\frac{dT}{dt}\right)\left(\frac{m_s}{m_m}\right) \tag{4}$$

where C is the specific heat capacity of the solvent, dT/dt the initial slope of the time-dependent temperature increase (heating curve), m_s the mass of the solvent, and m_m the mass of MNP. The SAR value crucially depends on many factors such as size, shape, size distribution, crystallinity, functionalization and magnetic properties of the MNP as well as the amplitude and frequency of the applied alternating magnetic field [94,95]. Commonly, the SAR value of a MNP suspension is determined experimentally by detecting the temperature increase (heating curve) with a fiber optical thermometer after switching on the excitation field at a given excitation frequency (typically, 100 to 500 kHz) and amplitude (20 to 30 kA/m). Alternatively, the SAR value can be extracted from the area of the measured dynamic magnetization curve at the same excitation parameters [96].

2.2 Synthesis of magnetic nanoparticles

Uniform characteristic MNP parameters such as shape, size, size distribution, and crystal structure are mandatory for their successful applications, especially under biomedical considerations. Since a small variation in the synthesis procedure might radically change the resulting MNP properties. Control over the thermodynamical and kinetic processes is crucial to fabricate MNP with desired properties for successful biomedical usage [97]. There are two general approaches to produce MNP, namely the "top-down" and "bottom-up" strategy. In the top-down approach, MNP are produced reducing the material size by different techniques e.g., laser ablation and mechanical milling, ultrasonication [98]. This approach is preferred in industry because it is cheap, simple and easy to scale up. However, the resulted MNP are exhibiting a broader size and shape distribution than MNP produced by bottom-up approaches and their functionalization is often problematic [30,99]. Therefore, the bottom-up approach, which depends on producing MNP starting from solution of ferrous (Fe^{2+}) or ferric (Fe^{3+}) ions, including synthetic routes such as co-precipitation, sol-gel, micro-emulsion, and thermal decomposition are preferably used to fabricate MNP with enhanced control over shape and size for medical applications. Numerous strategies have been developed to produce MNP with various sizes and shapes [100–105], shapes include, spherical [106], nanotubes [107], hierarchical superstructures, nanorods [108–110], nanowires [111,112], nanoflowers [113,114], nanocubes [115,116], etc.

2.2.1 Nanoparticle formation and ripening mechanisms

Kinetic factors have to be considered to influence the nanoparticle formation and achieve MNP synthesis with controlled size and desired narrow size distribution. The mechanism of nucleation and growth of MNP can generally be explained by the LaMer model postulated by Victor LaMer for colloidal sulphur in the 1950s. The mechanism is divided into two phases: Nucleation and growth.

If the concentration of the precursors that constitutes the NP reaches supersaturation, nucleation occurs. In this phase, homogeneous seeds are formed, continuously dissolved and reformed again. If the concentration of the precursors is further increased above a critical concentration, stable nuclei are formed, by which the precursor concentration decreases, accordingly. Below a certain nucleation threshold, further nucleation is inhibited. In the second phase, the size of the nuclei is increased by diffusion of precursor to the surface of the forming particle until no more precursor is available (see Figure 2 in publication: *Bioengineering*, paper No. 1) [117]. Generally, the two phases are present at the same time, especially in conventional batch synthesis, which leads to a broad size distribution of the NP. Size distribution narrowing can then be achieved by separating the two phases temporally and spatially. This approach is addressed by the continuous synthesis via micromixer. (See section 2.2.4)

After synthesis, NP are still subjected to a dynamic process called *Ostwald ripening*. Briefly, smaller NP tend to dissolve in favour of further growth of larger NP. Small particles have a higher surface energy and therefore dissolve to minimize their energy which favours the formation of larger particles [118]. Additionally, NP size can be increased by coalescence of multiple nanoparticles, also known as fusion [97].

Moreover, ligand binding to the NP surface plays a significant role in synthesis, especially in crystal growth and structure. In addition to the chemical bond between a NP surface and the anchor group of a ligand, ligand-ligand interactions at the NP surface are not negligible. These interactions increase with a higher packing density, size, and structure of the ligands [97].

In a colloidal solution, there is a dynamic equilibrium between ligands and NP, which means that ligands continually are adsorbing to and detaching from the particle surface [119]. NP growth only takes place if additional material can reach the particle surface, thus, only at moments when ligand molecules are detached from the surface. Therefore, the ligand density at the surface determines the rate of NP growth. Generally, nanosystems tend to minimize their total surface energy, which is the sum of individual surface energy contributions of different areas (facets) of the NP (Wulff

construction) [97,120,121]. The binding affinity of a ligand might vary within different areas of a NP surface. At a surface area with more adsorbed ligands, the growth will be inhibited because the accessibility of additional material for growth is reduced through the ligands, thereby reducing the growth rate (defects in nanocrystals should be taken into consideration) [122–125]. Which area is more preferred by the ligands depends on various factors such as the charge and the size of the anchor group. If all areas of an NP are equally favoured for chemisorption, spherical shape will be resulting since it has the lowest surface area to volume ratio. In the other extreme, a polyhedron with sharp edges will be formed if only one area is preferred for growth. Numerous intermediate NP shapes can occur between these extreme cases [97].

2.2.2 Co-precipitation

Due to the straightforward preparation and productivity without using harmful precursors, co-precipitation is a common method using nucleation and grain growth to fabricate MNP [126]. In this method, MNP are produced by aging a stoichiometric mixture of Fe^{2+} and Fe^{3+} in aqueous media [127]. Size, shape, and chemical composition of the resulting MNP depend on reaction parameters such as the type of iron salts (chloride, sulphate, etc.), the ratio of ions (Fe^{3+}/Fe^{2+}), ionic strength of the media, pH value of the solution, temperature, as well as the rate of adding the basic solution and stirring rate [128–135]. According to thermodynamical considerations, a (Fe^{3+}/Fe^{2+}) ratio of 0.5 should result in pure magnetite [101]. However, normally a mixture of magnetite and maghemite is obtained because of the oxidation sensitivity of magnetite to maghemite. Generally, smaller ratios of (Fe^{3+}/Fe^{2+}) lead to goethite, whereas larger ratios lead to formation of maghemite and magnetite. Additionally, smaller MNP sizes are obtain by increasing the pH, ionic strength, or temperature of the reaction [101,129].

Mainly, MNP are precipitated by two well-established synthetic methods. In Sugimoto and Matijević`s method established in 1980, Fe^{2+} is used in the presence of OH^- and NO_3^- ions and lead to MNP in the size range of 30 to 200 nm [136]. On the

other hand, in the most common method by Massart presented in 1981, a mixture of Fe^{3+}/Fe^{2+} is used in the presence of base and leads to smaller MNP sizes (<20 nm) and clusters [127]. However, stable dispersed single-core nanoparticles between 20 and 30 nm are not accessible by none of the two methods.

The chemical equations for the precipitation reaction according to Sugimoto can be written as:

$$Fe^{2+} + 2OH^- \rightarrow Fe(OH)_2$$

$$3Fe(OH)_2 + NO_3^- \rightarrow Fe_3O_4 + NO_2^- + 3H_2O$$

and according to Massart as:

$$Fe^{2+} + 2OH^- \rightarrow Fe(OH)_2$$

$$Fe^{3+} + 3OH^- \rightarrow Fe(OH)_3$$

$$Fe(OH)_2 + 2Fe(OH)_3 \rightarrow Fe_3O_4 + 4H_2O$$

Homogeneous nucleation and growth resulting in uniform MNP during the synthesis can be improved by mechanical stirring in a reduced reaction volume. Therefore, mass production of MNP is still challenging since in large reaction volumes insufficient mixing leading to heterogenity in nucleation and growth is lacking [137]. The synthesis parameters need to be carefully chosen and subsequent purification or fractionation is often carried out to improve the homogeneity of the resulting product [138].

The saturation magnetization of the material varies between 30 and 80 $Am^2/kg(Fe)$ [128,139]. These much lower values compared to bulk materials indicate the reduced quality of the MNP crystal structure (see Table 1).

In this work, the MNP were synthesized according to the synthesis of Sugimoto and Matijević using iron chloride ($FeCl_2$) and a strong base (NaOH) [136].

2.2.3 Thermal decomposition

Thermal decomposition is the second commonly used method to fabricate well defined MNP that possesses a good control over size with narrow size distribution and different shapes (cubic, spherical, etc.) [140,141]. This method depends on the decomposition of precursors such as iron pentacarbonyl ($FeCO)_5$) or iron acetylacetonate ($Fe(acac)_3$) in the presence of organic surfactants such as oleic acid at elevated temperatures up to 300 °C. The ratio of the precursors, the used surfactant, and solvent, the reaction time and temperature, as well as the aging duration are key factors for size and shape control in thermal decomposition. Single core MNP with sizes in the range 20 to 30 nm are accessible by thermal decomposition [47,84]. However, since the synthesis occurs in an organic solvent, the resulting MNP synthesized by thermal decomposition need to undergo a post-treatment (e.g., phase transfer into aqueous solvent) to be usable for biomedical applications. Thus, due to strong interparticle interactions of larger nanoparticles with high magnetic moments the transfer from organic to aqueous media often fails resulting in unstable, aggregated particles. Additionally, this method requires much more energy, material usage and time consumption than other synthetic routes such as co-precipitation.

2.2.4 Continuous synthesis of nanoparticles

In the last decades, continuous flow synthesis of NP was developed utilizing flow chemistry and micromixers to improve the quality and quantity of NP production due to its numerous advantages compared to conventional batch synthesis [142–146].

In contrary to conventional chemical synthesis routes with concentration gradients and inhomogeneous temperature distribution within a reaction flask, continuous synthesis significantly improves heat and mass transfer offering enhanced mixing and precise temperature control due to the higher surface area to volume ratio within the microchannels [49,146–149]. Hence, microfluidic systems have the potential to increase the reproducibility of NP production significantly resulting in lower batch-to-batch

variations with the feasibility to production upscaling [49]. Since the rapid nucleation phase of MNP takes place inside the micromixer and the growth phase in the connected capillary (ripening zone), spatial and temporal separation of the two phases can be achieved leading to more uniform MNP [49,150,151]. Micromixers allow to mix two fluids in close proximity in the micrometer channel within milliseconds [147,152]. Thus, a significant enhanced mixing is achieved compared to mixing in batch reactors. Moreover, complicated (hazardous) reactions such as peroxides, fluorides, or chlorination can be carried out safely in micromixers due to the small volume needed to run a reaction [153,154]. Nevertheless, NP precipitation in microstructured devices remain challenging due to the tendency of fouling and rapid blocking of microchannels. Careful experimental design and material selection is a mandatory prerequisite.

In continuous synthesis there are two major principles of mixing inside the micromixer: single-phase (continuous flow), where miscible phases can be homogeneously mixed by diffusion, and multi-phase (droplet-phase or plaque flow), where two immiscible phases such as gas-liquid or liquid-liquid (oil and water) form a droplet that works as a tiny reactor and is transported in the flow [49,155] (Figure 3 in publication, *Bioengineering*, paper No. 1).

Although continuous synthesis of MNP has been reported in many works so far, the presented procedures often do not comprise the entire production, including purification and stabilization steps. The resulted single core MNP are either too small, less than 10 nm, or not stable in aqueous phase forming clusters or agglomerates [156]. Stable, well dispersed single-core MNP in aqueous media with core size above 30 nm are still not accessible neither by continuous synthesis nor conventional batch approaches. Additionally, microfluidic processes based on photolithographic manufactured polydimethylsiloxane (PDMS) structures are commonly used, but usually, they do not tolerate high flow rates, pressure, and temperature. Subsequently, they are operated at very low flow rates in the range of microliter per minute, which limits the throughput and scalability [156–161].

Micromixers

Although numerous micromixer types with different structures and mixing profiles have been developed and applied for chemical synthesis in the last few decades, there are still ongoing developments to improve their performance. For example, currently micromixers are being developed to produce lipid nanoparticles as vehicles for novel mRNA vaccines. The Covid-19 pandemic demonstrates the urgent need for upscale production of the vaccines including the nanoparticle formulation process for mRNA. To this end, challenges such as channel clogging and scaling up the production reaching a yield in the range > 10 L/h still need to be solved to provide sufficient vaccines [162].

Simple micromixer types are the so-called T or Y micromixers, where two solutions are mixed by diffusion. Herein, the specific surface area between the fluids is determines the mixing time. Mixing efficiency can be improved by multi-lamination of fluids before mixing by a comb-like structure (interdigital-mixing) and subsequently focusing of the fluids at the outlet. An example of such a mixer is the Slit Interdigital Micro Mixer (SIMM), which has been developed at Fraunhofer IMM (Figure 6).

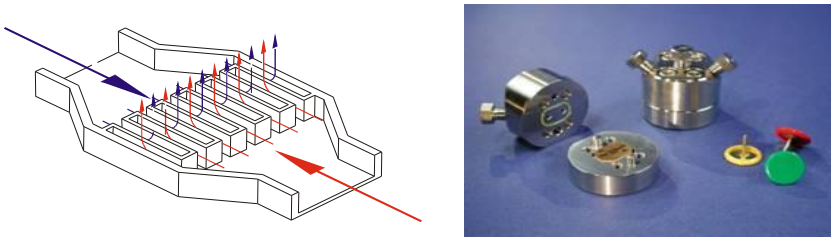

Figure 6. Slit Interdigital Micromixer (SIMM). Left: flow profile in a SIMM mixer. Right: Photograph (©Fraunhofer IMM) of the stainless-steel SIMM manufactured at Fraunhofer IMM. The left side shows a dismounted SIMM, the right an assembled SIMM.

Another version with improved mixing via mutilamination is the star-laminator micromixer (©Fraunhofer IMM). This type relies on stacking star-like thin foils with through-holes to generate an alternating interdigital feeding array resulting in a finely dispersed injection of the two fluids (Figure 7). These type of micromixers operate at relatively high flow rates providing improved mixing efficiency. For instance, for the

star laminator (StarLam 3000), high throughputs up to 3 m^3/h were demonstrated for aqueous systems [163].

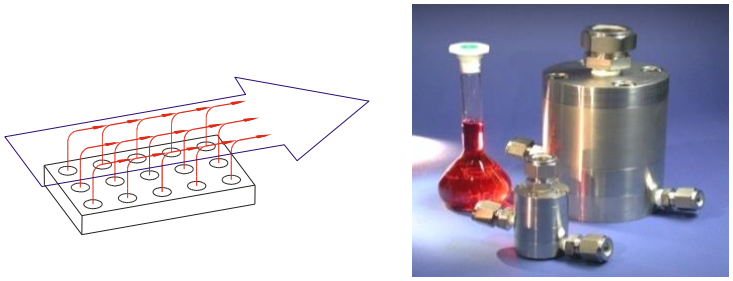

Figure 7. Star-laminitor Micromixer. Left: flow profile star-laminator. Right: Photograph (©Fraunhofer IMM) of StarLam 300/3000 mixers manufactured at Fraunhofer IMM.

The impinging-jet micromixer was developed to perform mixing in a wall-free environment to avoid micromixer plugging. The fluids are pumped into the jets of the micromixer forming a Y-shaped configuration. Smaller jet diameters improve the mixing quality [164] (Figure 8).

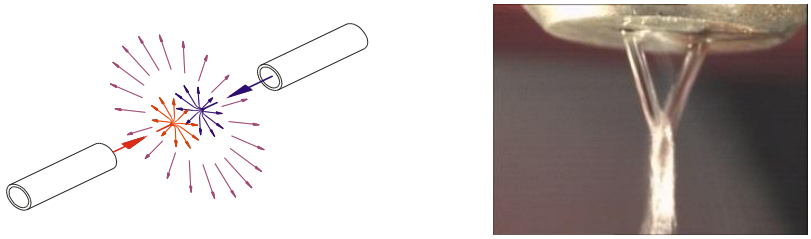

Figure 8. Impinging-jet Micromixer. Left: flow profile of an impinging-jet micromixer. Right: Photograph (©Fraunhofer IMM) of the mixer manufactured at Fraunhofer IMM.

The micromixer type used in the present work is the Caterpillar Micromixer (CPMM) developed by Fraunhofer IMM with a caterpillar-shaped mixing chamber. It is based on the split and recombine principle. This means that by dividing (splitting), folding over and then recombining of the solutions under laminar flow conditions, a large contact area of the substances can be achieved (simulation in Figure 9). In a CPMM, efficient mixing within milliseconds is achieved. The mixing chamber has an inner volume capacity of 10 µl. At a maximum flow rate of 4 L/h a mixing time below 4 ms is achieved. The mixing structure in a CPMM has a width of 300 µm and consists of 12 units. In each unit, the fluids are mixed in the split and recombine approach. Ideally, this leads to the formation of 4096 (= 2^{12}) lamellas. However, in realistic operation,

increased internal friction leads to lamellas flow distortions. These transversal forces dominate the flow profile with increasing distance in the mixing chamber, which in the end causes rather turbulence mixing and results in a chaotic flow profile [165,166]. By this efficient "controlled" turbulence mixing, a mixing time $t_{M,95\%}$ can be reached within milliseconds. The inlets of the CPMM are parallel, which minimize the impact of asymmetrical flows and the mixing times stays almost constant [166].

Figure 9. Flow conditions and concentration profile across the 300 μm caterpillar mixer. Copyright © 2012, De Gruyter. Asked for permission) [166].

Moreover, increasing the flow rates increases turbulences, which improve mixing efficiency and quality. Due to its robust construction and the advantageous low tendency for plugging, the CPMM is a micromixer type often used. Additionally, CPMM is available with larger inner diameters (600 and 1200 μm) giving the possibility of scaling up the production [167].

Compared to the SIMM or star-laminator, which have higher plugging risk, or the impinging-jet micromixer, which is wall-free and incapable to be connected with a residence loop, the CPMM is suitable for fast mixing and high throughput and can be used for precipitation reactions such as MNP synthesis with low plugging probability under pressure (up to 100 bar) and high flow rates. The narrow channels inside the micromixer allow rapid nucleation favouring the formation of uniform particle seeds. Particle growth takes place in the following residence loop, which enables the

separation between nucleation and growth phases (Figure 10). The residence loop has a total volume in the millilitre range. The fast mass and temperature transfer in the developed set-up including the micromixer (nucleation phase) and the connected residence loop or dwell zone (growth phase) offer excellent conditions for controlled MNP synthesis. Some technical specifications of the CPMM-R300 micromixer type are summarized in Table 2.

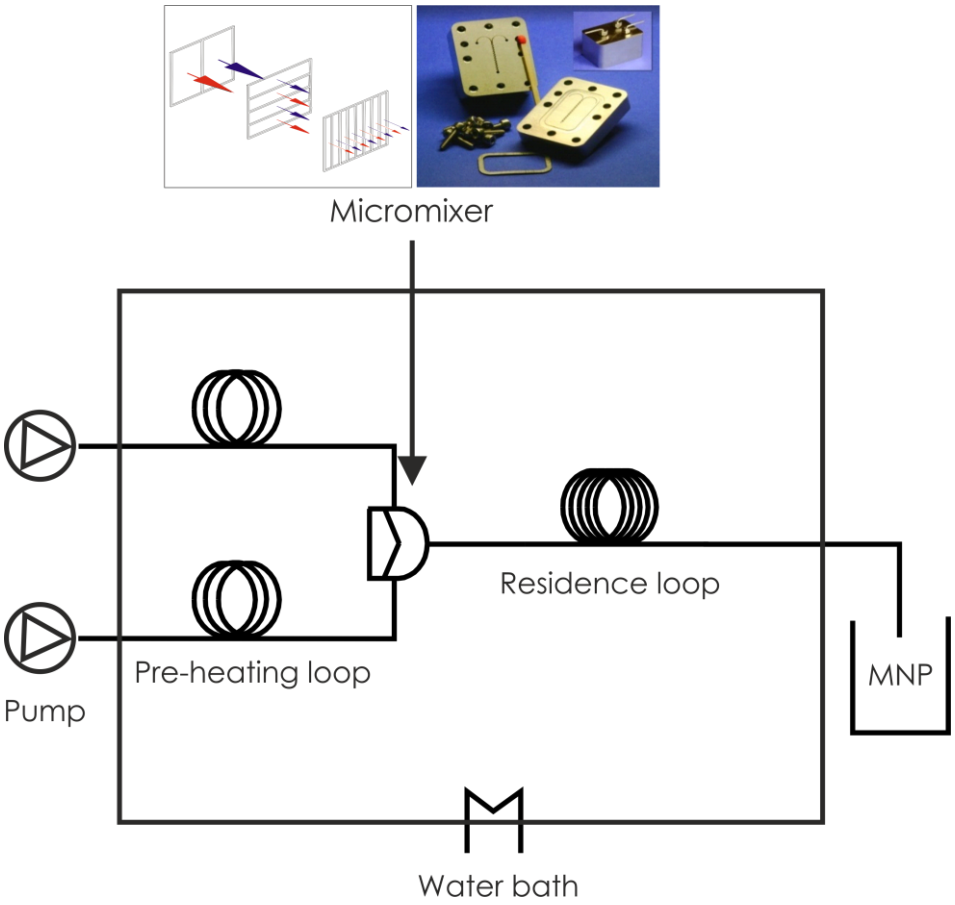

Figure 10. Schematic representation of continuous micromixer synthesis of MNP. Top row: The CPMM following the split and recombine principle. Left: Design principle and mixing of two precursor materials visualized as red and blue arrows. Right: Photograph of the caterpillar structure inside the CPMM-R300 developed at Fraunhofer IMM. Bottom: Synthesis process scheme, the precursors are pumped into the micromixer, where the MNP are precipitated with subsequent growth in the residence loop. To control the reaction and residence temperature, a water bath is used.

Table 2. Specifications of the CPMM-R300 (Fraunhofer IMM)

type	CPMM-R300
Size (L x B x H) [mm]	60 x 45 x 20
Standard mixing channels [µm]	300 x 300
Inner volume [µL]	10
Material- Stainless steel	1.4435
Temperature [°C]	-40 – 220
Pressure [bar]	100
Flow rate [L/h]	0.5 – 4
Residence time [ms]	3.6 – 72

The impact of temperature and residence time variation on the properties of continuously synthesized MNP are investigated in the publication: (*Nanomaterials*, paper No. 3). Here, continuously synthesized MNP using the CPMM-R300 micromixer were compared with MNP obtained by conventional synthesis routes.

2.3 Stabilization of MNP

The colloidal stability of MNP in a suspension depends on the concurring interactions between the huge number of individual nanoparticles, e.g., dipole-dipole interactions between the MNP. By exposure of a concentrated suspension of MNP to an external magnetic field, the effective magnetic field seen by each MNP is reduced because of the demagnetizing effect caused by the dipolar fields of all other MNP. Thus, changing the concentration of an MNP suspension might change their magnetic properties. Moreover, clustering of MNP leads (for large moment particles) to weaker magnetic response because of the increased dipole-dipole interactions and potential transition from Brownian to Neel relaxation [168]. Additionally, forces acting between the surface atoms and the surrounding environment, i.e. solvent, ligands or other nanoparticles in the medium possibly alter the magnetic behaviour of the MNP [97].

Colloidal stability can be improved by both, increasing the repulsion or decreasing the attraction between the particles in the dispersion. This can be achieved by various stabilization approaches. In **electrostatic stabilization**, the attractive van der Waals force is counterbalanced by the repulsive coulomb force of the negatively charged particle surface. Negatively charged surface ions attract counter-ions from the surrounding volume leading to a stabilizing electric double layer. **Steric stabilization** inhibits the approximation of neighbouring particles and hence their aggregation through adsorption of macromolecular stabilizers on the particles surface [169]. Polymers are ideally suited for steric stabilization. They can spatially expand and coil up in the suspension leading to an energy loss caused by elastic deformation. Furthermore, **depletion forces** can be used for colloidal stabilization involving unanchored (free) polymeric molecules which create forces between the particles [170].

Surface protection

Often, the surfaces of MNP have to be protected from external influences such as oxidation, which would convert magnetic magnetite to nonmagnetic hematite. Likewise, a protection against the presence of damaging substances such as strong acids (hydrochloric acid) could be necessary, which otherwise would lead to particle dissolution and the loss of their magnetic properties. Moreover, formation of reactive oxygen species (ROS) lead to reduced magnetic properties and could decline the biocompatibility of MNP [171]. Therefore, protective covering of the "bare" MNP is crucial part of the synthesis.

MNP surface coating can be achieved by two main approaches: in situ and post-synthetic coating [30]. For in situ coating, also known as one-pot synthesis, the coating material(s) are mixed with the precursors that form the MNP. Formation and coating of MNP take place simultaneously, which might negatively influence the crystallinity of the resulting MNP. Additionally, the pH-values of both, the MNP precipitation and the coating materials must be taken into consideration [172]. Post-synthetic coating can be achieved by ligand exchange, direct grafting, or hydrophobic interactions.

Surface modification can be achieved with organic compounds, mostly surfactants, polymers or di- and polysaccharides, or with an inorganic shell (e.g. silica) or metals. The selection of the stabilization mechanism has to be chosen based on the intended application field, as it also determines the possibilities for further functionalization of the particles with other ligands [173]. Polymers with functional groups such as carboxyl (carboxylic acids), phosphate or sulphate groups can be attached to the surface of MNP [53]. Examples of utilized coating materials for surface modifications of nanoparticles are pyrroles [174], polyacrylic acid [175], polyvinyl alcohol [176], and polyethylene glycol [177].

2.3.1 Functionalisation of MNP for biomedical applications

As already mentioned, MNP are of great interest for various biomedical applications, especially iron oxide nanoparticles because of their low toxicity [178]. Their small size, high saturation magnetization, and superparamagnetic behaviour make them preferable for biomedical applications due to the easy transport and distribution in physiological systems [179]. For successful in vivo and in vitro application, the long-term stability of MNP dispersions must be guaranteed. Moreover, prolonging the blood half-life and increasing the cellular internalization are required for successful translation into clinical applications. Furthermore, the surface properties of the MNP are very important for the inhibited recognition by the reticuloendothelial system (RES) recognition. Nanoparticles with a negatively charged surface exhibit less opsonisation, e.g. the covering of the NP by a protein corona, which will reduce unspecific NP uptake by phagocytosis, whereas a positively charged surface increases the interaction with a cell membrane and subsequently endocytosis [30]. Moreover, biocompatibility and suitable surface modification on the surface are particularly important for in-vivo cellular uptake of nanoparticles.

Functionalizing the surface of MNP with appropriate non-toxic, biocompatible, and biodegradable molecules can improve their half-life (stealth properties), enhance their colloidal stability and prevent their non-specific interaction with biological system components, e.g., serum proteins, blood, and endothelial cells. Additionally, by decorating MNP with medical active molecules multifunctional systems for theranostic applications are created [30].

Physisorption and chemisorption are further two strategies to coat the surfaces of MNP. Reversible physisorption is characterized by weak interactions (Van der Waals, hydrogen bonds, etc.) of surfactants, macromolecules and amphiphilic polymers on the surface of nanoparticles. The physical interaction between hydrophobic tails of an amphiphilic surfactant and hydrophobic ligands on the surface of MNP (e.g., MNP produced by thermal decomposition) leads to liposomal or micellar structures [180]. On the other hand, covalent bounds can be achieved by binding polymers that have

affinity to the complementary functional groups on the MNP surface to create a tethered chain [181].

The surface of MNP can be modified to increase a specific cellular binding employing different ligands such as antibodies, protein, peptides, or small molecules [30]. Organic polymers, metallic (e.g., gold) or other inorganic surfaces (e.g., silicon dioxide or aluminium oxide) are suitable for further modification or functionalization to enable the reaction with various bioactive molecules [182] .

2.3.2 Tannic acid used for MNP coating

Tannic acid (TA) is a natural product that is ingredient of many beverages such as green and black tee, beer, red wine and coffee and food such as grapes, peas, bananas, and chocolate. The chemical structure of TA (Figure 11) consists of organic polyphenol with sugar esters and like many other polyphenols, TA has antioxidant, anti-mutagenic, and anti-carcinogenic properties. It was also shown that TA has anti-proliferation activity in several cancer cell lines. Moreover, TA has affinity to bind to polyvalent cations in aqueous solution with complex formation. Additionally, the numerous phenol groups present in TA enable further functionalization [39,183]. Therefore, it was used as a stabilizer for iron oxide nanoparticles in this work.

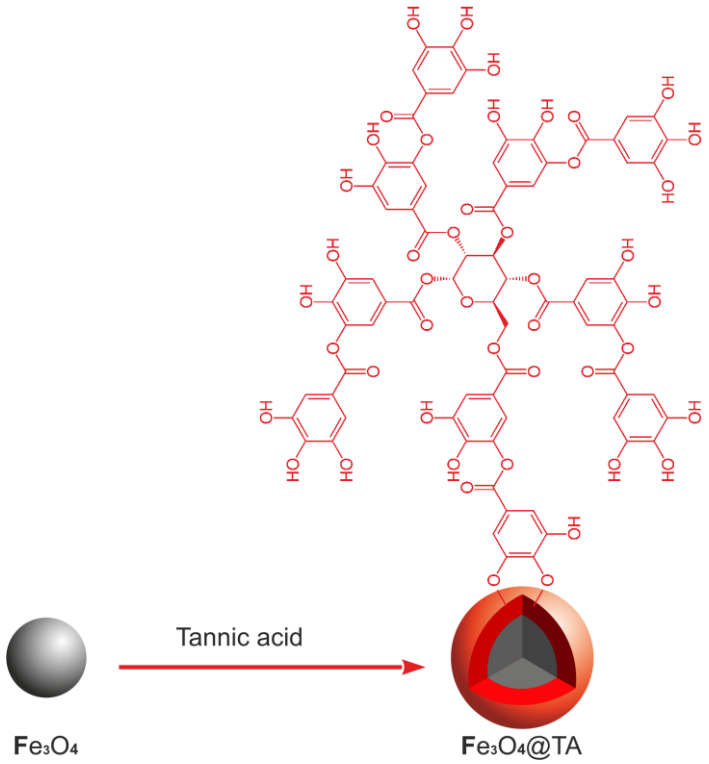

Figure 11. Structure of tannic acid used for MNP coating (adopted from [39]).

2.3.3 Serum albumin

Serum albumin (SA) is the most abundant protein in mammals with a molecular weight of about 66 kDa with negative charge. The water-soluble protein constitutes more than 50% of the blood plasma. The physiological function of SA is to maintain the pH and osmotic pressure of blood and to transport lipids and metabolites. Furthermore, SA is capable to transport drugs (covalent conjugated or adsorbed) with the blood stream and to facilitate a ligand-mediated association into cells [184].

Bovine serum albumin (BSA) is extensively used due to its good availability and ability to improve the colloidal stability of NP. Additionally, it has a similar sequence and structure as the human analogue human serum albumin (HSA). BSA is considered as a suitable biodegradable, biocompatible, and non-toxic coating material for MNP to improve their stability and prolong their circulation time [185–187]. Therefore, BSA coating was selected to further improve the synthesized MNP for their application in

biomedicine. The results are presented in publication: (*International Journal of Molecular Sciences IJMS*, paper No. 4).

3 Characterization methods

3.1 Transmission electron microscopy

Transmission electron microscopy (TEM) is an imaging technique to determine the geometry and structure of nano- and microscale objects.

In TEM, a beam of accelerated electrons is transmitted through the sample and partially scattered to form an image. Due to the smaller electron wavelength compared to the light wavelength used in optical microscopy, TEM-images of significantly higher resolution can be obtained. Generally, the maximum resolution of optical microscopy is estimated to be half of the wavelength of the used light. Thus, only particles up to 0.5 μm can be resolved by optical microscopy.

According to the wave-particle duality introduced by de Broglie [188], a corpuscular object like an electron of mass m and velocity v can be associated with a wavelength λ (Equation 5):

$$\lambda = \frac{h}{mv} \tag{5}$$

where h is Planck constant. The much shorter wavelength of the electrons used in TEM is depending on the energy of the electrons and enables a resolution up to approximately 0.2 nm.

The TEM design (illustrated in Figure 12) is similar to an optical microscope, save that the glass lenses are replaced by electromagnetic lenses. A tungsten cathode serves as a source (electron gun) for electron emission. The electrons are accelerated from the cathode to an anode within a vacuum chamber of about 1 m length thereby passing the sample. For this, high voltages of more than 10^5 Volt are used [189]. Images of the samples are taken by a CCD-camera.

Sample preparation is carried out on a thin cupper grid that is coated with a layer of carbon. A drop of a fluid nanoparticle sample is spread onto the grid and left drying. Then, the grid is fixed onto a holder that can be inserted into the vacuum chamber.

The drying procedure of the sample or general particle arrangements might lead to some uncertainty and ambiguity in the images, nevertheless TEM is used in this work as a fast and reliable technique to obtain information about morphology, size, and size distribution of the nanoparticle cores. The poor contrast of the organic coating of the magnetic nanoparticles and strong changes during the drying process on the copper grid limit the capability to extract information about the coating layer thickness and integrity from TEM imaging. However, from the observed spacing between the single cores, rough estimates of existence and dimensions of the coating layer can be obtained.

Image evaluation is carried out using the software ImageJ that determines the size distribution of a sample. After adjusting image sharpness and contrast using various filters, the image is converted into a black and white scaled image using a threshold value. Further criteria can be chosen during evaluation e.g., including only particles within a range of expected sizes, excluding erroneously detected "particles" such as pixel groups generated by noise or contamination, and defining a value for the circularity of the detected particles.

Since TEM resolves individual particles, a sufficiently large number of particles has to be included to obtain statistically significant results. The resulting mean parameters are arithmetic averages of the specific parameters determined for all selected particles. To minimize the effect of image selection and measurement adjustment, a minimum of 5000 particles taken from at least five different images is analysed.

Sample preparation in liquid environment can be investigated by Cryogenic Transmission Electron Microscopy (Cryo-TEM). Here, after dripping sample material onto the grid, the sample is shock-frozen in liquid propane (at about -42°C under ambient pressure) to avoid the formation of water crystals. Furthermore, Cryo-TEM is

used to obtain information about a biological sample preserving its natural environment.

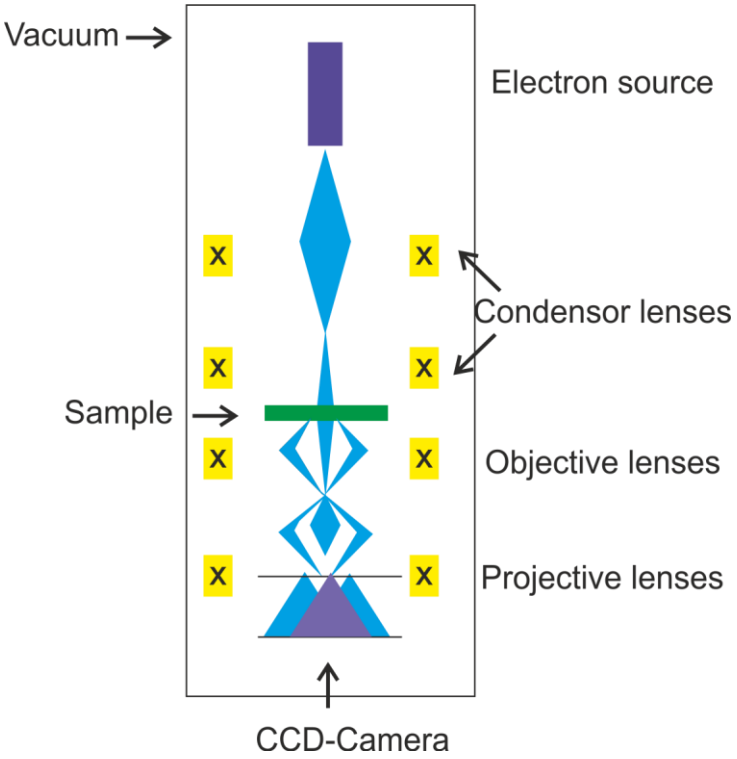

Figure 12. Illustration of the TEM principle. From the electron source, the tungsten cathode (Top), electrons are accelerated by a high voltage to the anode with the CCD camera (bottom) passing the grid with sample material on it. The path of the electrons is electromagnetically controlled and focused by a couple of coil systems (indicated by yellow crosses).

3.2 Differential centrifugal sedimentation

Differential Centrifugal Sedimentation (DCS) is a technique to determine the hydrodynamic size distribution of particles suspended in a liquid medium [190]. DCS applies centrifugal sedimentation to separate the particles with respect to their size and density in a gravitational field (Figure 13). Larger particles will sediment faster than smaller particles having the same density. The sedimentation can be described by Stokes' law (Equation 6):

$$\vartheta p = \frac{2\, r^2\, g\, (\rho_p - \rho_f\,)}{9\, n} \qquad (6)$$

where ϑp sedimentation velocity, r particle radius, g acceleration due to gravity, $\rho_p$particle density, ρ_f fluid density, n dynamic viscosity of fluid.

Since the sedimentation velocity increases with the square of particle radius, already small size differences lead to a significant change of the sedimentation velocity. Thus, hydrodynamic particle sizes can be differentiated with high resolution. Consequently, isolated (single-core) particles can be clearly distinguished from agglomerated particles.

Dynamic light scattering (DLS) is another method commonly used for determining the hydrodynamic diameter distribution of nanoparticles. In this work, DLS could not reliably resolve the hydrodynamic size distribution of the synthesized MNP since the light absorption by the nanoparticles with a large core size and only a thin tannic acid coating layer was too strong (in contrast to other polymeric coatings such as PEG that scatter the excitation light well). Therefore, DCS measurements were used, only.

In DCS measurements, the mean density of the core and shell materials should be taken in consideration to precisely determine the hydrodynamic diameter. In this work, a density of ϱ=5.2 g/cm^3 for the core material (magnetite) of MNP was used, neglecting a slight density reduction of the entire nanoparticle caused by the thin organic tannic acid coating layer. For BSA-coated MNP, the volume average of the core magnetite density ϱ=5.2 g/cm^3 and of ϱ_{BSA}=1.41 g/cm^3 for the shell material [191] with a hydrodynamic radius of $r_{h,BSA}$= 4 nm [192,193] were taken into account. Assuming a monolayer of BSA with a thickness of $d_{h,BSA}$=8 nm and an MNP core diameter of d_c~ 30 nm, a mean density $\varrho_{BSA\text{-}MNP}$~ 2.4 g/cm^3 for BSA-coated MNP was estimated and used for the hydrodynamic diameter determination by DCS.

A DCS measurement is carried out by injecting a sample volume of about 100 µL into the centre of a rotating disk. By the gravitational forces produced by the high rotation velocity (up to 24,000 rpm), the particles are driven through a density gradient (sucrose gradient) to the outer edge of the disk, where a light source (λ=470 nm) and a detector are located. When the particles approach the outer edge of the disc, they are detected

by absorption as they pass the light beam. The time required to reach the detector corresponds to a particular fraction of the hydrodynamic particle size distribution according to Stokes' law and Mie's theory of light scattering. Polyvinyl chloride (PVC) or Silica (SiO_2) particles of defined sizes are used for calibration of a DCS device [194].

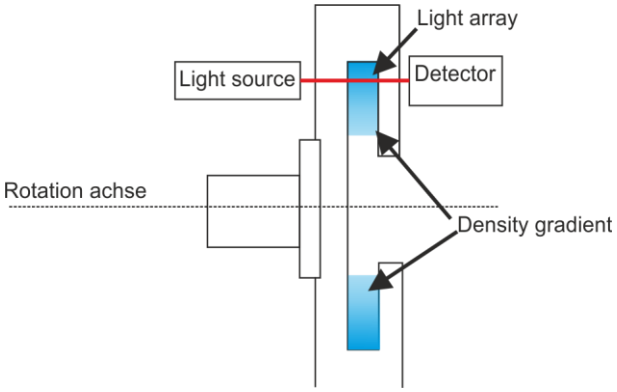

Figure 13. Illustration of the DCS principle. The particles are injected into the centre of the rotating disc and driven by gravitational force through a sugar matrix with density gradient. By arriving at the outer edge of the disc, they are detected by passing the light beam (adopted from [194]).

Data evaluation is carried out by the software Origin®. In this work, the volume weighted data set is analysed. In a data set, each peak is approximated by a Gaussian curve using an automatic fitting from which the mean peak position and distribution width are extracted.

3.3 X-ray diffraction

X-ray diffraction (XRD) is a technique used to determine the crystal structure and composition of a sample. The crystalline structure scatters an incident X-ray beam into specific directions as described by the Bragg equation (Equation 7):

$$n\lambda = 2d\,\sin\theta \qquad (7)$$

where n = 1, 2, 3, …, denotes the order of scattering, λ the wavelength of the radiation, d spacing between lattice planes, and θ the angle between incident and reflected beam.

A diffraction pattern is obtained by plotting the intensity of the reflected beam against 2θ. The main peak positions of the XRD spectra can be analyzed according to values reported in literatures [195–197].

3.4 Magnetic particle spectroscopy

Magnetic particle spectroscopy (MPS) derived from magnetic particle imaging (MPI) is a powerful tool to detect the non-linear dynamic magnetic response of MNP exposed to an alternating magnetic field. Though it was originally developed to determine the performance of a nanoparticle tracer in MPI and can be considered as a zero-dimensional MPI scanner [198], it has become an independent, highly sensitive, versatile platform for investigating MNP in different biological environments [199], for quantifying the cellular uptake of MNP [200], and for cell labelling and tracking [201].

In MPS, an alternating sinusoidal magnetic excitation field is applied to generate the non-linear magnetic dynamic response of the MNP (the non-linear magnetization curve of MNP as displayed in Figure 2, see section 2.1.2). Operating at an excitation frequency of typically 25 kHz, dedicated (gradiometric) coil systems are used to acquire the MNP response as a function of time. Operated in a batch mode, a sample volume of about 10-30 µL is filled into a PCR tube and positioned into the detection coil system. Typically, the temporal response of the MNP is recorded for about 10 s and averaged. By Fourier transformation the MPS spectra are obtained containing a kind of fingerprint for a given MNP system the dynamic magnetic moments A_i (i=1,3,5,…) of the excitation frequency f_0. Since the basic excitation field is contained in A_1 of the response, this harmonic is discarded (technically, a gradiometric detection coil arrangement and high-pass filtering are applied to suppress the excitation entering and saturating the receiving unit). To evaluate the MNP performance, three characteristic parameters are used, the A_3*, which represent the amplitude of the third harmonics normalized to the iron amount, A_5/A_3, representing the ratio between fifth

and third harmonic, and the phase of the 3rd harmonic ϕ_3. The latter two parameters are advantageous, since they are independent of the (exact) iron amount in the sample, in contrast to A_3*, for which the accurate knowledge of the iron concentration c(Fe) and sample volume V_S of the sample under investigation is mandatory. For comparison, the MRI liver contrast agent Resovist has become a kind of gold standard as a reference MPI tracer.

Recently, online-MPS measurements were demonstrated using a novel benchtop magnetic particle spectrometer with an integrated flow cell. The MPS was connected directly to the growth stage of the micromixer platform. The advantage of this method is its capability to directly monitor alterations of magnetic parameters when changing one or more synthesis parameters during the micromixer synthesis [202].

3.5 Static (DC) magnetization

Static or DC-magnetization (DCM) measurements are used to determine the magnetization $M(H,T)$ of a MNP sample in thermal equilibrium at a given external magnetic field H and temperature T. From the $M(H,T)$ curve the saturation magnetization M_S of an MNP sample can be determined, e.g. the value of the magnetization M that does not change upon further increasing the applied magnetic field H. For a high measurement sensitivity, a magnetic sensor based on a Superconducting Quantum Interference Device (SQUID) is employed to measure the current induced in the pick-up coil. Modern DC magnetometer operate in the field range up -5 T to 5 T and temperatures covering the range 1.3 K to 400 K.

3.6 AC susceptibility

AC susceptibility (ACS) measurements are an important tool for characterizing MNP [203]. To measure the ACS, a small sinusoidal magnetic field (typically smaller than 1 mT, e.g., small enough to ensure a linear response of the MNP, see Figure 2) is applied to a sample and the resulting AC moments of the MNP are measured. Because

the induced sample moment is time-dependent, AC measurements yield information about magnetization dynamics which are not obtained in DC measurements, where the sample moment is constant during the measurement time. It measures the differential (d*M*/d*H*) response of the MNP magnetization exposed to drive magnetic field with operating frequencies ranging from 1 Hz to 100 kHz [204].

In this method, a sinusoidal magnetic excitation field is generated by a cylindrical coil. The amplitude of the excitation field must be low enough to ensure a linear magnetization response of the MNP (otherwise MPS would be carried out). A gradiometer pick-up coil system is used, consisting of two identical coils connected anti-serially and positioned inside the excitation coil, so that the signal of the excitation coil cancels out. When placing a MNP sample inside one of the two detection coils, the AC response is phase sensitively detected by a lock-in amplifier, as real part χ' and imaginary part χ'' of the AC-magnetization divided by the excitation field amplitude *H* at a given frequency *f* (Figure 14). Using the Debye-model the ACS can be described as (Equation 8):

$$\chi' = \chi_0 \frac{1}{1 + (\omega\tau)^2} \tag{8}$$

And (Equation 9)

$$\chi'' = \chi_0 \frac{\omega\tau}{1 + (\omega\tau)^2} s \tag{9}$$

where, χ_0 is static susceptibility, ω the angular frequency $\omega = 2\pi f$ (*f* is the excitation frequency), and τ the characteristic relaxation time, which is related to the Neel and Brownian relaxation time (section 2.1.2).

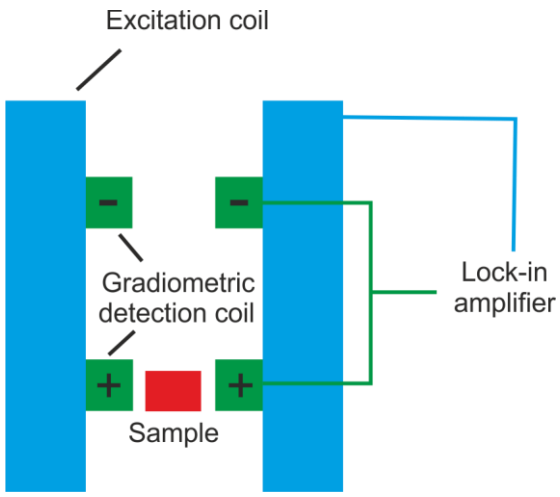

Figure 14. Illustration of the ACS principle. When a sample is located inside one of the two gradiometric detection coils (green), the AC response of the driving oscillating magnetic field provided by the excitation coil (blue) can be detected sensitively by the lock-in amplifier (adopted from [205]).

3.7 Nuclear magnetic resonance relaxivities (MNP as contrast agent)

MNP alter primarily the transversal relaxation T_2 of water protons in the vicinity of the particle. When MNP are present in tissue, the large magnetic moments of the MNP align with the strong external magnetic field of the MRI device thereby creating huge heterogeneous stray fields through which water protons diffuse. This causes efficient spin dephasing and shortening of the T_2 relaxation time leading to a decrease in signal intensity [206]. The contrast provided by MNP in a T_2 weighted image is termed negative contrast enhancement since areas with high MNP concentrations appear darker in the MR images. In contrast, ultrasmall iron oxide MNP with core diameters below 10 nm, are capable of producing positive contrasts in T1 weighted images [207]. Therefore, the knowledge of the longitudinal and transversal relaxation times T_1 and T_2 for a given MNP system is important to assess its performance as an MRI contrast agent. For this purpose, nuclear magnetic resonance (NMR) devices have been developed that are capable to determine the influence of the MNP concentration on the transversal T_2 and longitudinal T_1 relaxation times, also known as NMR relaxivities r_1 and r_2.

A spectroscopic NMR system works on the same physical principles as MRI but without using magnetic field gradients for spatial encoding. In general, NMR allows

higher sensitives compared to MRI due to the lack of magnetic gradients and much smaller coil geometries. In this work, NMR relaxivity measurements were performed using a commercial NMR relaxometer (mq 60, Bruker BioSpin). A homogenous magnetic field of 1.5 T is provided by a permanent magnet additional coils are used to generate the RF-pulses and to acquire the proton signals. Sample volumes up to about 500 µL can be measured, limited by the spatial sensitivity profile of the receive coil. MNP quantification was performed using a Carr-Purcell-Meiboom-Gill (CPMG) spin-echo sequence to determine r_2 [208] (Figure 15). This sequence uses an initial 90°-pulse for excitation of the proton spins, followed by a train of 180°-pulses for signal refocusing the spins at time intervals n ·TE – TE/2, ($n \in$ N). The transverse magnetization is measured at the so-called echo times n·TE. The transverse relaxation time is calculated by performing a mono-exponential fit using the signal amplitudes acquired for varying TE. The choice of TE has to be adapted depending on the MNP concentration to cover most of the exponential signal decay, with a minimal achievable TE ≥ 0.04 ms.

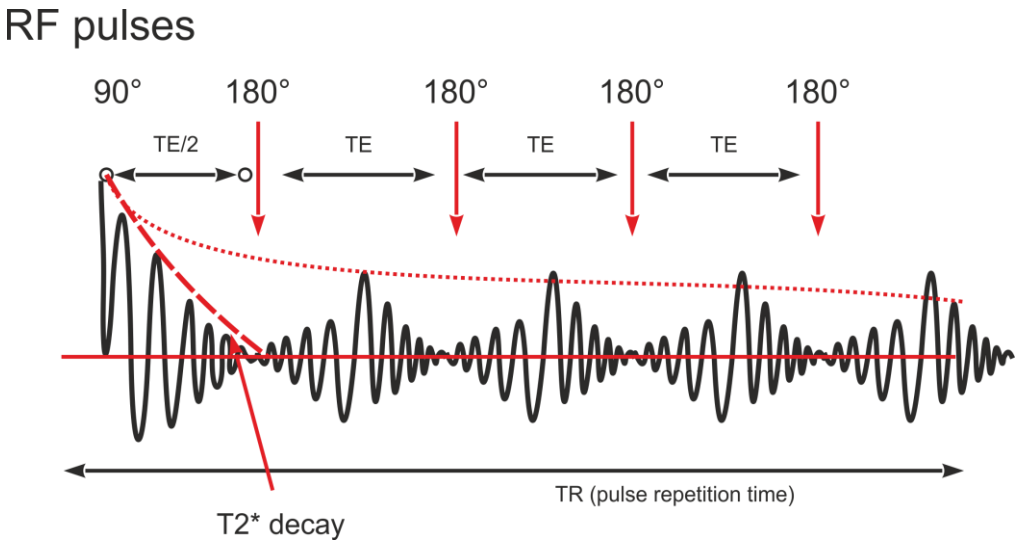

Figure 15: Carr-Purcell-Meiboom-Gill (CPMG) radiofrequency (RF) pulse sequence to determine the T_2-relaxation: Timing of the RF-pulses transmitted into the sample and FID (T_2* decay, dashed line) and spin echoes detected by the receiver coil of the relaxometry device. Typically, several hundreds RF pulses are applied in a single sequence. The envelope of the spin echo maxima decays exponentially with the time constant T_2.

To determine the longitudinal relaxation time T_1 a 2-pulse inversion-recovery sequence (see Figure 16). At time point t=0 a 180° pulse is applied to turn (invert by

180°) the magnetization M0 from +z to -z. Then, after the time interval τ during which the magnetization partially can relax back to +z, a 90° pulse is applied to the sample to probe the magnetization component that already has been returned to +z appearing as an FID. By stepwise increasing τ and analysing the FID after the 90° pulse, $M_z(\tau)$ is obtained e.g. the component of M_0 that has returned back to +z. By fitting the model $M_z(\tau)=M_0$ (1-2exp(-t/T_1), the longitudinal relaxation time T_1 is extracted. To avoid saturation effects, the repetition time TR between two subsequent inversion recovery sequences should at least by 5· T_1 so that the magnetization has completely returned to +z before the 180° is applied.

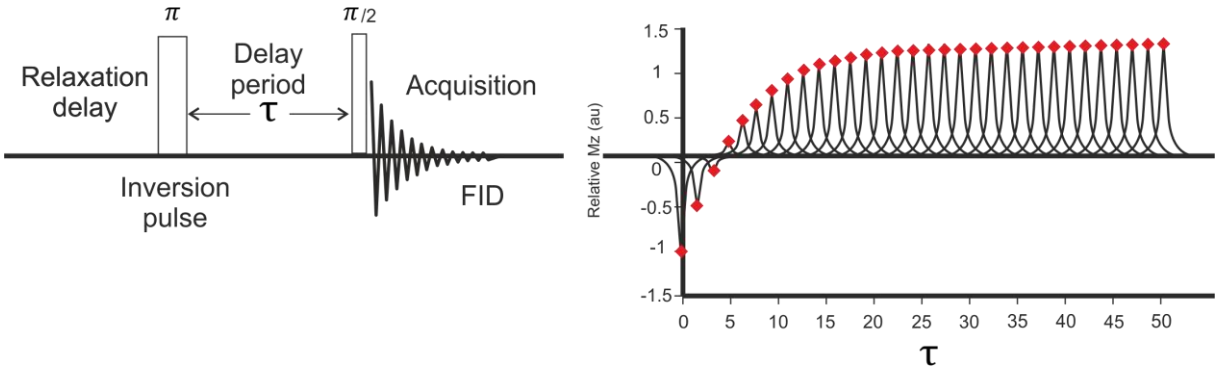

Figure 16: Inversion recovery pulse sequence to measure the T_1 relaxation time constant by NMR relaxometry. Left: 180° inversion pulse and 90° recovery pulse after time interval τ followed by the FID. Right: By repeating the sequence with stepwise increasing τ, the return of the longitudinal magnetization M_0 from -z to +z is extracted from the FID.

From the graphs of the iron-concentration c(Fe) dependent relaxation times r_1 and r_2 (r_1 = 1/ T_1 and r_2 = 1/ T_2), the corresponding relaxivities r_1 and r_2 (in units of L·mol^{-1}·s^{-1}) are determined (Figure 17). For graphical presentation the measured relaxation rates of a pure water sample (without any nanoparticles) is commonly subtracted.

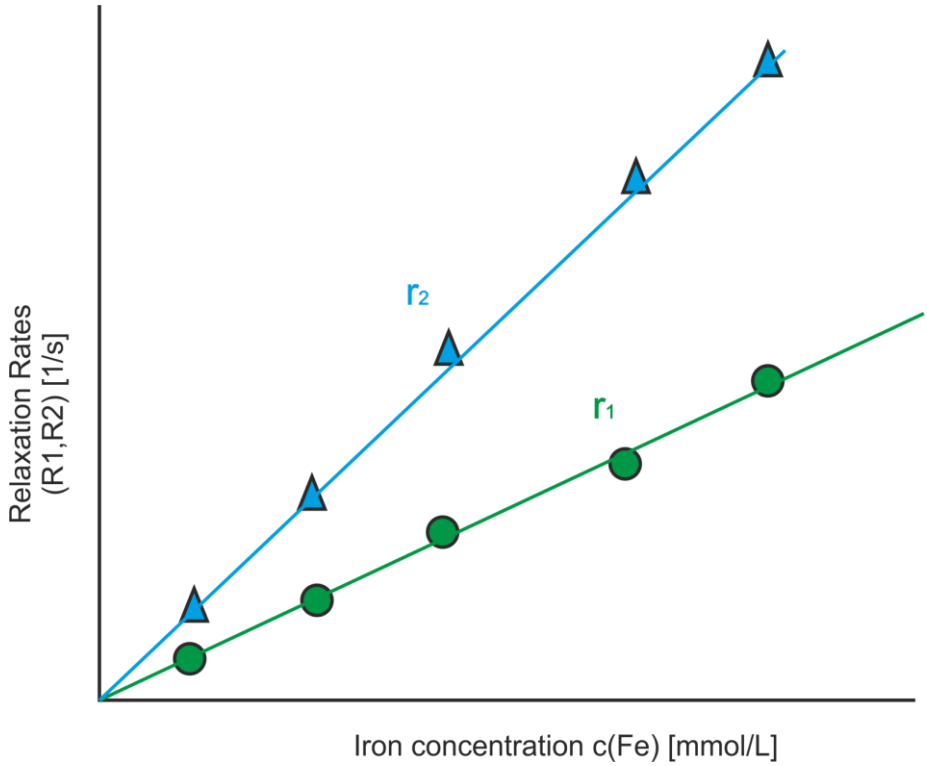

Figure 17. NMR proton relaxation rates $R_1 = 1/T_1$ and $R_2 = 1/T_2$ as a function of the iron concentration c(Fe). The slopes represent the relaxation rates r_1 and r_2.

4 Objectives

Magnetic iron oxide nanoparticles are well investigated and popular systems developed for numerous biomedical applications. Conventional synthesis routes provide MNP with core diameters up to 20 nm and clusters or aggregated magnetic structures larger than 40 nm.

This work aimed on establishing the continuous micromixer synthesis addressing five major aspects:

- Applying the micromixer synthesis to produce single core MNP with core sizes between 20 and 40 nm without forming any aggregates or clusters during synthesis to demonstrate the capability and high quality of the resulting MNP for their diagnostic and therapeutic biomedical application. (Publication: *Nanoscale advances*, No. 2).
- Further developing the micromixer synthesis with focus on sustainability and reliability. The entire synthesis route is shown to be aqueous, green, rapid, reproducible, and scalable with low energy consumption. This leads to an improved continuous manufacturing employing micromixer technology. (Publication: *Bioengineering,* No. 1, *Nanomaterials, No. 3*).
- Enhance the process control to achieve a higher product quality than batch synthesis approaches. (Publication: *Nanomaterials* No. 3,).
- Identify and assess physicochemical and magnetic properties for relevant biomedical applications in diagnostic imaging and treatment of diseases (Publication: *Nanoscale Advances* No. 2,).
- Further modify the surfaces of synthesized magnetic nanoparticles enabling their stable and reliable application in physiological environment. (Publication: *Nanoscale Advances* No. 2, *International Journal of Molecular Sciences*, No. 4).

5 Results and discussion (Publications)

5.1 Advances in Magnetic Nanoparticles Engineering for Biomedical Applications—A Review

Published in: ***Bioengineering, impact factor (Tracked for impact factor)***

In this review, the basics of common synthesis approaches to produce magnetic nanoparticles (MNP) are presented. The magnetic and physiological properties of the MNP as well as their specific biomedical application fields are addressed.

For this purpose, well established, conventional synthesis approaches together with recent, chemical and bio-based synthetic routes for MNP production are discussed and compared. The mechanism of MNP formation was explained forming the basis for the development of continuously synthesized MNP produced in this work. Furthermore, biomedical applications of MNP in diagnosis and therapy are introduced.

To this end, the state of the art of production and applications of MNP are investigated and summarized. The quality and performance of MNP produced in this work are compared with MNP obtained by other synthesis methods.

The publication draft is written and revised by me, Abdulkader Baki.

bioengineering

MDPI

Review

Advances in Magnetic Nanoparticles Engineering for Biomedical Applications—A Review

Abdulkader Baki [1], Frank Wiekhorst [2] and Regina Bleul [1,*]

[1] Fraunhofer Institute for Microengineering and Microsystems IMM, Carl-Zeiss-Straße 18-20,
55129 Mainz, Germany; Abdulkader.Baki@imm-extern.fraunhofer.de
[2] Physikalisch-Technische Bundesanstalt, Abbestraße 2-12, 10587 Berlin, Germany; Frank.Wiekhorst@ptb.de
* Correspondence: Regina.bleul@imm.fraunhofer.de

Abstract: Magnetic iron oxide nanoparticles (MNPs) have been developed and applied for a broad range of biomedical applications, such as diagnostic imaging, magnetic fluid hyperthermia, targeted drug delivery, gene therapy and tissue repair. As one key element, reproducible synthesis routes of MNPs are capable of controlling and adjusting structure, size, shape and magnetic properties are mandatory. In this review, we discuss advanced methods for engineering and utilizing MNPs, such as continuous synthesis approaches using microtechnologies and the biosynthesis of magnetosomes, biotechnological synthesized iron oxide nanoparticles from bacteria. We compare the technologies and resulting MNPs with conventional synthetic routes. Prominent biomedical applications of the MNPs such as diagnostic imaging, magnetic fluid hyperthermia, targeted drug delivery and magnetic actuation in micro/nanorobots will be presented.

Keywords: magnetic nanoparticle synthesis; microfluidic systems; microreactor; magnetosomes; magnetic resonance imaging; magnetic particle imaging; magnetic fluid hyperthermia; drug delivery; magnetic actuation; micro/nanorobotics

1. Introduction

In 1959, Richard Feynman drew the attention of scientists to the significance of size and miniaturization of materials with his famous lecture "*There is plenty of room at the bottom"* [1,2]. After the starting gun had been fired, many methods were developed to manipulate atoms chemically to form nanoparticles and engineer nanomaterials. Subsequently, the scientific community became fascinated with the enhanced functional properties of nanomaterials compared to the corresponding bulk materials [3], and opening the door for plenty of technical and medical applications.

In this way, the unique properties of magnetic nanoparticles (MNPs) have been broadly studied for potential biomedical applications in the last decades. In particular, their magnetic properties strongly differ from bulk materials and become size-dependent [4,5]. A deeper understanding of the magnetic behavior of MNPs with respect to size was gained by applying domain theory [6], realizing that the behavior of magnetic material changes if the geometrical extension is reduced below a critical value, the so-called critical diameter d_{cr}, which is normally a few tens of nanometers [7]. MNPs below this size only consist of one single magnetic domain, where all individual atomic magnetic moments of a MNP are uniformly coupled to exhibit a huge total magnetic moment. Above a certain temperature, thermal fluctuations permanently flip the magnetic moment of the MNPs into random directions so that no remnant magnetization will be measured for the MNP sample. Applying a magnetic field will (partially) align these moments leading to the strong magnetization of the MNPs that are exploited for the following applications: imaging, movement, heating or molecular sensing. MNPs with diameters > d_{cr} will comprise several magnetic domains, where inside each domain the individual magnetic moments are coupled and pointing in the same direction. By applying an external magnetic field, the structure of the domains can be altered, since it becomes energetically more favorable to form a larger domain with all moments aligned in the same direction. After removing the magnetic field, the MNP sample will exhibit remnant magnetization and show the typical hysteretic behavior, providing a powerful mechanism to produce

heat in magnetic fluid hyperthermia. Additionally, MNPs with sizes between 10 nm and 100 nm were reported to be suitable for successful clinical application. While MNPs with diameters below 10 nm are removed by renal clearance from the body, MNPs above 100 nm are eliminated by macrophages, mostly after accumulation in the liver and spleen [8]. Besides size, MNP core morphology is crucial for medical applications. 1D-nanostructures like rods or tubes exhibit longer circulation times than spherical MNPs due to an opsonin-independent phagocytosis [8,9]. MNPs with high saturation magnetization enable lower doses, and therefore minimize undesirable side effects [10]. Thus, nanorods and nanocubes show enhanced performance in magnetic hyperthermia therapy over spherical counterparts due to higher magnetization saturation [10,11]. In addition, the hollow nanotubes can be exploited for drug loading inside and functionalization at the surface [12]. On the other hand, rod-shaped structures exhibit higher toxicity than sphere-shaped MNPs [13,14]. However, not only the size and morphology, but also size distribution and chemical composition of the MNP core and coating are relevant characteristics [15]. Hence, specific MNP types have been designed for and utilized in a broad range of applications (Figure 1) such as diagnostic imaging [16–18], targeted drug delivery [19,20], magnetic fluid hyperthermia [21,22] and combined applications thereof, called theranostics [23,24]. Every application requires tailored MNPs with specific magnetic and structural properties, for which reproducible and reliable synthesis approaches to manufacture high-quality MNPs are mandatory [25]. Additionally, synthesis parameters e.g., temperature, educts concentration, mixing ratios, solvents and surface ligands must be controlled and adjusted to produce suitable MNPs. For a successful translation into clinical applications, requirements on the scalability, reproducibility and biocompatibility of the process and resulting MNPs are further aspects of utmost importance [26,27].

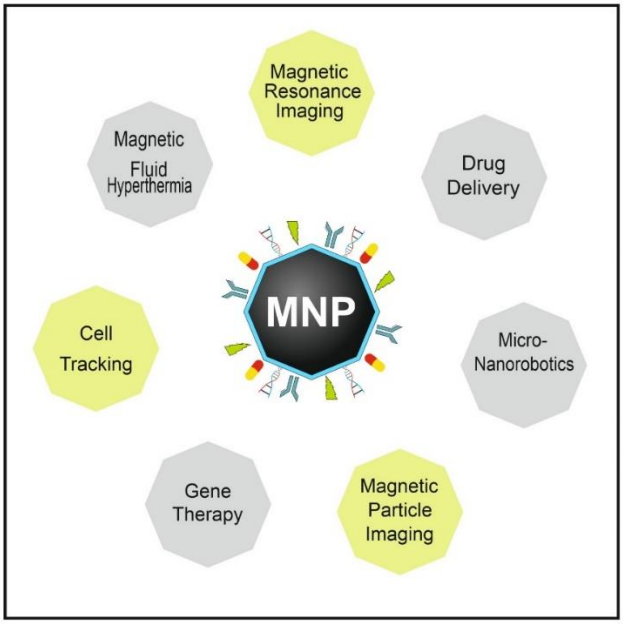

Figure 1. Biomedical application fields of MNPs. Due to the unique magnetic properties, the small particle diameter and the opportunity for additional functionalization with active substances connected to the surface, MNPs become ideally suited for diagnostic imaging (yellow: Magnetic Resonance Imaging, Magnetic Particle Imaging, cell tracking) and therapy (grey: gene transfection, drug-delivery, magnetic fluid hyperthermia, intervention by micro/nanorobots).

In the last few decades, numerous bottom-up synthesis routes based on conventional batch processes have been developed, such as co-precipitation [28–30], sol-gel [31,32], ultrasonication [33], thermal decom-position [34,35], microemulsion [36,37] and microwave assisted synthesis [38,39], as well as top-down methods such as e.g., laser ablation and me-chanical milling [40]. Because of the broad size and shape distribution of MNPs often produced by the top-down methods [41], bottom-up methods are preferable for medical applications. There, seed nucleation occurs when the precursors reach supersaturation (Figure 2). Subsequently, the particles grow by diffusion of solutes to the surface of the particles until a final size is reached, which is controlled by the solute concentration [42]. Stabilizing of the individual MNPs is crucial to prevent their aggregation to larger clusters [43]. During the nucleation and growth of the MNPs, factors such as surface energy, growth rate and temperature affect the final size, the size distribution, the crystal structure and the morphology, and thereby the magnetic properties of the product [43,44].

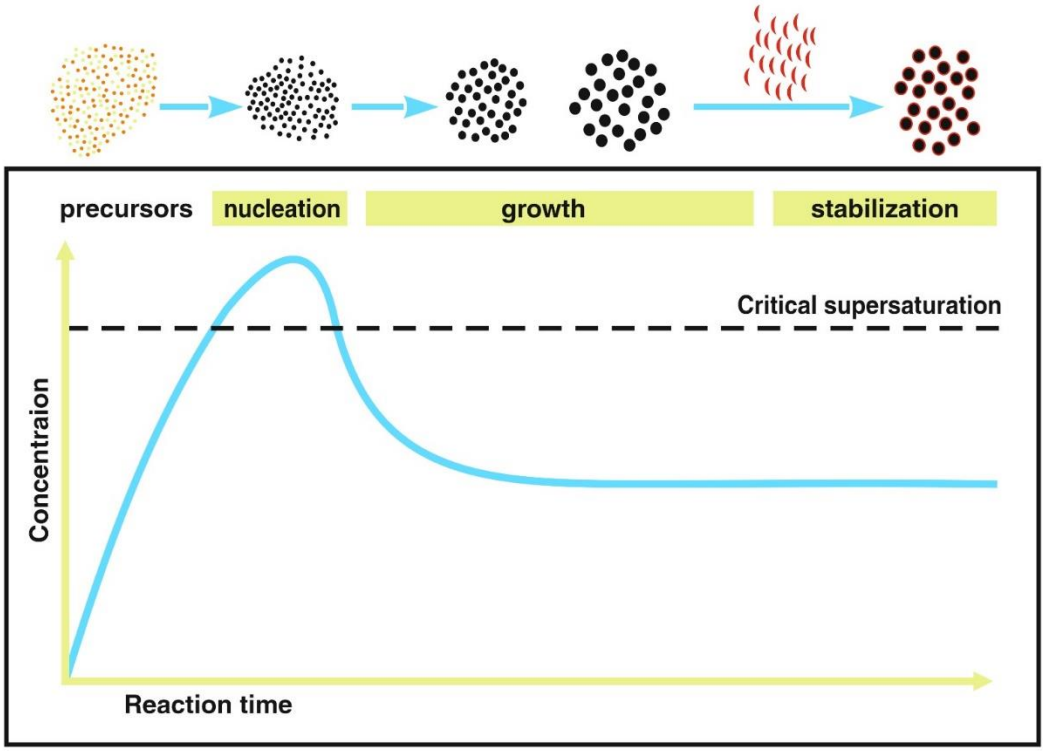

Figure 2. Steps during MNP synthesis in a bottom-up approach. When precursors reach supersaturation the nucleation of seeds occurs followed by growth. The stabilization of the MNP cores is carried out to prevent aggregation. Figure adapted from Ref [45].

Co-precipitation according to Massart's method [46] is the most commonly used and simplest conventional method for MNP production. Herein, a mixture of Fe^{2+}/Fe^{3+} is precipitated by adding an alkaline, such as sodium hydroxide (NaOH) or ammonium hydroxide (NH_4OH) at room or elevated temperatures (typically up to 100 °C). The pH-value of the reaction has a key role in controlling the properties of resulting MNPs [47]. Bhandari et al. presented a single step co-precipitation method for synthesizing curcumin functionalized MNPs that were employed to detect polychlorinated bi-phenyl 126, an inflammatory agent, in cell applications [48]. Thermal decomposition is another common MNP synthesis approach that relies on reactions of organometallic compounds, such as iron(iii) acetylacetonate $Fe(acac)_3$, tris (acetylacetonato)iron(iii) ($Fe(C_5H_7O_2)_3$) or iron pentacarbonyl ($Fe(CO)_5$) [6] at higher temperatures (typically 300 °C). Resulting MNPs consist of high-quality nanocrystals with narrow size distribution and uniformity in size and shape. Hyeon et al. fabricated cubic-shaped MNPs with sizes between 20–160 nm using $Fe(acac)_3$, oleic acid and benzyl ether at 290 °C by

varying reaction conditions [49]. A pioneer work on MNP production via thermal decomposition was presented by Krishnan group. By using iron(iii)-oleate as precursor and heating at 318 °C, they tailored polyethylene glycol (PEG)-coated MNPs with diameter of 26–28 nm and size and shape uniformity for cardio and cerebrovascular imaging applications [35,50]. In most batch approaches for MNP synthesis, a sufficiently homogeneous mixing and uniform heat transfer cannot be achieved due to the large size of the reaction volumes, especially in scaled-up batches [25,51]. Therefore, the control and adjustment of seed and growth conditions are inevitably reduced. This disadvantage circumvents microfluidic synthesis, an approach that by minimizing the synthesis equipment to a small chip size, achieves higher and more rapid control of reaction parameters such as mixing ratio, temperature and heat transfer, resulting in increased MNP size and shape uniformity with a narrower size distribution compared to batch synthesis [25,43]. Another unique approach is employed by nature in the biosynthesis, using magnetotactic bacteria (MTB), with outstanding uniformity of size and shape [52–54].

In the following, we review the latest developments in the synthesis of MNPs focusing on microfluidic methods. We compare those with conventional batch approaches and magnetosomes biosynthesis (Figure 3) regarding process requirements and efficiency for biomedical applications such as imaging, hyperthermia, drug delivery and magnetic actuation using micro/nanorobots.

2. Microfluidic Synthesis

In the last few decades, continuous flow processes, particularly using microfluidics have become a competitive and growing research field [55–59]. Scientists aim to optimize these methods to raise the quality of the produced MNPs and avoid typical drawbacks of conventional batch synthesis routes. Among others, these include inhomogeneous distribution of temperature, leading to hot spots that effect the reaction velocity locally and insufficient mixing, which cause concentration gradients. Both factors originate high batch-to-batch variability and a lack of reproducible product quality. As economic and ecologic drawbacks of conventional methods, e.g.,

the thermal decomposition method, high power demand due to reaction temperatures above 300 °C can be mentioned, as well as the use of organic solvents and toxic agents that might be present as undesirable residues in the final product [51,60–63]. Reaction routes in organic solvents are also generally time-consuming, as subsequent phase transfer to aqueous media is unavoidable before MNPs can act as imaging or therapeutic agents in biomedical applications. Microfluidic techniques have been discovered as promising approaches addressing the above-mentioned issues of conventional synthesis processes [64]. In microfluidic systems, the formation of products takes place in microchannels inside small devices called microreactors. The tiny paths increase the control of *reaction parameters* due to the high surface to volume ratio. Resulting in the following advantages: sufficient mixing in millisecond range and improved (rapid) heat and mass transfer. Additionally, the procedures offer other advantages such as flexible design and fabrication, fast change and screening of reaction parameters, cost efficiency, improved product quality, high throughput, higher reproducibility and the feasibility of automating the entire production process, including purification [27,65,66]. In contrast to conventional synthetic routes, continuous flow microreactors provide the separation of the two major steps during the formation of MNPs; (i) a rapid nucleation of the NP seeds occurs inside the microreactor, while the (ii) comparatively slow growth of NP takes place in the connected capillary, or ripening zone. Thus, a spatial and temporal separation of nucleation and growth can be achieved, leading to a high control of the particle formation process [67]. Generally, there are two main principles of mixing in the microreactor, (i) single-phase (continuous flow microfluidics) and (ii) multi-phase (droplet-phase or plaque flow microfluidics) [67,68]. In a single-phase or a continuous flow microfluidic system (Figure 3A), two or more miscible fluid streams containing the reagents flowing in a laminar stream are mixed in a homogenous phase by diffusion. Since the flow is laminar (turbulence free, e.g., Reynolds number < 10) [67], mixing is achieved by intermolecular diffusion. The mixing time is influenced by the flow rate and width of channels. A more effective mixing can be achieved at higher

Reynolds numbers due to turbulent advection through the folding and stretching of fluid streams [67]. Technically, this can be implemented, e.g., by using staggered herringbone mixers (Figure 3B), enabling helical flows [69]. T-junction, Y-mixing, capillary, coaxial tubes and different designs of static micromixers are also utilized as microreactors in microfluidic particle formation processes. The phase-homogeneity offers reliable control of reaction parameters, such as temperature and reaction time, which makes continuous microfluidic synthesis suitable for both non-magnetic [67,70], as well as for magnetic nanoparticle production [71–73]. Furthermore, the technique is capable for multi-step syntheses and the subsequent modification of the product [74]. In another approach, the droplet-phase or segmented flow microfluidic synthesis, two immiscible phases, either gas-liquid or liquid-liquid (typically an oil phase and a water phase) form a droplet. The formed droplets containing the reactants work as tiny reactors and are transported in a segmented flow. In this way, variations in the residence time due to the parabolic flow in continuous flow profile can be reduced. However, the control of droplet formation and the homogeneity of droplet size are crucial. Moreover, droplet coalescence has to be avoided to provide the same reaction conditions in each droplet, and to ensure a reliable processing [75]. The generation of droplets in segmented flow can be achieved by several techniques, which include T-junction, flow focusing and co-flow [76,77]. As shown in Figure 3C, the droplet is formed in a T-junction by shear forces and liquid-liquid interfacial tension at the surface of the capillary. The liquid with the lower interfacial tension (than the capillary wall) will form a continuous phase, while the other liquid acts as a dispersed phase [75]. Capillary width and geometry, the flow rate and viscosity of the streams all influence the droplet formation [78]. The viscosity of the continuous phase, together with viscous drag forces versus the surface tension of the capillary, determine the break-up of droplets, and is therefore a significant parameter influencing the droplet formation [79]. In the second way of flow segmentation (see Figure 3D), flow focusing, the continuous phase is injected from two sides symmetrically, and combined with the dispersed phase of the central channel. After passage through a narrow orifice into the

outlet capillary, stable droplets are formed [75,78]. Flow rate and geometric parameters of the setup influence the droplet characteristics [80]. In the third way, displayed in Figure 3E, a co-flow is used to produce segmented flow, where the dispersed phase is symmetrically enclosed by the continuous phase, both flowing in the same direction inside coaxial microchannels [81,82]. Segmented flow processing efficiently prevents the clogging and contamination of microchannels. Examples of MNP synthesis using segmented flow methods are reported in literature [83–85]. In contrast to continuous flow single phase processing, multistep reactions are challenging in segmented flow [67]. Moreover, to set up microfluidic processes for MNP synthesis successfully, numerous aspects have to be taken into consideration. These include: Flow profile inside the mixing structures as well as in capillary growth zones, capillary forces and material dependent surface effects, that can cause precipitation and agglomeration of MNPs on microwalls [86], leading to clogging of the capillary and finally process abortion [67]. Depending on the envisioned application, a careful material selection of the microfluidic device has to be performed. Photolithographic manufactured poly (dimethylsiloxane) (PDMS) microchips find broad application as the required equipment is easily available in many laboratories. However, their operation is limited regarding the process parameters such as flow rates, temperature and pressure. Usually, these chips can be run in a microliter per minute range. More resistant to pressure and temperature and suitable for higher flow rates are micromixers manufactured of stainless steel. However, the microstructuring of this inert material requires special and expensive microfabrication machining that is only available at specialized institutions and companies. Regarding possible throughputs and production scales, different approaches can be chosen. For *scale up through parallelization*, multiple micromixers are operated in parallel (or several parallel mixing structures are combined into one device), while for *internal scale up* the dimensions of the microchannels inside the microreactor are adjusted [87,88]. Scale-up through parallelization often lacks reliable processing, because as soon as one single channel is clogged, flow rates and flow profiles of all parallel mixers are disturbed. Consequently,

the product quality immediately decreases, and the whole run has to be discarded. Hessel et al. enlarged the fluid inlets for an internal scale up and reached a flow rate of up to 8 L/h for liquids at the viscosity of water and a pressure of 1.5 bar [88]. Lin et al. reported the high mass production of 4.4 g/h of iron oxide MNPs in their microfluidic system [89]. The throughput of the method here depends on educt concentrations, flow rates, and the temperature of the synthesis, which determine the structure and magnetic characteristics of the product [25].

3. Magnetosomes Biosynthesis

An elegant biotechnological alternative to the chemical synthesis of MNPs is magnetosome biosynthesis using MTB, which was first discoveredby Bellini in 1963 and Blackmore in 1975 independently [90,91]. Magnetosomes are single-domain MNPs and membrane enveloped [92,93]. The membrane is composed mainly of phospholipids and proteins [94]. In magnetosome biosynthesis, a variety of MTB are used as reactors for the formation of biomineralized crystals, which are aligned in chain-like agglomerates. In general, magnetosomes are uniform in shape and size within a specific strain but vary among different bacteria strains [52–54,95]. Magnetosome production depends on the cultivation of MTB for 36 to 60 h in complex media, supplemented with components that are essential for bacteria growth and magnetosome formulation such as yeast extract, minerals, ferric citrate, sodium lactate, magnesium sulfate and sodium thioglocate and ammonium chloride [96]. Additionally, a medium rich of iron ions, low dissolved oxygen concentration, neutral pH and moderate temperature range are some requirements for optimal biosynthesis [97]. The formation mechanism of magnetosomes is still not fully understood but can generally be divided into four major steps: (i) formation of the vesicle; (ii) magnetosome proteins are sorted to the vesicle membrane; (iii) iron is transported into the vesicle and mineralized as magnetite crystals; and (iv) magnetosomes are gathered in a chain-like structure and located for segregation during cell division. These steps of a complex process are controlled by over 40 genes, which encode the magnetosome-associated proteins. Thus, gen engineering and sequence modifications have key roles

in synthesis optimization [53]. After cultivation, magnetosomes should be extracted from MTB to be used for medical applications. Four main extraction methods were reported to lyse bacterial cells including: (i) mixing MTB with 5 M NaOH; (ii) sonication; (iii) French press; and (iv) pressure homogenization [96]. After extraction, a careful purification of the magnetosomes is required to remove undesirable components such as surface proteins and potential immunogenic lipid components [98]. Magnetosomes bioproduction offers a powerful and sophisticated MNP system for biomedical applications. However, mass production (mass production in gram scale and cultivation time between 36 to 60 days [52]) remains challenging. Furthermore, extensive purification of magnetosomes from bacterial cell components are inevitable for in-vivo applications. The complexity of process design and development, as well as the relatively long preparation time for a new developed mutant, are some limitations that have to be addressed in further developments to increase industrial relevance. Studies aimed at a comprehensive understanding of the role of specific genes and their potential for process optimization are still ongoing [99].

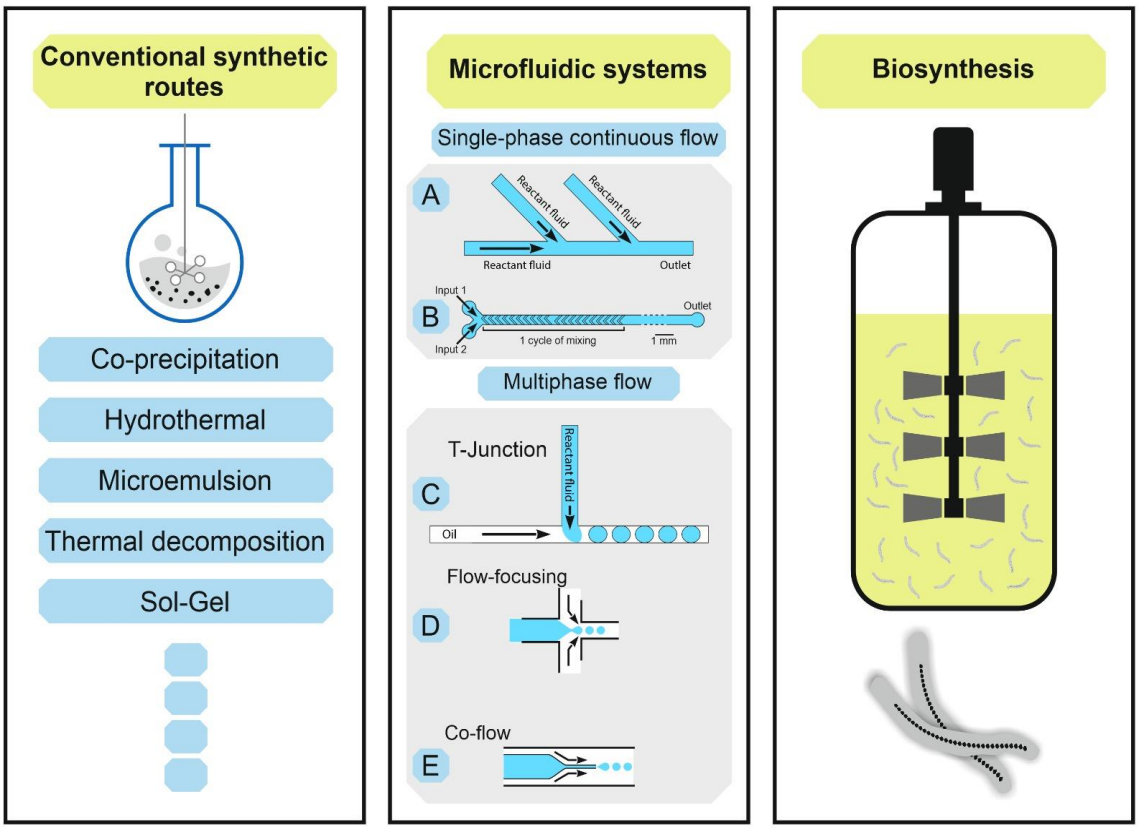

Figure 3. Synthetic routes of MNPs, left conventional synthetic routes in batch processes, middle microfluidic system with (**A**) homogenous continuous flow, (**B**) staggered herringbone mixer used in continuous flow (adopted from [100]), multiphase segmented flow (**C**) T-junction, (**D**) flow-focusing and E) co-flow (adopted from [101]), right is biosynthesis using MTB in fermenter.

4. Comparison of Different Syntheses

Recently, numerous techniques were developed to manufacture MNPs for different purposes (Figure 3). Conventional synthetic routes in batch are still dominant for many production processes. Although microfluidic and biosynthesis technologies promise enhanced production properties, especially for medical applications, they suffer from some drawbacks. In Table 1, we summarized the advantages and disadvantages of each technology.

Table 1. Comparison of conventional, microfluidic systems and biosynthesis of MNPs.

Parameter	Conventional Batch Methods	Microfluidic Systems	Magnetosome Biosynthesis
surface to volume ratio	about 100 m^2/m^3 [51,102]	10,000–50,000 m^2/m^3 [51,102]	-
mixing efficacy	mechanical stirring takes minutes to reach homogeneity [63]	homogenous, tunable, efficient, < 60 ms [70,103–106]	-
heat transfer	heating plate, heterogeneous, often require high temperature [25]	microchannels enable homogenous and rapid heat and cool transfer, small heat amount [67,70,86,103,105]	-
energy resource	conventional	conventional	ATP-based [52]
residence time	several hours to days	controllable and tuneable from seconds to minutes [25]	cultivation within 36 and 60 h [96]
separation between nucleation and growth stages	poor due to inhomogeneous mixing and heat transfer [25,51]	nucleation in the microreactor and growth in dwell zone [25,67,107–109]	nucleation in vesicle and the iron ions are transferred from the surrounding environment, protein-associated [53,54,110]
reaction time	minutes—hours [43]	seconds [25,86,105,111]	Several days to weeks [25,93,112]
control of reactions parameters	poor, except for thermal decomposition [50]	high due to efficient heat and mass transfer [67,103,105]	suitable environment required for bacteria growth [52,98]
reagent volume	millilitre to litre [44]	micro to nanolitre [44]	litre
purification	mandatory if solvents are used for phase-transfer and biocompatible coating [25]	on-line integration possible, e.g., Tangential Flow Filtration (TFF) [113]	magnetic separation, ultrasonication and removal of proteins, nucleic acids and lipopolysaccharides are mandatory to reduce immunotoxicity [98,114]. Coating (for example by poly-l-lysine) to obtain stable nonpyrogenic MNP suspension [115]
product homogeneity	quality reduction by concentration gradients and hot spots in the reaction flask [25,51]	enhanced quality due to homogeneous morphology, narrow size distribution [25,67,116]	high within one bacteria strain but strain variation possible [52–54,95]
reproducibility, production rate and scale-up capability	significant batch to batch variations in size, morphology, and magnetic properties [25,111,117–119], poor scaling up capability. A reported study from Lin et al. showed a production rate of 4.73 g/h for microfluidic synthesis	continuous production, no batch-to-batch variation, high scale-up capability	high at the defined environmental conditions [92], mg/(L· day) production rate [52], high scale-up capability, though challenging due to long term bacteriostatic growth conditions [38,40,46,78]

	comparing to 1.4 g/h for conventional synthesis with the same conditions [89]		
clogging	not applicable	microchannel-wall blocking during nucleation or by agglomeration [77,104,120–122]	not applicable
automation	poor	feasible/integratable [66,123,124]	-
capability of on-line characterization	not applicable for batch, though magnetic characterization of whole batches by magnetic particle spectroscopy is feasible	parameter control and synthesis adjustment feasible during synthesis, control of magnetic parameters by magnetic particle spectroscopy [25,125] and NMR [126]	-
cost	low, common lab equipment	expensive microreactor fabrication	expensive specialized equipment [112]
raw material and energy consumption	high, some reactions require organic solvents for phase-transfer to aqueous phase Some reactions are performed at temperatures above 320 °C [50,70,86,127]	aqueous synthesis at moderate temperatures feasible, raw materials and energy consumption can be saved [70,86,127]	sterile raw materials and cell cultivation materials required, temperature control during the bioproduction for days [52–54]
usability for medical applications	possible, long fabrication times, post-treatment and phase-transfer from organic solvents may be required [25]	possible, capable for sterile production, no FDA approved process yet [25]	possible due to biosynthesis, purification required to remove lipopolysaccharides [52,128]

5. Applications of MNPs

Magnetic nanoparticles have unique structural and magnetic properties that make them favorable as a tool for targeted transportation of active substances, generation of heat or local probe for imaging. In addition to their biocompatibility, stability, flexible surface modification, MNPs exhibit high magnetic moments that are utilized for biomedical applications [14,129,130]. Especially, iron oxide MNPs based on magnetite (Fe_3O_4) and maghemite (γ-Fe_2O_3) have been comprehensively studied. Resovist and Endorem are two examples of iron oxide MNPs that have been developed and applied as T_2-weighted contrast agents for clinical magnetic resonance imaging [129,131]. Coating the surface of MNPs prevents aggregation in physiological tissue and

bloodstream and enhances the biocompatibility. Often, it is a crucial step to prevent unwanted interactions of MNPs with their local biological environment as proteins and cells, and thus avoid their toxicity [132,133]. Commonly used coating materials are dextran [134–136] polyethylene glycol (PEG) [50,137] peptides [138] and serum albumin [132,139,140]. In this section, we present the latest developments in the translation of MNPs into biomedical applications like magnetic imaging, drug delivery, hyperthermia, and magnetic actuation.

5.1 Magnetic Imaging and Cell Tracking

Early diagnosis of diseases is advantageous in all treatment cases. Thus, imaging modalities have recently gained significant attention and are still developing. Magnetic resonance imaging (MRI) and magnetic particle imaging (MPI) are non-invasive imaging techniques that uses MNPs as contrast agents to deliver a high-resolution image without using ionizing radiation [132,141]. MRI detects the nuclear magnetic resonance signal of ^{1}H atoms after applying radiofrequency pulses. Hence, tissue environment rich of water molecules will generate a different MR signal than a carbohydrate or fat rich environment, leading to contrasted images to discriminate between different tissues [142]. Magnetic contrast agents can shorten the T_1 (longitudinal) and T_2 (or transverse) relaxation time of surrounding water protons. Thus, signal intensity of T_1-weighted images (positive contrast) will appear brighter and T_2-weighted (negative) images will appear darker, leading to images with higher resolution. The relaxivities $r_1 = 1/T_1$ and $r_2 = 1/T_2$ are used to characterize the MNPs [18,143,144]. Ultrasmall iron oxide nanoparticles (USIO NP) were reported in various studies as T_1-, T_2- and dual-weighted contrast agents in in-vitro as well as in-vivo experiments [141,145–151]. Shen et al. manufactured exceedingly small magnetic iron oxide nanoparticles (ES-MIONs) with a core diameter d_c = 3.6 nm by conventional co-precipitation and stabilization with polyacrylic acid (PAA). They resulted in r_1 = 8.8 and r_2 = 22.7 $L \cdot mmol^{-1}s^{-1}$ and a ratio of r_2/r_1 = 2.6 at a field strength of 1.5 T [152]. Whereas Besenhard et al. used continuous flow co-precipitation employing a millifluidic multistage flow reactor to produce dextran stabilized USIO NP. They

obtained diameters of d_c = 5.4 (core diameter) and d_h = 19 nm (hydrodynamic diameter) and higher relaxivity values r_1 = 10.7 L·mmol^{-1}s^{-1} and r_2 = 36.9 L·mmol^{-1}s^{-1} with a ratio of r_2/r_1 = 3.4 at a field strength of 1.5 T [153].

In contrast, MPI directly detects the non-linear dynamic magnetic response of the MNPs exposed to an (sinusoidally) oscillating magnetic field. Additional magnetic field gradients are used for spatial encoding of the MNP distribution in the measured object. MPI provides high spatial resolution (below one millimeter) and excellent temporal resolution (1–10 milliseconds) [154]. Theoretical calculations and experimental studies showed that optimized MNPs for MPI measurement are about d_c = 30 nm, which is not easily accessible by conventional synthesis routes [35,111]. The MPI performance of MNPs is characterized by the amplitude of the third harmonic normalized to the iron amount of the sample, A_3^* and the concentration-independent ratio between 5th and 3rd harmonic, A_5/A_3. Ferguson and Krishnan et al. reported 26–28 nm ±1.5 nm single-core MNPs with polyethylene glycol coating produced through thermal decomposition at 320 °C. The resulting MNPs have shown two to three-fold higher signal amplitudes compared to Resovist [35]. Resovist has been developed as MRI liver contrast agent and due to its good MPI performance became a gold standard for MPI measurements, even though it was withdrawn from the market, and they are not optimized for MPI [25].

Since MPI specifically detects the MNPs, the MP images are background-free, but do not provide any anatomical information. Thus, the combination of high-resolution 3D anatomical MRI data with molecular tracking of MNP tracers using MPI represents a promising hybrid MPI/MRI modality [155,156]. In a previous work, we presented our continuously synthesized MNPs via a micromixer in aqueous solution. After stabilization with tannic acid, the MNPs were coated with albumin which enhanced their colloidal stability in a physiological environment like a bloodstream. The MNPs exhibit diameters of dc = 27.7 nm and d_h = 42 nm and relaxivity values r_1 = 6.2 L·mmol^{-1}s^{-1} and r_2 = 600 L·mmol^{-1}s^{-1}, r_2 and a r_1/r_2 ratio and for MPI, a higher value for A_3^* = 26 Am^2/kg(Fe), A_5/A_3 ratio compared to Resovist (Table 2), which makes these

MNPs promising for clinical applications in the above-mentioned hybrid MP/MR imaging modality [132].

The magnetic performance of magnetosomes as potential contrast agents for MRI and MPI has also been studied [157]. Heinke et al. extracted magnetosomes and various mutants thereof from wild-type bacteria of the strain Magnetospirillum gryphiswaldense. They isolated magnetosomes with diameters of 36.5 nm for the wild type and of 23.0 nm to 44.2 nm for the mutants. Due to long range magnetic interactions in the larger crystal-lites, they formed chains and agglomerates. The r_1- and r_2 relativities and ratio r_2/r_1 of magnetosomes were determined at 0.94 T and 39 °C and showed higher r_2 relaxivities ($T2$-weighted) compared to Resovist (Table 2). The MPI measurements resulted in a 2.9- to 7.2-fold higher A_3*-value compared to Resovist [158].

Additionally, MPI and MRI can be utilized for cell tracking. Wang et al. developed cubic-shaped MNPs (edge length = 22 nm, d_h = 43 nm) for MPI to reveal in real time the migration and distribution pattern of transplanted bonemesenchymal stem cells given to hindlimb ischemia mice [159]. Song et al. coated 16 nm MNPs with a semiconducting polymer to fabricate the so called janus nanoparticles. After implanting these into mice, they showed efficient cell labeling and sensitive MPI tracking [160].

Table 2. Comparison of MNP properties for magnetic imaging (MRI, MPI) produced via microfluidic synthesis, conventional batch synthesis and biosynthesis. System information, coating and measurements field strength are given in the three columns to the left, followed by magnetic properties. Note, the specific non-linear dynamic susceptibility A_3* was determined by MPS at f_e = 25 kHz and an amplitude of B_e = 25 mT. All relaxivities are stated for a field strength of 1.5 T, except for the last three systems, wild type, mutant-3 magnetosomes and Resovist as standard-measurement to magnetosomes, which were measured at 0.94 T.

Sample System	Synthesis Approach	Coating	*Dc* *nm*	A_3* Am²/kg (Fe)	r_1 L/(mmol·s)	r_2 L/(mmol·s)	r_2/r_1	Ref
ES-MIONs	conventional co-precipitation	polyacrylic acid (PAA)	3.6	-	8.8	22.7	2.6	[152]
USIO NP	microfluidic multistage flow reactor	dextran	5.4		10.7	36.9	3.4	[153]

Single core MNPs	conventional thermal decomposition	Polyethylene glycol	26–28	26	-	-	-	[35]
Single core BSA-coated	continuously synthesized via micromixer	bovine serum albumin	27.7	26	6.2 (4)	600 (10)	97	[132]
Resovist, multi-core, bimodal size distribution mean cluster size 24 nm	conventional	carboxydextran T1.8 kDa	6	8,7	7.4 8.7	95 61	15	[132]
Wild type	MTB	Lipid bilayer	36.5	25–63	10.3	457	44.4	[158]
Mutant-3	MTB	Lipid bilayer	32		12.5	594	47.5	[158]
Resovist	conventional	carboxydextran	6		20.0	219	11.0	[158]

5.2 Hyperthermia

Hyperthermia is a powerful method for treating cancer cells by exposing tissue to elevated temperatures in a range of 42 °C to 48 °C. Since tumor cells are more sensitive to higher temperatures compared to healthy tissue, it can motivate either apoptosis (if the achieved temperature of the cells is below 45 °C) or necrosis (above 45 °C). Both apoptosis and necrosis have the capability to fight cancer cells with less damage of healthy human cells [161]. MNPs can be used to generate locally constrained heat at poorly accessible tissue regions by a magnetic fluid hyperthermia (MFH). An external alternating magnetic field of proper amplitude and frequency can be employed to generate heat by MNPs [162–165]. The enforced reorientation of the magnetic moments of the MNPs (either by the Néel mechanism of the moments inside the crystal structure or by Brownian rotation of the whole MNP) provides dissipative heat [166]. The efficiency of magnetic materials to generate heat in alternating magnetic fields is described by the specific absorption rate (SAR) or specific loss power (SLP). Besides frequency and amplitude of the applied magnetic field, the SAR strongly depends on structural and magnetic properties as shape, size distribution, crystallinity, saturation magnetization, anisotropy, relaxation time, concentration, and particle–particle

interactions [167]. For larger MNPs (>100 nm), the main source of heat generated is hysteresis loss. Generally, large MNPs have higher saturation magnetization and therefore a larger hysteresis loop, leading to higher heating efficiency and heat generation [168]. As a disadvantage of the large size, an increased aggregation tendency might reduce the SAR and make the MNPs suboptimal for targeted delivery into tumor cells [169]. In smaller MNPs consisting of only one single magnetic domain, Néel and Brownian mechanisms are relevant for heat generation [163]. Different synthesis strategies were developed regarding size, shape and anisotropy with promising results [22,170–172]. Continuously synthesized MNPs showed remarkably high SAR-values and are promising candidates for hyperthermia treatment [111]. Another promising candidate for hyperthermia is magnetosomes. Their large core size and cubic shape structure results in large heat production of both individual magnetosomes, as well as chains made of them [173–175]. However, magnetic field amplitudes should be higher than 10 mT to fully exploit the advantage of magnetosomes, otherwise the losses of heat per cycle will be smaller than those of chemically produced MNPs [176,177]. Le Fèvre coated magnetosomes with poly-L-lysine after removing the endotoxins. Magnetosomes-poly-L-lysine lead to improved antitumor efficacy with complete tumor regression achieved in 50% compared to 20% for conventional MNPs in the treatment of glioblastoma in mice [178]. The work of Gandia et al. [179] showed that magnetosome chains are advantageous to enhance the hyperthermia efficiency than isolated magnetosomes, as investigated by Muela et al. [180].

For efficient clinical application, low doses of MNPs with high SAR value are favorable. Therefore, it is crucial to further understand and optimize the heat dissipation mechanism. Additionally, changes of the pH value, viscosity, and heat transfer of the surrounding environment of the living tissue should be taken into consideration [111].

5.3 Drug Delivery

By conjugation of MNPs with drugs, a powerful transport system becomes available that can even help to reduce undesirable properties of drugs like poor solubility, toxicity, nonspecific delivery and short circulation half-lives [129]. Thus, MNPs are attractive nanocarriers for targeted therapeutic drug delivery. Drug delivery can be achieved by two mechanisms. "Passive targeting" depends on the enhanced permeability and retention (EPR) effect. Generally, tumor growth is accompanied by the development of a surrounding leaky vessel system and therefore, MNPs can diffuse and accumulate within the tumor tissue [181,182]. "Active targeting" relies on guiding and accumulating the MNPs (and drugs) using externally applied magnetic field gradients [183], sometimes assisted by surface functionalization of MNPs with biomarkers [129].

Huang et al. produced MNPs via thermal decomposition and coated with Polyethylene glycol/Polyethyleneimine resulting in diameters d_c = 9–14 nm and $d_h \approx$ 67 nm. These MNPs were then conjugated with folic acid for diagnosis and treatment of breast cancer and loaded with Doxorubicin, an anticancer drug. The MNPs were tested to target a xenograft MCF-7 breast cancer tumor in nude mice. Due to a high relaxivity r_2 = 81.8 L·mmol^{-1}·s^{-1}), they could successfully be monitored by MRI [184]. Similar results were achieved by Yang et al. using heparin coated MNPs with diameters d_c = 10 nm and d_h = 125 nm that were conjugated with the chemotherapeutic agent Doxorubicin [185]. Huang et al. used a microfluidic chip to embed SPIO-NP (d_c = 7 nm) into chitosan matrix and encapsulate Vinlastine. The composite resulted in well-defined spherical microparticles in a diameter range of 360 to 420 μm. The drug release of the chemotherapeutic agent was achieved by pulsatile external magnetic field [186]. Successful use of magnetosomes as nanocarriers was also reported by Long et al. Here, the chemotherapeutic agent Doxorubicin and asiRNA therapeutic agent were simultaneously conjugated to the magnetosomes using polyethyleneimine and succinimidyl 6-hydrazinonicotinate acetone hydrazone (SANH) as a bifunctional linker. Results showed that the Doxorubicin stayed stabile in normal pH blood

environment and 40% of the drug was released at a pH-value of 5.5 after 280 h (pH-sensitive drug release). The nanocarrier was also capable to inhibit the proliferation of HeLa cells, and even to induce apoptosis [187].

A good prospect in clinical tumor treatment offers the combination of more than one method. Piehler et al. showed that functionalization of MNPs produced by conventional precipitation method with diameter of d_c = 12 ± 3 nm with doxorubicin combined with magnetic fluid hyperthermia at 43 °C for 1 h results in tumor regression in vivo evidencing the increased therapeutic effect of the combination compared to the efficiency if either only magnetic fluid hyperthermia or intratumorally application of free doxorubicin has been carried out [188].

5.4 Gene Therapy

Gene therapy aims to treat diseases by transfer (or infection) of DNA or RNA sequences into targeted cells, generally by using viral vectors [189]. Alternatively, non-viral vectors can be used. Non-viral carrier systems offer crucial advantages for medical applications, such as stability, enzymatic degradation and low immunogenicity, as well as low toxicity and the ability to diffuse through cell membrane. Magnetofection is a non-viral method for transfection of nucleic acids using MNPs as carriers controlled by external magnetic fields [6,190]. For example, Zuvin et al. synthesized green fluorescent protein DNA-bearing polyethyleneimine-coated MNPs (average $d_c \approx 30$ nm und $d_h = 84$ nm). On MCF7 human breast cancer cells, an increase of transfection efficacy after magnetic field exposure could be demonstrated [191,192]. Li et al. used magnetosome-like iron oxide nanochains to achieve gene transfection to mesenchymal stem cells to inhibit tumor growth of glioma mode rats [193]. Yang et al. fabricated galactose (Gal) and polyethyleneimine (PEI) MNPs (Gal-PEI-MNPs $d_h = 98.2$ nm) to deliver siRNA to liver cancer cells and inhibited tumor growth in these cells [194].

5.5 Magnetic Actuation Using Micro/Nanorobots

An external magnetic field is a powerful means to remotely control the behavior of cells containing MNPs. Magneto-mechanical forces of the MNPs driven by an external magnetic field can destroy cells or cellular organelles in an anti-cancer treatment [195–197]. The mechanical forces of the MNPs are strong enough to destroy lysosomal membranes and lead to the permeabilization of membrane and subsequently initiate cell apoptosis [198–200]. Lunov et al. loaded clustered dextran coated MNPs with diameter $d_c \approx 5$ nm to liver cancer cells and achieved a lysosome-activated apoptosis by mechanical actuation using pulsed magnetic fields [201].

MNPs have been recently used to fabricate magnetic robots of micro- or even nanometer dimensions: These small-scale devices are intended to minimize invasive procedures in surgery or to avoid exposure to radiation [202]. Magnetic micro/nanorobots consist of two components, a biotemplate, a flexible part often in a shape of helix or filament to enhance the mobility in physiological fluids like bloodstream and a magnetic component containing MNPs for magnetically driven actuation by magnetic field gradients [203].

Magnetotatic bacteria are a natural example of nanorobots that can be used for drug delivery. Felfoul et al. transported in-vivo drug-loaded nanoliposomes into hypoxic regions of a tumor using magnetococcus mari-nus bacteria (strain MC-1) [204]. Another example is biohybrid magnetic robots as reported by Yan et al. fabricated from spirulina microalgae as a biological matrix via a facile dip-coating of MNPs. The movements of a swarm of the microrobots (microswimmers) inside rodent stomach have been successfully tracked using MRI [205]. Alapan et al. reported bacteria-driven microswimmer using red blood cells as autologous carriers for guided drug delivery. Red blood cells loaded with doxorubicin and MNPs were fixed on the Escherichia coli MG1655 via a biotin-avidinbiotin binding complex, and the microswimmers were directed using an external magnetic field gradient. After the treatment, the bacteria were removed using the on-demand light-activated hyperthermia [206].

5.6 MNPs in Theranostic Applications

In the last decades, theranostic nanomaterials have emerged that combine therapeutic components with diagnostic imaging capabilities of MNPs. They are promising for theranostic applications due to their biocompatibility, biodegradability, and surface modification capabilities. For diagnosis, the MNPs are tracers in imaging and cell tracking, while for therapeutic applications, their hyperthermia and drug delivery properties are utilized. Cho et al. demonstrated the assembly of 20 nm cubic MNPs (produced by thermal decomposition) into larger nanostructures up to 100 nm using serum albumin. The assembly showed high r_2 relaxivity (~500 $L \cdot mmol^{-1} \cdot s^{-1}$ at 1.41 T) in MRI and were successfully detected after injection into mice bearing U87-MG tumor cells. Additionally, tumor growth reduction was achieved by magnetic hyperthermia treatment [207]. A combination of MPI and drug delivery in vivo was presented by Zhu et al. They prepared nanocomposites of poly (lactide-co-glycolide acid) and MNPs (PLGA-MNPs) nanoclusters loaded with doxorubicin. The nanoclusters induced gradual decomposition in tumor environment at pH = 6.5. The disassembly of the iron oxide core cluster (detected by MPI) and the release rate of the drug over time showed linear correlation ($R_2 = 0.99$) [208]. Lu et al. developed MRI-visible nanocarriers using MNPs to monitor the targeted delivery of siRNA to neuronal stem cells, and at the same time, to direct their neuronal differentiation through gene silencing in stroke therapy. Additionally, an improvement in recovery of neural function from ischemic strokes in rats was achieved [209].

6. Clinical Translation of MNPs

In 2009 already, Ferumoxytol (Feraheme), a MNP-based drug capped by polyglucose sorbitol carboxymethyl ether [210], was approved by the US Food and Drug Administration (FDA) for treatment of iron deficiency anemia in adult patients with chronic kidney disease (CKD) [211]. Moreover, since Ferumoxytol is uptaken by macrophages, it can be applied for imaging of macrophages, tumors or vascular

lesions by MRI [212]. Magforce AG developed aminosilane-coated MNPs to treat solide tumors locally by hyperthermia. The MNPs can be presented to tumor directly or into the resection cavity wall. Subsequently, tumor cells are destroyed or become more sensitive to radiotherapy or chemotherapy. Currently, two centres in Germany started to commercially treat brain tumor patients and further clinical studies are under review by the FDA [213]. However, although several studies have demonstrated successful preclinical applications, many factors hinder the implementation of MNPs in versatile theranostic applications. These include high process complexity, high cost and long tumor treatment trial period, low drug delivery accumulation of MNPs in the target region and the possible lack of enhanced permeability and retention (EPR-effect) in a human solid tumor compared to mouse models [214]. However, the most significant factors preventing clinical translation are toxicity and safety of MNPs. MNP toxicity can be associated with toxicity of the precursor(s) used for preparation, coating, chemical composition, oxidation state of MNPs, protein interaction and high dosage [215,216]. Therefore, further improvements in these fields are required for the safe clinical translation of MNPs.

7. Conclusions

Magnetic nanoparticles have become an attractive and increasingly important part of diagnostics and therapeutic treatment of diseases. They are widely investigated and developed for a broad range of biomedical applications, each using one or more of their magnetic properties to generate a specific effect that is controlled from outside by magnetic fields. The wide variety of applications demonstrate the significance, but at the same time the need for reliable, reproducible and on top economic as well as ecological methods for successful translation into clinical applications.

Nevertheless, many challenges remain in finding and engineering an ideal magnetic nanoparticle system for an envisaged biomedical application. This is reflected in the major efforts still ongoing in further developing synthesis methods of magnetic

materials. Although considerable achievements have been made in these synthesis approaches, there still is huge demand for advanced synthesis methods. With microfluidic synthesis and biosynthesis of magnetosomes, two advanced techniques have been presented, both very powerful approaches to provide magnetic entities with outstanding structural and magnetic quality.

The actual state of extensive research on microfluidic synthesis methods of MNPs and the advantages over conventional (batch) synthesis methods have been discussed above. However, looking at the MNPs presently in biomedical applications as presented in Section 5, it is striking that mostly all diagnostic and therapeutic approaches rely on MNPs that have been synthesized by conventional synthesis methods. The reason for this is assumed to be constraints in the microfluidic approach regarding clogging of the reactor, sufficient throughput, effective purification strategies, GMP-compliant production, or scalability.

Aqueous synthesis as a method to continuously produce single core MNPs without immunogenic membrane and endotoxins is a very attractive approach, especially if combined with in line purification and in line process control. Thus, this straightforward, fast, and efficient approach additionally offers a high automation potential. However, in order to reach the MNP quality as provided in biosynthesis of magnetosomes, further optimization is required.

Although MNPs hold great promise in biomedical applications, there are still problems that have to be solved before the translation into clinical settings becomes feasible. One of the major challenges are the biocompatibility and the toxicity of the MNPs in the long term. Further detailed and comprehensive studies are required to resolve the effects of composition, morphology, size, shape, and structure of MNPs on their clearance and fate from a living organism. Further advancing techniques such as continuous microfluidic synthesis and biosynthesis will make a significant contribution to tailor MNPs for safe and effective clinical applications.

Author Contributions: A.B. wrote the manuscript; R.B. and F.W. reviewed and edited the manuscript; work was supervised by R.B.; and funding acquisition, R.B. and F.W. All authors have read and agreed to the published version of the manuscript.

Funding: This research was funded by Deutsche Forschungsgemeinschaft (DFG) within the researchgrants "Core Facility: Metrology of Ultra-Low Magnetic Fields", grant numbers KO 5321/3 and TR408/11" and the collaborative research center "Matrix in Vision" (SFB 1340/1 2018, No 372486779, project A02). Financial support by the German Federal Ministry of Education and Research (BMBF), grant number 13XP5113, is grate-fully acknowledged. A.B. thanks the Friedrich Ebert Stiftung for a PhD fellowship sup-porting his work related to this project. R.B. thanks the Fraunhofer-Gesellschaft for the support within the Fraunhofer TALENTA program. This work was furthermore supported in the framework of the Fraunhofer Lighthouse Project QMag.

Institutional Review Board Statement: Not applicable.

Informed Consent Statement: Not applicable.

Acknowledgments: Many thanks to Helen Onyema for proof reading of the manuscript.

Conflicts of Interest: The authors declare no conflict of interest.

References

1. Mani, S.A.; Sachdeva, S.; Mani, A.; Vora, H.R.; Gholap, S.S.; Kaur Sodhi, J. Nano-robotics: The future of health and dental care. IJPI 2021, 6, 6–10.
2. Lee, A.P. 2020 vision: Celebrating the 20th year of Lab on a Chip. Lab Chip 2020, 20, 1889–1890.
3. Baig, N.; Kammakakam, I.; Falath, W. Nanomaterials: A review of synthesis methods, properties, recent progress, and challenges. Mater. Adv. 2021, 2, 1821–1871.
4. Tong, S.; Quinto, C.A.; Zhang, L.; Mohindra, P.; Bao, G. Size-Dependent Heating of Magnetic Iron Oxide Nanoparti-cles. ACS Nano 2017, 11, 6808–6816.
5. Patsula, V.; Moskvin, M.; Dutz, S.; Horák, D. Size-dependent magnetic properties of iron oxide nanoparticles. J. Phys. Chem. Solids 2016, 88, 24–30.
6. Palanisamy, S.; Wang, Y.-M. Superparamagnetic iron oxide nanoparticulate system: Synthesis, targeting, drug delivery and therapy in cancer. Dalton Trans. 2019, 48, 9490–9515.
7. Estelrich, J.; Escribano, E.; Queralt, J.; Busquets, M.A. Iron oxide nanoparticles for magnetically-guided and magneti-callyresponsive drug delivery. Int. J. Mol. Sci. 2015, 16, 8070–8101.
8. Arami, H.; Khandhar, A.; Liggitt, D.; Krishnan, K.M. In vivo delivery, pharmacokinetics, biodistribution and toxicity of iron oxide nanoparticles. Chem. Soc. Rev. 2015, 44, 8576–8607.
9. Arnida; Janát-Amsbury, M.M.; Ray, A.; Peterson, C.M.; Ghandehari, H. Geometry and surface characteristics of gold nanoparticles influence their biodistribution and uptake by macrophages. Eur. J. Pharm. Biopharm. 2011, 77, 417–423.

10. Andrade, R.G.D.; Veloso, S.R.S.; Castanheira, E.M.S. Shape Anisotropic Iron Oxide-Based Magnetic Nanoparticles: Synthesis and Biomedical Applications. Int. J. Mol. Sci. 2020, 21, 2455.

11. Abenojar, E.C.; Wickramasinghe, S.; Bas-Concepcion, J.; Samia, A.C.S. Structural effects on the magnetic hyperther-mia properties of iron oxide nanoparticles. Prog. Nat. Sci. Mater. Int. 2016, 26, 440–448.

12. Son, S.J.; Bai, X.; Nan, A.; Ghandehari, H.; Lee, S.B. Template synthesis of multifunctional nanotubes for controlled release.

J. Control. Release 2006, 114, 143–152.

13. Lee, J.H.; Ju, J.E.; Kim, B.I.; Pak, P.J.; Choi, E.-K.; Lee, H.-S.; Chung, N. Rod-shaped iron oxide nanoparticles are more toxic than sphere-shaped nanoparticles to murine macrophage cells. Environ. Toxicol. Chem. 2014, 33, 2759–2766.

14. Arias, L.S.; Pessan, J.P.; Vieira, A.P.M.; Lima, T.M.T.d.; Delbem, A.C.B.; Monteiro, D.R. Iron Oxide Nanoparticles for Biomedical Applications: A Perspective on Synthesis, Drugs, Antimicrobial Activity, and Toxicity. Antibiotics 2018, 7, 46.

15. Kolhatkar, A.G.; Jamison, A.C.; Litvinov, D.; Willson, R.C.; Lee, T.R. Tuning the magnetic properties of nano-particles. Int. J. Mol. Sci. 2013, 14, 15977–16009.

16. Jeon, M.; Halbert, M.V.; Stephen, Z.R.; Zhang, M. Iron Oxide Nanoparticles as T1 Contrast Agents for Magnetic Reso-nance Imaging: Fundamentals, Challenges, Applications, and Prospectives. Adv. Mater. 2021, 33, e1906539.

17. Vazquez-Prada, K.X.; Lam, J.; Kamato, D.; Xu, Z.P.; Little, P.J.; Ta, H.T. Targeted Molecular Imaging of Cardiovascular Diseases by Iron Oxide Nanoparticles. Arterioscler. Thromb. Vasc. Biol. 2021, 41, 601–613.

18. Salehipour, M.; Rezaei, S.; Mosafer, J.; Pakdin-Parizi, Z.; Motaharian, A.; Mogharabi-Manzari, M. Recent advances in polymercoated iron oxide

nanoparticles as magnetic resonance imaging contrast agents. J. Nanopart. Res. 2021, 23, 1467.

19. Le Thu Huong, T.; Nam, N.H.; Doan, D.H.; My Nhung, H.T.; Quang, B.T.; Nam, P.H.; Thong, P.Q.; Phuc, N.X.; Thu, H.P. Folate attached, curcumin loaded Fe3O4 nanoparticles: A novel multifunctional drug delivery system for cancer treatment. Mater. Chem. Phys. 2016, 172, 98–104.

20. Unnikrishnan, B.S.; Sen, A.; Preethi, G.U.; Joseph, M.M.; Maya, S.; Shiji, R.; Anusree, K.S.; Sreelekha, T.T. Folic acid-appended galactoxyloglucan-capped iron oxide nanoparticles as a biocompatible nanotheranostic agent for tumor-targeted delivery of doxorubicin. Int. J. Biol. Macromol. 2021, 168, 130–142.

21. Dutz, S.; Hergt, R. Magnetic nanoparticle heating and heat transfer on a microscale: Basic principles, realities and physical limitations of hyperthermia for tumour therapy. Int. J. Hyperth. 2013, 29, 790–800.

22. Hedayatnasab, Z.; Dabbagh, A.; Abnisa, F.; Wan Daud, W.M.A. Polycaprolactone-coated superparamagnetic iron oxide nanoparticles for in vitro magnetic hyperthermia therapy of cancer. Eur. Polym. J. 2020, 133, 109789.

23. Dadfar, S.M.; Roemhild, K.; Drude, N.I.; Stillfried, S.; von Knüchel, R.; Kiessling, F.; Lammers, T. Iron oxide nanoparti-cles: Diagnostic, therapeutic and theranostic applications. Adv. Drug Deliv. Rev. 2019, 138, 302–325.

24. Ren, X.; Chen, H.; Yang, V.; Sun, D. Iron oxide nanoparticle-based theranostics for cancer imaging and therapy. Front. Chem. Sci. Eng. 2014, 8, 253–264.

25. Baki, A.; Löwa, N.; Remmo, A.; Wiekhorst, F.; Bleul, R. Micromixer Synthesis Platform for a Tuneable Production of Magnetic Single-Core Iron Oxide Nanoparticles. Nanomaterials 2020, 10, 1845.

26. Balasubramanian, V.; Liu, Z.; Hirvonen, J.; Santos, H.A. Nanomedicine: Bridging the Knowledge of Different Worlds to Understand the Big Picture of Cancer Nanomedicines. Adv. Healthc. Mater. 2018, 7, 1870005.

27. Liu, Z.; Fontana, F.; Python, A.; Hirvonen, J.T.; Santos, H.A. Microfluidics for Production of Particles: Mechanism, Methodology, and Applications. Small 2020, 16, e1904673.

28. Rane, A.V.; Kanny, K.; Abitha, V.K.; Thomas, S. Chapter 5—Methods for Synthesis of Nanoparticles and Fabrication of Nanocomposites. In Micro and Nano Technologies; Elsevier: Amsterdam, The Netherlands, 2018; pp. 121–139.

29. Jesus, A.C.B.; Jesus, J.R.; Lima, R.J.S.; Moura, K.O.; Almeida, J.M.A.; Duque, J.G.S.; Meneses, C.T. Synthesis and mag-netic interaction on concentrated Fe3O4 nanoparticles obtained by the co-precipitation and hydrothermal chemical methods. Ceram. Int. 2020, 46, 11149–11153.

30. Ali, A.; Zafar, H.; Zia, M.; Ul Haq, I.; Phull, A.R.; Ali, J.S.; Hussain, A. Synthesis, characterization, applications, and challenges of iron oxide nanoparticles. Nanotechnol. Sci. Appl. 2016, 9, 49–67.

31. Fernandes, M.T.C.; Garcia, R.B.R.; Leite, C.A.P.; Kawachi, E.Y. The competing effect of ammonia in the synthesis of iron oxide/silica nanoparticles in microemulsion/sol–gel system. Colloids Surf. A Physicochem. Eng. Asp. 2013, 422, 136–142.

32. Sundar, S.; Venkatachalam, G.; Kwon, S. Sol-Gel Mediated Greener Synthesis of γ-Fe2O3 Nanostructures for the Selec-tive and Sensitive Determination of Uric Acid and Dopamine. Catalysts 2018, 8, 512.

33. Badnore, A.U.; Salvi, M.A.; Jadhav, N.L.; Pandit, A.B.; Pinjari, D.V. Comparison and Characterization of Fe3O4 Nano-particles Synthesized by Conventional Magnetic Stirring and Sonochemical Method. Adv. Sci. Lett. 2018, 24, 5681–5686.

34. Unni, M.; Uhl, A.M.; Savliwala, S.; Savitzky, B.H.; Dhavalikar, R.; Garraud, N.; Arnold, D.P.; Kourkoutis, L.F.; Andrew, J.S.; Rinaldi, C. Thermal Decomposition Synthesis of Iron Oxide Nanoparticles with Diminished

Magnetic Dead Layer by Controlled Addition of Oxygen. ACS Nano 2017, 11, 2284–2303.

35. Hufschmid, R.; Teeman, E.; Mehdi, B.L.; Krishnan, K.M.; Browning, N.D. Observing the colloidal stability of iron oxide nanoparticles in situ. Nanoscale 2019, 11, 13098–13107.

36. Okoli, C.; Sanchez-Dominguez, M.; Boutonnet, M.; Järås, S.; Civera, C.; Solans, C.; Kuttuva, G.R. Comparison and functionalization study of microemulsion-prepared magnetic iron oxide nanoparticles. Langmuir 2012, 28, 8479–8485.

37. Malik, M.A.; Wani, M.Y.; Hashim, M.A. Microemulsion method: A novel route to synthesize organic and inorganic nanomaterials. Arab. J. Chem. 2012, 5, 397–417.

38. Aivazoglou, E.; Metaxa, E.; Hristoforou, E. Microwave-assisted synthesis of iron oxide nanoparticles in biocompatible organic environment. AIP Adv. 2018, 8, 48201.

39. Fernández-Barahona, I.; Muñoz-Hernando, M.; Herranz, F. Microwave-Driven Synthesis of Iron-Oxide Nanoparticles for Molecular Imaging. Molecules 2019, 24, 1224.

40. Arbain, R.; Othman, M.; Palaniandy, S. Preparation of iron oxide nanoparticles by mechanical milling. Miner. Eng. 2011, 24, 1–9.

41. Hudson, R.; Feng, Y.; Varma, R.S.; Moores, A. Bare magnetic nanoparticles: Sustainable synthesis and applications in catalytic organic transformations. Green Chem. 2014, 16, 4493–4505.

42. Tartaj, P.; Morales, M.a.d.P.; Veintemillas-Verdaguer, S.; Gonz lez-Carre o, T.; Serna, C.J. The preparation of magnetic nanoparticles for applications in biomedicine. J. Phys. Condens. Matter 2003, 36, R182–R197.

43. Mosayebi, J.; Kiyasatfar, M.; Laurent, S. Synthesis, Functionalization, and Design of Magnetic Nanoparticles for Theranostic Applications. Adv. Healthc. Mater. 2017, 6.

44. Krishna, K.S.; Li, Y.; Li, S.; Kumar, C.S.S.R. Lab-on-a-chip synthesis of inorganic nanomaterials and quantum dots for biomedical applications. Adv. Drug Deliv. Rev. 2013, 65, 1470–1495.

45. LaMer, V.K.; Dinegar, R.H. Theory, Production and Mechanism of Formation of Monodispersed Hydrosols. J. Am. Chem. Soc. 1950, 72, 4847–4854.

46. Massart, R. Preparation of aqueous magnetic liquids in alkaline and acidic media. IEEE Trans. Magn. 1981, 17, 1247–1248.

47. LaGrow, A.P.; Besenhard, M.O.; Hodzic, A.; Sergides, A.; Bogart, L.K.; Gavriilidis, A.; Thanh, N.T.K. Unravelling the growth mechanism of the co-precipitation of iron oxide nanoparticles with the aid of synchrotron X-Ray diffraction in solution. Nanoscale 2019, 11, 6620–6628.

48. Bhandari, R.; Gupta, P.; Dziubla, T.; Hilt, J.Z. Single step synthesis, characterization and applications of curcumin func-tionalized iron oxide magnetic nanoparticles. Mater. Sci. Eng. C 2016, 67, 59–64.

49. Kim, D.; Lee, N.; Park, M.; Kim, B.H.; An, K.; Hyeon, T. Synthesis of Uniform Ferrimagnetic Magnetite Nanocubes. J. Am. Chem. Soc. 2009, 131, 454–455.

50. Khandhar, A.P.; Keselman, P.; Kemp, S.J.; Ferguson, R.M.; Goodwill, P.W.; Conolly, S.M.; Krishnan, K.M. Evaluation of PEG-coated iron oxide nanoparticles as blood pool tracers for preclinical magnetic particle imaging. Nanoscale 2017, 9, 1299–1306.

51. Gutierrez, L.; Gomez, L.; Irusta, S.; Arruebo, M.; Santamaria, J. Comparative study of the synthesis of silica nanoparti-cles in micromixer–microreactor and batch reactor systems. Chem. Eng. J. 2011, 171, 674–683.

52. Basit, A.; Wang, J.; Guo, F.; Niu, W.; Jiang, W. Improved methods for mass production of magnetosomes and applica-tions: A review. Microb. Cell Fact. 2020, 19, 197.

53. Uebe, R.; Schüler, D. Magnetosome biogenesis in magnetotactic bacteria. Nat. Rev. Microbiol. 2016, 14, 621–637.

54. Barber-Zucker, S.; Zarivach, R. A Look into the Biochemistry of Magnetosome Biosynthesis in Magnetotactic Bacteria. ACS Chem. Biol. 2017, 12, 13–22.

55. Daw, R.; Finkelstein, J. Lab on a chip. Nature 2006, 442, 367.

56. Sackmann, E.K.; Fulton, A.L.; Beebe, D.J. The present and future role of microfluidics in biomedical research. Nature 2014, 507, 181–189.

57. Shang, L.; Cheng, Y.; Zhao, Y. Emerging Droplet Microfluidics. Chem. Rev. 2 017, 117, 7964–8040.

58. Yu, Y.; Shang, L.; Guo, J.; Wang, J.; Zhao, Y. Design of capillary microfluidics for spinning cell-laden microfibers. Nat. Protoc. 2018, 13, 2557–2579.

59. Zou, M.; Wang, J.; Yu, Y.; Sun, L.; Wang, H.; Xu, H.; Zhao, Y. Composite Multifunctional Micromotors from Droplet Microfluidics. ACS Appl. Mater. Interfaces 2018, 10, 34618–34624.

60. Zhang, L.; Chen, Q.; Ma, Y.; Sun, J. Microfluidic Methods for Fabrication and Engineering of Nanoparticle Drug Deliv-ery Systems. ACS Appl. Bio. Mater. 2020, 3, 107–120.

61. Augustine, R.; Hasan, A. Chapter 11—Multimodal applications of phytonanoparticles. In Micro and Nano Technolo-gies; Elsevier: Amsterdam, The Netherlands, 2020; pp. 195–219.

62. Liu, D.; Cito, S.; Zhang, Y.; Wang, C.-F.; Sikanen, T.M.; Santos, H.A. A versatile and robust microfluidic platform to-ward high throughput synthesis of homogeneous nanoparticles with tunable properties. Adv. Mater. 2015, 27, 2298–2304.

63. Liu, Y.; Jiang, X. Why microfluidics? Merits and trends in chemical synthesis. Lab Chip 2017, 17, 3960–3978.

64. Zhao, X.; Bian, F.; Sun, L.; Cai, L.; Li, L.; Zhao, Y. Microfluidic Generation of Nanomaterials for Biomedical Applica-tions. Small 2020, 16, e1901943.

65. Han, Z.; Jiang, X. Chapter 10—Microfluidic Synthesis of Functional Nanoparticles. In Nanotechnology and Microfluidics; Wiley: Hoboken, NJ, USA, 2019; pp. 319–345.

66. Amreen, K.; Goel, S. Review—Miniaturized and Microfluidic Devices for Automated Nanoparticle Synthesis. ECS J. Solid State Sci. Technol. 2021, 10, 17002.

67. Ma, J.; Lee, S.M.-Y.; Yi, C.; Li, C.-W. Controllable synthesis of functional nanoparticles by microfluidic platforms for biomedical applications—A review. Lab Chip 2017, 17, 209–226.

68. Yu, B.; Lee, R.J.; Lee, L.J. Microfluidic Methods for Production of Liposomes. In Liposomes: Part G, 1st ed.; Düzgünes¸, N., Ed.; Academic Press: Boston, MA, USA; Elsevier: Amsterdam, The Netherlands, 2009; pp. 129–141. ISBN 9780123813794.

69. Jung, H.I.; Park, J.E.; Jung, S.Y.; Kang, T.G.; Ahn, K.H. Flow and mixing characteristics of a groove-embedded partitioned pipe mixer. Korea-Aust. Rheol. J. 2020, 32, 319–329.

70. Shrimal, P.; Jadeja, G.; Patel, S. A review on novel methodologies for drug nanoparticle preparation: Microfluidic approach. Chem. Eng. Res. Des. 2020, 153, 728–756.

71. Ohannesian, N.; Leo, C.T.; de Martirosyan, K.S. Dextran coated superparamagnetic iron oxide nanoparticles produced by microfluidic process. Mater. Today Proc. 2019, 13, 397–403.

72. Suryawanshi, P.L.; Sonawane, S.H.; Bhanvase, B.A.; Ashokkumar, M.; Pimplapure, M.S.; Gogate, P.R. Synthesis of iron oxide nanoparticles in a continuous flow spiral microreactor and Corning®advanced flow™ reactor. Green Process. Synth. 2018, 7, 1–11.

73. As¸ık, M.D.; Kaplan, M.; Çetin, B.; Sag˘lam, N. Synthesis of iron oxide core chitosan nanoparticles in a 3D printed microfluidic device. J. Nanopart. Res. 2021, 23, 433.

74. Ying, Y.; Chen, G.; Zhao, Y.; Li, S.; Yuan, Q. A high throughput methodology for continuous preparation of monodispersed nanocrystals in microfluidic reactors. Chem. Eng. J. 2008, 135, 209–215.

75. Song, H.; Chen, D.L.; Ismagilov, R.F. Reactions in droplets in microfluidic channels. Angew. Chem. Int. Ed. Engl. 2006, 45, 7336–7356.

76. Seo, M.; Paquet, C.; Nie, Z.; Xu, S.; Kumacheva, E. Microfluidic consecutive flow-focusing droplet generators. Soft Matter 2007, 3, 986.

77. Abedini-Nassab, R.; Pouryosef Miandoab, M.; S¸as¸maz, M. Microfluidic Synthesis, Control, and Sensing of Magnetic Nanoparticles: A Review. Micromachines 2021, 12, 768.

78. Sohrabi, S.; Kassir, N.; Keshavarz Moraveji, M. Droplet microfluidics: Fundamentals and its advanced applications. RSC Adv. 2020, 10, 27560–27574.

79. Garstecki, P.; Fuerstman, M.J.; Stone, H.A.; Whitesides, G.M. Formation of droplets and bubbles in a microfluidic T-junctionscaling and mechanism of break-up. Lab Chip 2006, 6, 437–446.

80. Lashkaripour, A.; Rodriguez, C.; Ortiz, L.; Densmore, D. Performance tuning of microfluidic flow-focusing droplet generators. Lab Chip 2019, 19, 1041–1053.

81. Cramer, C.; Fischer, P.; Windhab, E.J. Drop formation in a co-flowing ambient fluid. Chem. Eng. Sci. 2004, 59, 3045–3058.

82. Zhang, J.; Xu, W.; Xu, F.; Lu, W.; Hu, L.; Zhou, J.; Zhang, C.; Jiang, Z. Microfluidic droplet formation in co-flow devices fabricated by micro 3D printing. J. Food Eng. 2021, 290, 110212.

83. Frenz, L.; El Harrak, A.; Pauly, M.; Bégin-Colin, S.; Griffiths, A.D.; Baret, J.-C. Droplet-based microreactors for the synthesis of magnetic iron oxide nanoparticles. Angew. Chem. Int. Ed. Engl. 2008, 47, 6817–6820

84. Siavashy, S.; Soltani, M.; Ghorbani-Bidkorbeh, F.; Fallah, N.; Farnam, G.; Mortazavi, S.A.; Shirazi, F.H.; Tehrani, M.H.H.; Hamedi, M.H. Microfluidic platform for synthesis and optimization of chitosan-coated magnetic nanoparticles in cisplatin delivery. Carbohydr. Polym. 2021, 265, 118027.

85. Kašpar, O.; Koyuncu, A.H.; Hubatová-Vacková, A.; Balouch, M.; Tokárová, V. Influence of channel height on mixing efficiency and synthesis of iron oxide nanoparticles using droplet-based microfluidics. RSC Adv. 2020, 10, 15179–15189.

86. Sengupta, P.; Khanra, K.; Chowdhury, A.R.; Datta, P. Lab-on-a-chip sensing devices for biomedical applications. In Bioelectronics and Medical Devices: From Materials to Devices-Fabrication, Applications and Reliability; Elsevier: Amsterdam, The Netherlands, 2019; pp. 47–95.

87. Schönfeld, F.; Hessel, V.; Hofmann, C. An optimised split-and-recombine micro-mixer with uniform chaotic mixing. Lab Chip 2004, 4, 65–69.

88. Hessel, V.; Löwe, H.; Stange, T. Micro chemical processing at IMM–from pioneering work to customer-specific ser-vices. Lab Chip 2002, 2, 14N–21N.

89. Lin, S.; Lin, K.; Lu, D.; Liu, Z. Preparation of uniform magnetic iron oxide nanoparticles by co-precipitation in a helical module microchannel reactor. J. Environ. Chem. Eng. 2017, 5, 303–309.

90. Frankel, R.B. The discovery of magnetotactic/magnetosensitive bacteria. Chin. J. Ocean. Limnol. 2009, 27, 1–2.

91. Blakemore, R. Magnetotactic bacteria. Science 1975, 190, 377–379.

92. Rosenfeldt, S.; Mickoleit, F.; Jörke, C.; Clement, J.H.; Markert, S.; Jérôme, V.; Schwarzinger, S.; Freitag, R.; Schüler, D.; Uebe, R.; et al. Towards standardized purification of bacterial magnetic nanoparticles for future in vivo applications. Acta Biomater. 2021, 120, 293–303.

93. Vargas, G.; Cypriano, J.; Correa, T.; Leão, P.; Bazylinski, D.A.; Abreu, F. Applications of Magnetotactic Bacteria, Mag-netosomes and Magnetosome Crystals in Biotechnology and Nanotechnology: Mini-Review. Molecules 2018, 23, 2438.

94. Grünberg, K.; Müller, E.-C.; Otto, A.; Reszka, R.; Linder, D.; Kube, M.; Reinhardt, R.; Schüler, D. Biochemical and Pro-teomic Analysis of the Magnetosome Membrane in Magnetospirillum gryphiswaldense. Appl. Environ. Microbiol. 2004, 70, 1040–1050.

95. McCausland, H.C.; Komeili, A. Magnetic genes: Studying the genetics of biomineralization in magnetotactic bacteria. PLoS Genet. 2020, 16, e1008499.

96. Alphandéry, E.; Chebbi, I.; Guyot, F.; Durand-Dubief, M. Use of bacterial magnetosomes in the magnetic hyperthermia treatment of tumours: A review. Int. J. Hyperth. 2013, 29, 801–809.

97. Lin, W.; Pan, Y.; Bazylinski, D.A. Diversity and ecology of and biomineralization by magnetotactic bacteria. Environ. Microbiol. Rep. 2017, 9, 345–356.

98. Liu, Y.; Li, G.R.; Guo, F.F.; Jiang, W.; Li, Y.; Li, L.J. Large-scale production of magnetosomes by chemostat culture of Magnetospirillum gryphiswaldense at high cell density. Microb. Cell Fact. 2010, 9, 99.

99. Yan, L.; Zhang, S.; Chen, P.; Liu, H.; Yin, H.; Li, H. Magnetotactic bacteria, magnetosomes and their application. Microbiol. Res. 2012, 167, 507–519.

100. Shenoy, V.J.; Edwards, C.E.R.; Helgeson, M.E.; Valentine, M.T. Design and characterization of a 3D-printed staggered herringbone mixer. BioTechniques 2021, 70, 285–289.

101. Li, W.; Zhang, L.; Ge, X.; Xu, B.; Zhang, W.; Qu, L.; Choi, C.-H.; Xu, J.; Zhang, A.; Lee, H.; et al. Microfluidic fabrication of microparticles for biomedical applications. Chem. Soc. Rev. 2018, 47, 5646–5683.

102. Chang, C.-H.; Paul, B.K.; Remcho, V.T.; Atre, S.; Hutchison, J.E. Synthesis and post-processing of nanomaterials using microreaction technology. J. Nanopart. Res. 2008, 10, 965–980.

103. Cabeza, V.S. High and Efficient Production of Nanomaterials by Microfluidic Reactor Approaches. In Advances in Microfluidics— New Applications in Biology, Energy, and Materials Sciences; Yu, X.-Y., Ed.; InTech: London, UK, 2016; ISBN 978-953-51-2785-7.

104. Hamdallah, S.I.; Zoqlam, R.; Erfle, P.; Blyth, M.; Alkilany, A.M.; Dietzel, A.; Qi, S. Microfluidics for pharmaceutical nanoparticle fabrication: The truth and the myth. Int. J. Pharm. 2020, 584, 119408.

105. Zhao, C.-X.; He, L.; Qiao, S.Z.; Middelberg, A.P.J. Nanoparticle synthesis in microreactors. Chemical Engineering Sci-ence 2011, 66, 1463–1479. [CrossRef]

106. Hong, T.; Lu, A.; Liu, W.; Chen, C. Microdroplet Synthesis of Silver Nanoparticles with Controlled Sizes. Micromachines 2019, 10, 274.

107. Watt, J.; Hance, B.G.; Anderson, R.S.; Huber, D.L. Effect of Seed Age on Gold Nanorod Formation: A Microfluidic, Real-Time Investigation. Chem. Mater. 2015, 27, 6442–6449.

108. Uson, L.; Sebastian, V.; Arruebo, M.; Santamaria, J. Continuous microfluidic synthesis and functionalization of gold nanorods. Chem. Eng. J. 2016, 285, 286–292.

109. Wang, J.; Song, Y. Microfluidic Synthesis of Nanohybrids. Small 2017, 13, 1604084.

110. Cornejo, E.; Subramanian, P.; Li, Z.; Jensen, G.J.; Komeili, A. Dynamic Remodeling of the Magnetosome Membrane Is Triggered by the Initiation of Biomineralization. mBio 2016, 7, e01898-15.

111. Bleul, R.; Baki, A.; Freese, C.; Paysen, H.; Kosch, O.; Wiekhorst, F. Continuously manufactured single-core iron oxide nanoparticles for cancer theranostics as valuable contribution in translational research. Nanoscale Adv. 2020, 2, 4510–4521.

112. Taher, Z.; Legge, C.; Winder, N.; Lysyganicz, P.; Rawlings, A.; Bryant, H.; Muthana, M.; Staniland, S. Magnetosomes and Magnetosome Mimics: Preparation, Cancer Cell Uptake and Functionalization for Future Cancer Therapies. Pharmaceutics 2021, 13, 367.

113. Zaloga, J.; Stapf, M.; Nowak, J.; Pöttler, M.; Friedrich, R.; Tietze, R.; Lyer, S.; Lee, G.; Odenbach, S.; Hilger, I.; et al. Tangential Flow Ultrafiltration Allows Purification and Concentration of Lauric Acid-/Albumin-Coated Particles for Im-proved Magnetic Treatment. Int. J. Mol. Sci. 2015, 16, 19291–19307.

114. Sun, J.; Tang, T.; Duan, J.; Xu, P.-x.; Wang, Z.; Zhang, Y.; Wu, L.; Li, Y. Biocompatibility of bacterial magnetosomes: Acute toxicity, immunotoxicity and cytotoxicity. Nanotoxicology 2010, 4, 271–283.

115. Alphandéry, E.; Idbaih, A.; Adam, C.; Delattre, J.-Y.; Schmitt, C.; Guyot, F.; Chebbi, I. Development of non-pyrogenic magnetosome minerals coated with poly-l-lysine leading to full disappearance of intracranial U87-Luc glioblastoma in 100% of treated mice using magnetic hyperthermia. Biomaterials 2017, 141, 210–222.

116. Niculescu, A.-G.; Chircov, C.; Bîrcă, A.C.; Grumezescu, A.M. Nanomaterials Synthesis through Microfluidic Methods: An Updated Overview. Nanomaterials 2021, 11, 864.

117. Niu, G.; Ruditskiy, A.; Vara, M.; Xia, Y. Toward continuous and scalable production of colloidal nanocrystals by switch-ing from batch to droplet reactors. Chem. Soc. Rev. 2015, 44, 5806–5820.

118. Xu, Y.; Musumeci, V.; Aymonier, C. Chemistry in supercritical fluids for the synthesis of metal nanomaterials. React. Chem. Eng. 2019, 4, 2030–2054.

119. Khan, I.U.; Serra, C.A.; Anton, N.; Vandamme, T. Microfluidics: A focus on improved cancer targeted drug delivery systems. J. Control. Release 2013, 172, 1065–1074.

120. Sicignano, L.; Tomaiuolo, G.; Perazzo, A.; Nolan, S.P.; Maffettone, P.L.; Guido, S. The effect of shear flow on micro-reactor clogging. Chem. Eng. J. 2018, 341, 639–647.

121. Kumar, K.; Nightingale, A.M.; Krishnadasan, S.H.; Kamaly, N.; Wylenzinska-Arridge, M.; Zeissler, K.; Branford, W.R.; Ware, E.; deMello, A.J.; deMello, J.C. Direct synthesis of dextran-coated superparamagnetic iron oxide nanoparticles in a capillary-based droplet reactor. J. Mater. Chem. 2012, 22, 4704.

122. Song, Y.; Hormes, J.; Kumar, C.S.S.R. Microfluidic synthesis of nanomaterials. Small 2008, 4, 698–711.

123. Heinzler, R.; Fischöder, T.; Elling, L.; Franzreb, M. Toward Automated Enzymatic Glycan Synthesis in a Compartmented Flow Microreactor System. Adv. Synth. Catal. 2019, 361, 4506–4516. [CrossRef]

124. Pan, L.-J.; Tu, J.-W.; Ma, H.-T.; Yang, Y.-J.; Tian, Z.-Q.; Pang, D.-W.; Zhang, Z.-L. Controllable synthesis of nanocrystals in droplet reactors. Lab Chip 2017, 18, 41–56.

125. Löwa, N.; Gutkelch, D.; Welge, E.-A.; Welz, R.; Meier, F.; Baki, A.; Bleul, R.; Klein, T.; Wiekhorst, F. Novel Benchtop Magnetic Particle Spectrometer for Process Monitoring of Magnetic Nanoparticle Synthesis. Nanomaterials 2020, 10, 2277.

126. Bemetz, J.; Wegemann, A.; Saatchi, K.; Haase, A.; Häfeli, U.O.; Niessner, R.; Gleich, B.; Seidel, M. Microfluidic-Based Synthesis of Magnetic Nanoparticles Coupled with Miniaturized NMR for Online Relaxation Studies. Anal. Chem. 2018, 90, 9975–9982.

127. Hu, Y.; Liu, B.; Wu, Y.; Li, M.; Liu, X.; Ding, J.; Han, X.; Deng, Y.; Hu, W.; Zhong, C. Facile High Throughput Wet-Chemical Synthesis Approach Using a Microfluidic-Based Composition and Temperature Controlling Platform. Front. Chem. 2020, 8, 579828.

128. Hamdous, Y.; Chebbi, I.; Mandawala, C.; Le Fèvre, R.; Guyot, F.; Seksek, O.; Alphandéry, E. Biocompatible coated magnetosome minerals with various organization and cellular interaction properties induce cytotoxicity towards RG-2 and GL-261 glioma cells in the presence of an alternating magnetic field. J. Nanobiotechnol. 2017, 15, 74.

129. Vangijzegem, T.; Stanicki, D.; Laurent, S. Magnetic iron oxide nanoparticles for drug delivery: Applications and characteristics. Expert Opin. Drug Deliv. 2019, 16, 69–78.

130. Wu, W.; Wu, Z.; Yu, T.; Jiang, C.; Kim, W.-S. Recent progress on magnetic iron oxide nanoparticles: Synthesis, surface functional strategies and biomedical applications. Sci. Technol. Adv. Mater. 2015, 16, 23501.

131. Reimer, P.; Schuierer, G.; Balzer, T.; Peters, P.E. Application of a superparamagnetic iron oxide (Resovist) for MR imaging of human cerebral blood volume. Magn. Reson. Med. 1995, 34, 694–697.

132. Baki, A.; Remmo, A.; Löwa, N.; Wiekhorst, F.; Bleul, R. Albumin-Coated Single-Core Iron Oxide Nanoparticles for Enhanced Molecular Magnetic Imaging (MRI/MPI). Int. J. Mol. Sci. 2021, 22, 6235.

133. Dulin´ska-Litewka, J.; Łazarczyk, A.; Hałubiec, P.; Szafran´ski, O.; Karnas, K.; Karewicz, A. Superparamagnetic Iron Oxide Nanoparticles-Current and Prospective Medical Applications. Materials 2019, 12, 617.

134. Unterweger, H.; Dézsi, L.; Matuszak, J.; Janko, C.; Poettler, M.; Jordan, J.; Bäuerle, T.; Szebeni, J.; Fey, T.; Boccaccini, A.R.; et al. Dextran-coated superparamagnetic iron oxide nanoparticles for magnetic resonance imaging: Evaluation of size-dependent imaging properties, storage stability and safety. Int. J. Nanomed. 2018, 13, 1899–1915.

135. Su, H.; Liu, Y.; Wang, D.; Wu, C.; Xia, C.; Gong, Q.; Song, B.; Ai, H. Amphiphilic starlike dextran wrapped superparamagnetic iron oxide nanoparticle clsuters as effective magnetic resonance imaging probes. Biomaterials 2013, 34, 1193–1203.

136. Predescu, A.M.; Matei, E.; Berbecaru, A.C.; Pantilimon, C.; Drăgan, C.; Vidu, R.; Predescu, C.; Kuncser, V. Synthesis and characterization of dextran-coated iron oxide nanoparticles. R. Soc. Open Sci. 2018, 5, 171525.

137. Kim, D.K.; Zhang, Y.; Kehr, J.; Klason, T.; Bjelke, B.; Muhammed, M. Characterization and MRI study of surfactant-coated superparamagnetic nanoparticles administered into the rat brain. J. Magn. Magn. Mater. 2001, 225, 256–261.

138. Chee, H.L.; Gan, C.R.R.; Ng, M.; Low, L.; Fernig, D.G.; Bhakoo, K.K.; Paramelle, D. Biocompatible Peptide-Coated Ultrasmall Superparamagnetic Iron Oxide Nanoparticles for In Vivo Contrast-Enhanced Magnetic Resonance Imaging. ACS Nano 2018, 12, 6480–6491.

139. Hosseinpour Moghadam, N.; Salehzadeh, S.; Rakhtshah, J.; Hosseinpour Moghadam, A.; Tanzadehpanah, H.; Saidijam, M. Preparation of a highly stable drug carrier by efficient immobilization of human serum albumin (HSA) on drug-loaded magnetic iron oxide nanoparticles. Int. J. Biol. Macromol. 2019, 125, 931–940.

140. Toropova, Y.G.; Zelinskaya, I.A.; Gorshkova, M.N.; Motorina, D.S.; Korolev, D.V.; Velikonivtsev, F.S.; Gareev, K.G. Albumin covering maintains endothelial

function upon magnetic iron oxide nanoparticles intravenous injection in rats. J. Biomed. Mater. Res. A 2021, 10, 2017–2026.

141. Ta, H.T.; Li, Z.; Hagemeyer, C.E.; Cowin, G.; Zhang, S.; Palasubramaniam, J.; Alt, K.; Wang, X.; Peter, K.; Whittaker, A.K. Molecular imaging of activated platelets via antibody-targeted ultra-small iron oxide nanoparticles displaying unique dual MRI contrast. Biomaterials 2017, 134, 31–42.

142. Jacobs, R.E.; Cherry, S.R. Complementary emerging techniques: High-resolution PET and MRI. Curr. Opin. Neurobiol. 2001, 11, 621–629.

143. Yurt, A.; Kazancı, N. Investigation of magnetic properties of various complexes prepared as contrast agents for MRI. J. Mol. Struct. 2008, 892, 392–397.

144. Shokrollahi, H. Contrast agents for MRI. Mater. Sci. Eng. C Mater. Biol. Appl. 2013, 33, 4485–4497.

145. Song, C.; Sun, W.; Xiao, Y.; Shi, X. Ultrasmall iron oxide nanoparticles: Synthesis, surface modification, assembly, and biomedical applications. Drug Discov. Today 2019, 24, 835–844.

146. Smits, L.P.; Tiessens, F.; Zheng, K.H.; Stroes, E.S.; Nederveen, A.J.; Coolen, B.F. Evaluation of ultrasmall superpara-magnetic iron-oxide (USPIO) enhanced MRI with ferumoxytol to quantify arterial wall inflammation. Atherosclerosis 2017, 263, 211–218.

147. Wei, H.; Bruns, O.T.; Kaul, M.G.; Hansen, E.C.; Barch, M.; Wis´niowska, A.; Chen, O.; Chen, Y.; Li, N.; Okada, S.; et al. Exceedingly small iron oxide nanoparticles as positive MRI contrast agents. Proc. Natl. Acad. Sci. USA 2017, 114, 2325–2330.

148. Mo, H.; Fu, C.; Wu, Z.; Liu, P.; Wen, Z.; Hong, Q.; Cai, Y.; Li, G. IL-6-targeted ultrasmall superparamagnetic iron oxide nanoparticles for optimized MRI detection of atherosclerotic vulnerable plaques in rabbits. RSC Adv. 2020, 10, 15346–15353.

149. Hedgire, S.; Krebill, C.; Wojtkiewicz, G.R.; Oliveira, I.; Ghoshhajra, B.B.; Hoffmann, U.; Harisinghani, M.G. Ultrasmall superparamagnetic iron oxide nanoparticle uptake as noninvasive marker of aortic wall inflammation on MRI: Proof of concept study. Br. J. Radiol. 2018, 91, 20180461.

150. Harris, M.; Ceulemans, M.; Verstraete, C.; Bloemen, M.; Manshian, B.; Soenen, S.J.; Himmelreich, U.; Verbiest, T.; de Borggraeve, W.M.; Parac-Vogt, T.N. Ultrasmall iron oxide nanoparticles functionalized with BODIPY derivatives as po-tential bimodal probes for MRI and optical imaging. Nano Select. 2021, 2, 406–416.

151. Wei, H.; Tan, T.; Cheng, L.; Liu, J.; Song, H.; Li, L.; Zhang, K. MRI tracing of ultrasmall superparamagnetic iron oxide nanoparticlelabeled endothelial progenitor cells for repairing atherosclerotic vessels in rabbits. Mol. Med. Rep. 2020, 22, 3327–3337.

152. Shen, Z.; Chen, T.; Ma, X.; Ren, W.; Zhou, Z.; Zhu, G.; Zhang, A.; Liu, Y.; Song, J.; Li, Z.; et al. Multifunctional Theranostic Nanoparticles Based on Exceedingly Small Magnetic Iron Oxide Nanoparticles for T1-Weighted Magnetic Resonance Imaging and Chemotherapy. ACS Nano 2017, 11, 10992–11004.

153. Besenhard, M.O.; Panariello, L.; Kiefer, C.; LaGrow, A.P.; Storozhuk, L.; Perton, F.; Begin, S.; Mertz, D.; Thanh, N.T.K.; Gavriilidis, A. Small iron oxide nanoparticles as MRI T1 contrast agent: Scalable inexpensive water-based synthesis us-ing a flow reactor. Nanoscale 2021, 13, 8795–8805.

154. Gleich, B.; Weizenecker, J. Tomographic imaging using the nonlinear response of magnetic particles. Nature 2005, 435, 1214–1217.

155. Kaul, M.G.; Weber, O.; Heinen, U.; Reitmeier, A.; Mummert, T.; Jung, C.; Raabe, N.; Knopp, T.; Ittrich, H.; Adam, G. Combined Preclinical Magnetic Particle Imaging and Magnetic Resonance Imaging: Initial Results in Mice. Rofo 2015, 187, 347–352.

156. Franke, J.; Heinen, U.; Lehr, H.; Weber, A.; Jaspard, F.; Ruhm, W.; Heidenreich, M.; Schulz, V. System Characterization of a Highly Integrated Preclinical Hybrid MPI-MRI Scanner. IEEE Trans. Med. Imaging 2016, 35, 1993–2004.

157. Fdez-Gubieda, M.L.; Alonso, J.; García-Prieto, A.; García-Arribas, A.; Fernández Barquín, L.; Muela, A. Magnetotactic bacteria for cancer therapy. J. Appl. Phys. 2020, 128, 70902.

158. Heinke, D.; Kraupner, A.; Eberbeck, D.; Schmidt, D.; Radon, P.; Uebe, R.; Schüler, D.; Briel, A. MPS and MRI efficacy of magnetosomes from wild-type and mutant bacterial strains. Int. J. Magn. Part. Imaging 2017, 3.

159. Wang, Q.; Ma, X.; Liao, H.; Liang, Z.; Li, F.; Tian, J.; Ling, D. Artificially Engineered Cubic Iron Oxide Nanoparticle as a High-Performance Magnetic Particle Imaging Tracer for Stem Cell Tracking. ACS Nano 2020, 14, 2053–2062.

160. Song, G.; Chen, M.; Zhang, Y.; Cui, L.; Qu, H.; Zheng, X.; Wintermark, M.; Liu, Z.; Rao, J. Janus Iron Oxides @ Semicon-ducting Polymer Nanoparticle Tracer for Cell Tracking by Magnetic Particle Imaging. Nano Lett. 2018, 18, 182–189.

161. Ding, Z.; Liu, P.; Hu, D.; Sheng, Z.; Yi, H.; Gao, G.; Wu, Y.; Zhang, P.; Ling, S.; Cai, L. Redox-responsive dextran based theranostic nanoparticles for near-infrared/magnetic resonance imaging and magnetically targeted photodynamic therapy. Biomater. Sci. 2017, 5, 762–771.

162. Behrouzkia, Z.; Joveini, Z.; Keshavarzi, B.; Eyvazzadeh, N.; Aghdam, R.Z. Hyperthermia: How Can It Be Used? Oman Med. J. 2016, 31, 89–97. [CrossRef]

163. Laurent, S.; Dutz, S.; Häfeli, U.O.; Mahmoudi, M. Magnetic fluid hyperthermia: Focus on superparamagnetic iron oxide nanoparticles. Adv. Colloid Interface Sci. 2011, 166, 8–23.

164. Blanco-Andujar, C.; Teran, F.J.; Ortega, D. Chapter 8—Current Outlook and Perspectives on Nanoparticle-Mediated Magnetic Hyperthermia. In Metal Oxides; Elsevier: Amsterdam, The Netherlands, 2018; pp. 197–245.

165. Mahmoudi, K.; Bouras, A.; Bozec, D.; Ivkov, R.; Hadjipanayis, C. Magnetic hyperthermia therapy for the treatment of glioblastoma: A review of the therapy's history, efficacy and application in humans. Int. J. Hyperth. 2018, 34, 1316–1328.

166. Bohara, R.A.; Thorat, N.D.; Pawar, S.H. Role of functionalization: Strategies to explore potential nano-bio applica-tions of magnetic nanoparticles. RSC Adv. 2016, 6, 43989–44012.

167. Bordelon, D.E.; Cornejo, C.; Grüttner, C.; Westphal, F.; DeWeese, T.L.; Ivkov, R. Magnetic nanoparticle heating effi-ciency reveals magneto-structural differences when characterized with wide ranging and high amplitude alternating magnetic fields. J. Appl. Phys. 2011, 109, 124904.

168. Carrey, J.; Mehdaoui, B.; Respaud, M. Simple models for dynamic hysteresis loop calculations of magnetic single-domain nanoparticles: Application to magnetic hyperthermia optimization. J. Appl. Phys. 2011, 109, 83921.

169. Dennis, C.L.; Jackson, A.J.; Borchers, J.A.; Hoopes, P.J.; Strawbridge, R.; Foreman, A.R.; van Lierop, J.; Grüttner, C.; Ivkov, R. Nearly complete regression of tumors via collective behavior of magnetic nanoparticles in hyperthermia. Nanotechnology 2009, 20, 395103.

170. Salimi, M.; Sarkar, S.; Hashemi, M.; Saber, R. Treatment of Breast Cancer-Bearing BALB/c Mice with Magnetic Hyper-thermia using Dendrimer Functionalized Iron-Oxide Nanoparticles. Nanomaterials 2020, 10, 2310.

171. Bender, P.; Fock, J.; Frandsen, C.; Hansen, M.F.; Balceris, C.; Ludwig, F.; Posth, O.; Wetterskog, E.; Bogart, L.K.; Southern, P.; et al. Relating Magnetic Properties and High Hyperthermia Performance of Iron Oxide Nanoflowers. J. Phys. Chem. C 2018, 122, 3068–3077.

172. Dadfar, S.M.; Camozzi, D.; Darguzyte, M.; Roemhild, K.; Varvarà, P.; Metselaar, J.; Banala, S.; Straub, M.; Güvener, N.; Engelmann, U.; et al. Size-isolation of

superparamagnetic iron oxide nanoparticles improves MRI, MPI and hyper-thermia performance. J. Nanobiotechnol. 2020, 18, 22.

173. Timko, M.; Molcan, M.; Hashim, A.; Skumiel, A.; Muller, M.; Gojzewski, H.; Jozefczak, A.; Kovac, J.; Rajnak, M.; Ma-kowski, M.; et al. Hyperthermic Effect in Suspension of Magnetosomes Prepared by Various Methods. IEEE Trans. Magn. 2013, 49, 250–254.

174. Martinez-Boubeta, C.; Simeonidis, K.; Makridis, A.; Angelakeris, M.; Iglesias, O.; Guardia, P.; Cabot, A.; Yedra, L.; Estradé, S.; Peiró, F.; et al. Learning from nature to improve the heat generation of iron-oxide nanoparticles for mag-netic hyperthermia applications. Sci. Rep. 2013, 3, 1652.

175. Alphandéry, E.; Guyot, F.; Chebbi, I. Preparation of chains of magnetosomes, isolated from Magnetospirillum mag-neticum strain AMB-1 magnetotactic bacteria, yielding efficient treatment of tumors using magnetic hyperthermia. Int. J. Pharm. 2012, 434, 444–452.

176. Alphandéry, E.; Faure, S.; Raison, L.; Duguet, E.; Howse, P.A.; Bazylinski, D.A. Heat Production by Bacterial Magneto-somes Exposed to an Oscillating Magnetic Field. J. Phys. Chem. C 2011, 115, 18–22.

177. Hergt, R.; Dutz, S.; Röder, M. Effects of size distribution on hysteresis losses of magnetic nanoparticles for hyper-thermia. J. Phys. Condens. Matter 2008, 20, 385214.

178. Le Fèvre, R.; Durand-Dubief, M.; Chebbi, I.; Mandawala, C.; Lagroix, F.; Valet, J.-P.; Idbaih, A.; Adam, C.; Delattre, J.-Y.; Schmitt, C.; et al. Enhanced antitumor efficacy of biocompatible magnetosomes for the magnetic hyperthermia treatment of glioblastoma. Theranostics 2017, 7, 4618–4631.]

179. Gandia, D.; Gandarias, L.; Rodrigo, I.; Robles-García, J.; Das, R.; Garaio, E.; García, J.Á.; Phan, M.-H.; Srikanth, H.; Orue, I.; et al. Unlocking the Potential of Magnetotactic Bacteria as Magnetic Hyperthermia Agents. Small 2019, 15, 1902626.

180. Muela, A.; Muñoz, D.; Martín-Rodríguez, R.; Orue, I.; Garaio, E.; Abad Díaz de Cerio, A.; Alonso, J.; García, J.Á.; FdezGubieda, M.L. Optimal Parameters for Hyperthermia Treatment Using Biomineralized Magnetite Nanoparticles: Theoretical and Experimental Approach. J. Phys. Chem. C 2016, 120, 24437–24448.

181. Karageorgis, A.; Dufort, S.; Sancey, L.; Henry, M.; Hirsjärvi, S.; Passirani, C.; Benoit, J.-P.; Gravier, J.; Texier, I.; Mon-tigon, O.; et al. An MRI-based classification scheme to predict passive access of 5 to 50-nm large nanoparticles to tumors. Sci. Rep. 2016, 6, 21417.

182. Dopfer, O.; Fujii, M. Probing Solvation Dynamics around Aromatic and Biological Molecules at the Single-Molecular Level. Chem. Rev. 2016, 116, 5432–5463.

183. Bietenbeck, M.; Florian, A.; Faber, C.; Sechtem, U.; Yilmaz, A. Remote magnetic targeting of iron oxide nanoparticles for cardiovascular diagnosis and therapeutic drug delivery: Where are we now? Int. J. Nanomed. 2016, 11, 3191–3203.

184. Huang, Y.; Mao, K.; Zhang, B.; Zhao, Y. Superparamagnetic iron oxide nanoparticles conjugated with folic acid for dual target-specific drug delivery and MRI in cancer theranostics. Mater. Sci. Eng. C Mater. Biol. Appl. 2017, 70, 763–771.

185. Yang, Y.; Guo, Q.; Peng, J.; Su, J.; Lu, X.; Zhao, Y.; Qian, Z. Doxorubicin-Conjugated Heparin-Coated Superparamagnetic Iron Oxide Nanoparticles for Combined Anticancer Drug Delivery and Magnetic Resonance Imag-ing. J. Biomed. Nanotechnol. 2016, 12, 1963–1974.

186. Huang, K.-S.; Yang, C.-H.; Wang, Y.-C.; Wang, W.-T.; Lu, Y.-Y. Microfluidic Synthesis of Vinblastine-Loaded Multifunc-tional Particles for Magnetically Responsive Controlled Drug Release. Pharmaceutics 2019, 11, 212.

187. Long, R.-M.; Dai, Q.-L.; Zhou, X.; Cai, D.-H.; Hong, Y.-Z.; Wang, S.-B.; Liu, Y.-G. Bacterial magnetosomes-based nanocarriers for co-delivery of cancer therapeutics in vitro. Int. J. Nanomed. 2018, 13, 8269–8279.

188. Piehler, S.; Dähring, H.; Grandke, J.; Göring, J.; Couleaud, P.; Aires, A.; Cortajarena, A.L.; Courty, J.; Latorre, A.; Somo-za, Á.; et al. Iron Oxide Nanoparticles as Carriers for DOX and Magnetic Hyperthermia after Intratumoral Application into Breast Cancer in Mice: Impact and Future Perspectives. Nanomaterials 2020, 10, 1016.

189. Dorer, D.E.; Nettelbeck, D.M. Targeting cancer by transcriptional control in cancer gene therapy and viral oncolysis. Adv. Drug Deliv. Rev. 2009, 61, 554–571.

190. Jiang, S.; Eltoukhy, A.A.; Love, K.T.; Langer, R.; Anderson, D.G. Lipidoid-Coated Iron Oxide Nanoparticles for Efficient DNA and siRNA delivery. Nano Lett. 2013, 13, 1059–1064.

191. Oral, O.; Cıkım, T.; Zuvin, M.; Unal, O.; Yagci-Acar, H.; Gozuacik, D.; Kos¸ar, A. Effect of Varying Magnetic Fields on Targeted Gene Delivery of Nucleic Acid-Based Molecules. Ann. Biomed. Eng. 2015, 43, 2816–2826.

192. Zuvin, M.; Kuruoglu, E.; Kaya, V.O.; Unal, O.; Kutlu, O.; Yagci Acar, H.; Gozuacik, D.; Kos¸ar, A. Magnetofection of Green Fluorescent Protein Encoding DNA-Bearing Polyethyleneimine-Coated Superparamagnetic Iron Oxide Nanopar-ticles to Human Breast Cancer Cells. ACS Omega 2019, 4, 12366–12374.

193. Li, A.; Zhang, T.; Huang, T.; Lin, R.; Mu, J.; Su, Y.; Sun, H.; Jiang, X.; Wu, H.; Xu, D.; et al. Iron Oxide Nanoparticles Promote Cx43-Overexpression of Mesenchymal Stem Cells for Efficient Suicide Gene Therapy during Glioma Treatment. Theranostics 2021, 11, 8254–8269.

194. Yang, Z.; Duan, J.; Wang, J.; Liu, Q.; Shang, R.; Yang, X.; Lu, P.; Xia, C.; Wang, L.; Dou, K. Superparamagnetic iron oxide nanoparticles modified with

polyethylenimine and galactose for siRNA targeted delivery in hepatocellular carcinoma therapy. IJN 2018, 13, 1851–1865.

195. Dobson, J. Remote control of cellular behaviour with magnetic nanoparticles. Nat. Nanotechnol. 2008, 3, 139–143.

196. Golovin, Y.I.; Gribanovsky, S.L.; Golovin, D.Y.; Klyachko, N.L.; Majouga, A.G.; Master, A.M.; Sokolsky, M.; Kabanov, A.V. Towards nanomedicines of the future: Remote magneto-mechanical actuation of nanomedicines by alternating magnetic fields. J. Control. Release 2015, 219, 43–60.

197. Colombo, M.; Carregal-Romero, S.; Casula, M.F.; Gutiérrez, L.; Morales, M.P.; Böhm, I.B.; Heverhagen, J.T.; Prosperi, D.; Parak, W.J. Biological applications of magnetic nanoparticles. Chem. Soc. Rev. 2012, 41, 4306–4334.

198. Kim, D.-H.; Rozhkova, E.A.; Ulasov, I.V.; Bader, S.D.; Rajh, T.; Lesniak, M.S.; Novosad, V. Biofunctionalized magnetic-vortex microdiscs for targeted cancer-cell destruction. Nat. Mater. 2010, 9, 165–171.

199. Master, A.M.; Williams, P.N.; Pothayee, N.; Pothayee, N.; Zhang, R.; Vishwasrao, H.M.; Golovin, Y.I.; Riffle, J.S.; Sokolsky, M.; Kabanov, A.V. Remote Actuation of Magnetic Nanoparticles For Cancer Cell Selective Treatment Through Cytoskeletal Disruption. Sci. Rep. 2016, 6, 33560.

200. Leulmi, S.; Chauchet, X.; Morcrette, M.; Ortiz, G.; Joisten, H.; Sabon, P.; Livache, T.; Hou, Y.; Carrière, M.; Lequien, S.; et al. Triggering the apoptosis of targeted human renal cancer cells by the vibration of anisotropic magnetic particles attached to the cell membrane. Nanoscale 2015, 7, 15904–15914.

201. Lunov, O.; Uzhytchak, M.; Smolková, B.; Lunova, M.; Jirsa, M.; Dempsey, N.M.; Dias, A.L.; Bonfim, M.; Hof, M.; Jurkiewicz, P.; et al. Remote Actuation of Apoptosis in Liver Cancer Cells via Magneto-Mechanical Modulation of Iron Oxide Nanoparticles. Cancers 2019, 11, 1873.

202. Yang, Y.; Wang, H. Perspectives of nanotechnology in minimally invasive therapy of breast cancer. J. Healthc. Eng. 2013, 4, 67–86.

203. Koleoso, M.; Feng, X.; Xue, Y.; Li, Q.; Munshi, T.; Chen, X. Micro/nanoscale magnetic robots for biomedical applications. Mater. Today Bio. 2020, 8, 100085.

204. Felfoul, O.; Mohammadi, M.; Taherkhani, S.; de Lanauze, D.; Zhong Xu, Y.; Loghin, D.; Essa, S.; Jancik, S.; Houle, D.; Lafleur, M.; et al. Magneto-aerotactic bacteria deliver drug-containing nanoliposomes to tumour hypoxic regions. Nat. Nanotechnol. 2016, 11, 941–947.

205. Yan, X.; Zhou, Q.; Vincent, M.; Deng, Y.; Yu, J.; Xu, J.; Xu, T.; Tang, T.; Bian, L.; Wang, Y.-X.J.; et al. Multifunctional biohybrid magnetite microrobots for imaging-guided therapy. Sci. Robot. 2017, 2, eaaq1155.

206. Alapan, Y.; Yasa, O.; Schauer, O.; Giltinan, J.; Tabak, A.F.; Sourjik, V.; Sitti, M. Soft erythrocyte-based bacterial micro-swimmers for cargo delivery. Sci. Robot. 2018, 3, eaar4423.

207. Cho, M.; Cervadoro, A.; Ramirez, M.; Stigliano, C.; Brazdeikis, A.; Colvin, V.; Civera, P.; Key, J.; Decuzzi, P. Assembly of Iron Oxide Nanocubes for Enhanced Cancer Hyperthermia and Magnetic Resonance Imaging. Nanomaterials 2017, 7, 72.

208. Zhu, X.; Li, J.; Peng, P.; Hosseini Nassab, N.; Smith, B.R. Quantitative Drug Release Monitoring in Tumors of Living Subjects by Magnetic Particle Imaging Nanocomposite. Nano Lett. 2019, 19, 6725–6733.

209. Lu, L.; Wang, Y.; Zhang, F.; Chen, M.; Lin, B.; Duan, X.; Cao, M.; Zheng, C.; Mao, J.; Shuai, X.; et al. MRI-Visible siRNA Nanomedicine Directing Neuronal Differentiation of Neural Stem Cells in Stroke. Adv. Funct. Mater. 2018, 28, 1706769.

210. Vallabani, N.V.S.; Singh, S. Recent advances and future prospects of iron oxide nanoparti-cles in biomedicine and diagnostics. 3 Biotech 2018, 8, 279.

211. Lu, M.; Cohen, M.H.; Rieves, D.; Pazdur, R. FDA report: Ferumoxytol for intravenous iron therapy in adult patients with chronic kidney disease. Am. J. Hematol. 2010, 85, 315–319.

212. Vasanawala, S.S.; Nguyen, K.-L.; Hope, M.D.; Bridges, M.D.; Hope, T.A.; Reeder, S.B.; Bashir, M.R. Safety and tech-nique of ferumoxytol administration for MRI. Magn. Reson. Med. 2016, 75, 2107–2111.

213. Magforce. Available online: https://www.magforce.com (accessed on 16 September 2021).

214. Zhao, S.; Yu, X.; Qian, Y.; Chen, W.; Shen, J. Multifunctional magnetic iron oxide nanoparticles: An advanced platform for cancer theranostics. Theranostics 2020, 10, 6278–6309.

215. Malhotra, N.; Lee, J.-S.; Liman, R.A.D.; Ruallo, J.M.S.; Villaflores, O.B.; Ger, T.-R.; Hsiao, C.-D. Potential Toxicity of Iron Oxide Magnetic Nanoparticles: A Review. Molecules 2020, 25, 3159.

216. Singh, N.; Jenkins, G.J.S.; Asadi, R.; Doak, S.H. Potential toxicity of superparamagnetic iron oxide nanoparticles (SPI-ON). Nano Rev. 2010, 1, 5358.

5.2 Continuously Manufactured Single-Core Iron Oxide Nanoparticles for Cancer Theranostics as Valuable Contribution in Translational Research

Published in: ***Nanoscale advances, impact factor (4.553)***

In this publication, the capability of continuously synthesized MNP translation for biomedical applications is evaluated. MNP of three different sizes, 23, 30, and 36 nm, are produced using continuous micromixer synthesis by controlling the process parameter reaction temperature.

It is shown that the single core MNP produced via micromixer have high signal amplitudes qualifying them as a promising tracer for Magnetic Particle Imaging (MPI), high potential for magnetic hyperthermia due to their high specific absorption rates (SAR values), and good T_2 contrast as a negative - contrast agent for Magnetic Resonance Imaging (MRI). Furthermore, the first cell and apoptosis tests on endothelial cells show no cytotoxicity indicating good biocompatibility of the MNP.

The following tasks were carried out by me, Abdulkader Baki:

1- Development of a continuous micromixer set-up for MNP synthesis.

2- Implementation and optimization of continuous synthesis of MNP.

3- Physicochemical characterization and data evaluation of the resulting MNP by:

a- Transmission electron microscopy (TEM)

b- Differential Centrifugal Sedimentation (DCS) measurements

c- Determination of iron concentration

4- Summary and evaluation of experimental results

5- Co-Authoring the publication

The determination of the magnetic properties is carried out at the Physikalisch-Technische Bundesanstalt (PTB) in Berlin.

Nanoscale Advances

ROYAL SOCIETY OF CHEMISTRY

PAPER

View Article Online
View Journal

Continuously manufactured single-core iron oxide nanoparticles for cancer theranostics as valuable contribution in translational research

Regina Bleul*[a], Abdulkader Baki[a], Christian Freese[a], Hendrik Paysen[b], Olaf Kosch[b], Frank Wiekhorst[b]

Abstract: Micromixer technology was used to manufacture magnetic single core iron oxide nanoparticles that combine imaging as well as therapeutic functions. In a continuous, scalable and highly controllable manner, synthesis with biocompatible educts via aqueous synthesis route was performed. Size control by varying relevant process parameters as e.g. temperature was confirmed by transmission electron microscopy measurements of experimental series and demonstrated the exceptional size control and homogenity. Furthermore, analytical centrifugation evidenced the stably dispersed state of the single core nanoparticles in aqueous media. Size controlled production of single-core iron oxide nanoparticles was used to design optimized nanoparticles with a core diameter of about 30 nm, showing high signal amplitudes in Magnetic Particle Imaging (MPI) as promising MPI tracer material. Moreover, therapeutic potential of these particles in magnetic fluid hyperthermia was evaluated and specific absorption rates (SAR values) up to 1 kW/(g(Fe) were obtained, that exceed the comparable SAR value of Resovist® by more than a factor of three. Relaxometry measurements clearly confirmed the capacity of these single-core magnetic nanoparticles to generate significant T_2-weighted Magnetic resonance imaging (MRI) contrast that potentially allows multimodal imaging for monitoring the particles *in-vivo* in a theranostic application scenario. Finally, first cell viability and apoptosis tests on endothelial cells did not show any cytotoxicity certifying a good biocompatibility of the iron oxide nanoparticles. This microtechnological approach

provides reproducible, scalable single core iron oxide nanoparticles as highly performing tracers for MPI diagnosis as well as efficient heat generators for hyperthermia therapy. These preliminary results contribute to translational research in image guided cancer therapy - a further step from basic research to future medicine.

Received 01st May 2020,
Accepted 09th August 2020

DOI: 10.1039/D0NA00343C

[a] *Fraunhofer Institute for Microengineering and Microsystems IMM), Carl-Zeiss-Strasse 18-20, 55129 Mainz, Germany. . E-mail:regina.bleul@imm.fraunhofer.de*
[b] *Physikalisch-Technische Bundesanstalt, Abbestr. 2-12, 10587 Berlin, Germany*

† Footnotes relating to the title and/or authors should appear here.
Electronic Supplementary Information (ESI) available: [details of any supplementary information available should be included here]. See DOI: 10.1039/x0xx00000x

Introduction

Cancer is still one of the leading causes of death worldwide, responsible for an estimated one million deaths in 2018. Even though many advances in both cancer diagnosis and cancer therapy have been achieved, aiming for early diagnosis and precise treatment at the right time and with appropriate dose, theranostic nanoparticles hold potential for revolutionizing future cancer treatment.[1–4] There are numerous multifunctional nanosystems designed for a more specific and personalized disease management, which combine diagnostic and therapeutic capabilities in one single biocompatible (and biodegradable) nanoparticle.[1,5,6]

However, present theranostic nanoparticle approaches offering real-time cancer therapy monitoring are not in clinical practice yet. The translation of existing promising research approaches into clinical application often fails because of the disproportionally high complexity of sophisticated nanosystems raising huge issues already in reproducibly manufacturing sufficient amounts for comprehensive preclinical testing. Even for magnetic nanoparticle systems already tested in clinical trials, one study has been withdrawn due to high lot to lot variation of the nanoparticles.[7]

Magnetic particle imaging (MPI) is a novel imaging technology with great potential for cancer diagnosis using magnetic nanoparticles as a tracer material.[8,9] MPI is in a preclinical state with further demand for improving both the MPI scanner infrastructure and the imaging performance of the tracer materials.[10] Theoretical models suggest that single-core iron oxide nanoparticles of about 20–30 nm core diameter are optimal MPI tracers.[9,11–13] Single-core iron oxide nanoparticles are of great interest not only for MPI, but also for the promising cancer treatment approach of magnetic fluid hyperthermia. Hyperthermia treatment using magnetic nanoparticles is already close to clinical practice particularly for brain tumours with further expanding indication fields *e.g.* prostate cancer.[14–16] Theoretical estimations as well as experimental results of bacterial magnetosomes suggest huge potential of single core magnetite nanoparticles also in hyperthermia applications.[17,18] Furthermore, cancer

treatment with drug loaded magnetic carriers exploiting magnetic drug targeting as well as drug carriers co-loaded with imaging agents for drug monitoring are also of high-profile in the research landscape.[19–22]

Single-core particles with sizes larger than 20 nm are not easily accessible by standard synthesis methods like co-precipitation of iron salts. The technically more demanding thermal decomposition involves toxic educts and requires high temperature and phase transfer leading to a time-consuming multistep procedure.[23] A promising alternative approach, the biotechnological production of single-core iron oxide nanoparticles, so-called magnetosomes from a bacterial origin, also suffers from effortful downstream processing, limited scalability, and potentially immunogenic residues inhibiting safe *in vivo* applications.[24]

Preliminary studies on the continuous synthesis of iron oxide nanoparticles demonstrated the high potential of micromixer technology as a valuable tool for the development of new magnetic nanomaterials.[25] However, the performances of reported tracers for magnetic particle imaging at this time were still far below the performance of Resovist®, which is an MRI contrast agent and is presently also considered as a gold standard for MPI.

Here, we report high performance single-core iron oxide nanoparticles for versatile theranostic applications obtained from an enhanced microfluidics-based synthesis platform including downstream processing resulting in exceptional aqueous dispersion stability. With single-cores in the size range between 20 and 35 nm, they are within a comparable range to that of bacterial magnetosomes, but are advantageous concerning biocompatibility and scalability. With our platform technology, the tuneable, scalable production of size-controlled magnetic nanoparticles that can combine imaging (MPI and MRI) with therapeutic functions (hyperthermia, and drug loading) in one single nanoparticle system becomes feasible.

Results and discussion

Preparation of magnetic single-core nanoparticles

Single-core magnetic iron oxide nanoparticles were manufactured continuously in a micromixer-based synthesis platform consisting of a nanoparticle generation module, and particle growth zone as well as a downstream processing module, as shown in the photograph in Fig. 1. Microfluidic systems for nanoparticle synthesis gained popularity in the last decade because of their promising potential in controlling critical stages such as nucleation and growth leading to improved size control, enhanced reproducibility and higher throughput than in batch synthesis.[26] Even though microfluidic systems for magnetic nanoparticle systems have already been described, those devices are either limited by very low flow rates and throughputs, e.g. for droplet generation,[27] or are based on thermal decomposition or supercritical organic solvents,[28–30] which require high energy input (high temperature and pressure) and partially toxic agents. None of these approaches are single step procedures. Thus, additional steps for washing, stabilization and purification of nanoparticles are generally required leading to undesirable agglomeration and aggregation of initial single-core nanoparticles, which is particularly crucial for larger cores >15–20 nm.

Fig. 1 Photograph of the micromixer platform used for synthesis of single core iron-oxide MNP.

This enhanced micromixer platform, based on a set-up already published previously,[25] enables control over the particle size of single-core nanoparticles that are

instantaneously coated and purified resulting in a ready-to-use stable aqueous nanoparticle dispersion.

To demonstrate the performance capacity of this modular manufacturing platform for the tuneable production of biocompatible iron oxide nanoparticles for versatile biomedical applications, a series of synthesis runs were performed. As a result, three single-core magnetic nanoparticle (MNP) systems T1, T2, and T3 with core size diameters in the range of 25, 30 and 35 nm were synthesized with analogous educt solutions and process parameters, solely by moderately varying the reaction temperature between 328 K and 338 K ($\boldsymbol{\Delta T}$ = 5 K) far below the boiling point of water as one example of the relevant steering parameters. The higher the reaction temperature is, the faster the particles grow, so that in the same time interval keeping all other parameters such as the flow rate, dwell time, educts constant, particles with larger diameters are obtained. The structural and magnetic properties of these particles were characterized by Transmission Electron Microscopy (TEM) (core diameter), Differential Centrifugal Sedimentation (DCS) (hydrodynamic diameter), quasi-static DC Magnetization (DCM) (saturation magnetization), dynamic AC Susceptibility (ACS) (initial susceptibility) and Magnetic Particle Spectroscopy (MPS) (non-linear dynamic susceptibility). The relevant structural and magnetic parameters for the three samples are summarized in Table 1. Furthermore, experiments to demonstrate the performance of the systems as MPI tracers, hyperthermia agents and MRI contrast agents were carried out. In addition, we analysed the biocompatibility with first cytotoxicity and apoptosis tests on endothelial cells.

Table 1 Structural and magnetic parameters of continuously synthesized single-core iron oxide nanoparticle samples T1 (d_c = 23 nm), T2 (d_c = 30 nm), and T3 (d_c = 36 nm). For comparison, the corresponding literature values for Resovist® have been added. The values for d_c determined by TEM from Kraupner 2017;[39] M_S and magnetic diameters of the bimodal multicore system from Eberbeck 2011,[11] MPS parameters A^*_3 and A_5/A_3 from Löwa 2017.[40] Note, the number in parentheses behind the value denotes the variations of the parameters found in different **N** = 3–5 synthesis runs, **e.g.** 23(5) nm means 23 ± 5 nm. The parameter $\sigma = d_{c,SDV}/d_{c,mean}$ denotes the relative standard deviation of the size distribution determined by TEM.

Syst	d_{core} nm	σ	d_{hydr} nm	M_S Am²/kg(Fe)	χ_{ini} m³/kg(Fe)	A_3* Am²/kg(Fe)	A_5/A_3 %
T1	23(5)	0.2(3)	21	90(5)	0.026(3)	13.5(8)	31.4(9)
T2	30(5)	0.16(2)	27.5	108(5)	0.055(3)	18.9(3)	33.4(3)
T3	36(6)	0.17(2)	35	101(6)	0.09(1)	16.1(8)	32(2)
Res.	6(3) 5 24		45(7)	90		8.67(3)	38.38(2)

Structural and magnetic characterization of magnetic singel-core nanoparticles

TEM and DCS results

The TEM image shown in Fig. 2 clearly reveals the envisaged core size increase by increasing the reaction temperature.[25] All three samples are mainly homogenous in morphology and size. A minor morphological shift from fully spherical shape for T1 (23 nm) synthesized at the lowest temperature to partly cubic particles for the larger particles T2 (30 nm) and T3 (36 nm) is visible. The MNPs produced with the micromixer platform are evidently single-core particles that have not formed any clusters or aggregates, which is often an unwanted effect for synthetic MNPs lacking sufficient stabilization. They show the same narrow size distribution with a relative standard deviation **σ** (ratio between the standard deviation and mean of the absolute diameter distribution as listed in the inset in Fig. 2) with **σ** ≤ 0.2 for all systems. To further evaluate dispersion stability and agglomeration status in aqueous dispersion,

analytical centrifugation (DCS) was carried out. This analytical technique, which sensitively resolves the occurrence of aggregates and agglomerates, confirmed a relatively narrow distribution of hydrodynamic diameters without strong aggregation. In contrast to dynamic light scattering, where the high absorbance of the black magnetite particles interferes with the optical analysis of hydrodynamic diameters, DCS provides more reliable size information, as sedimentation within the disc centrifuge is proportional to the size as well as the density of the particle. The data in Fig. 3 show the density of pure magnetite neglecting the decrease in density by the organic layer on the surface of the particle. This leads to slight shifting of the hydrodynamic diameters determined by DCS to smaller values (as the real density of the particles is smaller than the assumed magnetite density used for the data analysis). This effect diminishes with increasing core sizes as the proportion of the organic layer decreases.

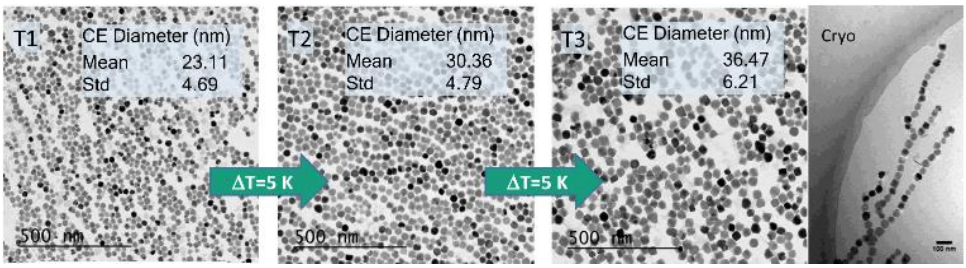

Fig. 2 TEM images of single-core iron-oxide nanoparticle samples T1, T2, and T3 manufactured at increasing synthesis temperatures (ΔT = 5 K). Corresponding particle core diameters (mean and standard deviation; Std) obtained from the TEM image are shown in the inset. The cryogenic TEM picture shows the tendency of chain formation for particles with a core size larger than 30 nm (T3 sample).

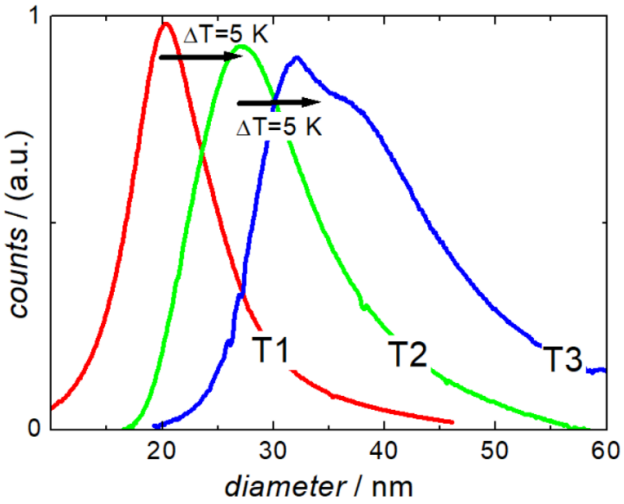

Fig. 3 Analytical centrifugation (DCS measurements) of single core iron oxide nanoparticle samples T1, T2, and T3 synthesized at three different temperatures (ΔT = 5 K).

DCS measurements of the three samples showed the expected increase in hydrodynamic size with increasing synthesis temperature. Furthermore, they confirmed the exceptional dispersion stability of the relatively large magnetic cores in aqueous media. Compared to other synthesis methods, the presented one-step continuous process avoids additional precipitation and resuspension steps for subsequent stabilization or washing, thus undesirable clustering does rarely occur.

Nonetheless, the appearance of a peak shoulder for sample T3 clearly indicates the occurrence of particle–particle interactions due to its high magnetic moments and the onset of dimer, trimer, and chain formation. Tendency of reversible chain formation also in the absence of a magnetic field was observed already for particles with core diameters larger than 30 nm and confirmed by cryogenic electron microscopy as shown in Fig. 2 (right) for sample system T3.

The micromixer manufacturing platform enables access to single-core MNPs in the relevant size range for potential applications in nanomedicine (MPI and magnetic hyperthermia). Since not (solely) the physical size, but more importantly the magnetic properties determine the performance in biomedical magnetic applications, a further comprehensive characterization with multiple magnetic measurements was conducted.

Magnetic characterization

DCM results: saturation magnetization, and moment estimation

The saturation magnetization M_S of magnetic nanoparticles is a valuable magnetic parameter indicating the quality of the crystal structure and its homogeneity achieved by the nanoparticle synthesis process.

The room temperature magnetization curves for the three systems are shown in Fig. 4 from which the saturation magnetization M_S is determined. We observe M_S-values above 108 A m² per kg(Fe) for sample T2, 101 A m² per kg(Fe) for sample T3, and 90 A m² per kg(Fe) for sample T1, which is the same value that is found for Resovist®.[11] All values are very close to M_S values (111–127 A m² per kg(Fe)) reported for bulk magnetite or maghemite[31,32] indicating the high crystallinity of the magnetite structure with a low amount of disorder reached by our synthesis.

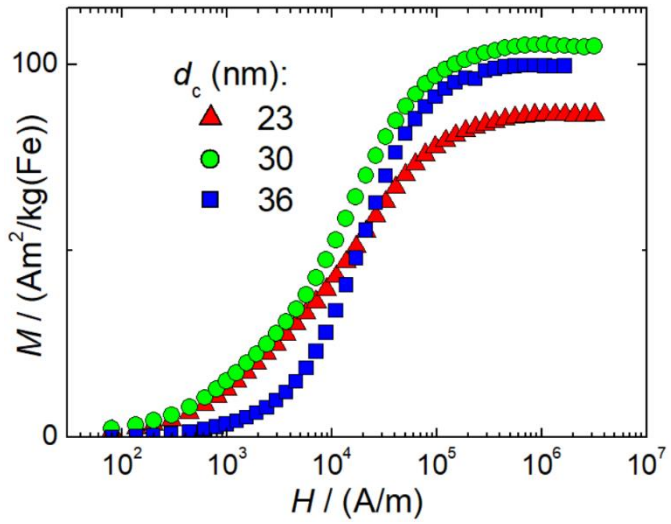

Fig. 4 Room temperature (T = 295 K) DC magnetization curves of single-core iron oxide samples T1 (d_c = 23 nm), T2 (d_c = 30 nm), and T3 (d_c = 36 nm) synthesized at three different temperatures (ΔT = 5 K).

The high M_S-values of our systems, we suppose can be attributed to the presence of large proportions of highly magnetic magnetite and maghemite phases, which both have very similar magnetic properties. The structural composition of our nanoparticle systems regarding the occurrence of other non-magnetic hematite, and wustite and other iron oxide compounds such as iron hydroxides was not analysed. Moreover, other iron oxide nanoparticle systems also consist of a mixture of magnetite and

maghemite, which are well tolerated by the body like the MRI contrast agent Resovist®.[33,34] This reduction is attributed to crystallographic disorder or surface disorder caused by the coordination effects of organic ligands. The former leads to local disorder of the spin arrangement (locally) within the particle, and the latter at the particle surface, both reducing the coupled total particle moment m_p in a nanoparticle and thereby M_S.

Generally, M_S-values for magnetite (or maghemite) nanoparticles are observed to be below that of the pure bulk material.

A pronounced correlation between the particle size and M_S is reported in the small diameter range 1 nm to 10 nm due to the large surface-to-volume-ratio of these particles. The observed slight reduction of M_S in T1 with the smallest diameter might therefore be attributed to this effect while for the larger systems T2, and T3 the influence of surface disorder becomes insignificant. This behavior has been observed for multi-core nanoparticle systems, where several small sized nanoparticles are embedded in a polymer matrix to form a larger nanoparticle, so-called nanoflowers. The even increased surface-to-volume ratio in this system leads to strongly reduced M_S-values of 60 A m^2 per kg(Fe).[35]

Finally, at larger diameters as in sample T3 dipole–dipole interactions between the particles could lead to chain formation, which in turn would reduce the measured magnetization and thereby M_S of the particles.

For 30 nm single core MNP obtained by thermal decomposition Teeman *et al.* reported a M_S-value of 96 A m^2 per kg(Fe),[36] which is close to the value of micromixer sample T2 (30 nm). In contrast to our aqueous synthesis approach, their laborious organic synthesis procedure requires a subsequent phase transfer step and takes about 40 h. Thus, not only concerning the presence of organic and toxic agents during the synthesis, but also regarding efficiency, our micromixer platform with residence times in the range of a few minutes represents an attractive alternative. From $M_S = m_p/V_p$ describing the ratio between the particle moment m_p and core volume $V_c = \pi/6\ 6\ d_c^3$ as

determined by TEM (see the TEM results above), we can estimate mean particle moments (=number of coupled individual atomic magnetic moments resulting in a single domain of total magnetic moment m_p within the nanoparticle) of $2 \times 10^5 \mu_B$ (T1), $6 \times 10^5 \mu_B$ (T2), and $10^6 \mu_B$ (T3), respectively. Here, $\mu_B = 9.27 \times 10^{-24}$ A m^2 denotes the Bohr magneton. Preserving these large magnetic moments for the use in (biomedical) magnetic applications, thorough stabilization of single-core nanoparticle systems is required. To this end, the presence of the stabilizing agent already during the aqueous synthesis is a great advantage, as no additional precipitation step or phase transfer for postprocessing stabilization is required, which, due to the existing huge magnetic moments, would inevitably result in strong and inextricable agglomeration. This undesired effect was observed for single-core nanoparticles even below 30 nm, which formed agglomerates after phase transfer from thermal decomposition synthesis.[36]

The successful stabilization strategy in the micromixer synthesis is confirmed by DCM and ACS measurements. The DCM and ACS results for sample T1 (23 nm) as well as T2 (30 nm) show no agglomeration. A slight tendency is seen in sample T3 (36 nm) due to the initial formation of dimers, trimers or chains as confirmed by TEM. However, this chain formation is reversible as evidenced by DCM measurements after dilution and vigorous mixing of the samples.

Initial susceptibility, hydrodynamic diameter and stability

ACS measures the response of the magnetic moments m_p of the nanoparticles exposed to an alternating magnetic field. The moments will follow the excitation field but with a phase lag. Real (in-phase) χ' and imaginary (out-of-phase) parts χ'' of the complex dynamic mass susceptibility as a function of frequency f for the three systems are displayed in Fig. 5. The initial mass susceptibility χ_{ini} extracted from the extrapolation of $\chi'(f)$ for $f \rightarrow 0$ increases with increasing core diameter from χ_{ini} = 0.026(3) m^3 per kg(Fe) for T1 up to 0.09(1) m^3 per kg(Fe) for T3. This is expected since $\chi_{ini} = (M_S V_c)^2/(3k_B T) = m_p^2/(3k_B T)$ is proportional to the square of the particle moment, *e.g.* to the square of the core volume V_c of the particles. Furthermore, in the imaginary

part $\chi''(f)$ pronounced peaks with visible maxima at frequencies of 9.3(1) kHz (T1), 6.21(5) kHz (T2) and 2.8(1) kHz (T3) are observed. Following the Debye model,[37] the excitation frequency f_P is at the peak position in the range of the inverse of the Brownian relaxation time $\tau_B = 3V_h\eta/(3k_BT)$ with η describing the viscosity of the medium of the nanoparticle with hydrodynamic volume V_h. Therefore, the peak positions shift towards smaller frequencies for larger hydrodynamic diameters (f_P(T3) < f_P(T3) < f_P(T1)) as a consequence that the larger particle moments already at lower frequencies cannot follow the sinusoidal excitation.

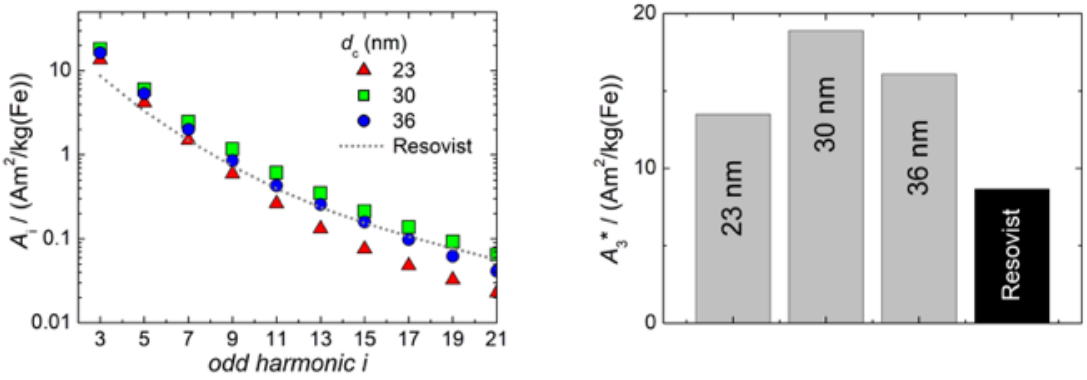

Fig. 5 Non-linear dynamic magnetization spectra (left) measured at 25 kHz excitation frequency and 25 mT amplitude of single core iron oxide nanoparticle samples T1 (d_c = 23 nm), T2 (d_c = 30 nm), and T3 (d_c = 36 nm).

In T3 with the largest particle diameters the beginning of dipole–dipole interactions leading to chain formation or smaller aggregates (dimers, trimers) is attributed to the observed non-constant extrapolation of χ' towards f = 0 and the broader maximum with a pronounced shoulder towards lower frequencies seen in χ''(f).

Non-linear dynamic magnetic susceptibility

The non-linear dynamic magnetic susceptibility as measured by MPS is an important parameter to assess magnetic nanoparticle systems for their behaviour in both magnetic hyperthermia and MPI. Generally, single core nanoparticles with larger magnetic moments are favourable for magnetic hyperthermia and MPI.

We determined the non-linear susceptibility by MPS at a fixed frequency (f_0 = 25 kHz) and amplitude (B_{excit} = 25 mT). As shown in Fig. 6, all three systems exhibit non-linear susceptibilities (parametrized by A^*_3 in units A m² per kg(Fe)) higher than that of the

MPI gold standard and MRI contrast agent Resovist (A^*_3 = 9.1 A m² per kg(Fe)) for T2 by nearly a factor of 2. These high A^*_3 -values imply a high sensitivity, *e.g.* for spectroscopic applications like quantification of nanoparticles in cells and tissues by MPS.[38] At higher harmonics A_i, the dynamic susceptibility of Resovist® gets closer to the susceptibility of T2, indicating that in MPI, where the amplitudes of the higher harmonics A_i are important to ensure spatial resolution, both samples should exhibit equal image quality (see next section). After a storage time of 15 months at room temperature, MPS revealed for all 3 MNP systems minor relative changes below 5% in the MPS parameters A^*_3 and A_5/A_3 the high shelf life stability of the synthesis approach.

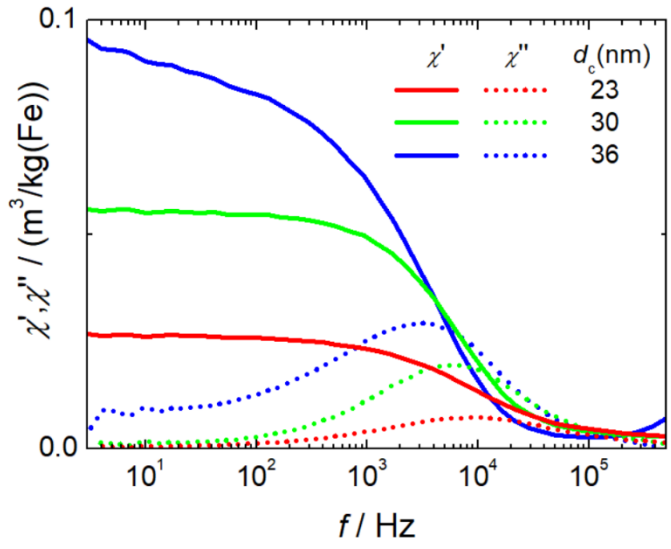

Fig. 6 ACS measurements of single core iron oxide nanoparticle samples T1 (d_c = 23 nm), T2 (d_c = 30 nm), and T3 (d_c = 36 nm) synthesized at three different temperatures (ΔT = 5 K). The straight lines denote the real part, and the dotted lines the imaginary part of the complex dynamic susceptibility.

Relevant structural and magnetic parameters for the three MNP samples in comparison to Resovist® as a well characterized "gold standard" in the literature are presented in Table 1 (see below).

It is evident from the results presented so far that the properties of the single-core iron oxide magnetic nanoparticles synthesized by micromixer flow chemistry *via* an aqueous synthesis route can be tuned effectively by adjusting solely the temperature, the one relevant process parameter. Within a certain process window, the increase in temperature results in larger core diameters as observed by TEM. Moreover, the

corresponding magnetic characterization confirms an increasing initial mass susceptibility χ_0 that is proportional to the square of the particle moment. Larger magnetic cores lead to chain formation, which to some extent was observed structurally by analytical centrifugation as well as by cryogenic TEM and also confirmed magnetically by ACS measurements. These findings lead to estimated optimized particles of about 30 nm core diameters for application in MPI and magnetic hyperthermia, showing relatively high magnetic moments retaining dispersion stability.

Performance of the nanoparticles in biomedical applications

Diagnostic application: imaging capability of the nanoparticles

Magnetic particle imaging performance

Magnetic Particle Imaging (MPI) is an emerging tomographic imaging technology with simultaneous good spatial (mm) and excellent temporal (ms) resolution as well as high sensitivity where the image contrast is provided specifically by the magnetic nanoparticles without tissue background and without any need of ionizing radiation or radioactive tracers.[41] The development and synthesis of tailored MPI contrast agents are an emerging and important actual research field.

MPI is based on the non-linear dynamic magnetic response of MNPs exposed to an alternating magnetic field, from which by using additional magnetic field gradients, an image of an MNP distribution can be obtained. To assess the potential of a nanoparticle system for MPI phantoms either MPS measurements – a kind of zero-dimensional MPI – of characteristic parameters A^*_3 and A_5/A_3 (see the section above) or direct MPI measurements of phantoms with a defined shape and nanoparticle concentration can be used. To exemplify the MPI imaging capabilities, Fig. 7 (middle) shows reconstructions of a spiral phantom filled with sample T2 (30 nm), which exhibits the highest non-linear susceptibility A^*_3 measured by MPS. For comparison, we performed MPI measurements of the phantom filled with Resovist® (Fig. 7, right) at an identical iron concentration of 15 mM. Resovist®, originally a developed liver

contrast agent for MRI, which is now extensively used as a tracer for MPI because of its good MPI performance.

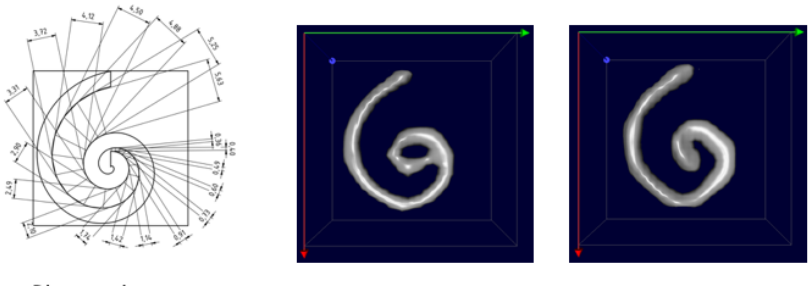

Fig. 7 Spiral phantom geometry (left) and MPI images of the phantom filled with 200 µL volume 15 mM iron concentration of T2 (30 nm) (right) and Resovist® (middle). The channel width of the phantom was 2 mm.

The reconstruction of the MPI phantom is resolving mostly the complete spiral structure for both sample T2 as well as Resovist® with the same high quality.

From the border between the clearly resolved outer part of the spiral and the non-resolved inner central part of the spiral, a spatial resolution in the range of 1.5 mm was estimated for T2 and Resovist® for the MPI scanner settings, the particle concentration and within the uncertainty of the reconstruction.

With this behaviour, the single-core iron oxide sample T2 already now ranks among the high performance MPI tracers such as Resovist®. But there is space for additional fine-tuning of magnetic parameters to enhance the MPI performance not only by adjusting the size but also by addressing the internal magnetic structure through synthesis parameters of our micromixer approach. Due to the high flexibility, scalability and control of the micromixer technology it is an ideal tool to pursue this fine tuning of magnetic properties.

Magnetic resonance imaging contrast agent

The ability of iron oxide particles to increase the proton relaxation rates of the surrounding water proton spins makes them suitable as contrast agents in MRI and is described by the longitudinal R_1 (=1/T_1) and transversal relaxation rate R_2 (=1/T_2). This contrast improvement is based on stray fields caused and induced by the magnetic moments of the nanoparticles in the huge external B_0 field acting on the proton

relaxation in MRI. This is associated with the magnetic susceptibility of the particles as a function of particle size, composition and experimental variables, such as the magnetic field, strength of MRI, temperature and medium of dispersion.[42] The relaxation rates as a function of iron concentration c(Fe) measured at B_0 = 1.5 T are shown in Fig. 8 for sample T2 (30 nm) from which the MRI relaxivities have been determined and compared to those of the clinically approved MRI liver contrast agent Resovist® (multi-core nanoparticles with bimodal size distribution clusters of d = 5 nm and 24 nm).[11]

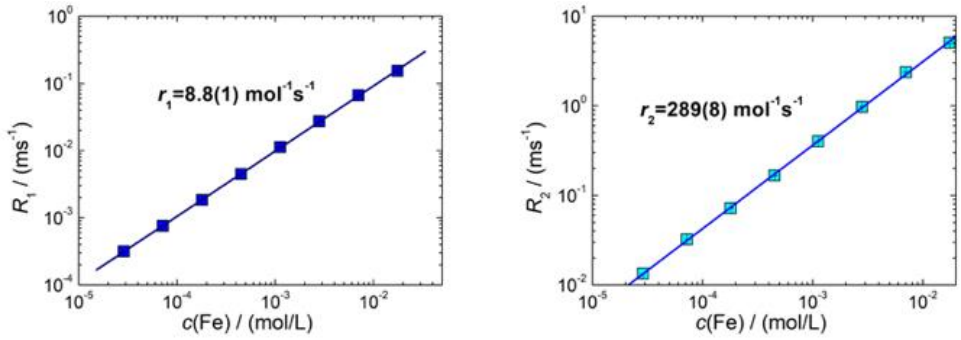

Fig. 8 Room temperature NMR relaxation rates $\mathbf{R}_1$ (left) and $\mathbf{R}_2$ (right) as a function of iron concentration **c**(Fe) of sample T2 (30 nm) nanoparticles measured at 1.5 T. Note, for graphical representation the corresponding rates obtained by linear regression are displayed as straight lines.

For sample T2 (30 nm) we determined relaxivities of r_1 = 8.8(1) L mol^{-1} s^{-1} and r_2 = 289(8) L mol^{-1} s^{-1}. For T3 (35 nm) we measured r_1 = 2.9(1) L mol^{-1} s^{-1} and r_2 = 59(1) L mol^{-1} s^{-1}. For the MRI liver contrast agent Resovist® values of r_1 = 7.4 L mol^{-1} s^{-1} and r_2 = 95 L mol^{-1} s^{-1} are reported in the literature at the same field B_0 = 1.5 T.[43] The relaxivities for these systems are shown in Table 2. We found a three times higher r_2-relaxivity for T2 compared to Resovist®. MNP with high transverse relaxivity r_2 can be used as an effective negative contrast agent. This feature is associated with the magnetic susceptibility and crucially depends on the particle size, composition and experimental variables such as the magnetic field, strength of MRI, temperature and medium of dispersion.[42] In addition to a high r_2 relaxivity, the efficiency of a T_2 contrast agent relies on the ratio r_2/r_1 between transversal and longitudinal relaxivities.[44] We find a specific enhancement of this ratio in both samples in comparison to Resovist®.

Our results indicate that already sample T3, but moreover sample T2 exhibits a better contrast in T_2-weighted MR imaging than Resovist®. Since Resovist® has been withdrawn from the market,[45] our synthesis approach would be useful to develop an alternative iron oxide MRI contrast agent like T2 that would yield even better image quality.

Table 2 NMR r_1- and r_2-relaxivities at B_0 = 1.5 T of single-core sample T2 (30 nm), and T3 (36 nm) together with values taken from Modo 2007 (ref. 43) for the liver contrast agent Resovist® (multi-core system, and bimodal size distribution)

System	d_c nm	B_0 T	r_1 L·mol^{-1}·s^{-1}	r_2 L·mol^{-1}·s^{-1}	r_2/r_1
T2	30	1.5	8.8(1)	289(8)	33
T3	35	1.5	2.9(1)	59(1)	20
Resovist® (multi-core)	5, 24	1.5	7.4	95	13

Therapeutic application: magnetic fluid hyperthermia (MFH)

Magnetic fluid hyperthermia is a potential technique for cancer therapy that exploits heat generated by magnetic nanoparticles exposed to a sinusoidal alternating magnetic field to kill cancerous cells.[46] Many studies have shown that MFH is effective in killing cancer cells both *in vitro* and *in vivo* and that MFH crucially depends on the magnetic properties of the nanoparticles, the excitation frequency and amplitude of the alternating field to generate heat. The specific absorption rate (SAR), sometimes also denoted as specific loss power, is an important parameter to assess the capability of a magnetic nanoparticle system for MFH. The SAR value defined as the power dissipated into heat per unit of mass of nanoparticles, crucially depends on external parameters such as frequency f and amplitude H of the excitation field, as well as on internal nanoparticle characteristics. Here, structural factors such as the core size, size distribution, particle shape and crystallinity as well as magnetic properties such as saturation magnetization, anisotropy, relaxation time, concentrations and particle–particle interactions are important.[47] To become independent of the external parameters f and H, the intrinsic loss power defined as ILP = SAR/($H^2 \times f$) in units of nH m^2 per kg(Fe) is useful since it allows the system-independent direct comparisons between experiments performed at different frequencies or amplitudes.

Fig. 9 shows the measured SAR values as a function of the frequency of sample T2 in two different formulations (as synthesized and concentrated) in comparison with Resovist®. All systems show the expected linear increase of SAR with frequency, while both T2 systems exhibit a much steeper slope compared to Resovist®. From the SAR values, corresponding ILP values for T2 (as synthesized) of 9.4(7) nH m² per kg(Fe), and for T2 (concentrated) of 8(1) nH m² per kg(Fe) were calculated. The values of T2 are much higher than typical ILP values found in the literature,[48] which are in the range of 0.2–5 nH m² per kg(Fe) (like the ILP = 3.0(5) nH m² per kg(Fe) measured for our Resovist® sample). These remarkably high ILP values for the T2 system documents the excellent hyperthermia capability of the single-core particles obtained by our micromixer synthesis platform.

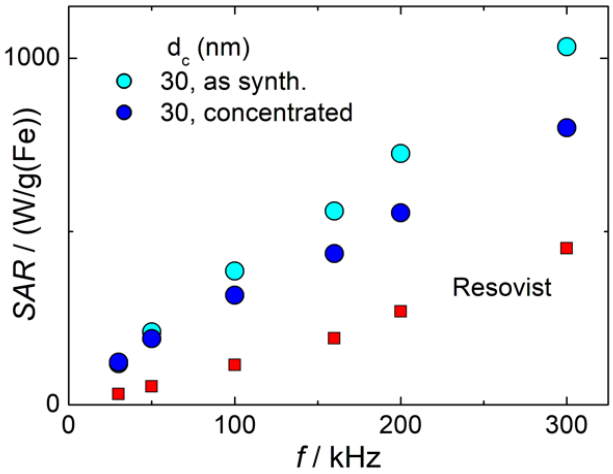

Fig. 9 Measured SAR values **versus** the frequency of single-core iron-oxide nanoparticle system T2 (30 nm) as synthesized (cyan circles), and concentrated (blue circles) and of the MRI contrast agent Resovist®.

From a clinical point of view, higher SAR (or ILP) values are beneficial since these allow lower nanoparticle doses to achieve the same hyperthermia efficacy. It is therefore important to further understand and optimize the parameters that affect heat dissipation of MFH, such as particle diameters, structures, and surface coating. A comprehensive understanding of the physics of the relevant effects employed in both imaging and magnetic hyperthermia is related to the structural and above all magnetic properties. This includes the effective saturation magnetization M_S, and the (dynamic)

magnetic moment relaxation, as well as particle sizes and surface characteristics. Additionally, the impact of the dispersion and surrounding medium as well as changes in the physiological environment (like viscosity, and pH values) has to be considered. Although there are many accepted models aiming to simulate the time-dependent magnetic response as a function of an applied magnetic field, there are no simple analytical solutions to directly obtain the synthesis parameters from which magnetic nanoparticles with maximum performance in magnetic hyperthermia and imaging could be manufactured. Therefore, a synthesis approach with accurate control of individual nanoparticle properties is highly valuable, not only for the development of nanoparticle systems with increased hyperthermia and imaging performance but also for numerical model validation describing the complex physics of magnetic nanoparticles in biological environments. Our micromixer-based synthesis platform producing single-core iron oxide nanoparticles is a valuable tool to support this research.

Biocompatibility evaluation in a cell culture

For all biomedical applications and particularly for future *in vivo* applications *e.g.* as imaging agents, hyperthermia agents or drug carriers in therapy, safety considerations are of significant importance. At this point we performed a preliminary cell culture cell viability study as a basic requisite for further preclinical investigations. Human Cardiac Microvascular Endothelial Cells (hCMEC) were used to assess cytotoxic effects of the synthesized nanoparticles.

Cell viability was investigated using the cellular deoxygenase assay, the WST-8 test with a cell counting kit-8 (CCK-8). Photometrical analysis of the amount of formazan produced by the cells allow the evaluation of the cell viability as it is directly proportional to the number of living cells. Since the CCK-8 solution is very stable, longer incubation periods, such as 24 to 72 hours, are also feasible. Moreover, the detection sensitivity is higher than that of of any other tetrazolium salts such as MTT, XTT or MTS. Furthermore, formazan dye is released in the medium and is analysed in

a cell free supernatant. Thus, interference of the absorbance of internalized nanoparticles is negligible.

No cytotoxic effects on cell viability of brain endothelial cells after treatment with MNP samples in the investigated concentration range were observed within the detection limits neither short-term (4 h), see Fig. 10, nor long term up to 72 h.

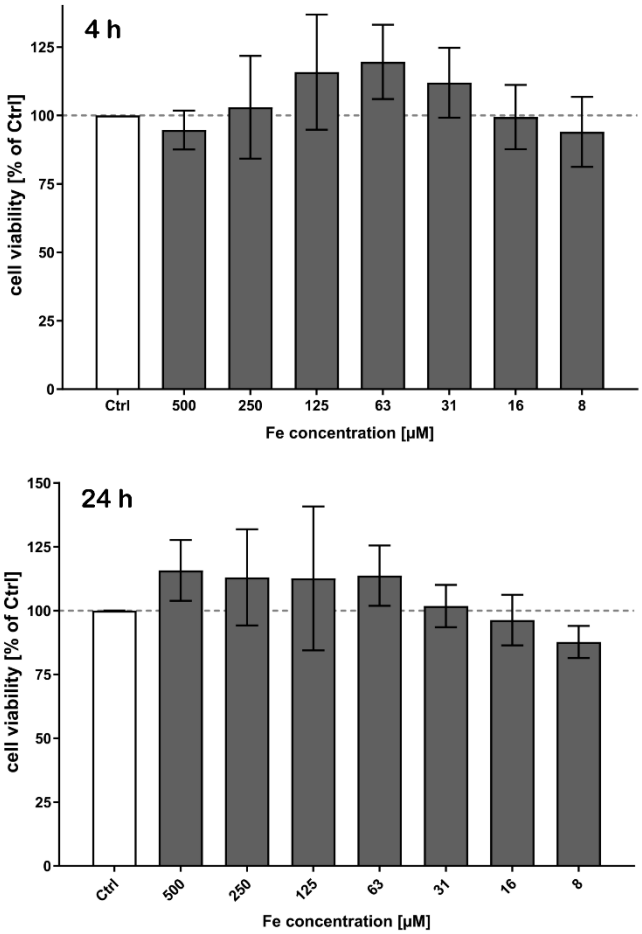

Fig. 10 Determination of cell viability of brain microvascular endothelial cells (hCMEC) after treatment with MNP samples (exemplarily T1). Cells were seeded on 96-well plates and treated with several concentrations of nanoparticles for various time periods. Cells were washed and thereafter incubated with a CCK-8 substrate. After 60 minutes, the absorbance was measured at λ = 450 nm. Untreated cells (Ctrl) were set to 100% viability. No cytotoxic effects were observed neither short term (4 h) (top) nor long-term up to 72 h (bottom).

Besides the cell viability, apoptosis caused by MNP incubation was studied. We used an annexin V-FITC kit that allows fluorescence detection of annexin V bound to apoptotic cells and enables the quantitative determination by flow cytometry. Propidium iodide (PI) was used to label the cellular DNA in necrotic cells with

comprised cell membrane. Thus, differentiation among early apoptotic cells (annexin V positive and PI negative), necrotic cells (annexin V positive and PI positive), and viable cells (annexin V negative and PI negative) was possible. The apoptosis test also did not show any significant cytotoxic effects after 24 h and 72 h (Fig. 11), respectively.

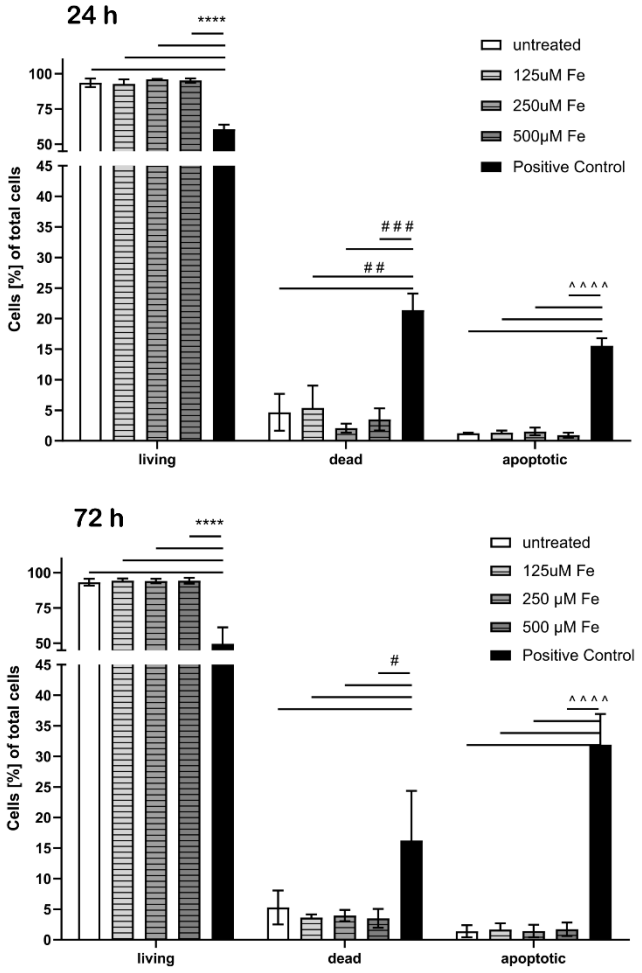

Fig. 11 Determination of cell death and apoptosis of brain microvascular endothelial cells after treatment with MNPs for 24 h (top) and 72 h (bottom). Cells were analyzed by flow cytometry after staining with annexin-V-FITC and propidium iodide. Cell populations in percent of total cells have been blotted. One-way ANOVA followed by Tukey's multiple comparisons test was performed. The data of each group (living, dead, and apoptotic) were statistically evaluated separately from each other (**n** = 3–4).

The proportion of apoptotic cells of the MNP incubated samples was below 2% while DMSO used as a positive control showed drastic effects and confirmed the reliability of the test.

This preliminary cell culture study with endothelial cells lining the blood vasculature confirms the expected biocompatibility of the continuously manufactured iron oxide single-core nanoparticles. The MNP production is based on an aqueous synthesis route with non-toxic agents or organic solvents. Thus, basic requirements for application in biomedical (*in vivo*) applications are fulfilled. Further studies on size-effects of MNPs are ongoing.

Experimental

Synthesis details

Single-core iron oxide nanoparticles were synthesised by precipitation from aqueous, alkaline solutions of iron salts based on a micromixer set-up as previously reported.[25] The microfluidic synthesis platform consists of HPLC pumps (Knauer, Germany), a caterpillar micromixer (Fraunhofer IMM, Germany) to induce particle nucleation and several temperature-controlled reaction loops to control particle growth and was enhanced by a downstream-processing-module to remove reactive agents and excess of stabilizing agents. Briefly, solutions of iron chloride, sodium nitrate as the oxidizing agent and sodium hydroxide were mixed in a caterpillar micromixer (Fraunhofer IMM) with symmetric liquid ratios and piped in a temperature-controlled reaction loop. Final nanoparticle dispersions were prevented from further oxidation as well as agglomeration with the addition of tannic acid (1.7 kDa) as the stabilizing agent. Finally, nanoparticles were purified by removal of unreacted educts and accessing of the stabilizing agent *via* diafiltration and magnetic separation and stored at room temperature for further analysis. In the present study, the size of magnetic nanoparticles was adjusted by varying only one process parameter: the reaction temperature from 328 K to 338 K (ΔT = 5 K). All other parameters including educt solutions, mixing ratios and flow rates were kept constant. Using a precise heat control (Huber thermostatic bath) and thin-walled tubes (thickness < 0.8 mm) for good thermal contact, a temperature stability below 1.5 K could be achieved. With our laboratory setup a temperature and reaction time dependent production yield in the range 20–50% can be achieved. Within 3 hours, a total volume of more than 4 liters can be

provided. By adjusting the size of the microfluidic mixer (internal scale up) or by using several mixers in parallel (parallelization scale-up), the throughput can be increased easily by a factor of 15. The reproducibility was observed to be mainly determined by the variation of the chemicals, *e.g.* iron chloride batches while only little variation, <3%, (in the magnetic parameters as determined by MPS) is observed in the reproduction of samples using the same batch of chemicals.

For the evaluation of hyperthermia performance, particle dispersion was concentrated (Eppendorf Concentrator plus) up to 280 mM final iron content.

Structural characterization of magnetic single-core nanoparticles

Transmission electron microscopy (TEM)

Transmission Electron Microscopy (TEM) measurements of nanoparticles droplet dried on carbon coated copper grids were performed with a Zeiss Libra 120 electron microscope at 120 kV acceleration voltage. A magnetic field was applied to the grids for a short period of time (about 10 minutes). The images were obtained using a CCD camera and from a selection of 1000–2000 individual nanoparticles the mean diameter and standard deviation of the core diameter were determined automatically using the open source software ImageJ.

For Cryo-TEM measurements, the same device at 120 kV acceleration voltage was used under liquid N_2 conditions. Samples were prepared by applying a 6 μL drop to a cleaned carbon-coated copper grid, blotting with filter paper, and immediately proceeding with vitrification in liquid ethane at −180 °C. Grids were stored under liquid nitrogen until being transferred to an electron microscope for imaging.

Analytical centrifugation (DCS)

An ensemble method to investigate the particle dispersion in aqueous media is analytical centrifugation (Differential Centrifugal Sedimentation, DCS). DCS measurements were performed at 20 000 rpm (21 504 rcf) (CPS Instruments Inc. Measurements) after calibration with a silicon dioxide standard (255 nm). A sucrose

gradient was built using 24% to 8% sucrose. The peak maximum was evaluated using Origin® software.

Magnetic characterization of magnetic single-core nanoparticles

DC magnetization measurements (DCM)

Room temperature (T = 295 K) DC magnetization measurements (DCM) of MNPs were performed using a SQUID magnetometer (MPMS-XL, Quantum Design, USA). The device measures the magnetic moment $m(H_e)$ of a 30 µL sample volume (immobilized in mannitol to prevent chain formation or aggregation effects during the measurements) as a function of an external magnetic field H_e up to 4×10^6 A m^{-1} (B = 5 T). The (mass) magnetization $M(H)$ (in units A m^2 per kg(Fe)) is obtained by normalizing to the total iron amount of the sample and the saturation magnetization $M_S = M|_{B=5\,T}$ was determined after subtracting a linear (paramagnetic or diamagnetic) background contribution. An overall measurement uncertainty of about 2.5% with 1% contribution from the measurement device and 2% due to preparation and the iron concentration determination is estimated. We did not perform any fitting of $M(H)$ curves using the common Langevin model because the assumptions of isotropy (no crystal anisotropy) and thermal equilibrium of this model at room temperature become invalid for diameters larger than 20 nm.

Linear dynamic susceptibility measurements (ACS)

Room temperature (T = 295 K) linear magnetic AC susceptibility (ACS) of MNPs was measured with a commercial AC susceptometer (DynoMag, RISE Acreo, Sweden). For the measurements, a quartz glass cuvette was filled with a sample volume of 100 µL MNP suspension and the real $\chi'(f)$ and imaginary $\chi''(f)$ parts of magnetic susceptibility were acquired in the frequency range 1 Hz to 100 kHz at an excitation amplitude of 0.2 mT. The initial mass susceptibility χ_0 (in units m^3 per kg(Fe), normalized to the sample iron mass) was obtained by extrapolation of the real part susceptibility $\chi'(f)|_{f\to 0}$.

Non-linear dynamic susceptibility measurements (MPS)

The non-linear dynamic AC susceptibility of MNPs is an important magnetic parameter for magnetic hyperthermia and magnetic particle imaging. Measurements were performed at T = 37 °C using a magnetic particle spectrometer (MPS) on a commercial spectrometer (MPS-3, Bruker, Germany) operating at an amplitude B_{excit} = 25 mT and fixed frequency f_0 = 25 kHz. For the measurements a fast reaction tube (Applied Biosystems®, MicroAmp) containing a sample volume of 30 µL was placed in the detection coil of the MPS system. After Fourier transform of the detected time signal, the spectral components A_i of the non-linear AC susceptibility were obtained showing distinctive amplitudes at odd multiples (harmonics) of the excitation frequency n lif_0, n = 3, 5, 7, …. Two characteristic parameters are extracted from the harmonic spectra, the amplitude of the third harmonic normalized to the iron amount of the sample, A^*_3 (in units A m² per kg(Fe)), and the concentration independent ratio between 5th and 3rd harmonic, A_5/A_3 (in units %). Both are correlated with the MPI performance with the general observation that the higher the A^*_3 , and A_5/A_3, the better the MPI images. To assess the shelf life stability of our samples, we remeasured sample aliquots of the stock suspension after 15 months of storage at room temperature and determined the relative changes in A^*_3, and A_5/A_3.

NMR relaxivities (r_1 and r_2)

MRI properties were investigated by measuring longitudinal T_1 and transversal T_2 protons relaxation times for selected nanoparticle systems of 200 µL volume diluted to different iron concentrations c(Fe). The relaxation time measurements were carried out in a Minispec mq60 (Bruker) at T = 37 °C and a magnetic field of 1.5 T. For T_1 a 2-pulse inversion-recovery sequence with a fixed relaxation delay of at least 5T_1 was used, and T_2 was determined employing a Carr–Purcell–Meiboom–Gill sequence, which consists of a 90° pulse followed by a series of 180° pulses, ideally covering the full decay of the signal. From the graphs of the iron-concentration c(Fe) dependent relaxation times $R_1 = 1/T_1$, and $R_2 = 1/T_2$, and the corresponding relaxivities r_1 and r_2 (in units of L mol^{-1} s^{-1}) were determined. For graphical presentation the measured relaxation rates of pure water samples have been subtracted.

Specific absorption rate (SAR) and intrinsic loss power (ILP)

Room temperature AC magnetometry measurements (hysteresis loops) were carried out using an Advanced AC Hyster magnetometer (Nanotech Solutions, Spain) in the frequency range from 30 kHz to 300 kHz at a magnetic field amplitude of 20 kA m^{-1}. The values of AC magnetization were normalized to the iron mass. AC hysteresis loop measurements include three repetitions to obtain average and standard deviation of the magnetic area values. Afterwards, SAR values were calculated according to SAR = $A \times f$, where A is the magnetic area and f is the AC magnetic field frequency. For system- and measurement-independent comparison of data, we calculated the intrinsic loss power (ILP) (in units nH m^2 per g(Fe)) by dividing the SAR value by the frequency and square of the excitation field, ILP = SAR/($f \times H_e^2$).

Magnetic particle imaging

Magnetic Particle Imaging (MPI) measurements of a spiral resolution phantom filled with nanoparticles was acquired using a preclinical 3D-MPI system (Bruker MPI 25/20 FF) working at an excitation frequencie of 25 kHz, an amplitude of 12 mT in three orthogonal dimensions (x,y,z) and a selection gradient of 2.5 T m^{-1} in the z-direction and 1.25 T m^{-1} in the x- and y-directions. Image reconstructions were performed based on the system function (SF) approach using a small (point-like) reference sample measured with identical parameters for all MNP systems. The spiral phantom (2 mm channel width) was filled with 200 µL of sample T2 (30 nm) at an iron concentration of c(Fe) = 15 mmol L^{-1}. Image reconstruction with a field of view of 28 × 28 × 14 voxels (mm^3) was performed using 1937 frequency components, 20 Kaczmarz-iterations, and a regularization parameter $\lambda = 10^{-5}$. For comparison, the liver contrast agent and MPI tracer gold standard Resovist® (Meito Sangyo Co. Ltd., Japan) was imaged using identical concentration and parameters.

Cell culture and determination of cell viability

Immortalized human cerebral microvascular endothelial cells (hCMEC/D3; Biozol) were maintained in rat tail collagen-I (50 µg mL^{-1}; Ibidi GmbH) -coated culture flasks

in ECBM MV cell culture media (PromoCell) supplemented with 15% fetal bovine serum (FBS), 2.5 ng mL^{-1} basal fibroblast growth factor, 10 µg mL^{-1} sodium heparin (all Sigma-Aldrich).

For nanoparticle treatment, cells were seeded onto 96-well plates coated with rat tail collagen-I (50 µg mL^{-1}; Ibidi GmbH) and cultured in the cell culture media for 24 hours. Nanoparticles were diluted in cell culture media and cells were treated starting with a concentration of 500 µM Fe for various time periods. After the treatment, cells were washed with phosphate buffered saline (PBS; Gibco) and a cell-counting-kit (CCK)-8-substrate was added as described by the manufacturer (Sigma-Aldrich). After 60 minutes, the solution was transferred to a new 96-well plate and measured in a microplate reader (VictorX, PerkinElmer) at a wavelength of λ = 450 nm. The absorbance of cells treated with the medium was set to 100%.

Determination of cytotoxicity and apoptosis by flow cytometry

Cells were seeded onto 6-well plates coated with rat-tail collagen-I (50 µg mL^{-1}; Ibidi GmbH) and cultured in cell culture media for 24 hours. Nanoparticles were diluted in media and cells were treated with various concentrations of nanoparticles for 24 and 72 hours. After the incubation the cells were washed with PBS (Gibco), detached using trypsin/EDTA solution (Sigma-Aldrich), transferred to a tube and centrifuged at 300*g* for 5 minutes. The cells were stained as described by the manufacturer (bimake), incubated for 15 minutes at room temperature and analyzed by flow cytometry (BD Accuri C6, BD Biosciences). Annexin-V-FITC was detected in the FL-1 channel, while dead (necrotic) cells stained with propidium iodide (PI) were detected in the FL-3 channel. Gating of the cell populations was performed using stained and untreated cells and cells treated with 5% dimethyl sulfoxide (DMSO; Sigma Aldrich) in cell culture media (positive control for apoptosis). 20 000 cells were analyzed for each sample.

Conclusions

We presented a micromixer synthesis platform for the continuous manufacturing of single-core iron oxide magnetic nanoparticles with well-defined core diameters in the range of 20 to 35 nm, which are stably dispersed in aqueous media. Physicochemical as well as magnetic tuning of particle properties can be achieved by adjusting relevant process parameters, *e.g.* the temperature. High quality particles with core diameters of about 30 nm were found to be optimal for combining imaging application (tracer for MPI and negative contrast agent in MRI) and therapeutic approach (MFH) application.

The micromixer synthesis platform will propel translational research for magnetic nanoparticle based theranostics applications, a further step from basic research to future medicine.

Conflicts of interest

There are no conflicts to declare.

Acknowledgements

This work was supported by DFG provided by the DFG core facility "Metrology of Ultra-Low Magnetic Fields", grant number KO5321/3 and grant number TR408/11. We gratefully acknowledge Nanotech Solutions (Francisco J. Terán) for AC magnetometry measurements to determine SAR values. R. B. thanks the Fraunhofer-Gesellschaft for the support within the Fraunhofer TALENTA program. A. B. thanks the Friedrich Ebert Stiftung for a PhD fellowship supporting his work related to this project.

Notes and references

1. K. Y. Choi, G. Liu, S. Lee and X. Chen, Nanoscale, 2012, 4, 330-342.
2. C. A. Cheng, W. Chen, L. Zhang, H. H. Wu and J. I. Zink, Journal of the American Chemical Society, 2019, 141, 17670-17684.
3. T. Lammers, S. Aime, W. E. Hennink, G. Storm and F. Kiessling, Accounts of Chemical Research, 2011, 44, 1029-1038.
4. X. L. Wu, H. Yang, W. T. Yang, X. M. Chen, J. X. Gao, X. Q. Gong, H. J. Wang, Y. Duan, D. H. Wei and J. Chang, Journal of Materials Chemistry B, 2019, 7, 4734-4750.
5. C. Sanson, O. Diou, J. Thévenot, E. Ibarboure, A. Soum, A. Brûlet, S. Miraux, E. Thiaudière, S. Tan, A. Brisson, V. Dupuis, O. Sandre and S. Lecommandoux, Acs Nano, 2011, 5, 1122-1140.
6. J. L. Arias, L. H. Reddy, M. Othman, B. Gillet, D. Desmaële, F. Zouhiri, F. Dosio, R. Gref and P. Couvreur, Acs Nano, 2011, 5, 1513-1521.
7. https://clinicaltrials.gov/ct2/show/NCT01411904, (2020).
8. B. Gleich and R. Weizenecker, Nature, 2005, 435, 1214-1217.
9. B. Gleich, Patent, 2004, WO2004091398 A2004091392.
10. N. Panagiotopoulos, R. L. Duschka, M. Ahlborg, G. Bringout, C. Debbeler, M. Graeser, C. Kaethner, K. Ludtke-Buzug, H. Medimagh, J. Stelzner, T. M. Buzug, J. Barkhausen, F. M. Vogt and J. Haegele, International Journal of Nanomedicine, 2015, 10.
11. D. Eberbeck, F. Wiekhorst, S. Wagner and L. Trahms, Applied Physics Letters, 2011, 98.
12. R. M. Ferguson, K. R. Minard and K. M. Krishnan, Journal of Magnetism and Magnetic Materials, 2009, 321, 1548-1551.

13. R. M. Ferguson, A. P. Khandhar, S. J. Kemp, H. Arami, E. U. Saritas, L. R. Croft, J. Konkle, P. W. Goodwill, A. Halkola, J. Rahmer, J. Borgert, S. M. Conolly and K. M. Krishnan, Ieee Transactions on Medical Imaging, 2015, 34, 1077-1084.

14. B. Thiesen and A. Jordan, International Journal of Hyperthermia, 2008, 24, 467-474.

15. D. Chang, M. Lim, J. Goos, R. R. Qiao, Y. Y. Ng, F. M. Mansfeld, M. Jackson, T. P. Davis and M. Kavallaris, Frontiers in Pharmacology, 2018, 9.

16. https://clinicaltrials.gov/ct2/show/NCT02033447, (2020).

17. R. Hergt, S. Dutz and M. Roder, Journal of Physics-Condensed Matter, 2008, 20.

18. E. Alphandery, I. Chebbi, F. Guyot and M. Durand-Dubief, International Journal of Hyperthermia, 2013, 29, 801-809.

19. C. Alexiou, R. Tietze, E. Schreiber, R. Jurgons, H. Richter, L. Trahms, H. Rahn, S. Odenbach and S. Lyer, Journal of Magnetism and Magnetic Materials, 2011, 323, 1404-1407.

20. W. T. Al-Jamal and K. Kostarelos, Accounts of Chemical Research, 2011, 44, 1094-1104.

21. T. Tagami, W. D. Foltz, M. J. Ernsting, C. M. Lee, I. F. Tannock, J. P. May and S. D. Li, Biomaterials, 2011, 32, 6570-6578.

22. R. Bleul, R. Thiermann, G. U. Marten, M. J. House, T. G. S. Pierre, U. O. Hafeli and M. Maskos, Nanoscale, 2013, 5, 11385-11393.

23. R. Hufschmid, H. Arami, R. M. Ferguson, M. Gonzales, E. Teeman, L. N. Brush, N. D. Browning and K. M. Krishnan, Nanoscale, 2015, 7, 11142-11154.

24. I. Ali, C. S. Peng, Z. M. Khan and I. Naz, Journal of Basic Microbiology, 2017, 57, 643-652.

25. A. Baki, N. Löwa, R. Thiermann, C. Bantz, M. Maskos, F. Wiekhorst and R. Bleul, International Journal on Magnetic Particle Imaging; Vol 3, No 1 (2017), 2017.

26. J. P. Ma, S. M. Y. Lee, C. Q. Yi and C. W. Li, Lab on a Chip, 2017, 17, 209-226.

27. L. Frenz, A. El Harrak, M. Pauly, S. Begin-Colin, A. D. Griffiths and J. C. Baret, Angewandte Chemie-International Edition, 2008, 47, 6817-6820.

28. W. Glasgow, B. Fellows, B. Qi, T. Darroudi, C. Kitchens, L. F. Ye, T. M. Crawford and O. T. Mefford, Particuology, 2016, 26, 47-53.

29. L. Uson, M. Arruebo, V. Sebastian and J. Santamaria, Chemical Engineering Journal, 2018, 340, 66-72.

30. O. Pascu, S. Marre, C. Aymonier and A. Roig, Nanoscale, 2013, 5, 2126-2132.

31. K. Schaifers and H. Voigt, eds., Schmidt-Kaler T. Landolt-Börnstein: Numerical data and functional relationships in

science and technology, 1982.

32. T. J. Hrens, Rock physics & phase relations: A handbook of physical constants. American Geophysical Union, 1995.

33. K. Ogrady, A. Bradbury, J. Popplewell, S. W. Charles and R. W. Chantrell, Journal of Magnetism and Magnetic Materials, 1985, 49, 106-116.

34. D. A. Vanleeuwen, J. M. Vanruitenbeek, L. J. Dejongh, A. Ceriotti, G. Pacchioni, O. D. Haberlen and N. Rosch, Physical Review Letters, 1994, 73, 1432-1435.

35. G. Thomas, F. Demoisson, R. Chassagnon, E. Popova and N. Millot, Nanotechnology, 2016, 27.

36. E. Teeman, C. Shasha, J. E. Evans and K. M. Krishnan, Nanoscale, 2019, 11, 7771-7780.

37. F. Ludwig, C. Balceris, C. Jonasson and C. Johansson, Ieee Transactions on Magnetics, 2017, 53.

38. W. C. Poller, N. Löwa, M. Schleicher, A. Münster-Wandowski, M. Taupitz, V. Stangl, A. Ludwig and F. Wiekhorst, Scientific Reports, 2020, 10, 3591.

39. A. Kraupner, D. Eberbeck, D. Heinke, R. Uebe, D. Schuler and A. Briel, Nanoscale, 2017, 9, 5788-5793.

40. N. Lowa, M. Seidel, P. Radon and F. Wiekhorst, Journal of Magnetism and Magnetic Materials, 2017, 427, 133-138.

41. L. C. Wu, Y. Zhang, G. Steinberg, H. Qu, S. Huang, M. Cheng, T. Bliss, F. Du, J. Rao, G. Song, L. Pisani, T. Doyle, S. Conolly, K. Krishnan, G. Grant and M. Wintermark, American Journal of Neuroradiology, 2019, 40, 206-212.

42. R. R. Qiao, C. H. Yang and M. Y. Gao, Journal of Materials Chemistry, 2009, 19, 6274-6293.

43. M. M. j. Modo and J. W. M. Bulte, Molecular and Cellular MR Imaging, CRC press, 2007.

44. Z. G. Lu, R. J. Deng, M. M. Zhen, X. Li, T. J. Zou, Y. Zhou, M. R. Guan, Y. Zhang, Y. Q. Wang, T. Yu, C. Y. Shu and C. R. Wang, Rsc Advances, 2017, 7, 43125-43131.

45. A. M. Hirt, M. Kumari, D. Heinke and A. Kraupner, Molecules, 2017, 22.

46. S. Laurent, S. Dutz, U. O. Häfeli and M. Mahmoudi, Advances in Colloid and Interface Science, 2011, 166, 8-23.

47. D. E. Bordelon, C. Cornejo, C. Gruttner, F. Westphal, T. L. DeWeese and R. Ivkov, Journal of Applied Physics, 2011, 109.

48. M. Kallumadil, M. Tada, T. Nakagawa, M. Abe, P. Southern and Q. A. Pankhurst, Journal of Magnetism and Magnetic Materials, 2009, 321, 1509-1513.

5.3 Micromixer Synthesis Platform for a Tuneable Production of Magnetic Single-Core Iron Oxide Nanoparticles

Published in: ***Nanomaterials, impact factor (5.076)***

In this publication, the continuous micromixer synthesis was employed for MNP production and compared with conventional batch synthesis regarding the physicochemical and magnetic properties as well as the reproducibility of the resulting MNP. To access single-core MNP in the specific key size range of 20-40 nm, which are particularly suitable for biomedical applications, two relevant synthesis parameters were varied. The specific effects of temperature and residence time (by flow rate and length of the residence loop) on the nanoparticle production process and their influence on the resulting nanoparticle characteristics are investigated. The MNP are comprehensively characterized regarding their structural and magnetic properties. In addition, the use of a newly developed online Magnetic Particle Spectroscopy (MPS) device for measuring the magnetic properties of the MNP during synthesis is successfully demonstrated.

MNP produced by continuous micromixer synthesis showed improved properties with reduced deviations compared to MNP synthesized in batch process. Stable single core MNP in the size range 20-40 nm are produced by adjusting synthesis parameters (temperature and residence time).

Additionally, using the online-MPS enabled the monitoring of modulation of the MNP characteristics by adjusting the synthesis parameters directly during synthesis.

The following tasks were carried out by me, Abdulkader Baki:

1- Development of the continuous micromixer device for MNP synthesis.

2- MNP production for comparison of continuous micromixer and batch synthesis approaches.

3- Methodical variation of the following synthesis parameters for continuous micromixer synthesis:

a- Temperature

b- Residence time, which can be varied by both length of the residence loop and flow rate, the latter also effects the mixing effect in the micromixer.

4- Physicochemical characterization and data evaluation of the MNP by:

a- Transmission Electron Microscopy (TEM)

b- Differential Centrifugal Sedimentation (DCS) measurements

c- Determination of iron concentration.

5- Implementation of the syntheses to evaluate the online MPS capability.

6- Summary and evaluation of experimental results

7- Draft conception and revising of the publication.

The determination of the magnetic properties was carried out at the Physikalisch-Technische Bundesanstalt (PTB) in Berlin.

nanomaterials

MDPI

Article

Micromixer Synthesis Platform for a Tuneable Production of Magnetic Single-Core Iron Oxide Nanoparticles

Abdulkader Baki [1], Norbert Löwa [2], Amani Remmo [2], Frank Wiekhorst [2] and Regina Bleul [1,*]

[1] Devision Energy and Chemical Technology, Fraunhofer Institute for Microengineering and Microsystems IMM, Carl-Zeiss-Straße 18-20, 55129 Mainz, Germany; abdulkader.baki@imm-extern.fraunhofer.de

[2] Physikalisch-Technische Bundesanstalt, 8.2 Biosignals, Abbestraße 2-12, 10587 Berlin, Germany; norbert.loewa@ptb.de (N.L.); Amani.Remmo@ptb.de (A.R.); frank.wiekhorst@ptb.de (F.W.)

* Correspondence: Regina.Bleul@imm.fraunhofer.de; Tel.: +49-6131-990168

Received: 7 August 2020; Accepted: 10 September 2020; Published: date

Abstract: Micromixer technology is a novel approach to manufacture magnetic single-core iron oxide nanoparticles that offer huge potential for biomedical applications. This platform allows a continuous, scalable, and highly controllable synthesis of magnetic nanoparticles with biocompatible educts via aqueous synthesis route. Since each biomedical application requires specific physical and chemical properties, a comprehensive understanding of the synthesis mechanisms is not only mandatory to control the size and shape of desired nanoparticle systems but, above all, to obtain the envisaged magnetic particle characteristics. The accurate process control of the micromixer technology can be maintained by adjusting two parameters: the synthesis temperature and the residence time. To this end, we performed a systematic variation of these two control parameters synthesizing magnetic nanoparticle systems, which were analyzed afterward by structural (transmission electron microscopy and differential sedimentation centrifugation) and, especially, magnetic characterization methods (magnetic particle spectroscopy and AC susceptibility). Furthermore, we investigated the reproducibility of the microtechnological nanoparticle manufacturing process compared to batch

preparation. Our characterization demonstrated the high magnetic quality of single-core iron oxide nanoparticles with core diameters in the range of 20 nm to 40 nm synthesized by micromixer technology. Moreover, we demonstrated the high capability of a newly developed benchtop magnetic particle spectroscopy device that directly monitored the magnetic properties of the magnetic nanoparticles with the highest sensitivity and millisecond temporal resolution during continuous micromixer synthesis.

Keywords: iron oxide magnetic nanoparticles; flow chemistry; continuous synthesis; micromixer; magnetic particle imaging; magnetic particle spectroscopy

1. Introduction

Due to their unique imaging, optoelectronics, catalysis, sensing, and drug delivery properties [1–3], nanocarriers and nanoparticulate systems have drawn significant attention in recent decades. Especially, magnetic iron oxide nanoparticles (MNP) with their unique properties comprising high magnetic moments, good biocompatibility [4], and highly flexible surface chemistry [5], belong to a material class suitable for a wide range of biomedical applications [6–8]. These include cell labeling, magnetic drug targeting [9], magnetic fluid hyperthermia [10,11], and diagnostic imaging [12]. Already in 1988, MNP (Resovist®) had been clinically evaluated as a negative contrast agent for magnetic resonance imaging of the liver [13]. Since 2005, MNP is also in development as tracer material for magnetic particle imaging (MPI), a novel quantitative imaging technology with potential for cancer diagnosis using MNP as local probes [14].

For the versatile biomedical applications of MNP, different requirements concerning their specific structural and chemical properties have to be considered by establishing an appropriate synthesis strategy. The particle properties, including size, crystal structure, and chemical composition of the core, in combination with surface chemistry [15] and surface charge (zeta potential) [16], influence the colloidal stability in a dispersion medium [17] as well as interactions with the biological environment. However, the most significant factor contributing to the characteristics of MNP for these applications is the magnetic behavior, which is determined in addition to the chemical composition, mainly by size, size distribution, and dispersion stability [18]. Bawendi et al. showed that very small MNP with a core magnetic diameter of about 3 nm and an ultrathin hydrophilic shell of about 1 nm was superior to larger particles as a positive T_1 contrast agent for magnetic resonance imaging and magnetic resonance angiography [19]. Contrary, theoretical models suggest that single-core iron oxide nanoparticles of about 30 nm core diameter are optimal for MPI [14]. The tailoring of size and morphology with an easy and controllable technique is the key to optimize the magnetic behavior of MNP for their envisaged in vivo applications. Thus, a deep

and comprehensive understanding of the synthesis mechanisms is not only mandatory to control the size and shape of synthesized MNP but, above all, to obtain the envisaged magnetic particle functionality.

To date, conventional batch methods of synthesizing MNP like micro-emulsion, hydrothermal reactions, sol-gel, and coprecipitation have been mostly used [20–28]. The simplest route already proposed in 1980 by Khalafalalla and Reimes [29] and Massart [30] produces MNP depending on a precipitating iron salt Fe(III)/Fe(II) mixture with a base, normally NaOH, followed by oxidation. The resulting diameters in the range of 5 to 15 nm usually show a rather broad size distribution, and nanoparticles are rarely stabilized as single cores in aqueous media. An exceptional technique to produce unique MNP is biosynthesis. Faivre and Schüler used magnetotactic bacteria and magnetosomes to prepare 20–45 nm magnetite MNP with uniform morphology and excellent magnetic properties for different applications, especially for hyperthermia [31]. Probably, due to their immunogenic bacterial lipid layer containing (glyco) proteins coating, biosynthesized MNPs have not found their way into the clinic, yet. Additionally, preparation, cultivation, and harvesting of the bacteria and magnetosomes are time- and labor-intensive and take up to several weeks. Another common technique to produce MNP with narrow size distribution and good control over size and morphology is the thermal decomposition of organometallic precursor in a boiling organic solvent. Many groups use this technique to produce high-quality MNP [32–34]. Ferguson and Krishnan et al. presented tailored 26–28 nm ±1.5 nm single-core MNP with polyethylene glycol coating for MPI application [35,36]. Although these MNP show two to three-fold higher signal amplitudes compared to Resovist®, their thermal decomposition route requires heating of the mixture for at least 24 h at 320 °C, followed by a phase transfer, resulting in a rather limited product quantity. Recently, Laurent et al. reported a continuous flow approach with a simple capillary reactor via the thermal decomposition synthesis route to obtain very small iron oxide nanoparticles. In this study, different synthesis parameters were varied, such as temperatures (200 to 300 °C), pressure (5 to 100 psi),

and concentration of the surfactant. The system was operated at relatively low flow rates between 0.05 and 2 mL·min^{-1}, and the process included further downstream processing by multiple precipitation and resuspension steps. Variation of the synthesis parameters resulted in MNP in a relatively limited core size range between 3.4 ± 0.64 and 5.86 ± 1.38 nm [37].

Generally, conventional batch synthesis methods suffer from limited reaction control, scalability issues, and often require high temperature and post-treatment, such as washing or phase-transfer from organic solvents, leading to the time-consuming multi-step procedure. Complex methods additionally lead to pure reproducibility and cause high batch-to-batch variations of resulting particle characteristics [38]. Issues of insufficient mixing and mass and heat transfer challenges even increase with increasing batch sizes [39]. Thus, further advances in MNP development is impeded, and the transfer of academic results into the technological and medical application is often hindered. Even though during the last decade, several authors have dealt with the continuous synthesis of magnetic nanoparticles, many of these issues remain unsolved [40–43]. The described processes often do not comprise the entire production procedures, including purification and stabilization steps; thus, the single cores are not stably dispersed in an aqueous medium, but clusters are obtained. Moreover, microfluidic processes based on PDMS (polydimethylsiloxane) structures usually do not tolerate high flow rates with the consequence that they often have to be operated at very low flow rates in the microliter per minute range, which limits the throughput and scalability [44,45].

To surmount these obstacles, a microtechnological manufacturing platform using flow chemistry for the controlled synthesis of magnetic iron oxide nanoparticles via an aqueous synthesis route has been developed. Microreaction technology in flow chemistry has been known and well-studied in the last decades. Outstanding is the simplicity of the approach together with the ability to precisely control reactions' parameters, e.g., temperature, residence time, rapid heat and mass transfer, high mixing efficacy, and hence reproducibility [46–48]. However, producing nanoparticles

in micromixers remains challenging as precipitating solid materials can block the microchannels of the reactors and endanger the process stability. Thus, a comprehensive process understanding is required to be able to exploit the advantages of a microstructured device and successfully run a micromixer for nanoparticles' synthesis.

In the micromixer, permanent homogenous nucleation of core seeds takes place by the reaction of two or more educts, continuously administered by pumps. Connected to the micromixer, locally separated dwell zones ensure optimal control of particle growth. Hence, the micromixer setup enables both the spatial as well as the temporal separation of nucleation and growth stages during the continuous synthesis of MNP [38].

Generally, the size and shape of MNP can be tailored by the variation of synthesis parameters, e.g., the used precursor, iron salt ratio Fe^{2+}/Fe^{3+}, temperature, pH, and the base used to precipitate the magnetic iron oxide core [49].

In this study, we presented the use of aqueous micromixer synthesis to produce high-quality magnetic single-core iron oxide nanoparticles using biocompatible educts. Solely by the adjustment of two significant process parameters: the temperature and the residence time during particles' growth, a tunable production of single-core magnetic nanoparticles could be achieved. A comparison with the conventional batch approach was carried out to study the properties and reproducibility of the two methods. The influence of temperature and variation of residence time by both changing the total flow rate as well as adjusting the volume of the residence loop was demonstrated.

To determine the resulting magnetic properties of synthesized MNP, a thoroughly magnetic characterization was carried out, mainly using a technique named magnetic particle spectroscopy (MPS). MPS can be considered as 0-dimensional MPI, e.g., it detects the non-linear dynamic magnetic response of MNP exposed to an alternating magnetic field but without technical challenging gradient fields used for spatial

encoding. Originally MPS was developed to assess the MPI performance of tracer materials, but here, we used MPS to determine the reproducibility of the continuous MNP manufacturing process compared to batch synthesis using the same precursors and to quantify magnetic effects in the synthesis caused by changes in reaction temperature and reaction time. Since MPS is a very fast (2 ms) and sensitive (moments below 10^{-11} Am^2 can be detected) technique, we presented the first results using MPS directly during continuous micromixer synthesis. Furthermore, linear AC-susceptibility measurements were used to obtain supporting information about the linear magnetization dynamics and aggregation behavior of the MNP when a small oscillating magnetic field was applied. The characterization of size, size distribution, particle shape, and morphology was determined using transmission electron microscopy (TEM) and differential centrifugal sedimentation (DCS).

2. Materials and Methods

2.1. Micromixer Synthesis

Single-core iron oxide nanoparticles were synthesized by precipitation from aqueous, alkaline solutions of iron salts based on a micromixer set-up, as previously reported [50,51]. The microfluidic synthesis platform consisted of HPLC pumps (Knauer, Berlin, Germany), a caterpillar micromixer (Fraunhofer IMM, Mainz, Germany) with 10 µL inner volume to induce particle nucleation, and several temperature-controlled reaction loops (Teflon tubing) with 3.2 mm diameter at lengths in the range 5 m to 50 m to control particle growth. Educt solutions were preheated, and a thermostatic bath (Huber, Offenburg, Germany) ensured the control of the reaction temperature T_s of the micromixer as well as the residence loop (temperature stability <1.5 K). By adjusting the length of the reaction loops and the flow rate Q, the residence time t_r, available for particle growth, could be controlled. The synthesis platform was enhanced by a downstream-processing-module to remove reactive agents and excess of a stabilizing agent. Briefly, solutions of iron chloride, sodium nitrate as an oxidizing agent, and sodium hydroxide (all reagents were used without further purification, purity grade ≥98%, Sigma Aldrich, Schnelldorf. Germany), prepared in degassed and deionized

water, were mixed in a caterpillar micromixer (Fraunhofer IMM, Mainz, Germany) with symmetric liquid ratios and piped in a temperature-controlled reaction loop. Nanoparticle dispersions were prevented from further oxidation as well as agglomeration with the addition of tannic acid (1.7 kDa, Fluka, Schwerte Germany) as a stabilizing agent. Though tannic acid, as a natural product, is not well defined and characterized, our experiences have shown that it can be successfully utilized to enhance dispersion stability in aqueous media and is able to prevent aggregation behavior. Since tannic acid acts mainly as an electrostatic stabilizer to ensure dispersion stability also in media with higher salt concentration, further functionalization by a sterically stabilizing agent is required. This can be realized, e.g., by pegylation.

Finally, nanoparticles were purified by the removal of unreacted educts and access of a stabilizing agent via diafiltration and magnetic separation and stored at room temperature for further analysis. In the present study, the size of the magnetic nanoparticles was adjusted by the two individual process parameters: the synthesis temperature T_s and the residence time t_r. While T_s was directly adjusted by the temperature chosen in the heat bath with T_s in the range of 30 to 65 °C, there were two ways to set the residence time t_r, either by the tubing length L of the dwell zone or by flow rate Q in the range of 0.6 to 11.3 min. To avoid any residence time distribution deterioration generally observed in long tubing, the inner diameter of the tubes should not be larger than 4 mm for the flow rates used in our experiments. At larger diameters, we observed a significant increase in heterogeneity of the resulting particles. Other parameters, including educts solutions, mixing ratios, and flow rates, were kept constant. With our laboratory setup, a temperature and reaction time-dependent production yield in the range of 20–50% could be achieved. The yield was calculated from total iron content used in the starting reaction mixture relative to the amount quantified by phenanthroline protocol (described below in the section: photospectroscopical determination of iron concentration) of the final product after purification. We observed the general trend that with increasing temperature and

residence time, the production yield increased, e.g., at T_s = 52.5 °C from about 21% at t_r = 3.4 min to 48% at t_r = 7.5 min).

Within 3 h, a total volume of more than 4 L could be provided with our current lab-scale set-up. By adapting the inner dimensions of the microfluidic mixer (internal scale-up) or by using several mixers in parallel (parallelization scale-up), the throughput can be increased easily by a factor of 15 [52,53].

Additionally, MNPs were synthesized by a batch precipitation approach in a flask (total volume 100 mL) with preheated educt solutions, vigorously mixed, and stirred using the same reagents and reaction times to determine batch-to-batch variations compared to micromixer MNP.

2.2. Physicochemical Characterization

2.2.1. Transmission Electron Microscopy (TEM)

TEM measurements were performed with a Zeiss Libra 120 (Zeiss, Oberkochen, Germany) electron microscope of nanoparticles' dispersion dried on carbon-coated copper grids at 120 kV acceleration voltage. A magnetic field was applied to the grids for a short period of time (about 10 min) to accumulate MNP for subsequent TEM imaging. The images were taken by a CCD camera, and from a selection of $N > 5000$ individual nanoparticles, the mean diameter and standard deviation of the core diameter were determined automatically using the open-source software ImageJ (National Institutes of Health, Bethesda, MD, USA).

2.2.2. Differential Centrifugal Sedimentation (DCS)

Accurate information on the dispersion properties of MNP in colloidal systems can be obtained by DCS (often termed analytical ultracentrifugation), where the measured sedimentation properties of the particle are directly linked to the hydrodynamic particle size distribution [54].

In contrast to characterization techniques based on light scattering, the measurement of even broad size distributions or highly light-absorbing materials is possible by DCS

as different size fractions become differentially accelerated in the gravitational field. Compared to TEM, the statistics obtained in this ensemble method were much better due to the fact that the counting of individual particles is not necessary. DCS measurements were performed at 20,000 rpm (=21,504 relative centrifugal force) (CPS Instruments Inc. Measurements, Darmstadt, Germany) after calibration with a silicon dioxide (SiO_2) standard (255 nm). The sucrose gradient was built up using 24% to 8% sucrose. Peak maximum and full width at half maximum (FWHM) were evaluated using Origin® software (ADDITIVE Soft- und Hardware für Technik und Wissenschaft GmbH, Friedrichsdorf, Germany).

2.2.3. Photospectroscopical Determination of Iron Concentration *c*(Fe)

The iron concentration *c*(Fe) of the nanoparticle samples was determined photospectroscopically following a phenanthroline protocol [55]. Ten microliters of nanoparticles were dissolved in 20 µL hydrochloric acid (37%). After complete dissolution, 470 µL of H_2O was added. Fifty microliters of hydroxylamine hydrochloride (10%) and 150 µL of 1,10-phenanthrolinehydrochloride (0.1%) were added to the 50 µL of this solution. After a reaction time of 15 min, the absorbance of the formed ferroin complexes was measured photospectroscopically by a microplate reader at a wavelength of 510 nm (SpectraMax Plus 348, Molecular Devices, CA, USA), and the iron concentrations were calculated using an iron standard calibration curve (ICP (inductively coupled plasma) iron standard, *c*(Fe) = 1.25 µg/mL to 80 µg/mL, Merck, Darmstadt, Germany).

2.3. Magnetic Characterization

2.3.1. Magnetic Particle Spectroscopy (MPS)

MPS measurements of single nanoparticle samples were performed using a commercial magnetic particle spectrometer (MPS-3, Bruker Biospin, Etllingen, Germany) operating at an amplitude B_{ex} = 25 mT and a frequency f_0 = 25 kHz. MPS detected the non-linear dynamic magnetic response of MNP exposed to an alternating magnetic field, from which their MPI performance could be assessed. For the

measurement, a fast reaction tube (Applied Biosystems®, MicroAmp, ThermoFischer, Schwerte, Germany) containing a sample volume of 30 µL was placed in the detection coil of the MPS system. The induced magnetization could be measured simultaneously by the coils. By Fourier transform of the detected time signal, the spectral components of an MPS measurement were obtained, showing distinctive amplitudes at odd multiples (harmonics) of the excitation frequency f_0. We used three characteristic parameters of the MPS harmonic spectra, the amplitude of the third harmonic normalized to the iron amount of the sample, A_3*, the (concentration-independent) ratio between 5th and 3rd harmonic, A_5/A_3., and the phase of the 3rd harmonic ϕ_3. All values were correlated to the MPI performance with the general observation that the higher the A_3* and A_5/A_3, the better the MPI images. The phase ϕ_3 described how well the particle moments could follow the excitation field at the given frequency f_0. Generally, it is observed that the smaller the particle, the better the magnetic moments follow the excitation field, and the closer is the value of ϕ_3 to zero. For comparison, we used measurements of the MRI liver contrast agent Resovist with an A_3* = 8.7 $Am^2/kg(Fe)$ at 25 mT [56] excitation amplitude. Resovist is appreciated as a gold standard due to good dynamic magnetic properties in MPS. Though withdrawn from the market, the precursor Ferucarbotran, offering the same magnetic properties, can be purchased from Meito Sanyo, Japan.

Online-MPS measurements were performed using a novel benchtop magnetic particle spectrometer with an integrated flow cell so that it could be connected directly to the growth stage of the micromixer platform. This device was recently developed at Physikalisch-Technische Bundesanstalt and is described in detail in [57]. It operates at the same basic frequency of 25 kHz as the commercial MPS device and is calibrated using reference samples measured with the calibrated commercial MPS device before. All online-MPS measurements were carried out at B_e = 12 mT to avoid any heat transfer contribution from the heating of the excitation coil of the device that might influence the synthesis of nanoparticles.

2.3.2. Alternative Current Susceptibility (ACS)

The linear dynamic magnetic susceptibility of MNP at room temperature was determined using an AC susceptometer (DynoMag, RISE Acreo, Goeteborg, Sweden). The complex linear dynamic magnetization response χ', χ'' of 100 µL stock MNP suspension filled into a glass vial was measured in the frequency range 1 Hz to 100 kHz at an excitation amplitude of 0.2 mT. Typical ACS spectra normalized to the iron amount are shown in the appendix for single-core iron oxide nanoparticles synthesized at different residence times t_r (Figute A1) and as a function of synthesis temperature T_s (Figure A2). From the measurements, the initial mass susceptibility χ_{ini} (χ' normalized to the sample's iron mass and extrapolated to $f \rightarrow 0$ Hz) in units of m^3/kg(Fe) and the frequency $f_p = f(\max(\chi''(\omega)))$ were extracted. We used χ_{ini} to assess the particle moment (χ_{ini} is proportional to the square of the particle moment, and f_p is a magnetic measure of the hydrodynamic diameter). The overall shape of the spectra was used as an indicator if aggregation occurred in a sample.

2.3.3. X-ray Diffraction (XRD)

X-ray diffraction scans at room temperature were carried using a diffractometer (Rigaku SmartLab diffractometer, Neu-Isenburg, Germany) in parallel beam reflection geometry, equipped with a monochromatic copper radiation source (λ = **1.540593** Å). The patterns were collected in the 20–70° (2θ) range with a scan step of 0.01° at a speed of 0.1°/min. The main peak positions of the XRD spectra were analyzed according to the *JCPDS* card no. #75-0033 (Fe_3O_4) and # 39-1346 (γ-Fe_2O_3).

3. Results and Discussion

Magnetic single-core iron oxide nanoparticles were manufactured using a micromixer synthesis platform via an aqueous synthesis route. Additionally, batch syntheses employing identical educt solutions were carried out to assess performance and reproducibility between continuous micromixer and batch synthesis approach. For a comprehensive understanding of the particle formation process during continuous synthesis, the influence of the two main parameters—reaction temperature

T_S and reaction time t_r—on particle properties were investigated. To evaluate the magnetic properties of the single-core nanoparticles, MPS and ACS measurements were carried out. In addition to the magnetic measurements, XRD measurements of three samples with core sizes in the range 25 nm to 35 nm were performed to confirm the crystal structure and iron oxide phase (Appendix A Figure A3). Furthermore, the physicochemical analysis was augmented by TEM to assess core size and morphology and DSC to determine the hydrodynamic diameter size distribution. Since MPS is an outstanding sensitive (magnetic moments below 10^{-11} Am^2 can be detected) and fast (2 ms for a single measurement) technique, its capability for magnetic online analysis during the continuous MNP production process was presented for the first time. Thus, direct quantitative monitoring of relevant process parameters during synthesis becomes feasible.

3.1. Reproducibility of Continuous Micromixer Synthesis Compared to Conventional Batch Synthesis

The magnetic properties of iron oxide nanoparticles depend on their composition, crystal structure, crystal quality, and morphology. Hence, a suitable synthesis route should be selected, which allows optimum control over shape, size, size distribution, and crystallinity of the particles. Several different synthesis routes to produce iron oxide nanoparticles exist. Well-established methods are thermal decomposition, sol-gel-approaches, mini emulsion, as well as coprecipitation [58]. Though all batch methods are based on different synthetic routes, each of them is usually running in a reaction vessel or flask at a predetermined reaction temperature while stirring. Thus, inhomogeneities in mixing and temperature within the reaction volume cause concentration gradients and hot spots, which influence the product quality. With increasing reaction volume, sufficient mixing and adequate reaction temperature control become even more challenging. For these reasons, the continuous synthesis approach of using microfluidics has gained a strong interest in recent years. However, particularly the synthesis of inorganic nanoparticles remains challenging because precipitated solids tend to block the microchannels and endanger the process stability.

We investigated the process reproducibility and stability of MNP obtained from our micromixer approach with particles manufactured by a conventional batch coprecipitation. We chose one specific set of synthesis parameters where we expected to obtain single-core nanoparticles with core sizes below 25 nm. In this case, a stable aqueous dispersion was easily achieved since interparticle interactions at these small diameters were rather negligible. Since we intended to show how insufficient mixing efficiency leads to inhomogeneous seed formation and, consequently, to broader size distribution, we did not investigate the influence of the different synthesis parameters here. To this end, we performed five individual continuous synthesis runs and compared the resulting nanoparticle samples with the properties of samples synthesized by five analogous batch synthesis runs using identical parameters. For the batch synthesis, we prepared 100 mL total volume with preheated educt solutions in a temperature-controlled reaction vial. Analogous to the continuous synthesis run, it was mixed vigorously in a 1:1 ratio at 52.5 °C and stirred for a reaction time of 2.5 min. The physicochemical characterization of representative nanoparticle samples by TEM and DSC for both synthesis routes is displayed in Figure 1.

The TEM images clearly indicated that core size distribution and morphology for the continuously manufactured samples were superior over the batch synthesis samples. Since the nucleation that determines the size distribution is a very fast process, the efficient mixing in the micromixer synthesis ensures a more homogenous distribution of core seeds, which, in the second stage, can uniformly grow at similar velocities because of the homogenous distribution of ripening educts as well as homogenous temperature conditions. This was confirmed by DSC measurements, which showed a larger variation of the hydrodynamic size distribution within the individual synthesis runs for the batch samples. Furthermore, the size distribution of the batch samples was generally broader and showed aggregates with average sizes even above 100 nm, while the core diameters were less than 30 nm. The DSC measurements of the continuous micromixer samples displayed similar and narrow hydrodynamic size distributions with relative standard deviations $\sigma < 0.2$. We attributed the observed

stronger variation in hydrodynamic diameters in the batch synthesis to be caused by the more inhomogeneous seed nucleation conditions due to incomplete or insufficient mixing of educts compared to the micromixer approach. This resulted not only in a broader distribution of core sizes but in the cohesion of cores, as well. As a consequence, this led to observed increased hydrodynamic diameters.

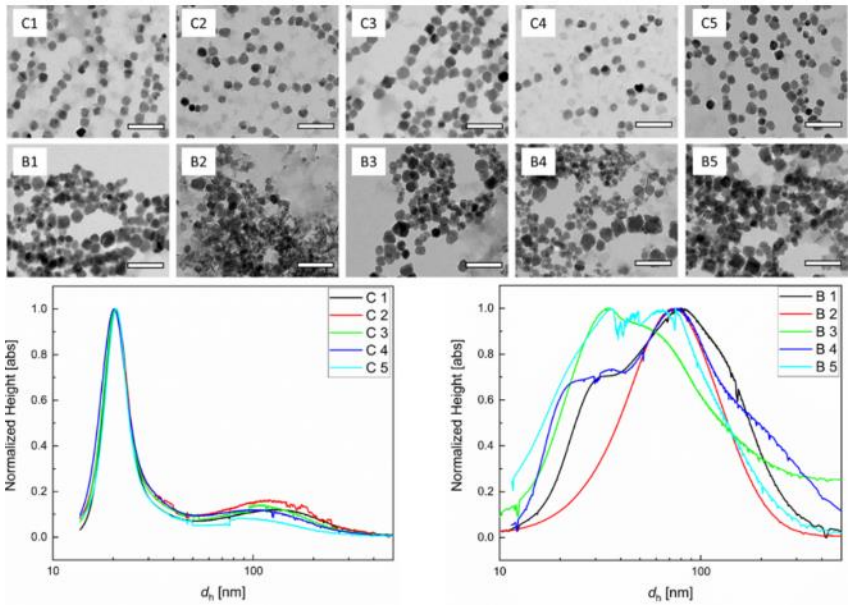

Figure 1. Comparison of structural nanoparticle properties between continuous micromixer synthesis and batch synthesis: Representative transmission electron microscopy (TEM) images of five individual continuous micromixers (C1–C5) at a total flow rate of 8 mL/min and batch (B1–B5) synthesis runs with 100 mL total reaction volume (scale bar 100 nm). Experiments were performed with preheated educt solutions at 52.5 °C, mixing ratio of 1:1, and a reaction time of 2.5 min. Bottom: Corresponding hydrodynamic diameter d_h distribution determined by differential centrifugal sedimentation (DCS) measurements of these samples (left: continuous micromixer synthesis, right: batch synthesis). Each line depicts the size distribution of one individual synthesis run. The narrower size distribution and higher homogeneity of the magnetic iron oxide nanoparticles (MNP) synthesized by continuous micromixer synthesis approach compared to batch synthesis were clearly visible in both TEM and ACS measurements.

Regarding the magnetic properties of the five individual synthesis runs, Figure 2 shows the mean and the standard variation (plotted as uncertainty bar) of the characteristic MPS parameters A_3*, A_5/A_3, and ϕ_3 of the five individual runs synthesized either by micromixer (red) or batch synthesis (green). The specific amplitude A_3* was a measure of the sensitivity of the MNP to give a dynamic magnetization response at a chosen excitation frequency f_0 per unit amount of iron, whereas the ratio A_5/A_3 could be considered as a parameter to describe the shape of the harmonics spectrum [59–61]. Finally, phase ϕ_3 was related to the relaxation effects of the MNP and parametrized the

lag of the MNP moments to follow the excitation field. Though the same general synthetic route and the same chemical reagents were used, the MNP resulting from the micromixer synthesis showed a higher MPS performance and a much smaller variation of A_3*, indicating the superior defined process control. The resulting value for A_3* = 20(1) Am²/kg(Fe) of the micromixer samples was about twice the value of A_3* = 10(2) Am²/kg(Fe) found for the batch samples, while the standard deviation of the batch samples was twice the value of the micromixer samples. Note, the value in brackets denotes the format standard variation of the five samples, e.g., 20(1) Am²/kg(Fe) = 20 +/− 1 Am²/kg(Fe). Both samples exhibited a higher specific MPS amplitude compared with A_3* = 8.7 Am²/kg(Fe) reported for Resovist® at 25 mT excitation amplitude [56]. Showing such high signal amplitudes, MNPs obtained by micromixer synthesis MNP were capable of competing with single-core iron oxide nanoparticles synthesized by sophisticated thermal decomposition synthesis with subsequent phase transfer [36]. Similarly, the mean value of A_5/A_3 = 35.6(3)% of the micromixer samples was far above the value of A_5/A_3 = 26(2)%, with six times higher standard deviation of the batch synthesis samples. This was a consequence of the much broader and more varying core and hydrodynamic size distributions found by TEM and DCS for the batch synthesis samples, which led to reduced A_3 and A_5/A_3 values. Accordingly, the mean value and standard deviation of phase ϕ_3 were increased (note the negative sign to emphasize the increased phase lag) for the batch synthesis samples.

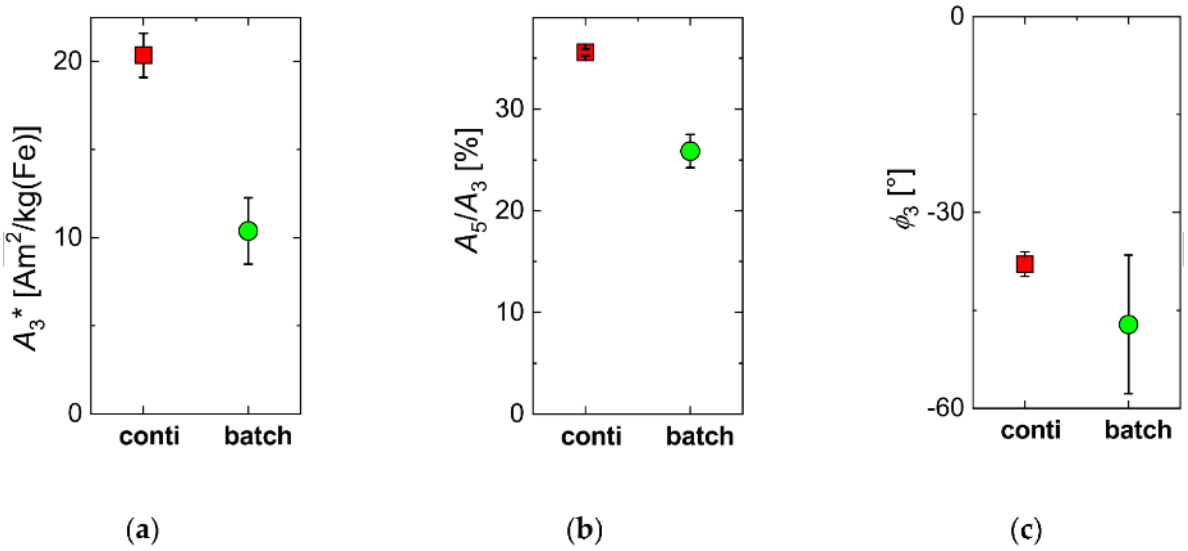

Figure 2. Mean (symbols) and standard deviation (displayed as uncertainty bars) of the variation of magnetic particle spectroscopy (MPS) parameters (B_e = 25 mT) of MNP samples synthesized by the two different synthesis approaches, micromixer (squares) and conventional batch (circles) procedure. For each synthesis procedure, five individual runs were carried out. (**a**) specific amplitude A_3*; (**b**) ratio A_5/A_3; (**c**) phase ϕ_3.

In a simplified description, the non-linear dynamic response, on which MPS relies, crucially depends on the size and mobility of the magnetic moments of the nanoparticles, which are exposed to the magnetic excitation field. The larger the magnetic moment of the particle, the larger the values of A_3* and A_5/A_3 will be, as long as the moments can follow the excitation. With the increasing magnetic moment, its mobility to align (or switch) with the excitation field will decrease, which, in turn, will lead to a phase lag, e.g., increasing (by convention negative) ϕ_3 value and resulting decrease of the two parameters A_3* and A_5/A_3. Since the size of the magnetic moment is mainly determined by the particle size and core crystal quality, whereas the mobility is given by the viscosity of the suspending medium and by the effective anisotropy, there will be an optimum particle size at a given MPS excitation frequency f_0. Smaller particles (low moments with high mobility) will have reduced values of A_3* and A_5/A_3, and a ϕ_3 value close to zero, while particles larger than the optimum size (huge moments but with low mobility) will also show reduced values of A_3* and A_5/A_3 and an increased ϕ_3 value—above the optimum phase value. Therefore, samples with broad distributions will always exhibit reduced MPS parameters compared to a sample with optimum particle size and crystal structure for a given frequency f_0.

3.2. Influence of Residence Time Adjusted by the Total Flow Rate

The micromixer synthesis platform provided the spatial and temporal separation of nucleation and growth. Core seeds formed in the micromixer at the first contact of the educts were then piped into the residence loop where subsequent particle ripening took place, e.g., the cores grew to a certain size depending on the time as well as the temperature in the residence loop. Different effects influencing the MNP properties could become addressable by changing the mixing profile (or efficiency) and the duration the particles stay in the growth stage. The residence time t_r was one main parameter that could be used to accurately control the MNP growth in continuous micromixer synthesis. With increasing t_r, larger MNPs were obtained because of the longer time interval, and the seed particles produced in the micromixer resided in the growth stage. One possibility to adjust the residence time was to change the total flow rate. The higher the flow rate, the shorter the residence time in the growth stage (assuming a constant loop volume); thus, particles had less time to grow, leading to smaller particles. Reversely, lower flow rates implied longer residence times, resulting in larger particles.

However, the total flow rate not only determined the residence time but, at the same time, affected the mixing efficiency in the micromixer stage. Optimal mixing could be achieved in a relatively small window only. Since the micromixer is a static mixer without rotation or stirring elements, its mixing efficiency strongly depends on the flow conditions [62].

Therefore, the influence of the residence time t_r adjusted by the total flow rate on the structural and magnetic nanoparticle characteristics was investigated. To this end, total flow rates were varied from 4 mL/min to 18 mL/min, which corresponded to residence times from t_r = 7.5 min to 1.7 min for a constant residence volume V = 30 mL, since $t_r = V/Q$.

As expected, the average particle size decreased with increasing flow rate since residence time t_r was decreased. In the parameter window investigated, mean hydrodynamic MNP diameters ranging from about 20 nm to 33 nm (Figure 3) were found. Larger particles displayed a slightly more broadened size distribution

(displayed as uncertainty bars in Figure 3b); nevertheless, no larger agglomerates with diameters larger than 50 nm were detected. Thus, the chosen flow rate range of 4 to 18 mL/min resembled a reliable process parameter window in the present setup.

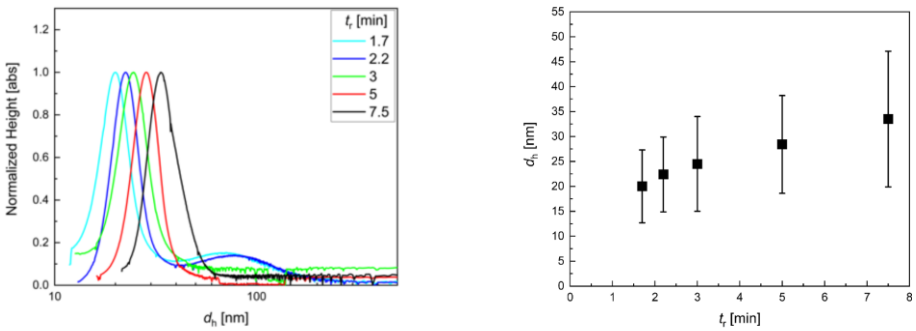

(**a**) (**b**)

Figure 3. DCS analysis for iron oxide single-core nanoparticles manufactured by continuous micromixer synthesis at different total flow rates Q from 4 to 18 mL/min (resulting residence times t_r depicted in the legend). The reaction temperature was kept at 52.5 °C. (**a**) Hydrodynamic particle size distributions as measured by DCS; (**b**) Resulting peak maximum (symbols), resembling the mean diameter, and full width at half maximum (FWHM) (plotted as uncertainty bars), indicating the width of size distribution. Varying the total flow rate was one possibility to manipulate the particle size in the growth stage. The higher the flow rate, the smaller the resulting particles since the time for particle growth was too short for reaching an equilibrium in the residence loop.

TEM data (Figure 4) confirmed the DCS observations. The core sizes increased in the same way as the hydrodynamic sizes. Moreover, particles, particularly at lower t_r, were clearly separated from each other again, confirming the stable dispersion as single cores in aqueous media. This was rarely observed for particles from aqueous synthesis, even for very small cores obtained from continuous synthesis with the aid of a T-mixer [63]. However, at lower flow rates, the particle homogeneity was slightly lower than at higher flow rates. This indicated that the micromixer was not operated at optimum flow conditions, and thus, the mixing efficiency was not sufficient to ensure a homogenous distribution of core seeds, leading to the broader size distribution observed for the final particles. Furthermore, at very high flow rates (= lower t_r), the final concentration seemed to decrease, indicating that, in this case, not only the core size but also the total number of seeds was reduced or that the reduced residence time allowed not all seeds to form magnetic cores.

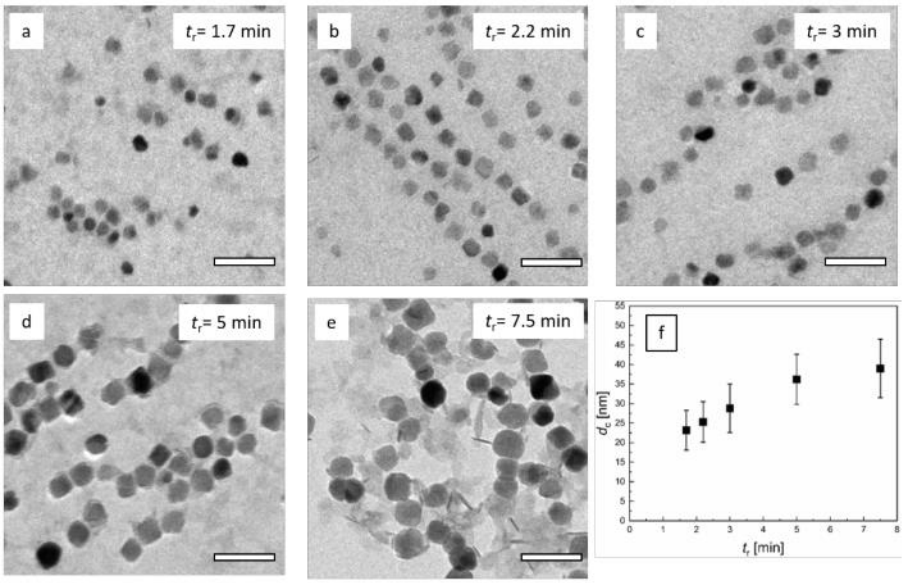

Figure 4. TEM analysis of micromixer nanoparticle synthesis at a reaction temperature of 52.5 °C. **a**–**e**: Variation of residence time t_r by adjusting the flow rate. Residence times from 1.7 min (Q = 18 mL/min) to 7.5 min (Q = 4 mL/min). With increasing t_r, particle size increased, and homogeneity slightly decreased for the largest particles. **f**: Resulting mean diameter (symbol) and standard deviation (uncertainty bar) determined by analysis of N > 5000 individual nanoparticles imaged by TEM as a function of t_r.

The impact of the residence time adjusted by the flow rate on the dynamic magnetic properties of the MNP, as characterized by the three MPS parameters A_3^*, A_5/A_3, and ϕ_3, is shown in Figure 5. While the specific amplitude exhibited a distinct maximum of $A_3^* \approx 28$ Am^2/kg(Fe) at a residence time t_r of about 3 min, the ratio A_5/A_3 showed a weak decrease with increasing t_r, only. The phase ϕ_3 showed the same, but more pronounced trend as A_5/A_3. Since at diameters d_c > 20 nm, the magnetic moments of the MNP were blocked at room temperature, we assumed that the dynamics of the MNP moments were determined by Brownian rotation (the whole particle was rotating to follow the MPS excitation field). Therefore, we found, at the excitation parameters used for MPS (f_0 = 25 kHz, B_e = 25 mT), a corresponding core size of about 25 nm (see Figure 4f), and hydrodynamic diameter of about 27 nm (Figure 3b).

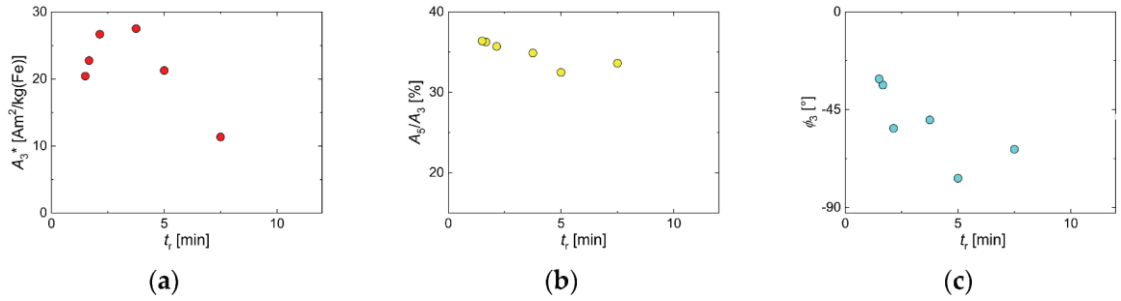

Figure 5. MPS parameters of MNP samples obtained by continuous micromixer synthesis at different residence times t_r = 1.7, 2.2, 3, 5, 7.5 min by adjusting the flow rate Q. (**a**) specific amplitude A_3*; (**b**) ratio A_5/A_3; (**c**) phase ϕ_3.

The ACS measurements (Appendix A Figure A1) confirmed that with increasing t_r, the resulting initial susceptibility χ_{ini} (e.g., core size) was increasing. Accordingly, the peak frequency $f(\chi'')$, which was related to the hydrodynamic diameter of the MNP, was shifting towards lower frequency with increasing t_r, e.g., the resulting particle became larger, slowing down the Brownian rotation. A slight aggregation tendency of larger MNP produced at lower flow rates resulting in residence times ≥ 5 min Q < 20 mL/min was observed in the ACS measurements indicated by distorted, broader spectra with a pronounced shift of $f(\chi'')$ towards lower frequencies (supplemental data shown in Appendix A). The tendency of agglomeration was observed also for larger single-core nanoparticles with core sizes of 27.8 nm, which are synthesized by thermal decomposition during the phase transfer [16].

3.3. Influence of Residence Time Adjusted by the Volume of the Growth Stage Tubing

An alternative way to adjust the residence time t_r was by selecting the reaction volume of the growth stage, e.g., by the length of the tubing of the growth section. In this case, t_r could be adjusted while keeping all other synthesis parameters constant, e.g., without any further secondary effects as inhomogeneities caused by insufficient mixing (e.g., at very low flow rates). To this end, we varied, at Q = 8 mL/min total flow rate and T_s = 52.5 °C, the length of the tubing to adjust t_r, while the inner diameter was kept constant to avoid flow profile changes by modifying the tubing diameter. By this, t_r in the range 1 min to 12 min (corresponding to a tubing volume of 5 mL to 90 mL) was adjusted, which was slightly larger than the range that was addressed by the flow rate, as presented in Section 3.2.

The DCS analysis for samples synthesized at different residence times t_r identified an optimal process window, wherein a safe control over particles' characteristics was feasible (Figure 6a). In the t_r range from 1.3 min to 7.5 min, DCS revealed narrow monomodal hydrodynamic size distributions with mean diameters of about 18 nm to 25 nm. Analogous to the experiments with a variation of the total flow rate, again, the average particle size in this process parameter range increased gradually with increasing t_r For longer residence times t_r = 8.8 min and 11.3 min, multimodal and broad size distributions became visible in the DCS analysis, as visualized by the uncertainty bars in Figure 6b. This clearly indicated agglomeration or aggregation behavior due to larger magnetic moments of larger cores. At a certain critical core size, the stabilizing agent could no longer protect the strong particle-particle interactions, and agglomeration occurred by forming superstructures. This was partly reversible, and the superstructures could be dissembled by stirring or vortexing; nevertheless, also stable aggregates were formed that could not be separated anymore.

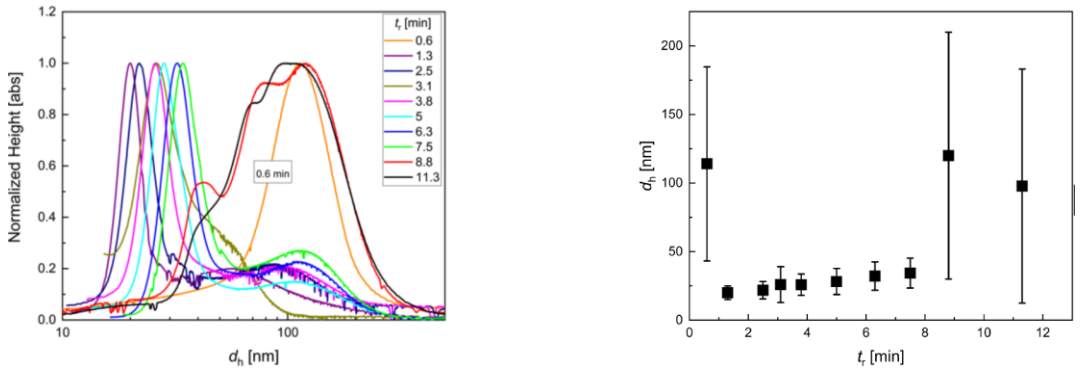

Figure 6. DCS analysis for iron oxide single-core nanoparticles manufactured by continuous micromixer synthesis at Q = 8 mL/min total flow rate and T_s = 52.5 °C for various residences times t_r = 0.6, 1.3, 2.5, 3.1, 3.8, 5, 6.3, 7.5, 8.8, 11.3 min: (**a**) hydrodynamic size distribution extracted from DCS measurements; (**b**) mean hydrodynamic diameter d_h (symbols) and FWHM values (plotted as uncertainty bars) as a function of t_r.

Interestingly, also, at very short residence times below 1 min (t_r = 0.6 min), MNPs with larger hydrodynamic sizes and broad size distribution were observed in DCS analysis. However, in this case, the agglomeration or aggregation did not seem to be caused by strong magnetic interaction between large magnetic cores but indicated the presence of insoluble intermediate states. The corresponding TEM analysis (Figure 7a)

showed aggregates of inhomogeneous particles of different size and morphology, which supported this hypothesis. It has been reported that the reaction mechanism of metal oxide synthesis in aqueous media generally involves hydrolysis of metal salts, followed by dehydration of the resulting hydroxides. A large number of different redox reactions are possible; thus, also hydroxide networks can be formed during hydrolysis [64]. If the residence time was below a critical value, the particle formation process was interrupted at a non-final stage; thus, particles were resulting, which were neither uniform nor electrostatically stabilized. Furthermore, these particles might contain fractions of non-magnetic iron hydroxides, which were able to crosslink and lead to agglomerates (See also Figure 8).

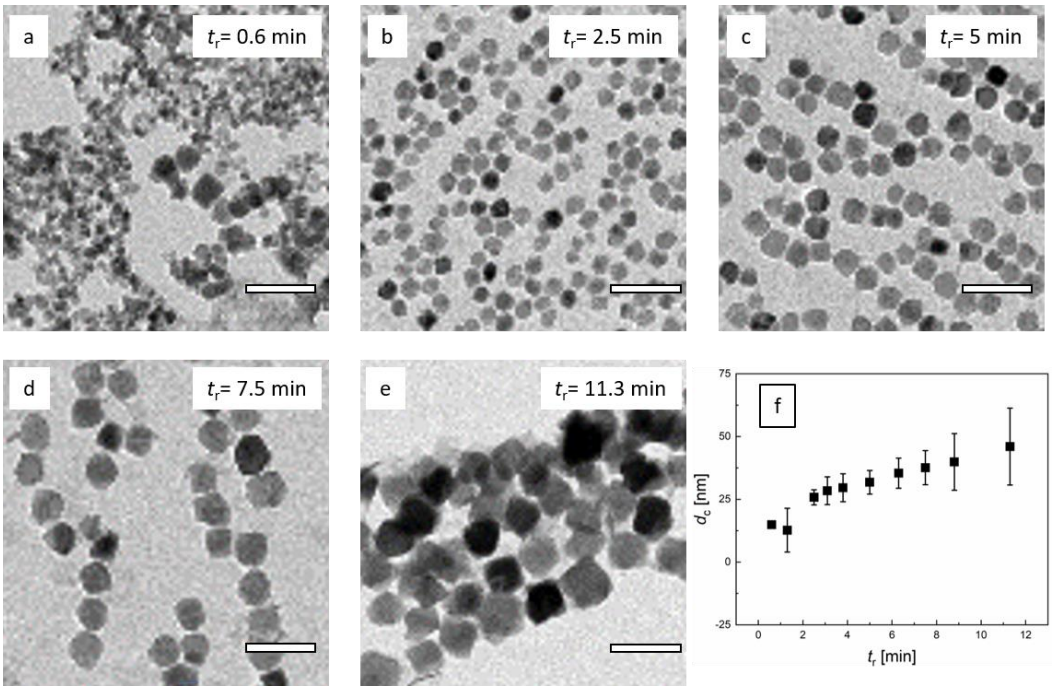

Figure 7. TEM analysis of micromixer nanoparticle synthesis at Q = 8 mL/min total flow rate and T_S = 52.5 °C. **a–e**: Variation of residence time t_r by adjusting the tubing length. Residence times from 0.6 min (V = 5 mL) to 11.3 min (L = 90 mL). With increasing residence time, particle core size increased. Off optimal process window, size control was limited, and the particle homogeneity decreased (**a and e**); **f**: Resulting mean diameter (symbol) and standard deviation (plotted as uncertainty bar) determined by the analysis of N > 5000 individual nanoparticles imaged by TEM as a function of residence time t_r. Note, the TEM image analysis of particles synthesized at the lowest residence time t_r = 0.6 min did not yield reliable core diameter values.

As depicted in Figure 7, the TEM data confirmed the observations of DCS analysis. Increasing t_r resulted in MNP with larger core sizes. Particles in the optimal process window were relatively homogenous in size and shape. Even the larger particles obtained at t_r = 11.3 min were still relatively homogenous in size, though shape

transition from spherical to more cubic morphology was visible. The core sizes between 13 +/− 3 and 46 +/−7 nm were obtained. The sample synthesized at t_r = 0.6 min showed inhomogeneous MNP, indicating non-stable intermediate states, as discussed above.

Considering the effect of the residence time variation adjusted by the tubing length on the dynamic magnetic properties of the MNP, we saw a similar behavior as found for t_r variation by flow rate adjustment in Section 3.2. The three MPS parameters—A_3^*, A_5/A_3, and ϕ_3—are shown in Figure 8, together with the results of Section 3.2 (Figure 5). Again, the specific amplitude exhibited a distinct maximum at a residence time t_r of about 3 min, but with a slightly increased value of A_3^* ≈ 30 Am²/kg(Fe). The corresponding A_5/A_3 parameter showed the same weak decrease with increasing t_r. At the A_3^* maximum, the same A_5/A_3 value of 35% was determined for t_r adjustment by tubing length as well as by flow rate. The phase ϕ_3 showed a linear (negative) increase with increasing t_r with a value of about -45 ° at the A_3^* maximum, where t_r = 3 min. Thus, also, here, we found the core size of about 25 nm (see Figure 7f) and hydrodynamic diameter of about 27 nm (Figure 6b) to be optimum. Comparing the two ways of t_r selection, the tubing length adjustment seemed to result in a more stable MNP synthesis than by controlling the flow rate, leading to slightly higher MPS values.

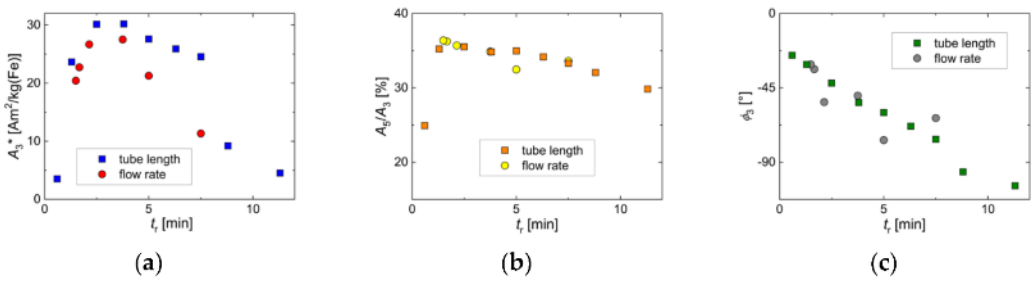

Figure 8 MPS parameters of MNP samples were obtained by continuous synthesis at different residence times t_r by adjusting the tubing length. For comparison, the corresponding MPS parameters obtained by the flow rate in Section 3.2 were added to the graphs. (**a**) specific amplitude A_3^*; (**b**) ratio A_5/A_3; (**c**) phase ϕ_3.

The crystallographic analysis by X-ray diffraction (see Figure A3 in the appendix A) according to the *JCPDS* card no. #75-0033 (Fe_3O_4) confirmed a pure magnetic phase for three representative samples with core sizes between 25 and 35 nm. All diffraction

patterns exhibited the characteristic XRD spectrum of Fe_3O_4 (or γ-Fe_2O_3) nanoparticles without any significant fraction of FeO (indicated by the lack of a (200) peak or α-Fe_2O_3 (no (104) and (110) peaks) phases [65]. The γ-Fe_2O_3 phase would exhibit a small peak shift to higher angles and the appearance of two weak characteristic superlattice diffractions from the (210) and (213) planes at lower angles (around 24.8 and 26.8°, respectively). Consistent with this, the samples in this size range obtained by micromixer synthesis exhibited a very high room temperature saturation magnetization in the range 111–117 $Am^2/kg(Fe)$, as recently published [66]. These values were close to the value for bulk magnetite or maghemite, indicating the high crystallinity of the magnetic phases with a low amount of disorder reached by our synthesis.

3.4. Influence of Reaction Temperature T_s

The reaction temperature T_s is the second important parameter to control the micromixer synthesis. During the aqueous synthesis of iron oxide nanoparticles, the reaction temperature determines the reaction velocity, particularly during particle growth, since the nucleation is a very fast process even at low temperatures. Therefore, the impact of different reaction temperatures T_s in the range from 30 °C to 65 °C on particle growth at a fixed residence time of t_R= 3.4 min was investigated. All T_s were far below the boiling point of water and well above the room temperature (to suppress interfering seasonal variation of T_s if a sufficient temperature-controlled lab environment could not be maintained). Temperature control in the micromixer set-up was provided by a thermostat bath (Huber), preheated educt solutions, and thin-walled tubing (Teflon material); thus, temperature stability better than 1.5 K was achieved over the whole T_s range.

We observed a general trend to yield larger particles at higher T_s, as also reported in the literature for iron oxide particle growth during a hydrothermal process [67]. Higher T_s enhanced the mobility of active educts and accelerated the particle growth; thus, at an identical residence time, particles grew larger, as long as enough educt material was provided. As displayed in Figure 9, DSC resolved a single fraction of

particles with hydrodynamic diameters (peak position) ranging from 12 nm for T_s = 30°C up to about 36 nm for T_s = 62.5 °C with narrow size distribution. Especially in the range from T_s = 40 °C to 57.5 °C, the hydrodynamic size smoothly increased, exhibiting a narrow and nearly constant size distribution. Particles synthesized at higher temperatures showed a tendency for the formation of suprastructures, e.g., chains of several particles, visible in the DCS data by peak broadening and a shoulder at higher diameters.

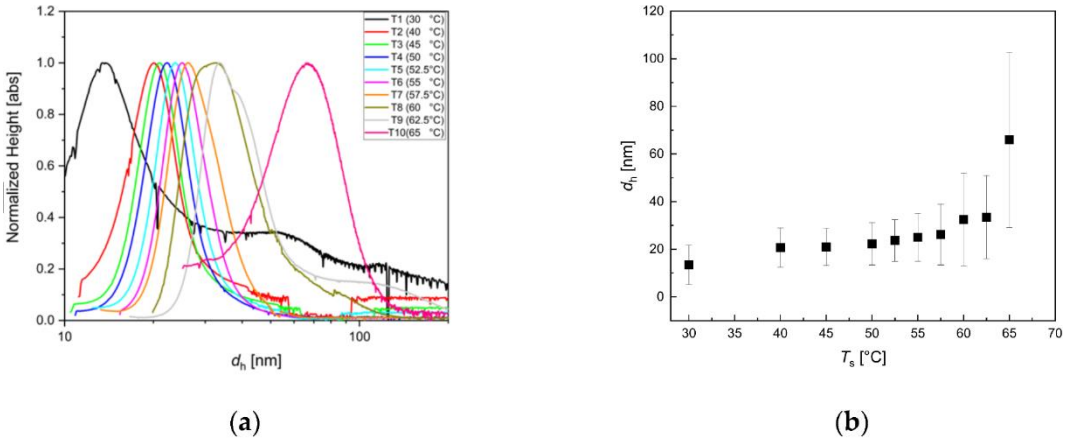

Figure 9. DCS analysis for iron oxide single-core nanoparticles manufactured by continuous micromixer synthesis at Q = 8 mL/min total flow rate and t_r = 3.4 min for different synthesis temperatures T_s = 30, 40, 45, 50, 52.5, 55, 57.5, 60, 62.5 and 65 °C. (**a**) Hydrodynamic size distribution extracted from DCS measurements; (**b**) mean hydrodynamic diameter d_h (symbols) and FWHM values (depicted as uncertainty bars) as a function of T_s.

For the highest reaction temperature, T_s = 65°C, MNP with hydrodynamic diameters even about 70 nm and a much broader distribution were detected. This indicated the growing tendency of aggregation due to the increasing magnetic particle-particle interaction of MNP of this size, which no longer could be prevented with the chosen shell stabilization (surfactant layer) [68]. For the lowest reaction temperature T_s = 30 °C, the formation of aggregates was clearly visible by a distinct second broad distribution with a maximum at about 50 nm. Here, a similar effect, as at very low residence times discussed above, could cause this aggregation behavior. If the reaction temperature was too low at a given residence time, the dynamic particle formation process might not be finalized within this time frame, resulting in intermediate growth states with an inhomogeneous structure, which were insufficiently stabilized during particle growth. Thus, the subsequent addition of a protective layer could not avoid agglomeration efficiently.

The TEM images confirmed the results obtained by DCS measurements. The core size of the monotonic increased with increasing T_s. The TEM analysis, shown in Figure 10f, revealed mean cores sizes from less than 20 nm to almost 40 nm for the T_s range. For particles synthesized at T_s = 30 °C, TEM clearly showed that at this temperature, the residence time of t_r = 3.4 min was too short for obtaining homogeneous well-separated single-core nanoparticles but resulted in a significant amount of agglomerated small size iron oxide structures with rather diffuse morphology (Figure 10a). Therefore, a large proportion of the sample could not be considered as isolated single nanoparticles. Besides, the geometry of MNP synthesized at T_s =30 °C was not very uniform, containing spherical as well as disk-like particle shapes. Furthermore, the particle concentration obtained after magnetic separation was very low, which indicated the presence of a significant amount of poor-quality magnetic particles.

The mean core diameter obtained by TEM image analysis of N > 5000 single MNP ranged from 21.2 nm for T_s = 40 °C up to 36.6 nm T_s = 65 °C, smoothly increasing with increasing T_s, as shown in Figure 10f. The standard deviation (displayed as uncertainty bars in Figure 10f) remained quite constant at about 5.5 nm in the central range of T_s = 40 °C to 62.5 °C. Only for syntheses at the lowest and the highest reaction temperature, the standard deviations in the core size analysis increased to 7.3 nm for T_s = 30 °C and 7.9 nm for T_s= 65 °C, respectively. The corresponding relative standard deviations (σ = mean/standard deviation) of about 0.25 were determined. The number of particles per unit TEM grid area clearly increased with increasing T_s, as can be seen in Figure 10. Regarding the core sizes accessible by the micromixer synthesis of up to about 40 nm, we assumed a single domain magnetic structure of the single-core iron oxide MNP. Theoretically, a critical core size for forming a multi-domain structure larger than 75 nm for cubic and even larger than 120 nm for spherical particle shape has been estimated [69]. Whereas experimentally, a much lower border between single and multidomain structure at critical sizes in the range 30 nm to 50 nm has been reported for cubic MNP. Therefore, a fraction of particles with a multi-domain structure cannot be excluded, which would require further analysis methods to clarify.

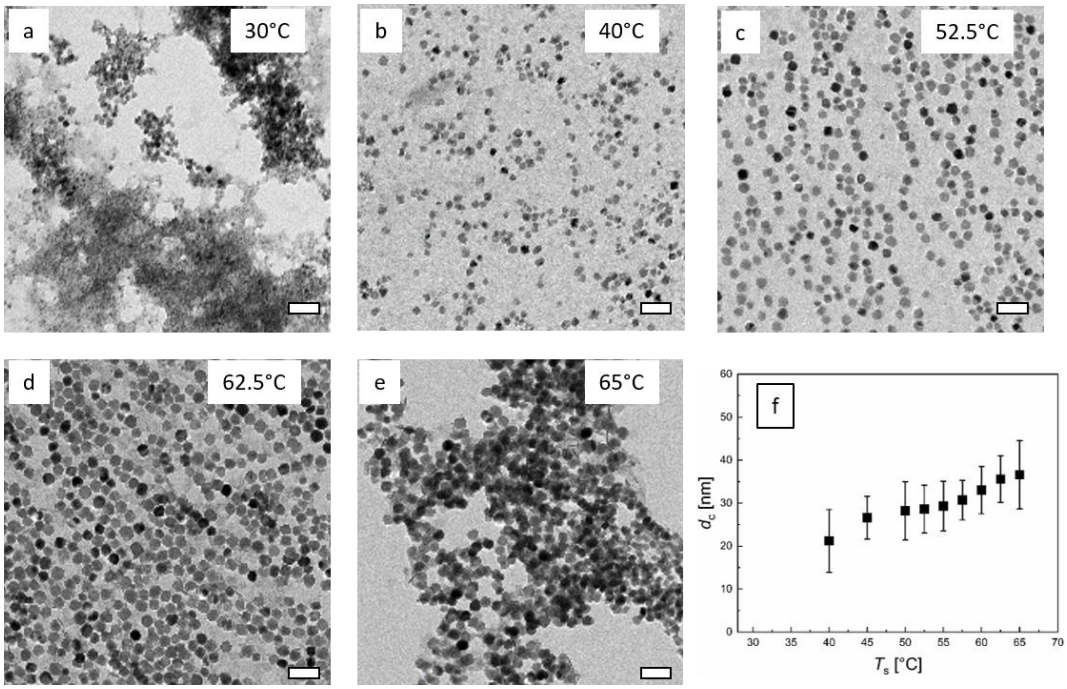

Figure 10. TEM images of continuous micromixer-synthesized nanoparticles at Q = 8 mL/min total flow rate and t_r = 3.4 min. **a–e**: Variation of synthesis temperature T_s. Images of MNP obtained by continuous synthesis at defined reaction temperatures in the range of 30 °C to 65 °C. The scale bar is 100 nm. **f**: Resulting mean diameter (symbols) and standard deviation (uncertainty bars) determined by the analysis of N > 5000 individual nanoparticles imaged by TEM as a function of T_s.

From DCS and TEM measurements, we identified an optimal process operation window between T_s = 40 °C and 60 °C, in which tunable MNP with core sizes between 20 nm and 35 nm could be produced that were stable in an aqueous suspension medium. Particles of this size range are particularly interesting for versatile biomedical applications like magnetic fluid hyperthermia, magnetic separation, or drug targeting, where huge magnetic moments are advantageous [70]. In a recently published paper, we investigated single-core magnetic nanoparticles of this size range for their capacity in biomedical applications as MRI contrast agents, as tracer materials for magnetic particle imaging, or as heating agents for hyperthermia applications [66]. For instance, for single-core nanoparticles with an average core diameter of 30 nm, relaxivities of r_1 = 8.8(1) L mol^{-1} s^{-1} and r_2 = 289(8) L mol^{-1} s^{-1} were determined. This clearly exceeded the r_2 value of Resovist® (r_2 = 95 L mol^{-1} s^{-1}, reported in the literature at the same field B_0 = 1.5 T) [71], indicating a good performance as a negative contrast agent. Usually, single-core iron oxide nanoparticles in this size range are not easily accessible by other

synthesis methods, especially nanoparticles that are stably dispersed in an aqueous environment. For instance, Hufschmid et al. presented a method based on thermal decomposition envisaging this specific core size range. Producing a set of particles in this size range required numerous synthesis runs, each with different educt solutions and reaction times for more than 10 h, followed by time-consuming phase transfer to aqueous media [72].

To assess the magnetic behavior that can be adjusted by T_s variation, we carried out MPS and ACS measurements. The dynamic magnetic response at B_e = 25 mT, parametrized by the three characteristic MPS quantities—the specific amplitude A_3*, the ratio A_5/A_3, and the phase ϕ_3 as a function of T_s—is summarized in Figure 11. The nanoparticles synthesized at T_s = 30 °C exhibited a rater low A_3* value of about 5 Am²/kg(Fe), indicating a low magnetic moment of the MNP responding to the dynamic excitation at f_0 = 25 kHz. For T_s = 40 °C and higher, A_3* significantly increased far above 20 Am²/kg(Fe) due to the increasing size and more uniform morphology compared to particles synthesized at T_s= 30 °C. The magnetic response reached a maximum at about T_s = 50 °C, and for higher temperatures, A_3* gradually decreased again. Though the particle moments still increased in size, they became too slow to follow the excitation frequency. At the highest temperature of T_s = 65 °C, A_3* had dropped down to a value slightly above 5 Am²/kg(Fe). The (concentration-independent) harmonic amplitude A_5/A_3 showed the same behavior as a function of T_s with a maximum value of about 38% at T_s = 42 °C, but with less pronounced reduction at the lowest and highest temperatures. The phase angle ϕ_3 showed a linear (negative) increase with increasing T_s passing −45° at the maximum values of A_3 and A_5/A_3, indicating that for angles larger than −45°, the moments could not follow the excitation fast enough and were thereby reducing A_3* and A_5/A_3.

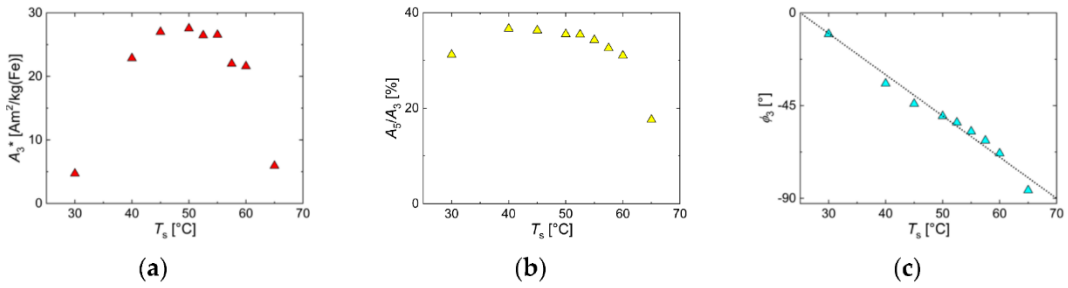

Figure 11. MPS parameters of MNP samples obtained by continuous synthesis at different synthesis temperatures T_s. (**a**) Specific amplitude A_3*; (**b**) ratio A_5/A_3; (**c**) phase ϕ_3. The dotted line in (**c**) displays the phenomenological linear relation ($\phi_3 = 50° - 2 \cdot T_s$) between phase and T_s.

MPS and ACS results could be combined by relating them to the corresponding residence times t_r or synthesis temperatures T_s, respectively. Hence, the MPS parameters—A_3^*, A_5/A_3, and ϕ_3 as a function of the initial susceptibility χ_{ini} obtained by ACS (Appendix A Figure A2)—are displayed in Figure 12 for the different micromixer synthesis parameters. The initial susceptibility χ_{ini}, reflecting the moment of the MNP achieved at a synthesis parameter t_r or T_s, served as the x-axis for the three MPS parameters—A_3^*, A_5/A_3, and ϕ_3. It showed that synthesis temperature T_s and residence time t_r impacted the magnetic properties in a slightly different manner. Though the curves for both parameters showed a very similar shape, the maximum in A_3* was reached at lower χ_{ini} values. The same was observed for the A_5/A_3 parameter.

The results indicated the significant influence of T_s on the reaction, the obtained single-core nanoparticle structures, and finally, the resulting magnetic characteristics determined by size, size distribution, stability, and magnetic properties. Increasing the reaction temperature of the micromixer synthesis already in a very narrow interval of 2.5 K significantly affected the MNP characteristics and confirmed the rapid and efficient heat transfer of the continuous micromixer synthesis. Compared with this, the residence time t_r seemed to have a finer setting of magnetic parameters with slightly higher A_3* values than obtained by T_s adjustment. Furthermore, MPS and ACS were two highly sensitive magnetic techniques capable of resolving the changes in magnetic parameters addressed by T_s variation.

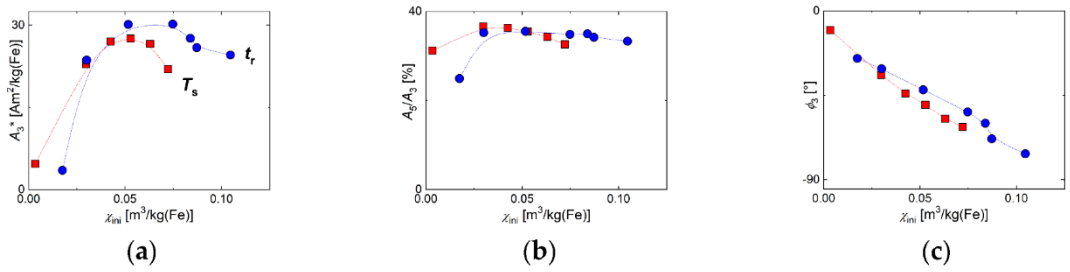

Figure 12. MPS parameters of MNP samples obtained by continuous synthesis at different reaction temperatures T_s (red squares) and residence time t_r adjusted by tubing length (blue circles) plotted against the corresponding initial susceptibility χ_{ini} determined by alternative current susceptibility (ACS). (**a**) Specific amplitude A_3*; (**b**) ratio A_5/A_3; (**c**) phase ϕ_3. Note the lines are guide to the eyes.

3.5. Online-MPS as a Valuable Tool for Efficient Magnetic Process Analysis During the Continuous, Tunable Synthesis of High-Quality Single-Core MNP by Micromixer Synthesis

Though MPS is a powerful technique to evaluate the dynamic magnetic behavior of the micromixer synthesis products, it generally requires taking individual samples after each synthesis. Nevertheless, the short measurement time of a few milliseconds combined with the extremely high sensitivity to detect magnetic moments below 10^{-11} Am^2 makes the MPS technique ideally suited to detect the magnetic properties during the entire micromixer synthesis process. For this purpose, a compact MPS device was developed capable of easy looping into the dwell-zone tubing system used to adjust the residence time during micromixer synthesis. The setup and operation of this novel device are described in detail in the following article of this volume [61]. For the first demonstration of the capability of this device for magnetic process control, we performed a micromixer synthesis run, where Ts was stepwise increased by 5 K (except for an intermediate 2.5 K temperature step at 52.5 °C) every 10 min starting at T_s = 30 °C while keeping all other synthesis parameters constant. During the complete synthesis run, the online-MPS device was looped into the growth stage tubing used for residence time adjustment, and MPS measurements were continuously acquired with a temporal resolution of Δt = 1 s at an excitation field strength of B_e = 12 mT.

Figure 13 displays the MPS parameter A_5/A_3 (red line) during the synthesis run, sensitively reflecting changes in the magnetic properties directly after each increase of T_s (red line). Starting the synthesis at t = 0, it took about 4 min (at 30 °C) until the first reliable MPS spectra with A_5/A_3 values above noise floor appeared, which, then after a

small overshoot within the following 4 min approach, reached a stable value of about 20%. With the next T_s set-point at 35 °C, a significant increase in A_5/A_3—maximum value of about 25%—was observed, while for all higher T_s values, A_5/A_3 dropped again. Roughly, this behavior was in accordance with the MPS results of the previous Section 3.3. Note, the maximum value detected inside the dwell-zone tubing by online-MPS was significantly lower than the maximum found by MPS of extracted individual samples of about 35%. The reason is that for the online MPS measurements, we chose a much lower excitation field amplitude (B_e = 12 mT) than for all other MPS measurements (B_e = 25 mT), which mainly explains the difference in the absolute values of A_5/A_3. By this excitation field reduction, we intended to avoid any additional heat transfer from the excitation coil of the online-MPS device. Additional experiments are envisaged to further characterize any heat transfer effects of the coil at higher temperatures on micromixer synthesis in the growth stage tubing.

The general benefit of probing the magnetic properties inline during synthesis has been demonstrated in [73], where an NMR detection scheme was developed and tested for online characterization of iron oxide nanoparticles synthesized in a flow-based microreactor. To this end, an automated NMR relaxometer device was presented to determine the transversal and longitudinal relaxation times of magnetic iron oxide nanoparticles obtained by online flow-based microreactor synthesis. Though this system showed very high sensitivity, it requires a rather long time (minutes) to determine the relaxation times compared to the MPS measurement time of the system presented here. Furthermore, the magnetic field of 0.5 T required to detect the proton resonance was much higher than the excitation field of some tens of millitesla and might lead to aggregation or chain formation of the MNP during the NMR-measurements. However, both techniques are efficient tools capable of speeding up synthesis optimization and product characterization of MNP to be developed for biomedical, theranostic, and biosensing applications.

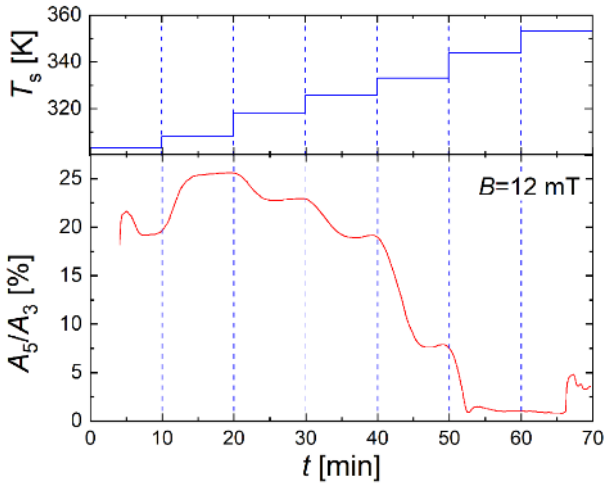

Figure 13. Monitoring of micromixer synthesis by online-MPS. The concentration-independent MPS parameter A_5/A_3 directly reflected changes in the magnetic properties during MNP synthesis, here provoked by step-wisely increasing T_s. Every 10 min, T_s (top panel, blue line) was increased by 5 K (with one additional intermediate T_s setpoint at 52.5 °C) starting at T_s = 30 °C. The synthesis started at t = 0 and was monitored by continuous MPS acquisition (Δt = 1 s, B_e = 12 mT) to obtain the parameter A_5/A_3 values (bottom panel, red line). The synthesis was performed at Q = 8 mL/min total flow rate and t_r = 3.4 min.

4. Summary and Conclusions

In this work, the continuous micromixer synthesis of single-core iron oxide magnetic nanoparticles was presented and compared with batch synthesis. Continuous micromixer synthesis has many advantages over conventional batch synthesis regarding reproducibility, simplicity, time exposure, quality of the product, and upscaling capability of the procedure. The influence of the two (most) important synthesis parameters—the reaction temperature and the residence time (either adjusted by the total flow rate or the tubing volume)—of the reaction was studied. The impact of T_s and t_r on size, size distribution, and the stability of the MNP was directly reflected in the magnetic properties measured by magnetic particles spectroscopy and AC-susceptibility measurements. In this way, the tunability of our approach was clearly demonstrated since, by variation of input parameters, the resulting product properties are changed in a unique and highly reproducible way.

The operation of the newly developed benchtop MPS device connected to the growth stage of the micromixer platform directly probing the magnetic properties during the synthesis pointed out the great potential of this highly sensitive and fast magnetic technique. Once established as an integrated inline analytic process tool, it could

substantially accelerate particle development while monitoring the magnetic quality of the nanoparticles.

The advantage of the micromixer technology is that the influence of different process parameters can be investigated comprehensively to gain a better process understanding. With this, the superiority of microfluidics can be fully exploited, i.e., its excellent mass and heat transfer and its rapid and controlled synthesis conditions. We understand that our micromixer approach in this way is unique, that is, it is tunable: by variation of input parameters, the resulting product properties are manipulated in a highly reproducible way. Moreover, the micromixer technology is capable of operating under nearly identical process conditions at large scales (at least in the decaliter range), as well.

The presented continuous micromixer technology to produce high-quality single-core iron oxide magnetic nanoparticles might become a valuable tool to promote the standardized manufacturing of magnetic nanoparticle systems for nanomedicine applications, thereby fostering the translation of laboratory nanoparticle systems into clinical products, including safety, regulatory, and ethical requirements.

Author Contributions: A.B. performed the synthesis and physicochemical characterization of the samples; A.R. carried out magnetic characterization; N.L., A.B. performed online-MPS measurements; A.B., R.B., F.W. wrote the manuscript; R.B., F.W. reviewed and edited the manuscript. Work was supervised by R.B. (synthesis, characterization) and F.W. (magnetic measurements); project administration, R.B. and F.W.; funding acquisition, R.B. and F.W. All authors have read and agreed to the published version of the manuscript.

Funding: This research was funded by the Deutsche Forschungsgemeinschaft (DFG) within the research grants "Core Facility: Metrology of Ultra-Low Magnetic Fields", grant numbers KO5321/3 and TR408/11" and the collaborative research center "Matrix in Vision" (SFB 1340/1 2018, no 372486779, projects A02). R.B. thanks the Fraunhofer-Gesellschaft for the support within the Fraunhofer TALENTA program. Abdulkader Baki thanks the *Friedrich Ebert Stiftung* for a Ph.D. fellowship supporting his work related to this project.

Acknowledgments: Many thanks to Michael Steiert from the Department of Physical Chemistry of Polymers at the Max Planck Institute for Polymer Research for supporting XRD measurements. Special thanks to Helen Onyema for the proofreading of the manuscript.

Conflicts of Interest: The authors declare no conflict of interest.

Appendix A

The magnetic AC susceptibility (ACS) was a complex signal measured in the form $\chi = \chi' + i\chi''$, where the real part χ' denoted the susceptibility component of the nanoparticle moments that was in-phase with the applied AC magnetic field, and the imaginary part χ'' was the corresponding out-of-phase component. The relative ratio of the two components revealed the phase lag between particle moment and applied AC field, and this led for $\chi' = \chi''$ to a 45° phase angle. The maximum of χ'' was reached for blocked nanoparticles (no Néel relaxation, e.g., iron oxide cores with diameters larger 20 nm at room temperature) when the Brownian relaxation time was equal to the rotational cycle time of the applied field. This was revealed as a peak in the χ'' susceptibility component as a function of frequency. For larger hydrodynamic sizes, e.g., for longer Brownian relaxation times, this peak shifted to lower frequencies. Thus, ACS measurements as a function of frequency enabled the assessment of hydrodynamic sizes of magnetic nanoparticles.

Figure A1 shows the ACS signals normalized to the iron amount of single-core iron oxide nanoparticles synthesized by continuous micromixer synthesized at different residence times t_r (adjusted by tube length) as a function of frequency. At low frequencies, χ' was constant, e.g., the moments could follow the AC field, from which the initial susceptibility χ_{ini} could be determined, extrapolating χ' for $f \rightarrow 0$. At higher frequencies, χ' was gradually decreasing, and the larger moments no longer could follow the excitation, leading to a phase lag, and thus the imaginary part χ'' was increasing, showing a pronounced peak at the inflection point of χ'. With increasing residence time t_r, e.g., increasing core particle size, the initial susceptibility χ_{ini} increased. At the same time, the peak in χ'' was shifted towards lower frequencies because with increasing core size, the hydrodynamic diameter increased, as well.

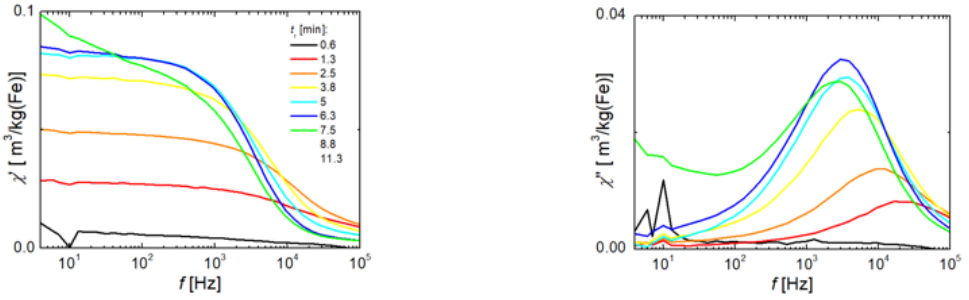

(**a**) (**b**)

Figure A1. AC susceptibility versus frequency of continuous micromixer samples synthesized at different residence times adjusted by tubing length. (**a**) real part c', (**b**) imaginary part c''.

Similar behavior was observed for the ACS signals normalized to the iron amount of single-core iron oxide nanoparticles synthesized by continuous micromixer at different reaction temperatures T_s. As displayed in Figure A2, here again, an increase of χ_{ini} with increasing T_s was observed. But for $T_s \geq 60$ °C, χ_{ini} dropped again. The sample synthesized at $T_s = 65$ °C showed an aggregation tendency since it exhibited a non-zero χ'' component and no constant plateau in the χ' component for lower frequencies.

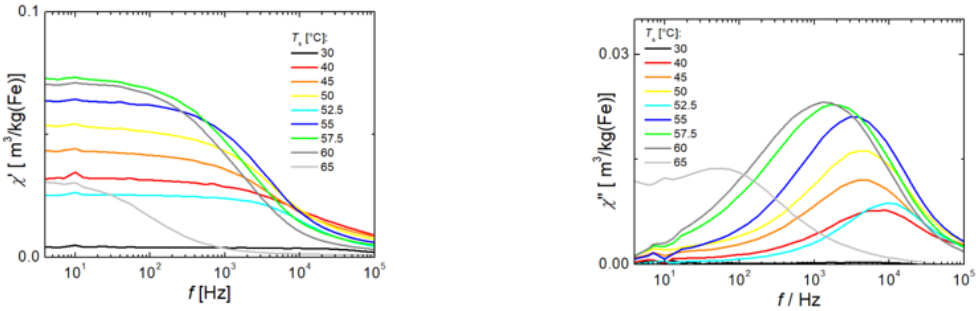

(**a**) (**b**)

Figure A2. AC susceptibility versus frequency of continuous micromixer samples synthesized at different reaction temperatures T_s. (**a**) real part c', (**b**) imaginary part c''.

The initial susceptibility χ_{ini} was proportional to the (mean) size of the magnetic nanoparticle moments and could be related to the characteristic three MPS parameters—A_3^*, A_5/A_3, and ϕ_3—via the corresponding residence time t_r or synthesis temperature T_s, as shown in Figure 12. This allowed the magnetic assessment of the impact of T_s and t_r variation on the magnetic behavior of the resulting nanoparticles.

To assess the crystal structure and iron oxide phase of samples manufactured at three different core diameter sizes in the range 25 nm to 35 nm by variation of the residence time, XRD 2θ wide-angle scans were carried out, as shown in Figure A3. The corresponding indices of a magnetite crystal structure (which are nearly the same as for γ-Fe_2O_3) at the main peak positions were taken from the JCPDS card no. #75-0033 (Fe_3O_4) and # 39-1346 (γ-Fe_2O_3).

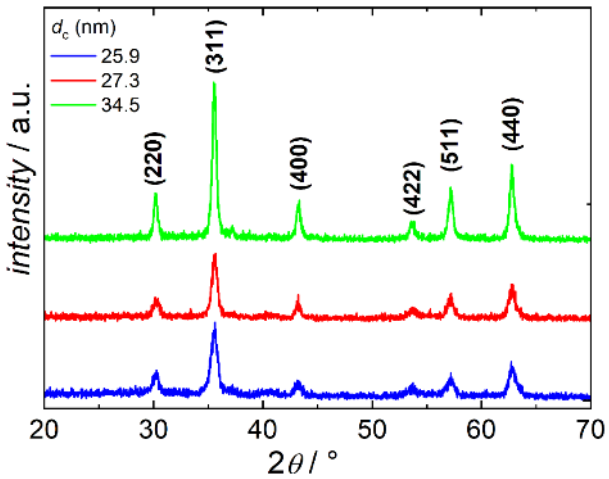

Figure A3. XRD spectra of three micromixer samples with average core diameters d_c of about 25 nm (blue), 27 nm (red), and 35 nm (green) obtained by micromixer synthesis at different residence times t_r at a synthesis temperature of T_s = 52 °C.

References

1. Weissleader, R.; Elizondo, G.; Wittenberg, J.; Rabito, C.A.; Bangele, H.H.; Josephon, L. Ultrasmall superparamagnetic iron oxide: Characterization of a new class of contrast agents for MR imaging. *Radiology* **1990**, 489–493, doi:10.1148/radiology.175.2.2326474.s.
2. Jariwala, D.; Sangwan, V.K.; Lauhon, L.J.; Marks, T.J.; Hersam, M.C. Carbon nanomaterials for electronics, optoelectronics, photovoltaics, and sensing. *Chem. Soc. Rev.* **2013**, *42*, 2824–2860, doi:10.1039/c2cs35335k.
3. Astruc, D. *Nanoparticles and catalysis*, Volume 1; Wiley-VCH: Weinheim, Germany, 2008.
4. Cornell, R.M.; Schwertmann, U. The Iron Oxides: Structure, Properties, Reactions, Occurences and Uses, Second Edition; Wiley-VCH: Weinheim, Germany, 2003.
5. Gupta, A.G.; Gupta, M. Synthesis and surface engineering of iron oxide nanoparticles for biomedical applications. *Biomaterials* **2005**, 3995–4021, doi:10.1016/j.biomaterials.2004.10.012.
6. Moghimi, S.M.; Hunter, A.C.; Murray, J.C. Long-circulating and target-specific nanoparticles: Theory to practice. *Pharmacol. Rev.* **2001**, 283–318.
7. Curtis, A.S.G.; Wilkonson, C. Nanotechniques and approaches in biotechnology. *Trends Biotechnol.* **2001**, 97–101, doi:10.1016/s0167-7799(00)01536-5.
8. Wilkinson, J.M. Nanotechnology applications in medicine. *Med. Device Technol.* **2003**, 29–31.
9. Mody, V.V.; Cox, A.; Shah, S.; Singh, A.; Bevins, W.; Parihar, H. Magnetic nanoparticle drug delivery systems for targeting tumor. *Appl. Nanosci.* **2014**, *4*, 385–392, doi:10.1007/s13204-013-0216-y.
10. Dutz, S.; Hergt, R. Magnetic nanoparticle heating and heat transfer on a microscale: Basic principles, realities and physical limitations of hyperthermia for tumour therapy. *Int. J. Hyperthermia* **2013**, *29*, 790–800, doi:10.3109/02656736.2013.822993.

11. Dennis, C.L.; Ivkov, R. Physics of heat generation using magnetic nanoparticles for hyperthermia. *Int. J. Hyperthermia* **2013**, *29*, 715–729, doi:10.3109/02656736.2013.836758.
12. Jin, R.; Lin, B.; Li, D.; Ai, H. Superparamagnetic iron oxide nanoparticles for MR imaging and therapy: Design considerations and clinical applications. *Curr. Opin. Pharmacol.* **2014**, *18*, 18–27, doi:10.1016/j.coph.2014.08.002.
13. Stark, D.D.; Weissleder, R.; Elizondo, C.; Hahn, P.F.; Saini, S.; Todd, L.E.; Wittenberg, J.; Ferrucci, J.T. Superparamagnetic iron oxide: Clinical application as a contrast agent for MR imaging of the liver. *Radiology. 168(2),* **1988**, 297–301, doi:10.1148/radiology.168.2.3393649.
14. Gleich, B.; Weizenecker, J. Tomographic imaging using the nonlinear response of magnetic particles. *Nature* **2005**, 1214–1217, doi:10.1038/nature03808.
15. Ali, A.; Zafar, H.; Zia, M.; Ul Haq, I.; Phull, A.R.; Ali, J.S.; Hussain, A. Synthesis, characterization, applications, and challenges of iron oxide nanoparticles. *Nanotechnol. Sci. Appl.* **2016**, *9*, 49–67, doi:10.2147/NSA.S99986.
16. Teeman, E.; Shasha, C.; Evans, J.E.; Krishnan, K.M. Intracellular dynamics of superparamagnetic iron oxide nanoparticles for magnetic particle imaging. *Nanoscale* **2019**, *11*, 7771–7780, doi:10.1039/c9nr01395d.
17. Ludwig, F.; Guillaume, A.; Schilling, M.; Frickel, N.; Schmidt, A.M. Determination of core and hydrodynamic size distributions of $CoFe_2O_4$ nanoparticle suspensions using ac susceptibility measurements. *J. Appl. Phys.* **2010**, *108*, 33918, doi:10.1063/1.3463350.
18. Patsula, V.; Moskvin, M.; Dutz, S.; Horák, D. Size-dependent magnetic properties of iron oxide nanoparticles. *J. Phys. Chem. Solids* **2016**, 24–30, doi:10.1016/j.jpcs.2015.09.008.
19. Wei, H.; Bruns, O.T.; Kaul, M.G.; Hansen, E.C.; Barch, M.; Wiśniowska, A.; Chen, O.; Chen, Y.; Li, N.; Okada, S.; et al. Exceedingly small iron oxide nanoparticles as positive MRI contrast agents. *PNAS* **2017**, 2325–2330, doi:10.1073/pnas.1620145114.

20. Yu, W.W.; Falkner, J.C.; Yavuz, C.T.; Colvin, V.L. Synthesis of monodisperse iron oxide nanocrystals by thermal decomposition of iron carboxylate salts. *Chem. Commun. (Camb.)* **2004**, 2306–2307, doi:10.1039/b409601k.
21. Gash, A.E.; Tillostonm, T.M.; Stacher, J.H.; Poco, J.F.; Hrubesh, L.W.; Simpson, R.L. Use of Epoxides in the Sol−Gel Synthesis of Porous Iron(III) Oxide Monoliths from Fe(III) Salts. *Chem. Mater.* **2001**, 999–1007, doi:10.1021/cm0007611.
22. Fernandes, M.T.C.; Garcia, R.B.R.; Leite, C.A.P.; Kawachi, E.Y. The competing effect of ammonia in the synthesis of iron oxide/silica nanoparticles in microemulsion/sol–gel system. *Colloids Surf. A Physicochem. Eng. Asp.* **2013**, *422*, 136–142, doi:10.1016/j.colsurfa.2013.01.025.
23. Kandpal, N.D.; Sah, N.; Loshali, R.; Prasad, J. Co-Precipitation method of synthesis and characterization of iron oxide nanoparticles. *J. Sci. Ind. Res.* **2014**, 87–90.
24. Okoli, C.; Sanchez-Dominguez, M.; Boutonnet, M.; Jaras, S.; Civera, C.; Solans, C.; Kuttuva, G.R. Comparison and Functionalization Study of Microemulsion-Prepared Magnetic Iron Oxide Nanoparticles. *Langmuir* **2012**, 8479–8485, doi:10.1021/la300599q.
25. Lv, Y.; Wang, H.; Wang, X.; Bai, J. Synthesis, characterization and growing mechanism of monodisperse Fe3O4 microspheres. *J. Cryst. Growth* **2009**, *311*, 3445–3450, doi:10.1016/j.jcrysgro.2009.03.046.
26. Hoa, Y.; Teja, A.S. Continuous hydrothermal crystallization of α–Fe_2O_3 and Co_3O_4 nanoparticles **2003**, 415–422, doi:10.1557/JMR.2003.0053.
27. Chen, D.; Xu, R. Hydrothermal synthesis and characterization of nanocrystalline Fe3O4 powders. *Mater. Res. Bull.* **1998**, 1015–1021, doi:10.1016/S0025-5408(98)00073-7.
28. Xu, C.; Teja, A.S. Continuous hydrothermal synthesis of iron oxide and PVA-protected iron oxide nanoparticles. *J. Supercrit. Fluids* **2008**, *44*, 85–91, doi:10.1016/j.supflu.2007.09.033.
29. Khalafalla, S.; Reimers, G. Preparation of dilution-stable aqueous magnetic fluids. *IEEE Transactions on Magnetics*, **1980**, 178–183, doi:10.1109/TMAG.1980.1060578.

30. Massart, R. Preparation of aqueous ferrofluids without using surfactant—Behavior as a function of the pH and the counterions. *C. R. Seances Acad. Sci. Ser. C* **1980**, 1–3.
31. Faivre, D.; Schuler, D. Magnetotactic Bacteria and Magnetosomes. *Chem. Rev.* **2008**, 4875–4898, doi:10.1021/cr078258w.
32. Hyeon, T.; Lee, S.S.; Park, J.; Chung, Y.; Bin Na, H. Synthesis of highly crystalline and monodisperse maghemite nanocrystallites without a size-selection process. *J. Am. Chem. Soc* **2001**, 12798–12801, doi:10.1021/ja016812s.
33. Park, J.; Lee, E.; Hwang, N.M.; Kang, M.S.; Kim, S.C.; Hwang, Y.; Park, J.G.; Noh, H.J.; Kini, J.Y.; Park, J.H.; et al. One-nanometer-scale size-controlled synthesis of monodisperse magnetic iron oxide nanoparticles. *Angew. Chem. Int. Ed.* **2005**, 2872–2877, doi:10.1002/anie.200461665|.
34. Pablico-Lansigan, M.H.; Situ, S.F.; Samia, A.C.S. Magnetic particle imaging: Advancements and perspectives for real-time in vivo monitoring and image-guided therapy. *Nanoscale* **2013**, *5*, 4040–4055, doi:10.1039/c3nr00544e.
35. Khandhar, A.P.; Ferguson, R.M.; Simon, J.A.; Krishnan, K.M. Tailored magnetic nanoparticles for optimizing magnetic fluid hyperthermia. *J. Biomed. Mater. Res. A* **2012**, *100*, 728–737, doi:10.1002/jbm.a.34011.
36. Ferguson, R.M.; Khandhar, A.P.; Kemp, S.J.; Arami, H.; Saritas, E.U.; Croft, L.R.; Konkle, J.; Goodwill, P.W.; Halkola, A.; Rahmer, J.; et al. Magnetic Particle Imaging with Tailored Iron Oxide Nanoparticel Tracers. *IEEE T. Magn.* **2015**, 1077–1084, doi:10.1109/TMI.2014.2375065.
37. Vangijzegem, T.; Stanicki, D.; Panepinto, A.; Socoliuc, V.; Vekas, L.; Muller, R.N.; Laurent, S. Influence of Experimental Parameters of a Continuous Flow Process on the Properties of Very Small Iron Oxide Nanoparticles (VSION) Designed for T1-Weighted Magnetic Resonance Imaging (MRI). *Nanomaterials (Basel)* **2020**, *10*, doi:10.3390/nano10040757.

38. Ma, J.; Lee, S.M.-Y.; Yi, C.; Li, C.-W. Controllable synthesis of functional nanoparticles by microfluidic platforms for biomedical applications - a review. *Lab Chip* **2017**, *17*, 209–226, doi:10.1039/c6lc01049k.
39. Gutierrez, L.; Gomez, L.; Irusta, S.; Arruebo, M.; Santamaria, J. Comparative study of the synthesis of silica nanoparticles in micromixer–microreactor and batch reactor systems. *Chem. Eng.* **2011**, *171*, 674–683, doi:10.1016/j.cej.2011.05.019.
40. Girod, M.; Vogel, S.; Szczerba, W.; Thünemann, A.F. How temperature determines formation of maghemite nanoparticles. *J. Magn. Magn. Mater.* **2015**, *380*, 163–167, doi:10.1016/j.jmmm.2014.09.057.
41. Panariello, L.; Wu, G.; Besenhard, M.O.; Loizou, K.; Storozhuk, L.; Thanh, N.T.K.; Gavriilidis, A. A Modular Millifluidic Platform for the Synthesis of Iron Oxide Nanoparticles with Control over Dissolved Gas and Flow Configuration. *Materials (Basel)* **2020**, *13*, doi:10.3390/ma13041019.
42. Suryawanshi, P.L.; Sonawane, S.H.; Bhanvase, B.A.; Ashokkumar, M.; Pimplapure, M.S.; Gogate, P.R. Synthesis of iron oxide nanoparticles in a continuous flow spiral microreactor and Corning® advanced flow™ reactor. *Green Process. Synth.* **2018**, *7*, 1–11, doi:10.1515/gps-2016-0138.
43. Simmons, M.; Wiles, C.; Rocher, V.; Francesconi, M.G.; Watts, P. The Preparation of Magnetic Iron Oxide Nanoparticles in Microreactors. *J. Flow Chem.* **2013**, *3*, 7–10, doi:10.1556/JFC-D-12-00024.
44. Abou Hassan, A.; Sandre, O.; Cabuil, V.; Tabeling, P. Synthesis of iron oxide nanoparticles in a microfluidic device: Preliminary results in a coaxial flow millichannel. *Chem. Commun. (Camb.)* **2008**, 1783–1785, doi:10.1039/b719550h.
45. Norfolk, L.; Rawlings, A.E.; Bramble, J.P.; Ward, K.; Francis, N.; Waller, R.; Bailey, A.; Staniland, S.S. Macrofluidic Coaxial Flow Platforms to Produce Tunable Magnetite Nanoparticles: A Study of the Effect of Reaction Conditions and Biomineralisation Protein Mms6. *Nanomaterials (Basel)* **2019**, *9*, doi:10.3390/nano9121729.

46. Niu, G.; Ruditskiy, A.; Vara, M.; Xia, Y. Toward continuous and scalable production of colloidal nanocrystals by switching from batch to droplet reactors. *Chem. Soc. Rev.* **2015**, *44*, 5806–5820, doi:10.1039/c5cs00049a.
47. Xu, Y.; Musumeci, V.; Aymonier, C. Chemistry in supercritical fluids for the synthesis of metal nanomaterials. *React. Chem. Eng.* **2019**, *4*, 2030–2054, doi:10.1039/C9RE00290A.
48. Khan, I.U.; Serra, C.A.; Anton, N.; Vandamme, T. Microfluidics: A focus on improved cancer targeted drug delivery systems. *J. Control. Release* **2013**, 1065–1074, doi:10.1016/j.jconrel.2013.07.028.
49. Biehl, P.; Lühe, M. von der; Dutz, S.; Schacher, F.H.; Synthesis, Characterization, and Applications of Magnetic Nanoparticles Featuring Polyzwitterionic Coatings. *Polymers (Basel)* **2018**, *10*, doi:10.3390/polym10010091.
50. Baki, A.; Bleul, R.; Banz, C.; Thiermann, R.; Maskos, M. Continuous synthesis of single-core iron oxide nanoparticles for biomedical applications. *6th International Workshop on Magnetic Particle Imaging (IWMPI)* **2016**, 100.
51. Baki, A.; Löwa, N.; Thiermann, R.; Banz, C.; Maskos, M.; Wiekhorst, F.; Bleul, R. Continuous synthesis of single core iron oxide nanoparticles for MPI tracer development. *IJMPI,* **2017**, *3(1)*, doi:10.18416/ijmpi.2017.1703004.
52. Hessel, V.; Löwe, H.; Stange, T. Micro chemical processing at IMM--from pioneering work to customer-specific services. *Lab Chip* **2002**, *2*, 14–21, doi:10.1039/b200366j.
53. Schönfeld, F.; Hessel, V.; Hofmann, C. An optimised split-and-recombine micro-mixer with uniform chaotic mixing. *Lab Chip* **2004**, *4*, 65–69, doi:10.1039/b310802c.
54. Walter, J.; Thajudeen, T.; Süß, S.; Segets, D.; Peukert, W. New possibilities of accurate particle characterisation by applying direct boundary models to analytical centrifugation. *Nanoscale* **2015**, *7*, 6574–6587, doi:10.1039/c5nr00995b.
55. Pyenson, H.; Tracy, P.H. A 1,10—Phenanthroline Method for the Determination of Iron in Powdered Milk. Int. *J. Dairy Sci.* **1945**, *28*, 401–412, doi:10.3168/jds.S0022-0302(45)95191-5.

56. Löwa, N.; Seidel, M.; Radon, P.; Wiekhorst, F. Magnetic nanoparticles in different biological environments analyzed by magnetic particle spectroscopy. *J. Magn. Magn. Mater.* **2017**, *427*, 133–138, doi:10.1016/j.jmmm.2016.10.096.
57. Löwa, N.; Gutkelch, D.; Welge, E.A.; Welz, R.; Meier, F.; Baki, A.; Bleul, R.; Klein, T.; Wiekhorst, F. Novel benchtop Magnetic Particle Spectrometer for process monitoring of magnetic nanoparticle synthesis. *Nanomaterials* **2020**.
58. Dadfar, S.M.; Roemhild, K.; Drude, N.I.; Stillfried, S. von; Knüchel, R.; Kiessling, F.; Lammers, T. Iron oxide nanoparticles: Diagnostic, therapeutic and theranostic applications. *Adv. Drug Deliv. Rev.* **2019**, *138*, 302–325, doi:10.1016/j.addr.2019.01.005.
59. Poller, W.C.; Löwa, N.; Wiekhorst, F.; Taupitz, M.; Wagner, S.; Möller, K.; Baumann, G.; Stangl, V.; Trahms, L.; Ludwig, A. Magnetic Particle Spectroscopy Reveals Dynamic Changes in the Magnetic Behavior of Very Small Superparamagnetic Iron Oxide Nanoparticles During Cellular Uptake and Enables Determination of Cell-Labeling Efficacy. *J. Biomed. Nanotechnol.* **2016**, *12*, 337–346, doi:10.1166/jbn.2016.2204.
60. Schilling, M.; Ludwig, F.; Kuhlmann, C.; Wawrzik, T. Magnetic particle imaging scanner with 10-kHz drive-field frequency. *Biomed. Eng. – Biomed. Te.* **2013**, *58*, doi:10.1515/bmt-2013-0014.
61. Eberbeck, D.; Löwa, N.; Steinhoff, U.; Viereck, T.; Schilling, M.; Trahms, L. Characterization of magnetic nanoparticle systems with respect to their magnetic particle imaging performance. *Biomed. Tech. (Berl)* **2013**, *58*, 1–11, doi:10.1515/bmt-2013-0013.
62. Ziegenbalg, D.; Kompter, C.; Schönfeld, F.; Kralisch, D. Evaluation of different micromixers by CFD simulations for the anionic polymerisation of styrene. *Green Process. Synth.* **2012**, *1*, doi:10.1515/gps-2012-0004.
63. LaGrow, A.P.; Besenhard, M.O.; Hodzic, A.; Sergides, A.; Bogart, L.K.; Gavriilidis, A.; Thanh, N.T.K. Unravelling the growth mechanism of the co-precipitation of

iron oxide nanoparticles with the aid of synchrotron X-Ray diffraction in solution. *Nanoscale* **2019**, *11*, 6620–6628, doi:10.1039/C9NR00531E.

64. Blesa, M.A.; Matijević, E. Phase transformations of iron oxides, oxohydroxides, and hydrous oxides in aqueous media. *Adv. Colloid Interface Sci.* **1989**, 173–221, doi:10.1016/0001-8686(89)80009-0.
65. Hou, Y.; Xu, Z.; Sun, S. Controlled synthesis and chemical conversions of FeO nanoparticles. *Angew. Chem. Int. Ed Engl.* **2007**, *46*, 6329–6332, doi:10.1002/anie.200701694.
66. Bleul, R.; Baki, A.; Freese, C.; Paysen, H.; Kosch, O.; Wiekhorst, F. Continuously manufactured single-core iron oxide nanoparticles for cancer theranostics as valuable contribution in translational research. *Nanoscale Adv.* **2020**, doi:10.1039/D0NA00343C.
67. Ozel, F.; Kockar, H.; Karaagac, O. Growth of Iron Oxide Nanoparticles by Hydrothermal Process: Effect of Reaction Parameters on the Nanoparticle Size. *J Supercond Nov Magn* **2015**, *28*, 823–829, doi:10.1007/s10948-014-2707-9.
68. Lu, A.-H.; Salabas, E.L.; Schüth, F. Magnetische Nanopartikel: Synthese, Stabilisierung, Funktionalisierung und Anwendung. *Angew. Chem.* **2007**, *119*, 1242–1266, doi:10.1002/ange.200602866.
69. Li, Q.; Kartikowati, C.W.; Horie, S.; Ogi, T.; Iwaki, T.; Okuyama, K. Correlation between particle size/domain structure and magnetic properties of highly crystalline Fe3O4 nanoparticles. *Sci. Rep.* **2017**, *7*, 9894, doi:10.1038/s41598-017-09897-5.
70. Gul, S.; Khan, S.B.; Rehman, I.U.; Khan, M.A.; Khan, M.I. A Comprehensive Review of Magnetic Nanomaterials Modern Day Theranostics. *Frontiers in Mater.* **2019**, *6*, 179, doi:10.3389/fmats.2019.00179.
71. Modo, M.M.J.; Bulte, J.W.M.; Kim, E.E. *Molecular and Cellular MR Imaging*. CRC Press: Florida, USA, 1st Edition, 2007.
72. Hufschmid, R.; Arami, H.; Ferguson, R.M.; Gonzales, M.; Teeman, E.; Brush, L.N.; Browning, N.D.; Krishnan, K.M. Synthesis of phase-pure and monodisperse iron

oxide nanoparticles by thermal decomposition. *Nanoscale* **2015**, *7*, 11142–11154, doi:10.1039/C5NR01651G.

73. Bemetz, J.; Wegemann, A.; Saatchi, K.; Haase, A.; Häfeli, U.O.; Niessner, R.; Gleich, B.; Seidel, M. Microfluidic-Based Synthesis of Magnetic Nanoparticles Coupled with Miniaturized NMR for Online Relaxation Studies. *Anal. Chem.* **2018**, *90*, 9975–9982, doi:10.1021/acs.analchem.8b02374.

5.4 Albumin-Coated Single-Core Iron Oxide Nanoparticles for Enhanced Molecular Magnetic Imaging (MRI/MPI)

Published in: ***International Journal of Molecular Sciences (IJMS), impact factor (5.924)***

In this publication, the surface of MNP produced by continuous micromixer synthesis is additionally functionalized with bovine serum albumin (BSA) to improve the colloidal stability and reduce the agglomeration behavior in physiological environment. Physiological systems contain serum proteins and highly ionic strengths that might lead to MNP agglomeration. Therefore, stabilizing surface modification of MNP is crucial if using them as a contrast agent for biomedical applications e.g., in imaging modalities such as Magnetic Resonance Imaging (MRI) or Magnetic Particle Imaging (MPI). The synthesized MNP systems without and after further surface modification are physicochemically and magnetically characterized.

MNP after BSA surface modification exhibited an improved stability at different salt (NaCl) concentrations (0.05, 0.1, and 0.15 mol/L) after 2, 24, and as well after 72 hours of incubation. In contrast to MNP without BSA surface modification, the physicochemical and magnetic properties remained largely preserved in BSA-coated MNP in a physiological environment.

The evaluation of the performance of the BSA-coated MNP as an MPI tracer is carried out using Magnetic Particle Spectroscopy (MPS) and as an MRI contrast agent using Nuclear Magnetic Resonance (NMR) relaxivity measurements. The MNP showed promising imaging capabilities in both modalities of about the same as and better than commercial MNP systems.

The following tasks were carried out by me, Abdulkader Baki:

1- Development of the continuous micromixer device for MNP syn thesis.

2- Implementation of the continuous syntheses.

3- Implementation of MNP fractionation by centrifugation.

4- Surface functionalization with BSA.

5- Physicochemical characterization and data evaluation of the MNP without and after a- BSA-functionalization by:

b- Transmission Electron Microscopy (TEM)

c- Differential Centrifugal Sedimentation (DCS) measurments

d- Determination of iron concentration

e- Zeta potential

f- Gel electrophoresis analysis

6- Summary and evaluation of experimental results

7- Draft conception and revising of the publication

The determination of the magnetic properties is carried out at the Physikalisch-Technische Bundesanstalt (PTB) in Berlin.

International Journal of *Molecular Sciences*

MDPI

(Article)

Albumin-coated single-core iron oxide nanoparticles for enhanced molecular magnetic imaging (MRI/MPI)

Abdulkader Baki [1], Amani Remmo [2], Norbert Löwa [2], Frank Wiekhorst [2], Regina Bleul [1, *]

1 Fraunhofer Institute for Microengineering and Microsystems IMM, Carl-Zeiss-Straße 18-20, 55129 Mainz, Germany; Abdulkader.Baki@imm-extern.fraunhofer.de
2 Physikalisch-Technische Bundesanstalt, Abbestraße 2-12, 10587 Berlin, Germany; Amani.Remmo@ptb.de (A.R.); Norbert.Loewa@ptb.de (N.L.); Frank.Wiekhorst@ptb.de (F.W.)
* Correspondence: Regina.Bleul@imm.fraunhofer.de; Tel.: +49-6131-990168

Abstract: Colloidal stability of magnetic iron oxide nanoparticles (MNP) in physiological environments is crucial for their (bio) medical application. MNP are potential contrast agents for different imaging modalities like magnetic resonance imaging (MRI) and magnetic particle imaging (MPI). Applied as hybrid method (MRI/MPI), these are valuable tools for molecular imaging. Continuously synthesized and in-situ stabilized single-core MNP were further modified by albumin coating. Synthesizing and coating of MNP were carried out in aqueous media without using any organic solvent in a simple procedure. The additional steric stabilization with the biocompatible protein, namely bovine serum albumin (BSA), lead to potential contrast agents suitable for multimodal (MRI/MPI) imaging. Colloidal stability of BSA-coated MNP were investigated in different sodium chloride concentrations (50 to 150 mM) in short- and long-term incubation (from two hours to one week) using physiochemical characterization techniques like Transmission electron microscopy (TEM) for core size and differential centrifugal sedimentation (DCS) for hydrodynamic size. Magnetic characterization like magnetic particle spectroscopy (MPS) and nuclear magnetic resonance (NMR) measurements confirmed successful surface modification as well as exceptional colloidal stability of the relatively large single-core MNP. For comparison, two commercially available MNP systems were investigated, MNP-clusters, the former liver contrast agent (Resovist) and single-core MNP (SHP-30) manufactured by

thermal decomposition. The tailored core size, colloidal stability in physiological environment and magnetic performance of our MNP indicate their ability to be used as molecular magnetic contrast agent for MPI and MRI.

Keywords: Iron oxide nanoparticles; serum albumin; magnetic particle spectroscopy; magnetic particle imaging; magnetic resonance imaging.

1. Introduction

Molecular imaging provides an integrative technology to study biological processes using non-invasive visualization of specific molecules in vivo [1] with the aim of early disease diagnosis and treatment evaluation [2]. To this end, numerous imaging techniques have been developed for molecular imaging such as magnetic resonance imaging (MRI) [1], positron emission tomography (PET) [3], computed tomography (CT) [4], single-photon emission computed tomography (SPECT) [5,6], or ultrasound (US) [7]. Aside from the physical principle (detection of frequency, radionuclides, emitted light, X-ray, etc.), these modalities are different regarding invasiveness and cost-effectiveness.

MRI relies on detecting the nuclear magnetic resonance signal of protons of the hydrogen atom ^{1}H after applying radiofrequency pulses. Therefore, MRI is not specific to molecules and requires the use of contrast agents or tracers to provide specificity and sensitivity for molecular imaging. Due to their magnetic properties, contrast agents such as paramagnetic Gd-compounds can shorten the T_1 (or longitudinal) and T_2 (or transverse) relaxation time of neighboring water protons. These effects increase the signal intensity of T_1-weighted images (positive contrast, contrast-agent-containing regions appear brighter) or reduce the signal intensity of T_2-weighted images (negative contrast, region with contrast agent appears darker). Transition metal ions, such as high-spin manganese (II) and iron oxide nanoparticles (iron-(III) oxides), are known to strongly affect the T_2 relaxation and represent the typical content of negative contrast agents [8,9].

Generally, magnetic nanoparticles (MNP) constitute a class of potent contrast agents providing positive or negative contrast depending on their concentration and on the MRI sequences used [10]. To characterize an MRI contrast agent, the relaxivities r_1 and r_2 are considered, that is, the ability of the contrast agent (normalized to the iron concentration c(Fe)) to increase the longitudinal $R_1 = 1/T_1$ and transversal $R_2 = 1/T_2$ relaxation rate of the proton magnetization. By immobilization or aggregation of the MNP, e.g., by binding to biomolecular targets or after internalization into cells, these

contrast properties might be drastically changed [11]. Even though iron-oxide-based MNP were already clinically approved in the late 90 s as negative MRI contrast agents for liver MRI (Feridex, Endorem, Resovist) [12], most of them were withdrawn from the European market in the meantime due to claims such as limitation of their field applications, deficiency of diagnostic impact, and economic factors. Additionally, the occurrence of harmful side effects was reported caused either by labile iron or hypersensitivity reactions attributed to the coating of the MNP [13,14]. However, ferumoxytol (Feraheme or Rienso) is approved for ironreplacement therapies, and additional approval is being sought for imaging applications, which are beyond its authorized indication. To date, iron-oxide-based MNP have attracted growing attention as a newly discovered biocompatible alternative to the clinically widely used gadolinium (Gd)-based contrast agents [15]. For instance, (ultra)small iron oxide nanoparticles are currently investigated as potential MRI positive contrast agents to replace the critically observed Gd agents due to their potentially harmful side effects [16–19].

A further imaging modality with high potential in sensitive molecular imaging is magnetic particles imaging (MPI), first presented in 2005 [20]. MPI stands out due to high spatial (below mm) and excellent temporal (1–10 ms) resolution without any ionizing radiation exposure [20]. Though MPI so far is not in clinical use for medical applications, its high potential for diagnostic vascular or perfusion imaging, imaging-guided vascular interventions [21], or cancer diagnostics is acknowledged [20,22]. MPI has reached preclinical levels, but still requires the development of suitable MNP as tracers with improved dynamic magnetic and biological properties such as sufficient magnetic response, blood half-life time, and stability in a physiological environment.

Since MPI is a direct imaging technique that specifically detects the MNP, the generated MP images are background-free, and subsequently, no anatomical information is provided. However, combining the high resolution 3D anatomical MRI data with molecular tracking of MNP tracers by MPI constitutes a promising hybrid imaging technology [23,24]. Besides their application as tracers in diagnostic imaging,

MNP can also be utilized as functional components in therapeutic applications for, e.g., hyperthermia and drug delivery [25–27].

Depending on their intended application, MNP require specific properties for an optimal performance in these different fields. For instance, according to theoretical models and preliminary experimental studies of different groups, single-core iron-oxide MNP with a distinct size of about 25–30 nm diameter are indicated to be effective tracers for MPI [25,28]. Moreover, investigations on magnetosomes (single-core iron-oxide MNP grown by biotechnological processing) have already demonstrated a good performance for MPI as well as for magnetic hyperthermia [29–31]. The provision of single-core iron oxide MNP in this size range requires highly controllable synthesis strategies. Conventional batch synthesis approaches such as thermal decomposition, microemulsion, the sol–gel method, ultrasonication, and coprecipitation are either time-consuming and require phase transfer or display considerable batch-to-batch variations in both size and size distribution, leading to undefined magnetic properties [32]. A more robust synthesis method is the continuous micromixing approach, which has already been shown to provide good control of particle size and magnetic characteristics in aqueous synthesis [32,33]. Here, the stages of nucleation and particle growth can be isolated as a function of distance. The position where initial mixing induces nucleation is spatially separated from the particle growth occurring in the ripening zone. Due to in situ stabilization during this microfluidic production process, electrostatically stable dispersed single-core MNP in an aqueous medium are obtained. As described in the literature, alternative approaches, e.g., laser target evaporation from bulk material, can also produce stable aqueous magnetic nanofluids even without the need for an electrostatic stabilizer [34]. Coating with a double layer of oleic acid of magnetic nanoparticles obtained by combustion synthesis was reported as a biocompatible strategy for self-stabilizing particle dispersions in water [35]. Stable aqueous nanoparticle dispersions provide a safe starting product for biomedical development. Further surface modification can be performed straightforwardly by coating without preceding phase transfer. MNP surface characteristics play a key role

in signal generation in medical imaging, as they influence the dispersion stability in the physiological environment and act as a linker for further functionalization. Moreover, the surface coating of iron oxide MNP is reported to improve biocompatibility and reduce cytotoxic effects that can be caused by reactive oxygen species (ROS) [36–38]. Potent agents for molecular imaging are supposed to prevent non-specific interaction with the biological system, e.g., with serum proteins, high ionic strength, blood and endothelial cells, while specifically targeting biological markers or receptors. The attachment of specific ligands helps to identify signal molecules or bind to and detect, e.g., cancer cells that overexpress typical receptors.

The biocompatibility, non-toxicity, and stability of MNP are crucial for in vivo applications. The MNP surface can be modified with different strategies utilizing macromolecules with different functional groups such as dextran [39,40], polyethylene glycol (PEG) [41,42], or numerous peptides [43]. Serum albumin is a main blood plasma protein with significant vital functions such as maintaining the pH and osmotic pressure of blood and exhibit excellent stability in physiological systems [44,45]. Moreover, the functional groups existing in albumin such as amino and carboxy groups enable it to bind different drug-targeting ligands. For instance, Abraxane®, an albumin–paclitaxel nanoparticle, is a clinically approved chemotherapeutic drug conjugate. Its efficacy was confirmed in clinical trials and showed a significant activity in pancreatic cancer patients [46] and antitumoral effects in women with breast cancer [47]. Mesken et al. have investigated plasmid-loaded albumin nanoparticles for cellular uptake and gene delivery [48]. Due to its similar biological function and chemical composition, bovine serum albumin (BSA) as analogue to human serum albumin (HSA) is a widely used component for investigations and developments in the field of drug delivery and cancer diagnostic [49]. Many research groups have also used BSA for MNP surface coating after synthesis, mainly resulting in clusters of small MNP in a size range between 4 and 10 nm [50–53]. Kalidasan et al. have investigated the conjugation of BSA to 10 and 30 nm non-spherical, rhombus-shaped MNP using cetyl trimethyl ammonium bromice (CTAB) and 3-Amino-Trimethoxysilane (APTM)

as linker molecules. Due to the improved colloidal stability of these BSA-MNP, the specific absorption rate (SAR) values for magnetic hyperthermia could be increased from 1700 W/g for MNP without BSA to 2300 W/g for BSA-MNP [54]. To conclude, for a successful surface modification, not only does the coating material have to be carefully selected, but also effects occurring due to the required post-synthesis procedures such as phase transfer or purification steps might lead to clustering effects or undesirable residue of solvents that can be disadvantageous for their application as contrast agents.

In this study, we demonstrate that surface modification of continuously synthesized single-core MNP with BSA effectively improves their stability and ensures a robust performance as tracers in molecular imaging. Manufacturing and surface modification were carried out in an aqueous medium without the addition of harmful chemicals or the need for phase transfer. The as-synthesized (tannin-coated) and BSA-coated MNP were comprehensively studied regarding changes in their colloidal stability and magnetic properties at different physiological relevant salt (NaCl) concentrations. Average size, size distribution, and particle morphology were investigated by transmission electron microscopy (TEM) and differential centrifugal sedimentation (DCS). Changes in particle surface were studied by Zeta potential measurements and gel electrophoresis. Using AC-susceptibility (ACS) measurements of the linear magnetic susceptibility, changes in the hydrodynamic properties of the MNP systems have been investigated. To determine the MPI performance of the MNP, we used magnetic particle spectroscopy (MPS). MPS detects the non-linear dynamic magnetic response of MNP exposed to an alternating magnetic field. Since it is based on the same physical mechanisms, it can be considered zero-dimensional MPI. Furthermore, to evaluate the capability of the MNP systems as contrast agents in MRI, nuclear magnetic resonance (NMR) relaxivity measurements were carried out. For comparison, MPS and NMR measurements of the two commercial MNP systems Resovist (multi-core system, MRI liver contrast agent) and SHP-30 (single-core

nanoparticle system synthesized by thermal decomposition, preclinical research) have been included.

2. Results and Discussion

The capability of a continuous micromixer technique to synthesize aqueous single-core MNP with diameters of up to 40 nm has been demonstrated recently [32]. By adjusting the two synthesis parameters T_S = 55 °C and residence time t_R = 4 min, MNP with mean core size diameter of about d_c = 30 nm were found to possess high performance in MRI and MPI.

Based on this MNP system, further improvement using surface modification with a BSA protein coating is envisaged regarding stability in a physiological environment and magnetic performance for molecular imaging applications. We show that centrifugation significantly improves the magnetic performance of the as-synthesized MNP in Section 2.1, demonstrate the structural and magnetic changes by surface modification using a BSA-coating in Section 2.2, and present the steady stability of the BSA-coated system in different physiological saline concentrations together with the maintenance of the powerful MRI and MPI imaging capability of this MNP system. For comparison, all measurements were performed with as-synthesized MNP (tannic acid coated) without any further surface modification and the centrifuged MNP as well. Furthermore, we included data of the two commercial systems Resovist and SHP-30.

2.1 Particle Fractionation by Centrifugation

Our continuous micromixer synthesis approach provides stable dispersions of single core nanoparticles with narrow size distribution, as shown in Figure 1a. Spherical single core particles with a mean diameter d_c of 27.6 ± 5.5 nm were determined by TEM analysis of the as-synthesized MNP (containing the basic tannic acid coating). The apparent hydrodynamic diameter d_h distribution determined by DCS shows a narrow peak with a maximum at 26.5 nm close to, but slightly smaller than, the core diameter

obtained by TEM. Notably, the hydrodynamic size distribution obtained by DCS for the as-synthesized and centrifuged MNP shown in Figure 1a assumes a density of pure magnetite neglecting the decrease in density resulting from the organic tannic acid coating on the surface. This leads to slightly shifting the hydrodynamic diameters determined by DCS to smaller values (as the real density of the particles is smaller than the assumed magnetite density used for the data analysis).

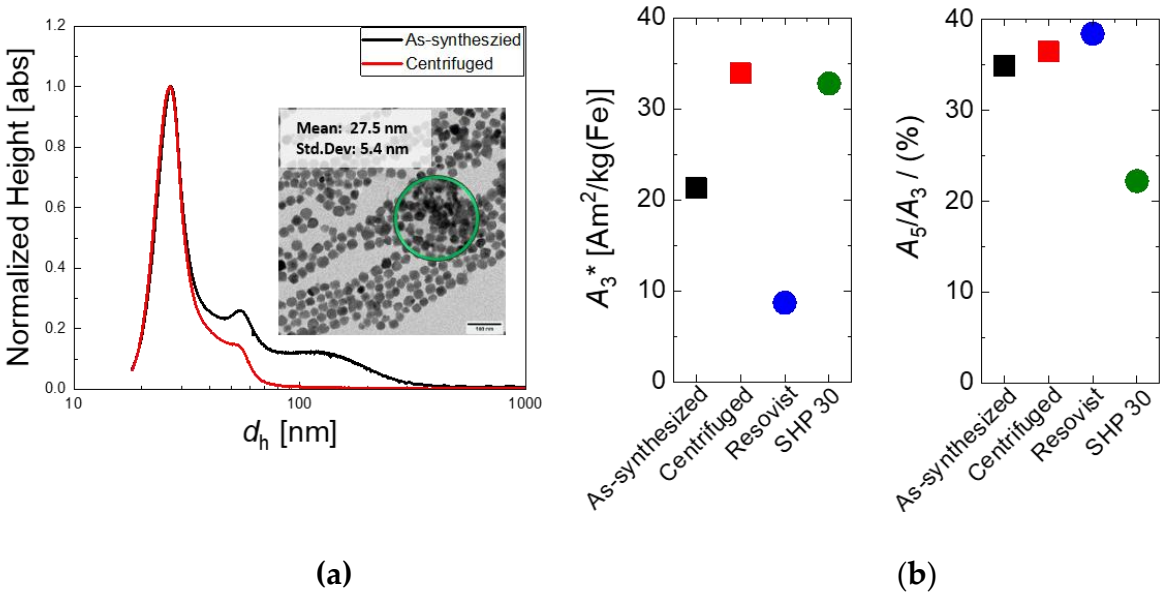

(a) **(b)**

Figure 1. (**a**) Particle fractionation by centrifugation (prior to BSA-coating): Hydrodynamic size distribution measured by DCS of as-synthesized (black line) and centrifuged (red line) MNP, where the broad shoulder from 70 up to 300 nm is significantly reduced. Inset: Representative TEM image of as-synthesized MNP with areas of aggregated particles marked by the green circle (scale bar 100 nm). (**b**) MPS parameters A_3* and A_5/A_3 measured at B_{ex} = 25 mT for as-synthesized (black symbols) and centrifuged MNP (red symbols) showing the signal increase gained by particle fractionation. Included are the corresponding MPS parameters of the two commercial systems Resovist (blue symbols) and SHP-30 (green symbols).

Furthermore, a minor fraction with d_h > 30 nm of MNP attributed to agglomerates or superstructures is observed in DCS. These larger entities might affect the signal generation in magnetic imaging due to undesired particle–particle interaction of the particle magnetic moments. Therefore, we performed an additional centrifugation prior to BSA-coating and analyzed the resulting structural and magnetic changes of the particle fractionation.

DCS measurements of the centrifuged MNP system confirm the successful separation of agglomerates with d_h > 80 nm, as illustrated in Figure 1a. The centrifugation results in a yield reduction of about 35%, as estimated from the corresponding MNP content of the individual fractions determined by iron concentration analysis. The small shoulder right to the main peak in DCS still indicates the tendency to form small superstructures such as dimers or trimers, which in our experience is reversible. The DCS results are confirmed by TEM, where no clustering is found in TEM images of the MNP system after centrifugation, as shown in the next section (see Figure 2a).

The effect of centrifugation is also expressed in the magnetic properties of the MNP. As displayed in Figure 1b, the MPS measurements showed an increase of about 37% of the specific (MPS moment normalized to iron content) A_3* amplitude from 21.3 $Am^2/kg(Fe)$ to 33.9 $Am^2/kg(Fe)$ by centrifugation. This indicates the remarkable enhancement of signal sensitivity as a consequence of isolating stable single-core MNPs from the fractioncontaining agglomerates. The MNP concentration-independent shape parameter A_5/A_3 showed a slight increase from 34.9% to 36.4%. Generally, this increase of the A_5/A_3 parameter results in a better MPI performance and image resolution.

The centrifuged MNP system was then used for surface modification by BSA-coating, as described in the next section.

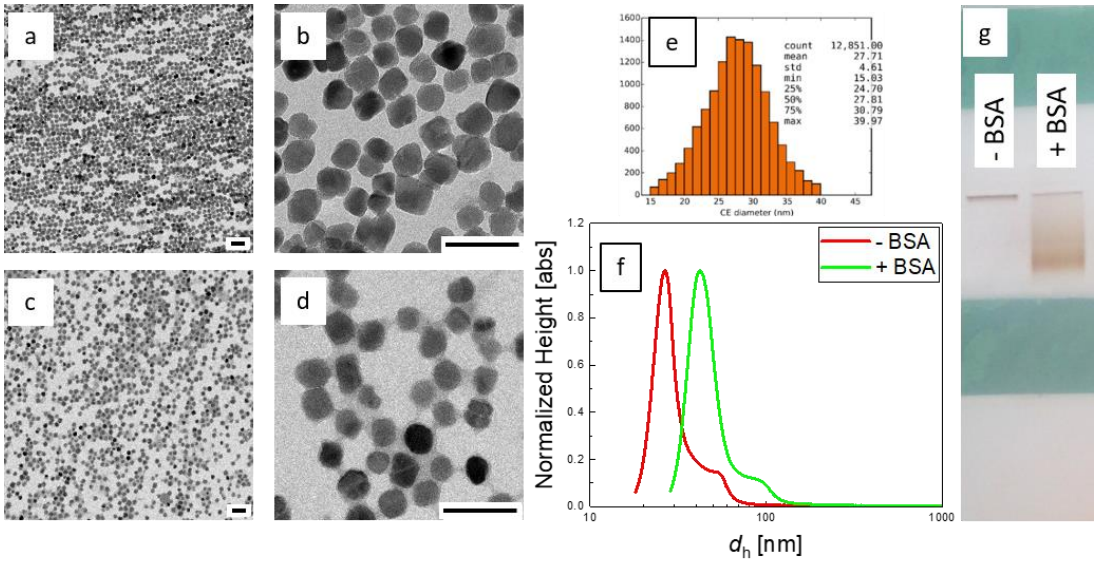

Figure 2. Physicochemical characterization of continuously synthesized MNP. TEM images (scale bar 100 nm) of centrifuged MNP without BSA-coating (**a**,**b**) and with BSA-coating (**c**,**d**). Core diameter histogram from TEM image analysis of uncoated MNP (**e**). Hydrodynamic size distribution obtained by DCS (**f**) of centrifuged MNP without BSA (red line), and with BSA-coating (green line). Agarose gel electrophoresis (**g**) shows a high mobility of BSA-coated MNP (+BSA, **right**) and nearly immobilized MNP without BSA-coating (−BSA, **left**).

2.2 BSA-Coating of Single-Core Magnetic Nanoparticles for Imaging Applications

Generally, iron oxide nanoparticles are stabilized in situ during continuous micromixer synthesis with tannic acid, which acts mainly as an electrostatic stabilizing agent. However, high salt concentrations as present in a physiological environment (typically 150 mM NaCl, isotonic saline) strongly affect the colloidal stability of electrostatically stabilized nanoparticles. Thus, a further modification, preferably with a steric stabilizer, is required. In biomedical and pharmaceutical applications, biocompatible synthetic as well as biologic polymers are commonly used, e.g., polyethylene glycol and copolymers, polypeptides or proteins, and polysaccharides [55,56].

In this study, bovine serum albumin (BSA) was chosen for surface modification to prevent aggregation of the single-core magnetic nanoparticles. This blood plasma protein has high concentrations in blood and is known to form a protein corona to particles injected in the blood stream very rapidly [57]. BSA-coating is a frequently reported strategy [50] to prevent non-specific interaction and enhance colloidal

stability and biocompatibility of nanoformulations. Here, we evaluated the effect of BSA-coating as further surface modification on the structural and magnetic imaging properties and compared them with the corresponding behavior of the uncoated systems.

TEM analysis of the original, centrifuged sample compared to the BSA-treated sample confirmed the successful protein coating (Figure 2a–d). The size and shape of both samples were relatively homogenous and displayed mostly spherical single-core particles. No significant changes of the cores were observed after the coating procedure. The mean core size of centrifuged sample was estimated by automatic image analysis and showed 27.7 nm with relative standard deviation of 0.17 (Figure 2e). Though the presence of protein coating is poorly visible in TEM analysis due to the low contrast of BSA, the effect of the coating increasing the interparticle distances is clearly seen in the images (Figure 2a–d) indicating the successful coating. An increase of the apparent hydrodynamic diameter from d_h = 26.5 nm to d_h = 42 nm after BSA-coating was determined by DCS analysis (Figure 2f), where the effective density of magnetite and a BSA monolayer was taken into account this time (see methods section for details). From the d_h difference, a mean BSA layer thickness of about 8 nm could be estimated.

Changes in the surface characteristics of the MNP after BSA-coating were investigated by zeta potential measurements and agarose gel electrophoresis. The latter technique is commonly used for the separation and analysis of biomacromolecules, e.g., oligonucleotides. Separation depends generally on the (surface) charge as well as the molecular weight. It has been shown that gel electrophoresis is also a useful tool to analyze surface charge, size, and stability of nanoparticles [58]. The as-synthesized MNP possess a high negative surface charge with a zeta potential of about −51 mV. This highly negative value can be explained by anionic polyphenolic groups of the tannic acid coating. The BSAcoated sample displayed a value of about −25 mV in distilled water, which agrees with values for BSA at pH 6.5 in the literature [34]. Generally, sufficient electrostatic stabilization of

nanoparticles can be assumed for samples with a zeta potential that exceeds 20 mV, irrespective of their sign [59]. Apparently, the MNP without BSA-coating did not pass the electrophoresis gel, as shown in Figure 2g. This was attributed to the high affinity of tannic acid to polysaccharide that might have caused crosslinking and hydrogel formation, as reported in the literature [60]. In contrast, BSA-coated samples displayed significant migrations through the gel, as displayed in Figure 2g. This qualitative finding evidences that BSA-coating was successful and changed the surface characteristics of the MNP.

The effect of BSA-coating on the magnetic properties of the MNP was investigated by ACS and MPS measurements. ACS measurements in Figure 3 display the typical shape observed for a colloidal MNP system with a step-like decrease of the real part χ' with increasing frequency (Figure 3a) and a distinct maximum in the imaginary part $\chi''(f)$ of the complex linear susceptibility (Figure 3b). The as-synthesized and centrifuged MNP show nearly identical spectra, only differing in the linear susceptibility amplitude χ_0, which increases by about 26% from $\chi_0 = 0.062$ m^3/kg(Fe) for the as-synthesized to 0.084 m^3/kg(Fe) for the centrifuged MNP. This shows the improvement in the magnetic quality of the MNP without changing the fraction of sizes responsible for the dynamic magnetic behavior. In other words, the increase in amplitude is attributed to the effective removal of the aggregates by centrifugation, which, due to their inhibited Brownian rotation, do not contribute notably to the linear susceptibility in the measured frequency range. The χ'' (f) curves of both uncoated systems have the maximum at nearly the same frequency of $f = 5.92(2)$ kHz, indicating that by centrifugation the hydrodynamic size distribution of the free MNP is not changed in agreement with the DCS measurements after centrifugation (see Figure 1a).

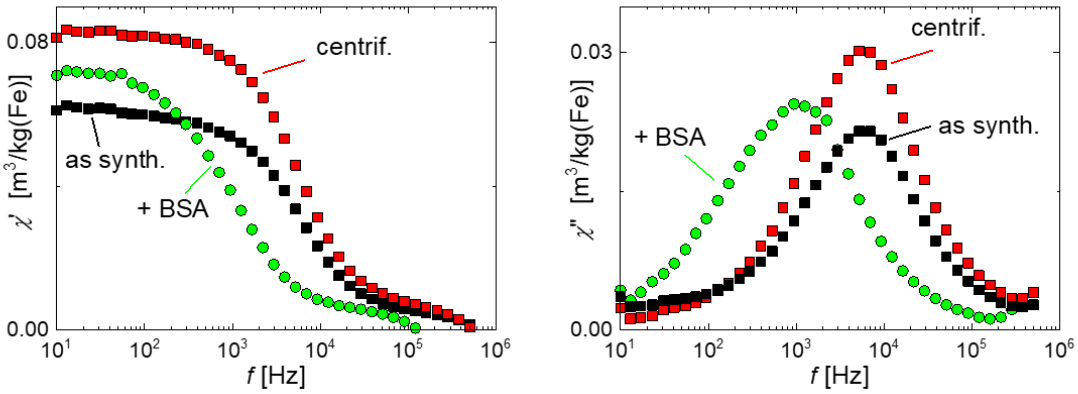

Figure 3. Linear AC susceptibility versus frequency of as-synthesized (black symbols), centrifuged (red symbols), and BSA-coated (green symbols) MNP. (**a**) real part χ', (**b**) imaginary part χ''. While as-synthesized and centrifuged MNP show the same spectra with an increased susceptibility for the centrifuged MNP of about 26%, the BSA-coated MNP show a shift of the χ' peak towards lower frequencies due to the increase of hydrodynamic diameter by the additional BSA-layer.

The increase in hydrodynamic diameter by adding the BSA-layer was apparent in ACS measurements as a shift of the peak position of the imaginary part χ'' from about 5 kHz to about 1 kHz (see Figure 3b). The increased hydrodynamic diameter of the BSA-coated particles augments the rotational inertia of the moments to follow the oscillating excitation field, resulting in the observed shift of the χ'' peak towards lower frequencies. At the same time the susceptibility amplitude χ_0 (χ' for $f \rightarrow 0$) is slightly decreased by about 14% after BSA-coating, still remaining above the amplitude of the as-synthesized MNP (Figure 3a). This indicates the effective coating of the MNP by the BSA layer.

As displayed in Figure 4a, the MPS specific amplitude decreased slightly from

A_3* = 33.9 Am²/kg (Fe) to 26 Am²/kg (Fe) after BSA-coating, which is still a remarkably high value that is three times higher than the value A_3* = 8.7 Am²/kg (Fe) of Resovist. The reason for the A_3* reduction is assumed to again be the increase of hydrodynamic diameter by the additional BSA-coating reducing to some extent the capability of the magnetic moments of the MNP to follow the excitation magnetic field, diminishing the resulting magnetic response in MPS. Thus, both the observed reduction of the linear magnetic AC susceptibility amplitude χ_0 and the measured decrease in the MPS signal amplitude A_3* are caused by the increase of hydrodynamic diameter after BSA-coating.

As displayed in Figure 4b, the A_5/A_3 ratio remained nearly constant at the comparable high level of 35.8% for BSA-coated MNP (compared to 36.4% for MNP without BSA), indicating that the BSA-coating will maintain the MPI performance.

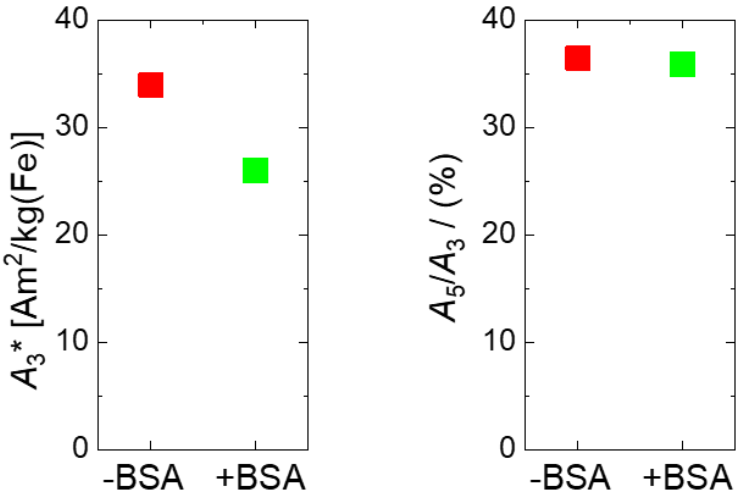

(a) (b)

Figure 4. MPS parameters A_3* (**a**) and A_5/A_3 (**b**) of uncoated MNP (red symbols) and BSA-coated MNP (green symbols). The specific MPS amplitude A_3* is reduced by about 20% while the shape parameter A_5/A_3 remains nearly unchanged. This reduction is attributed to the increase in hydrodynamic diameter of from 26.5 to 42 nm by BSA coating.

Similar effects of reduced MPS performance have been observed for MNP where the local viscosity has been increased, leading to the same increase of rotational inertia of MNP moments [61].

To assess the performance of BSA-coated MNP in the second magnetic imaging modality, MRI, we determined the NMR relaxivities r_1 and r_2, as shown in Figure 5.

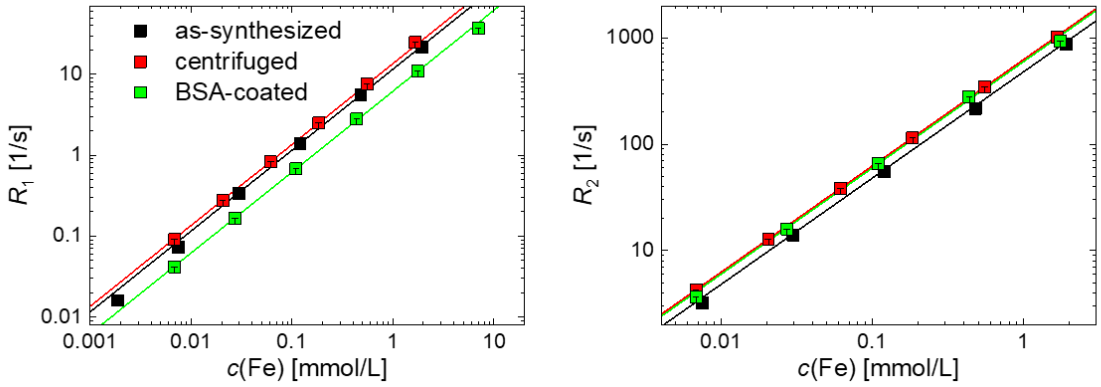

(a) (b)

Figure 5. Room temperature NMR relaxation rates R_1 (**a**) and R_2 (**b**) measurements as a function of iron concentration c(Fe) of as-synthesized, centrifuged, and BSA-coated MNP measured at 1.5 T. The relaxation rates are obtained by linear regression and drawn as straight lines; the corresponding for the r_1 and r_2 values are listed in Table 1.

Table 1. Properties of the investigated MNP systems together with the two commercial MNP systems, Resovist and SHP-30 MNP. System information and coating are provided in the first two columns, followed by magnetic parameters obtained by MPS (amplitude of the 3 rd harmonic normalized to iron amount, A3*), ACS (initial susceptibility χ_0), and NMR (relaxivities r_1 and r_2 and the ratio r_2/r_1 measured at 1.5 T).

Sample System	Coating	A_3* Am²/kg(Fe)	χ_0 m³/kg(Fe)	r_1 L/(mmol·s)	r_2 L/(mmol·s)	r_1/r_2
as-synthesized MNP single core, d_c = 27.7 nm, cont. micromixer synthesis	tannic acid	21.3	0.062	11.6(9)	482(8)	42
centrifuged MNP	tannic acid	33.9	0.084	13.6(6)	620(7)	46
BSA-coated	Bovine serum albumin	26	0.072	6.2(4)	600(10)	97
Resovist multi-core [2], 6 nm cores bimodal size distribution mean cluster size 24 nm	carboxydextran T1.8 kDa	8.7	-	7.4 [1] 8.7 [2]	95 [1] 61 [2]	15
SHP-30 single core, thermal decomposition, 30 nm +/− 2.5 nm	amphiphilic coating with carboxylic acid groups	32.8	-	8.0(5)	660(10)	83

[1] Literature values for Resovist relaxivities at 1.5 T: r_1 = 7.4 L·mol⁻¹·s⁻¹ and r_2 = 95 [1], or r_1 = 8.7 L·mol⁻¹·s⁻¹ and r_2 = 61 L·mol⁻¹·s⁻¹ [62]. [2] Size distribution values for Resovist from [1,29]. Note that the uncertainty of a r_1 or r_2 value is denoted in brackets, e.g., 11.6(9) L·mol⁻¹·s⁻¹ is short-hand notation for 11.6 ± 0.9 L·mol⁻¹·s⁻¹.

The relaxation rates $R_1 = 1/T_1$ and $R_2 = 1/T_2$ as a function of iron concentration c(Fe) measured at $B_0 = 1.5$ T are shown in Figure 5 for as-synthesized, centrifuged, and BSA-coated MNP. We obtained relaxivities of $r_1 = 11.6(9)$ and $r_2 = 482(8)$ L mol^{-1} s^{-1}, for as-synthesized MNP, $r_1 = 13.6(6)$ and $r_2 = 620(7)$ L mol^{-1} s^{-1} for centrifuged MNP, and $r_1 = 6.4(1)$ and $r_2 = 600(1)$ L mol^{-1} s^{-1} for BSA-coated MNP, indicating their high capability as negative contrast agents. For the MRI liver contrast agent Resovist, values of $r_1 = 7.4$ and $r_2 = 95$ L mol^{-1} s^{-1} are reported in literature at the same field $B_0 = 1.5$ T [1,62]. The r_2 relaxivity is about six times higher than Resovist. Additionally, the high ratio between transversal and longitudinal relaxivities r_2/r_1 indicates the efficiency of a T_2 as contrast agent. Hence, the coated MNP can be considered an alternative to Resovist with even better MR imaging performance.

Interestingly, we observe a higher relaxivity for BSA-coated particles, which at first argues against classical theory, since the diffusing hydrogen protons are shielded from the magnetic core. However, there is the possibility that the BSA shell prolongs the residence time of the hydrogen protons near the magnetic core, thereby leading to a higher relaxivity. Monte Carlo simulations contribute to the understanding of the relationship between layer thickness and changes in relaxivity [63].

To summarize, the comprehensive characterization of BSA-coated MNP indicates their competitive high performance in MRI and MPI (Table 1). Compared to commercial systems, our BSA-coated MNP surpass Resovist in both imaging modalities. The r_2 relaxivity is about six times higher than Resovist. MPI signal amplitude A_3* reaches that of SHP-30, a well-defined, commercial single-core MNP system manufactured by thermal decomposition and modified after phase transfer with an amphiphilic polymer.

2.3 Stability in Physiological Environment

Preserving the MNP stability in physiological systems is a key requirement for their in vivo clinical applicability [64]. Unprotected MNP exposed to serum proteins or isotonic salt concentrations will form aggregates and agglomerates with potential

severe consequences for the biological system. Additionally, salt-induced agglomeration might affect the magnetic properties of MNP and thereby lower the diagnostic information of magnetic imaging modalities.

In this section, we incubate BSA-coated MNP as well as as-synthesized MNP (tannic acid coating) at three different saline concentrations, *c*(NaCl) = 0.05, 0.10, and 0.15 mol/L, to evaluate the stability of MNP after short- (2 h) as well as long-term (1 day, 1 week) incubation time. Colloidal stability changes impacting the hydrodynamic size distribution and aggregation were analyzed by DCS, while changes in magnetic properties were deducted from MPS measurements.

The BSA-coated MNP remained highly stable over the complete observation time even at the highest saline concentration, *c* (NaCl) = 0.15 mol/L (Figure 6), without any noticeable aggregation visible in DCS. In contrast, the as-synthesized MNP without BSA-coating showed a slight increase in hydrodynamic diameter already at the lowest saline concentration (*c*(NaCl) = 0.05 mol/L) and rapid aggregation at higher saline concentration (*c*(NaCl) = 0.10 and 0.15 mol/L) independent of incubation time. As shown in Figure 7, visual inspection by eye after one-week saline incubation revealed strong precipitation of the as-synthesized MNP, while the BSA-coated MNP appeared as a stable colloidal suspension.

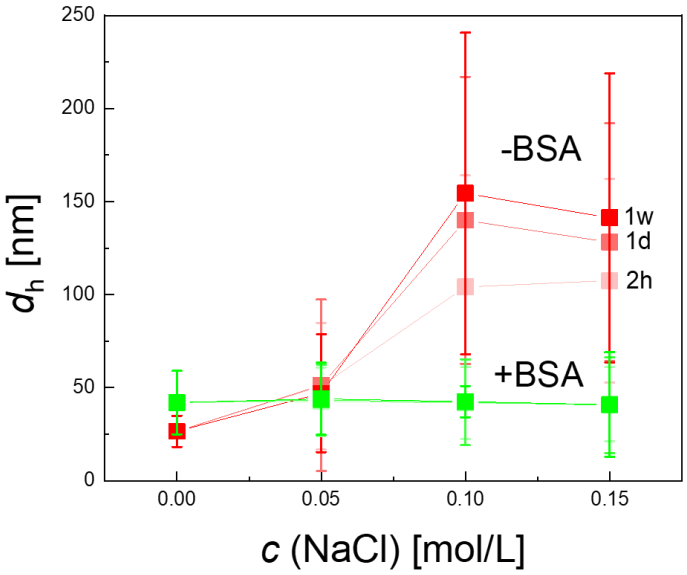

Figure 6. Colloidal stability of MNP. The hydrodynamic diameter as function of saline concentration (c(NaCl) = 0.05, 0.10, 0.15 Mol/L) measured by DCS 2 h (2 h), 1 day (1 d), and 1 week (1 w) after incubation. Notably, for BSA-coated MNP (green symbols), all three curves coincide within symbol thickness, proving that the hydrodynamic diameters d_h of BSA-coated MNP remain unchanged (<1%). For BSA-coated MNP (red symbols), d_h is already significantly increased at the lowest saline concentration. The full-width-at-half-maximum (FWHM) of the size distribution is displayed as uncertainty bars. The lines between the symbols are reading aids.

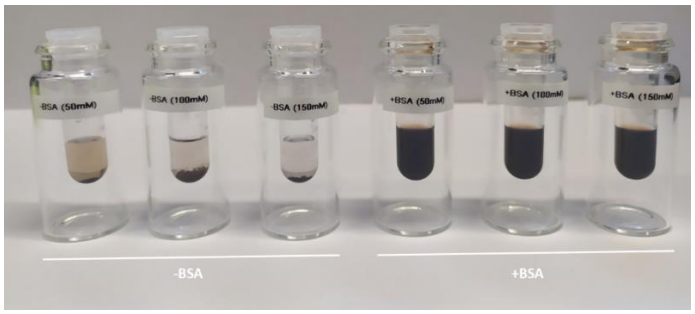

Figure 7. Visualization of colloidal stability of MNP at different saline concentrations. MNP without BSA-coating (left) and with BSA-coating. The photograph was taken one week after saline incubation at c (NaCl) = 0.05, 0.10, and 0.15 mol/L. While the uncoated MNP are almost entirely precipitated at the vial bottom, the BSA-coated MNP visually show a homogenous dispersion with no aggregation tendency.

As shown in Figure 8, MPS measurements confirm the results obtained from DCS measurements. The specific MPS amplitude of the MNP without BSA decreases from A_3* = 33.9 to 24.4 Am²/km (Fe) already at the lowest saline concentration c (NaCl) = 0.05 mol/L, and almost a complete loss of signal can be observed at higher saline concentrations c (NaCl) = 0.10, 0.15 mol/L, independently of the incubation time (see Figure 8a). Modification of MNP by BSA-coating preserved the magnetic signal

properties. The A_3* value remained constant at c(NaCl) = 0.05 and 0.10 mol/L and showed a slight decrease from A_3* =26 Am²/kg(Fe) to 22.4 Am²/kg(Fe) at c(NaCl) = 0.15 mol/L. The A_5/A_3 ratio shown in Figure 8b of BSA-coated MNP remained constant at a high level, exceeding 35% for all saline concentrations independent of incubation time. These high values indicate the high spatial resolution of the MNP and hence a high image quality in MPI. The uncoated MNP showed a significant reduction of the ratio A_5/A_3 for the lower saline concentrations, slightly increasing again at c(NaCl) = 0.15 mol/L. Notably, A_5/A_3 is independent of the number of MNP in the sample, and due to the very low A_3* values of the uncoated MNP in a saline environment, this behavior is attributed to the magnetic response of a very small fraction of MNP (below 5% as estimated from the A_3* drop) that are not completely aggregated or agglomerated and emphasizes the high sensitivity of MPS. Based on these promising results, an investigation of the behavior of BSA-coated MNP in different other physiological media such as plasma, full blood, or even living cells will follow soon.

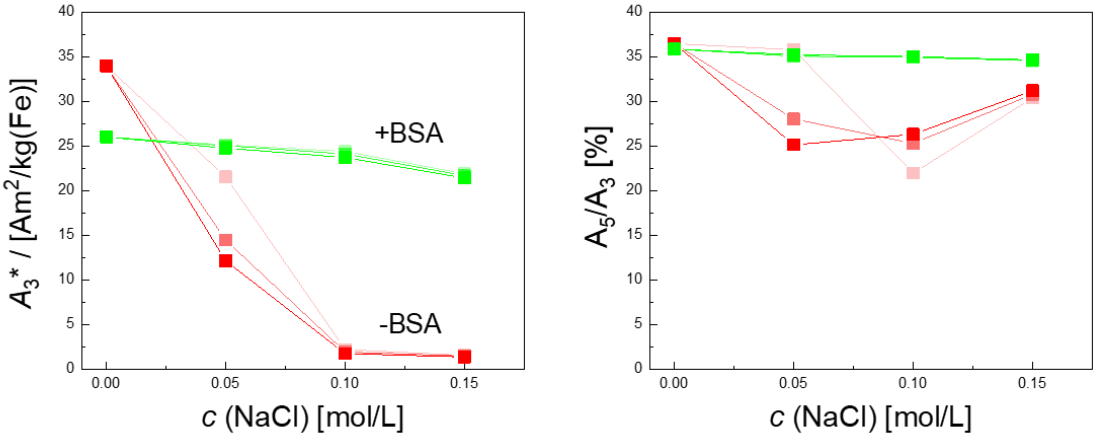

(a) (b)

Figure 8. Colloidal stability of MNP in NaCl solution after different incubation times as measured by MPS. MPS parameter A_3* (**a**) of uncoated (red symbols) and BSA-coated MNP (green symbols) at different NaCl concentrations after 2 h, 1 day, and 1 week of incubation (symbols from bright to dark with increasing time). Nearly no changes (less than 10%) of the specific MPS amplitude A_3* were observed in the BSA-coated MNP, indicating colloidal stability up to physiological saline concentrations of 0.15 mol/L. By contrast, the uncoated MNP show a strongly reduced stability visible in the strong A_3* reduction at NaCl concentrations below 0.10 mol/L. As for A_3*, the corresponding parameter A_5/A_3 (**b**) remains unchanged up to physiological NaCl concentration for BSA-coated MNP, while for uncoated MNP, a reduction in the parameter is visible. Since A_5/A_3 is concentration-independent, only a very small fraction (below 5% as estimated from the A_3* drop) of not completely aggregated MNP are contributing to A_5/A_3.

With their physicochemical and magnetic properties, continuously synthesized BSA-coated MNP in aqueous phase offer a superior alternative as tracers for MRI and MPI compared to MNP prepared by other synthetic routes. Small and ultrasmall MNP are suboptimal candidates for MPI. Increasing the core size often leads to increasing magnetic particle–particle interactions with resulting aggregation. Hence, stabilizing the MNP with a suitable coating is crucial to shield these interactions. Choosing the coating material is significant as well. Here, not only the steric stabilization but also the behavior in the physiological environment has to be considered. Pegylation, the attachment of polyethylene glycol (PEG) on the particle surface, is common practice to improve the colloidal stability of nanoparticles in biomedical applications. Kandahar et al. investigated the functionalization of 25 nm single-core MNP with PEG in a time-consuming multi-step process after phase transfer to enhance blood circulation [42]. However, it is frequently reported that PEG can lead to pseudo allergic reactions in clinical applications and can provoke IgE-mediated reactions and recurrent anaphylaxis [65,66]. Chanan-Khan et al. found a direct relation between complement activation and immediate hypersensitivity reactions after initial Doxil® (PEGylated liposomal doxorubicin) dose [67]. Albumin is a safe and very efficient coating approach displaying generally high tolerability. It provides MNP protection from agglomeration mediated by blood constituents such as blood cells, proteins, and high salt concentrations. At the same time, protein coating on the MNP surface can prevent harmful effects of reactive oxygen species [38]. Moreover, the capability to add specific ligands to the functional amino or carboxy groups of the protein empowers BSA-coated MNP for further diagnostic and therapeutic medical applications.

3. Materials and Methods

3.1 Micromixer Synthesis

Iron oxide nanoparticles were produced continuously using micromixer set-up by precipitation of alkaline solutions of iron chloride in an aqueous medium, as previously reported in [32]. Briefly, solutions of iron chloride, sodium nitrate, and sodium hydroxide (all reagents were used without further purification, purity grade

98%, Sigma Aldrich, Darmstadt, Germany) were mixed in a caterpillar micromixer (Fraunhofer IMM, Mainz, Germany) with symmetric liquid ratios and piped in a 55 °C reaction loop with a residence time of 4 min. Tannic acid (1.7 kDa, Fluka, Schwerte, Germany) was added as a stabilizing agent. MNP were purified by removing unreacted educts and accessing the stabilizing agent via magnetic separation.

Additional centrifugation of 50 mL of MNP dispersion filled falcon tubes at 3300 revolutions per minute (g-force = 2118 relative centrifugal force) for 15 min was used to remove aggregates and superstructure. The pellet was discarded, and the supernatant was taken for further surface modification. The iron concentration *c*(Fe) of the sample was determined photospectroscopically using the phenanthroline protocol (see Section 3.3 below).

3.2 Bovine Serum Albumin Coating (BSA-Coating)

Finally, MNP were modified with a protein coating through incubation with 10 mg/mL BSA (Sigma Aldrich, Darmstadt, Germany) in a 50 mM, Ph ≈ 8.5, sodium bicarbonate buffer (Sigma Aldrich, Darmstadt, Germany) at 60 °C for 12 h. The sample was purified by magnetic separation with a LS-column (Miltenyi Biotec, Bergisch-Gladbach, Germany). After passing through the column, the BSA-coated MNP were washed five times with 3 mL sodium bicarbonate buffer to remove excess BSA in the sample and eluted in a 3 mL sodium bicarbonate buffer.

To assess the colloidal stability, NaCl solution at three different saline concentrations

(*c* (NaCl) = 0.05, 0.10, and 0.15 mol/L) was added to the centrifuged and BSA-coated MNP, and the resulting changes in hydrodynamic diameter were analyzed by DCS and magnetically by MPS measurements.

3.3 *Physicochemical Characterization*

3.3.1 Transmission Electron Microscopy (TEM)

Core size and shape were obtained by TEM measurements. Samples were prepared by placing a drop of the sample on a carboncoated copper grid and left at room

temperature to evaporate after applying a magnetic field for a short period of time (10 min) to accumulate the MNP. A Zeiss Libra 120 electron microscope (Zeiss, Oberkochen, Germany) at 120 kV acceleration voltage was used to perform the measurement. The images were taken by a CCD camera. The obtained images were evaluated using the open-source software ImageJ

(National Institutes of Health, Bethesda, MD, USA) to calculate the mean diameter and standard deviation of the individual nanoparticles (N > 10,000).

3.3.2 Differential Centrifugal Sedimentation (DCS)

DCS (or analytical ultracentrifugation) offers detailed information on the dispersion properties of MNP in colloidal systems. In a DCS measurement, sedimentation properties of the particle are measured according to the hydrodynamic particle size distribution [68]; the different size fractions can be differently accelerated in a gravitational field, leading to better fractionalization. Dynamic light scattering (DLS), the standard method to determine the hydrodynamic diameter, gave no results, since the absorption of the nanoparticles with the relatively large core and only a thin tannic acid coating layer was too strong (in contrast to other polymeric coatings such as PEG or dextran that scatter the excitation light well).

Thus, no reliable correlation of the fluctuation of the particles could be detected, and size determination with light scattering was not reliably feasible. However, analytical centrifugation is a well-established method to determine size and size distributions, particularly for samples with larger densities such as iron oxide, and also to sensitively display different fractions of polymodal samples. Hence, agglomerated and single-core particles will be accurately detected compared to DLS. Since the density influences MNP sedimentation, a mean density of core (magnetite) and shell material (BSA-coating) of the MNP was taken into account to determine the hydrodynamic diameter by DCS. For BSA, we used a BSA densi-ty of ϱ = 1.41 g/cm^3 [69] and a hydrodynamic radius of $d_{h,BSA}$ = 4 nm. Assuming a monolayer BSA-coating of 8 nm

thickness, an MNP core size of d_c = 28 nm, and a magnetite density ϱ_{Fe3O4} = 5.2 g/cm^3, a mean density $\varrho_{BSA\text{-}MNP}$ = 2.45 g/cm^3 for BSAcoated MNP was calculated. DCS measurements (CPS Instruments Inc. Measurements, Darmstadt, Germany) were carried out at 20,000 rpm (=21,504 relative centrifugal force) after calibration with a silicon dioxide (SiO_2) standard (255 nm). Sucrose gradient was built up using 24% to 8% sucrose. Peak maximum and full width at half maximum (FWHM) were evaluated using Origin® software (ADDI-TIVE Soft- und Hardware für Technik und Wissenschaft GmbH, Friedrichsdorf, Germany).

3.3.3 Zeta Potential Measurements

Zeta potentials in aqueous dispersion were derived from electrophoretic mobility measurements using a Litesizer 500 (Anton Paar GmbH, Ostfildern, Germany). The measurements were carried out in an Anton Paar Omega cuvette at a temperature of 20 °C (temperature equilibration time 30 s). Automatic mode was used for conducting the measurements (automatically chosen parameters: runs processed: 100, adjusted voltage: 200 V). For data evaluation, the Smoluchowski approximation (Henry factor: 1.5) was chosen.

3.3.4 Agarose Gel Electrophoresis

Agarose gel electrophoresis was used to investigate the presence of protein on the surface of the MNP; 1% agarose gel (Carl Roth, Karlsruhe, Germany) was prepared by melting 1 g in 100 mL of 10 mM borat buffer (Sigma Aldrich, Darmstadt, Germany) (pH = 8.3). The mixture was heated using a microwave in intervals of 30 s until the agarose completely dissolved. The gel was poured into a mold with a comb and left for two hours to cool down to room temperature. The agarose gel was placed in an electrophoresis apparatus and a buffer was added to cover the gel. A total of 20 µL of the samples was mixed with 5 µL OrangeG dye (Carl Roth, Karlsruhe, Germany). A

total of 20 µL of the mixture was then added to the gel. The power supply of the apparatus was turned on at 290 V and ran for 30 min.

3.3.5 Photospectroscopical Determination of Iron Concentration c(Fe)

The iron concentration *c*(Fe) of the nanoparticle samples was determined photospectroscopically using the phenanthroline protocol [70]. A total of 10 µL of nanoparticles was dissolved in 20 µL hydrochloric acid (37%). After complete dissolution, 470 µL of H_2O was added. A total of 100 µL hydroxylamine hydrochloride (10%) and 700 µL 1,10 phenanthrolinehydrochloride (0.1%) were added to 200 µL of this solution. After a reaction time of 15 min, the absorbance of the formed ferroin complexes was measured by UV-Vis spectrometer (Cary 50, Varian, Palo Alto, CA, USA) at a wavelength of 510 nm, and the iron concentrations were calculated using an iron standard calibration curve (Iron (II,III) Oxid (Sigma Aldrich, Darmstadt, Germany) as standard in the range *c*(Fe) = 1.25 to 40 mM).

3.4 Magnetic Characterization

3.4.1 Magnetic Particle Spectroscopy (MPS)

MPS measurements of single nanoparticle samples were performed using a commercial magnetic particle spectrometer (MPS-3, Bruker, Ettlingen, Germany) operating at an amplitude B_{ex} = 25 mT and a frequency f_0 = 25 kHz. MPS detects the non-linear dynamic magnetic response of MNP exposed to an alternating magnetic field from which their MPI performance can be assessed. Originally, MPS was developed to assess the performance of MNP tracer materials in MPI. However, here, we use MPS to quantitatively reveal changes in the dynamic magnetic behavior of MNP mediated by the direct environment of the MNP, e.g., as a consequence of surface modification by BSA-coating or physiological conditions as different saline concentrations.

For MPS measurement, a fast reaction tube (Applied Biosystems®, MicroAmp, Thermo Fisher Scientific, Schwerte, Germany) containing a sample volume of 30 µL

was placed in the detection coil of the MPS system. The induced magnetization could be measured simultaneously by the coils. By Fourier transform of the detected time signal, the spectral components of an MPS measurement were obtained, showing distinctive amplitudes at odd multiples (harmonics) of the excitation frequency f_0. We used two characteristic parameters of the MPS harmonic spectra, the amplitude of the third harmonic normalized to the iron amount of the sample, A_3*, and the concentration-independent ratio between the 5th and 3rd harmonic, A_5/A_3. Both values are correlated to the MPI performance, with the general observation that the higher the A_3* and A_5/A_3, the better the MPI images. The specific signal amplitude A_3* indicates the sensitivity of the MNP to give a dynamic magnetization response at the chosen excitation frequency f_0 per unit amount of iron, and the ratio A_5/A_3 is used to describe the shape of the harmonic spectrum to assess the resolution capacity.

Two commercial MNP systems were considered as references with high MPS performance. For the MRI liver contrast agent Resovist (Meito Sanyo, Japan), we used the literature values A_3* = 8.7 Am²/kg (Fe) and A_5/A_3 = 38.4% [71]. Furthermore, carboxyl iron oxide MNP with 30 nm core diameter (SHP-30-10, Ocean NanoTech, US) measured by MPS at Bex 25 mT resulted in A_3* = 32.8 Am²/kg (Fe) and A_5/A_3 = 22.2%.

To analyze the colloidal stability of MNP at different saline concentrations by MPS, 10 µL aliquots of as-synthesized, centrifuged, and BSA-coated MNP incubated with a final concentration of c (NaCl) = 0.05, 0.10, and 0.15 mol/L were taken after 2 h, 1 day, and 1 week. The MPS measurements were carried out at B_{ex} = 25 mT and T = 37 °C.

3.4.2 NMR Relaxivities r_1 and r_2

MRI imaging properties were investigated by measuring longitudinal T_1 and transversal T_2 proton relaxation times for an MNP sample of 200 µL volume diluted to different iron concentrations c(Fe). The relaxation time measurements were carried out on a Minispec mq60 relaxometer (Bruker, Ettlingen, Germany) at T = 37°C and a magnetic field of 1.5 T (60 MHz proton resoncane frequency). For T_1, a 2-pulse

inversion-recovery sequence with a fixed relaxation delay of at least 5 T_1 was used, T_2 was determined employing a Carr–Purcell–Meiboom–Gill sequence, which consists of a 90° pulse followed by a series of 180° pulses, ideally covering the full decay of the signal.

From the graphs of the iron-concentration c(Fe)-dependent relaxation times $R_1 = 1/T_1$ and $R_2 = 1/T_2$, the corresponding relaxivities r_1 and r_2 (in units of L·mmol^{-1}·s^{-1}) were determined:

$$\frac{1}{T_i} = \frac{1}{T_{i,H_2O}} + r_i\, c(\mathrm{Fe}), \qquad i = 1,2 \tag{1}$$

For graphical presentation, the measured relaxation rates of pure water samples have been subtracted ($R_{1,H2O}$ = 0.25952 s^{-1} and $R_{2,H2O}$ = 0.29 s^{-1}).

3.4.3. Linear Dynamic Susceptibility Measurements (ACS)

Room temperature (T = 295 K) linear magnetic AC susceptibility (ACS) of MNP was measured with a commercial AC susceptometer (DynoMag, RISE Acreo, Gothenburg, Sweden). For the measurements, a sample volume of 200 µL MNP suspension was filled into a quartz glass cuvette, and the real $\chi'(f)$ and imaginary $\chi''(f)$ magnetic susceptibility were acquired in the frequency range 1 Hz to 100 kHz at an excitation amplitude of 0.2 mT.

The initial mass susceptibility χ_0 (in units m^3/kg (Fe), normalized to the sample iron mass) was obtained by extrapolation of the real part susceptibility $\chi'(f)^{|f\to 0}$.

4. Conclusions

Surface modification was performed to optimize the stability and performance of continuously manufactured MNP for molecular imaging applications such as MPI and MRI in a physiological environment. Protein coating of electrostatically stabilized nanoparticles with BSA led to a significant improvement in dispersion stability in the presence of an increasing concentration of NaCl solution. No drop in signal amplitude and constant A_5/A_3 values prove the good performance of the MNP as MPI contract agents. Additionally, r_1 and r_2 values are promising to apply MNP as MRI contrast

agents. Since Resovist was withdrawn from the market, our MNP are promising candidates to further accelerate the research on MPI and MRI molecular imaging.

Even after 40 years of MRI contrast agent developments for clinical use (the first MRI contrast agent, introduced in 1981, was ferric chloride), newer and safer MRI agents capable of specifically targeting organs, sites of inflammation, and tumors are still demanded. The presented micromixer technique to synthesize MNP-based contrast agents with tailored magnetic properties provides a major contribution to future developments.

The same applies to MPI being under development for medical imaging of the cardiovascular system, for oncology or for stem cell tracking, where the structural, magnetic, and surface properties of the MNP are of utmost importance and need further optimization. With its excellent control of particle size, crystal growth, and scalability, the micromixer technique in combination with additional surface modification can also foster the further development of high-performing tracer materials for this promising imaging modality.

Author Contributions: A.B. performed synthesis and physiochemical characterization of the samples; A.R. and N.L. carried out magnetic characterization. A.B., N.L., R.B. and F.W. wrote the manuscript. R.B. and F.W. reviewed and edited the manuscript. Work was supervised by R.B. (synthesis, characterization) and F.W. (magnetic measurements); project administration, R.B. and F.W.; funding acquisition, R.B. and F.W. All authors have read and agreed to the published version of the manuscript.

Funding: This research was funded Deutsche Forschungsgemeinschaft (DFG) within the research grants "Core Facility: Metrology of Ultra-Low Magnetic Fields", grant numbers KO 5321/3 and TR 408/11" and the collaborative research center "Matrix in Vision" (SFB 1340/1 2018, No 372486779, projects A02). Financial support by the German Federal Ministry of Education and Research (BMBF), grant number 13XP5113, is gratefully acknowledged. A.B. thanks the *Friedrich Ebert Stiftung* for a PhD fellowship supporting his work related to this project. R.B. thanks the Fraunhofer-Gesellschaft for the sup-port within the Fraunhofer TALENTA program. This work was furthermore supported in the framework of the Fraunhofer Lighthouse Project QMag.

Institutional Review Board Statement: Not applicable.

Informed Consent Statement: Not applicable.

Data Availability Statement: Data is contained within the article.

Acknowledgments: Many thanks to Helen Onyema for proof reading of the manuscript.

Conflicts of Interest: The authors declare no conflict of interest.

References

1. Modo, M.M.J.; Bulte, J.W.M.; Kim, E.E. Molecular and Cellular MR Imaging. J. Nucl. Med. 2007, 48, 2087.
2. Massoud, T.F.; Gambhir, S.S. Molecular imaging in living subjects: Seeing fundamental biological processes in a new light. Genes Dev. 2003, 17, 545–580.
3. Zhang, X.; Cherry, S.R.; Xie, Z.; Shi, H.; Badawi, R.D.; Qi, J. Subsecond total-body imaging using ultrasensitive positron emission tomography. Proc. Natl. Acad. Sci. USA 2020, 117, 2265–2267.
4. Church, T.R.; Black,W.C.; Aberle, D.R.; Berg, C.D.; Clingan, K.L.; Duan, F.; Fagerstrom, R.M.; Gareen, I.F.; Gierada, D.S.; Jones, G.C.; et al. Results of initial low-dose computed tomographic screening for lung cancer. N. Engl. J. Med. 2013, 368, 1980–1991.
5. Rosenthal, M.S.; Cullom, J.; Hawkins, W.; Moore, S.C.; Tsui, B.M.W.; Yester, M. Quantita-tive SPECT Imaging: A Review and Recommendations by the Focus Committee of the Socie-ty of Nuclear Medicine Computer and Instrumentation Council. M.S. J. Nucl. Med. 1995, 36, 1489–1513.
6. Sharifi, S.; Seyednejad, H.; Laurent, S.; Atyabi, F.; Saei, A.A.; Mahmoudi, M. Superparamagnetic iron oxide nanoparticles for in vivo molecular and cellular imaging. Contrast Media Mol. Imaging 2015, 10, 329–355.
7. Weissleder, R. Molecular imaging in cancer. Science 2006, 312, 1168–1171.
8. Yurt, A.; Kazancı, N. Investigation of magnetic properties of various complexes prepared as contrast agents for MRI. J. Mol. Struct. 2008, 892, 392–397.
9. Shokrollahi, H. Contrast agents for MRI. Mater. Sci. Eng. C Mater. Biol. Appl. 2013, 33, 4485–4497.
10. Salehipour, M.; Rezaei, S.; Mosafer, J.; Pakdin-Parizi, Z.; Motaharian, A.; Mogharabi-Manzari, M. Recent advances in polymercoated iron oxide

nanoparticles as magnetic resonance imaging contrast agents. J. Nanopart. Res. 2021, 23, 1467.

11. Billotey, C.; Wilhelm, C.; Devaud, M.; Bacri, J.C.; Bittoun, J.; Gazeau, F. Cell internalization of anionic maghemite nanoparticles: Quantitative effect on magnetic resonance imaging. Magn. Reson. Med. 2003, 49, 646–654.

12. Reimer, P.; Balzer, T. Ferucarbotran (Resovist): A new clinically approved RES-specific contrast agent for contrast-enhanced MRI of the liver: Properties, clinical development, and applications. Eur. Radiol. 2003, 13, 1266–1276.

13. Wang, Y.-X.J. Superparamagnetic iron oxide based MRI contrast agents: Current status of clinical application. Quant. Imaging Med. Surg. 2011, 1, 35–40.

14. Shah, A.; Dobrovolskaia, M.A. Immunological effects of iron oxide nanoparticles and iron-based complex drug formulations: Therapeutic benefits, toxicity, mechanistic insights, and translational considerations. Nanomedicine 2018, 14, 977–990.

15. Tietze, R.; Alexiou, C. Improving cancer imaging with magnetic nanoparticles: Where are we now? Nanomedicine 2017, 12, 167–170.

16. Li, F.; Liang, Z.; Liu, J.; Sun, J.; Hu, X.; Zhao, M.; Liu, J.; Bai, R.; Kim, D.; Sun, X.; et al. Dynamically Reversible Iron Oxide Nanoparticle Assemblies for Targeted Amplification of T1-Weighted Magnetic Resonance Imaging of Tumors. Nano Lett. 2019, 19, 4213–4220.

17. Li, P.; Chevallier, P.; Ramrup, P.; Biswas, D.; Vuckovich, D.; Fortin, M.-A.; Oh, J.K. Mussel-Inspired Multidentate Block Copolymer to Stabilize Ultrasmall Superparamagnetic Fe3O4 for Magnetic Resonance Imaging Contrast Enhancement and Excellent Colloidal Stability. Chem. Mater. 2015, 27, 7100–7109.

18. Shen, Z.; Chen, T.; Ma, X.; Ren, W.; Zhou, Z.; Zhu, G.; Zhang, A.; Liu, Y.; Song, J.; Li, Z.; et al. Multifunctional Theranostic Nanoparticles Based on Exceedingly

Small Magnetic Iron Oxide Nanoparticles for T1-Weighted Magnetic Resonance Imaging and Chemotherapy. ACS Nano 2017, 11, 10992–11004.

19. Vangijzegem, T.; Stanicki, D.; Panepinto, A.; Socoliuc, V.; Vekas, L.; Muller, R.N.; Laurent, S. Influence of Experimental Parameters of a Continuous Flow Process on the Properties of Very Small Iron Oxide Nanoparticles (VSION) Designed for T1-Weighted Magnetic Resonance Imaging (MRI). Nanomaterials 2020, 10, 757.

20. Gleich, B.; Weizenecker, J. Tomographic imaging using the nonlinear response of magnetic particles. Nature 2005, 435, 1214–1217.

21. Bakenecker, A.C.; Ahlborg, M.; Debbeler, C.; Kaethner, C.; Buzug, T.M.; Lüdtke-Buzug, K. Magnetic particle imaging in vascular medicine. Innov. Surg. Sci. 2018, 3, 179–192.

22. Yu, E.Y.; Bishop, M.; Zheng, B.; Ferguson, R.M.; Khandhar, A.P.; Kemp, S.J.; Krishnan, K.M.; Goodwill, P.W.; Conolly, S.M. Magnetic Particle Imaging: A Novel In Vivo Imaging Platform for Cancer Detection. Nano Lett. 2017, 17, 1648–1654.

23. Kaul, M.G.; Weber, O.; Heinen, U.; Reitmeier, A.; Mummert, T.; Jung, C.; Raabe, N.; Knopp, T.; Ittrich, H.; Adam, G. Combined Preclinical Magnetic Particle Imaging and Mag-netic Resonance Imaging: Initial Results in Mice. Rofo: Fortschritte auf dem Gebiete der Rontgenstrahlen und der Nuklearmedizin 2015, 187, 347–352

24. Franke, J.; Heinen, U.; Lehr, H.; Weber, A.; Jaspard, F.; Ruhm, W.; Heidenreich, M.; Schulz, V. System Characterization of a Highly Integrated Preclinical Hybrid MPI-MRI Scanner. IEEE Trans. Med. Imaging 2016, 35, 1993–2004.

25. Bleul, R.; Baki, A.; Freese, C.; Paysen, H.; Kosch, O.; Wiekhorst, F. Continuously manufactured single-core iron oxide nanoparticles for cancer theranostics as valuable contribution in translational research. Nanoscale Adv. 2020, 2, 4510–4521.

26. Hergt, R.; Dutz, S.; Röder, M. Effects of size distribution on hysteresis losses of magnetic nanoparticles for hyperthermia. J. Phys. Condens. Matter 2008, 20, 385214.

27. Laurent, S.; Saei, A.A.; Behzadi, S.; Panahifar, A.; Mahmoudi, M. Superparamagnetic iron oxide nanoparticles for delivery of therapeutic agents: Opportunities and challenges. Expert Opin. Drug Deliv. 2014, 11, 1449–1470.

28. Hufschmid, R.; Arami, H.; Ferguson, R.M.; Gonzales, M.; Teeman, E.; Brush, L.N.; Browning, N.D.; Krishnan, K.M. Synthesis of phase-pure and monodisperse iron oxide nanoparticles by thermal decomposition. Nanoscale 2015, 7, 11142–11154.

29. Heinke, D.; Kraupner, A.; Eberbeck, D.; Schmidt, D.; Radon, P.; Uebe, R.; Schüler, D.; Briel, A. MPS and MRI efficacy of magnetosomes from wild-type and mutant bacterial strains. Int. J. Magn. Part. Imaging 2017, 3, 1706004.

30. Rosenfeldt, S.; Mickoleit, F.; Jörke, C.; Clement, J.H.; Markert, S.; Jérôme, V.; Schwarzinger, S.; Freitag, R.; Schüler, D.; Uebe, R.; et al. Towards standardized purification of bacterial magnetic nanoparticles for future in vivo applications. Acta Biomater. 2021,120, 293–303.

31. Orlando, T.; Mannucci, S.; Fantechi, E.; Conti, G.; Tambalo, S.; Busato, A.; Innocenti, C.; Ghin, L.; Bassi, R.; Arosio, P.; et al. Characterization of magnetic nanoparticles from Magne-tospirillum Gryphiswaldense as potential theranostics tools. Contrast Media Mol. Imaging 2016, 11, 139–145.

32. Baki, A.; Löwa, N.; Remmo, A.; Wiekhorst, F.; Bleul, R. Micromixer Synthesis Platform for a Tuneable Production of Magnetic Single-Core Iron Oxide Nanoparticles. Nanomaterials 2020, 10, 1845.

33. Baki, A.; Löwa, N.; Thiermann, R.; Bantz, C.; Maskos, M.; Wiekhorst, F.; Bleul, R. Continuous synthesis of single core iron oxide nanoparticles for MPI tracer development. Int. J. Magn. Part. Imaging 2017, 3, 1703004.

34. Safronov, A.P.; Beketov, I.V.; Komogortsev, S.V.; Kurlyandskaya, G.V.; Medvedev, A.I.; Leiman, D.V.; Larrañaga, A.; Bhagat, S.M. Spherical magnetic nanoparticles fabricated by laser target evaporation. AIP Adv. 2013, 3, 52135.

35. Coricovac, D.-E.; Moacă, E.-A.; Pinzaru, I.; Cîtu, C.; Soica, C.; Mihali, C.-V.; Păcurariu, C.; Tutelyan, V.A.; Tsatsakis, A.; Dehelean, C.-A. Biocompatible Colloidal Suspensions Based on Magnetic Iron Oxide Nanoparticles: Synthesis, Characterization and Toxicological Profile. Front. Pharmacol. 2017, 8, 154.

36. Paunovic, J.; Vucevic, D.; Radosavljevic, T.; Mandic´-Rajc˘evic´, S.; Pantic, I. Iron-based nano-particles and their potential toxicity: Focus on oxidative stress and apoptosis. Chem.-Biol. In-teract. 2020, 316, 108935.

37. Patil, R.M.; Thorat, N.D.; Shete, P.B.; Bedge, P.A.; Gavde, S.; Joshi, M.G.; Tofail, S.A.M.; Bohara, R.A. Comprehensive cytotoxicity studies of superparamagnetic iron oxide nanoparticles. Biochem. Biophys. Rep. 2018, 13, 63–72.

38. Abakumov, M.A.; Semkina, A.S.; Skorikov, A.S.; Vishnevskiy, D.A.; Ivanova, A.V.; Mironova, E.; Davydova, G.A.; Majouga, A.G.; Chekhonin, V.P. Toxicity of iron oxide nanoparticles: Size and coating effects. J. Biochem. Mol. Toxicol. 2018, 32, e22225.

39. Su, H.; Liu, Y.; Wang, D.; Wu, C.; Xia, C.; Gong, Q.; Song, B.; Ai, H. Amphiphilic starlike dextran wrapped superparamagnetic iron oxide nanoparticle clsuters as effective magnetic resonance imaging probes. Biomaterials 2013, 34, 1193–1203.

40. Liu, G.; Hong, R.Y.; Guo, L.; Li, Y.G.; Li, H.Z. Preparation, characterization and MRI applica-tion of carboxymethyl dextran coated magnetic nanoparticles. Appl. Surf. Sci. 2011, 257, 6711–6717.

41. Kim, D.K.; Zhang, Y.; Kehr, J.; Klason, T.; Bjelke, B.; Muhammed, M. Characterization and MRI study of surfactant-coated superparamagnetic nanoparticles administered into the rat brain. J. Magn. Magn. Mater. 2001, 225, 256–261.

42. Khandhar, A.P.; Keselman, P.; Kemp, S.J.; Ferguson, R.M.; Goodwill, P.W.; Conolly, S.M.; Krishnan, K.M. Evaluation of PEG-coated iron oxide nanoparticles as blood pool tracers for preclinical magnetic particle imaging. Nanoscale 2017, 9, 1299–1306.

43. Chee, H.L.; Gan, C.R.R.; Ng, M.; Low, L.; Fernig, D.G.; Bhakoo, K.K.; Paramelle, D. Biocompatible Peptide-Coated Ultrasmall Superparamagnetic Iron Oxide Nanoparticles for In Vivo Contrast-Enhanced Magnetic Resonance Imaging. ACS Nano 2018, 12, 6480–6491.

44. Hankins, J. The role of albumin in fluid and electrolyte balance. J. Infus. Nurs. 2006, 29, 260–265.

45. Hirayama, K.; Akashi, S.; Furuya, M.; Fukuhara, K. Rapid confirmation and revision of the primary structure of bovine serum albumin by ESIMS and Frit-FAB LC/MS. Biochem. Biophys. Res. Commun. 1990, 173, 639–646.

46. Jameson, G.S.; Borazanci, E.; Babiker, H.M.; Poplin, E.; Niewiarowska, A.A.; Gordon, M.S.; Barrett, M.T.; Rosenthal, A.; StollD'Astice, A.; Crowley, J.; et al. Response Rate Following Albumin-Bound Paclitaxel Plus Gemcitabine Plus Cisplatin Treatment Among Patients with Advanced Pancreatic Cancer: A Phase 1b/2 Pilot Clinical Trial. JAMA Oncol. 2020, 6, 125–132.

47. Gianni, L.; Mansutti, M.; Anton, A.; Calvo, L.; Bisagni, G.; Bermejo, B.; Semiglazov, V.; Thill, M.; Chacon, J.I.; Chan, A.; et al. Comparing Neoadjuvant Nab-paclitaxel vs Paclitaxel Both Followed by Anthracycline Regimens in Women with ERBB2/HER2-Negative Breast Cancer—The Evaluating Treatment with Neoadjuvant Abraxane (ETNA) Trial: A Randomized Phase 3 Clinical Trial. JAMA Oncol. 2018, 4, 302–308.

48. Mesken, J.; Iltzsche, A.; Mulac, D.; Langer, K. Modifying plasmid-loaded HSA-nanoparticles with cell penetrating peptides— Cellular uptake and enhanced gene delivery. Int. J. Pharm. 2017, 522, 198–209.

49. Gou, Y.; Miao, D.; Zhou, M.; Wang, L.; Zhou, H.; Su, G. Bio-Inspired Protein-Based Nanoformulations for Cancer Theranostics. Front. Pharmacol. 2018, 9, 421.

50. Yu, S.-M.; Laromaine, A.; Roig, A. Enhanced stability of superparamagnetic iron oxide nanoparticles in biological media using a pH adjusted-BSA adsorption protocol. J. Nanopart Res. 2014, 16, 83.

51. Wang, Y.; Xu, C.; Chang, Y.; Zhao, L.; Zhang, K.; Zhao, Y.; Gao, F.; Gao, X. Ultrasmall Superparamagnetic Iron Oxide Nanoparticle for T2-Weighted Magnetic Resonance Imaging. ACS Appl. Mater. Interfaces 2017, 9, 28959–28966.

52. Tao, C.; Zheng, Q.; An, L.; He, M.; Lin, J.; Tian, Q.; Yang, S. T1-Weight Magnetic Resonance Imaging Performances of Iron Oxide Nanoparticles Modified with a Natural Protein Macro-molecule and an Artificial Macromolecule. Nanomaterials 2019, 9, 170.

53. Mikhaylova, M.; Kim, D.K.; Berry, C.C.; Zagorodni, A.; Toprak, M.; Curtis, A.S.G.; Mu-hammed, M. BSA Immobilization on Amine-Functionalized Superparamagnetic Iron Oxide Nanoparticles. Chem. Mater. 2004, 16, 2344–2354.

54. Kalidasan, V.; Liu, X.L.; Herng, T.S.; Yang, Y.; Ding, J. Bovine Serum Albumin-Conjugated Ferrimagnetic Iron Oxide Nanoparticles to Enhance the Biocompatibility and Magnetic Hyperthermia Performance. Nanomicro Lett. 2016, 8, 80–93.

55. Zhu, N.; Ji, H.; Yu, P.; Niu, J.; Farooq, M.U.; Akram, M.W.; Udego, I.O.; Li, H.; Niu, X. Surface Modification of Magnetic Iron Oxide Nanoparticles. Nanomaterials 2018, 8, 810.

56. Wu, Y.; Lu, Z.; Li, Y.; Yang, J.; Zhang, X. Surface Modification of Iron Oxide-Based Magnet-ic Nanoparticles for Cerebral Theranostics: Application and Prospection. Nanomaterials 2020, 10, 1441.

57. Tenzer, S.; Docter, D.; Kuharev, J.; Musyanovych, A.; Fetz, V.; Hecht, R.; Schlenk, F.; Fischer, D.; Kiouptsi, K.; Reinhardt, C.; et al. Rapid formation of plasma protein corona critically af-fects nanoparticle pathophysiology. Nat. Nanotechnol. 2013, 8, 772–781.

58. Pellegrino, T.; Sperling, R.A.; Alivisatos, A.P.; Parak, W.J. Gel electrophoresis of gold-DNA nanoconjugates. J. Biomed. Biotechnol. 2007, 2007, 26796.

59. Zeta Potential BSA. Available online: https://pssnicomp.com (accessed on 20 May 2021).

60. Ninan, N.; Forget, A.; Shastri, V.P.; Voelcker, N.H.; Blencowe, A. Antibacterial and Anti-Inflammatory pH-Responsive Tannic Acid-Carboxylated Agarose Composite Hydrogels for Wound Healing. ACS Appl. Mater. Interfaces 2016, 8, 28511–28521.

61. Teeman, E.; Shasha, C.; Evans, J.E.; Krishnan, K.M. Intracellular dynamics of superparamag-netic iron oxide nanoparticles for magnetic particle imaging. Nanoscale 2019, 11, 7771–7780.

62. Rohrer, M.; Bauer, H.; Mintorovitch, J.; Requardt, M.; Weinmann, H.J. Comparison of Mag-netic Properties of MRI Contrast Media Solutions at Different Magnetic Field Strengths. In-vestig. Radiol. 2005, 40, 715–724.

63. LaConte, L.E.W.; Nitin, N.; Zurkiya, O.; Caruntu, D.; O'Connor, C.J.; Hu, X.; Bao, G. Coating thickness of magnetic iron oxide nanoparticles affects R2 relaxivity. J. Magn. Reson. Imaging 2007, 26, 1634–1641.

64. Yan, M.; Yang, C.; Huang, B.; Huang, Z.; Huang, L.; Zhang, X.; Zhao, C. Systemic toxicity induced by aggregated layered double hydroxide nanoparticles. Int. J. Nanomed. 2017, 12, 7183–7195.

65. Stone, C.A.; Liu, Y.; Relling, M.V.; Krantz, M.S.; Pratt, A.L.; Abreo, A.; Hemler, J.A.; Phillips, E.J. Immediate Hypersensitivity to Polyethylene Glycols and

Polysorbates: More Common than We Have Recognized. J. Allergy Clin. Immunol. Pract. 2019, 7, 1533–1540e8.

66. Castells, M.C.; Phillips, E.J. Maintaining Safety with SARS-CoV-2 Vaccines. N. Engl. J. Med. 2021, 384, 643–649.

67. Chanan-Khan, A.; Szebeni, J.; Savay, S.; Liebes, L.; Rafique, N.M.; Alving, C.R.; Muggia, F.M. Complement activation following first exposure to pegylated liposomal doxorubicin (Doxil®): Possible role in hypersensitivity reactions. Ann. Oncol. 2003, 14, 1430–1437.

68. Walter, J.; Thajudeen, T.; Süß, S.; Segets, D.; Peukert, W. New possibilities of accurate particle characterisation by applying direct boundary models to analytical centrifugation. Nanoscale 2015, 7, 6574–6587.

69. Fischer, H.; Polikarpov, I.; Craievich, A.F. Average protein density is a molecular-weight-dependent function. Protein Sci. 2004, 13, 2825–2828.

70. Pyenson, H.; Tracy, P.H. A 1,10—Phenanthroline Method for the Determination of Iron in Powdered Milk. J. Dairy Sci. 1945, 28, 401–412.

71. Löwa, N.; Seidel, M.; Radon, P.; Wiekhorst, F. Magnetic nanoparticles in different biological environments analyzed by magnetic particle spectroscopy. J. Magn. Magn. Mater. 2017, 427, 133–138.

6 Conclusions and outlook

In this work the continuous micromixer synthesis was established to produce multifunctional magnetic nanoparticles with high potential for safe diagnosis and treatment of serious diseases. An example are the treatment methods of cancer, which normally are accompanied by severe side effects. Magnetic iron oxide nanoparticles have already been approved by the food and drug administration (FDA) to be used for diagnosis as contrast agents for MRI. One ultimate goal of utilizing MNP in nanomedicine is to create a safe, multifunctional, theranostic drug delivery system that is capable to target and to release a therapeutic cargo most suitably with online monitoring, so that the therapy can be adjusted individually. Additionally, a full understanding of the interaction of MNP with the surrounding environment such as blood stream, tissues and cells has to be achieved before successful clinical translation.

To meet these requirements, the micromixer synthesis for producing single core MNP in the diameter range 20 to 40 nm was developed. The resulting MNP were characterized, functionalized, and finally evaluated for their capability in biomedical applications. Producing high quality MNP in this size range in an efficient, reproducible, and sustainable way became only possible by employing continuous synthesis via micromixer. The entire synthesis and the following modifications were carried out in aqueous media to ensure the biocompatibility of MNP. In this work, the potential of the continuous synthesis to fabricate tailored MNP regarding their physicochemical propertied such as core size, size distribution, colloidal stability as well as their performance such as relaxitivity, susceptibility, and specific absorption rate was shown. The suitability of the MNP for biomedical applications was demonstrated with the enhanced long-term stability in salt solution and their non-toxicity in cell culture.

Additionally, the high performance of MNP for versatile biomedical applications such as MRI- and MPI-imaging and cancer treatment by magnetic fluid hyperthermia was investigated. This demonstrates their huge potential to be combined in diagnosis

and therapy (theranostic) as one powerful tool. Perspectively, further studies on the MNP capabilities in drug delivery and drug release will help to improve their potential in next generation drug delivery applications.

The MNP developed in this work might become a promising alternative to other MNP systems that were intended for biomedical applications. Actually, most of the approved iron-oxide MNP systems like the liver MRI contrast agent Resovist have been withdrawn from the market - mostly for economical reasons or safety concerns. As presented in this work, the new class of highly performing MNP produced by a generally GMP capable micromixer synthesis approach could foster the reentrance of magnetic nanoparticle system in biomedical diagnostic and therapeutic applications. In this way, micromixer synthesis has become a promising tool to contribute to translational research to pave the way for laboratory MNP into theranostic clinical application.

7 References

1. Richard Feynman: There's Plenty of Room at the Bottom 1960 [1959]. In *Nanotechnologie als Kollektivsymbol* Dissertation; Nowak, F., Ed.; transcript Verlag, 2016; pp 459–470, ISBN 9783839438039.
2. US National Nanotechnology Initiative. Available online: https://www.nano.gov/.
3. Huang, C.; Dong, J.; Sun, W.; Xue, Z.; Ma, J.; Zheng, L.; Liu, C.; Li, X.; Zhou, K.; Qiao, X.; et al. Coordination mode engineering in stacked-nanosheet metal–organic frameworks to enhance catalytic reactivity and structural robustness. *Nat Commun* **2019**, *10*, doi:10.1038/s41467-019-10547-9.
4. Narayan, N.; Meiyazhagan, A.; Vajtai, R. Metal Nanoparticles as Green Catalysts. *Materials (Basel)* **2019**, *12*, doi:10.3390/ma12213602.
5. Zhang, J.; Li, Z.; Chen, Y.; Gao, S.; Lou, X.W. Nickel–Iron Layered Double Hydroxide Hollow Polyhedrons as a Superior Sulfur Host for Lithium–Sulfur Batteries. *Angew. Chem.* **2018**, *130*, 11110–11114, doi:10.1002/ange.201805972.
6. Becheri, A.; Dürr, M.; Lo Nostro, P.; Baglioni, P. Synthesis and characterization of zinc oxide nanoparticles: application to textiles as UV-absorbers. *J Nanopart Res* **2008**, *10*, 679–689, doi:10.1007/s11051-007-9318-3.
7. Kokura, S.; Handa, O.; Takagi, T.; Ishikawa, T.; Naito, Y.; Yoshikawa, T. Silver nanoparticles as a safe preservative for use in cosmetics. *Nanomedicine* **2010**, *6*, 570–574, doi:10.1016/j.nano.2009.12.002.
8. Q A Pankhurst; J Connolly; S K Jones; J Dobson. Applications of magnetic nanoparticles in biomedicine. *Journal of Physics D: Applied Physics* **2003**, *36*, R167-R181, doi:10.1088/0022-3727/36/13/201.

9. Freitas, R.A. *Nanomedicine Volume I;* Landes Bioscience: Georgetown, 1999, ISBN 9781570596803.

10. Salata, O.V. Applications of nanoparticles in biology and medicine. *J. Nanobiotechnology* **2004**, *2*, 3, doi:10.1186/1477-3155-2-3.

11. Lin, W. Introduction: Nanoparticles in Medicine. *Chem. Rev.* **2015**, *115*, 10407–10409, doi:10.1021/acs.chemrev.5b00534.

12. Khan, I.; Saeed, K.; Khan, I. Nanoparticles: Properties, applications and toxicities. *Arabian Journal of Chemistry* **2019**, *12*, 908–931, doi:10.1016/j.arabjc.2017.05.011.

13. Dreaden, E.C.; Alkilany, A.M.; Huang, X.; Murphy, C.J.; El-Sayed, M.A. The golden age: gold nanoparticles for biomedicine. *Chem. Soc. Rev.* **2012**, *41*, 2740–2779, doi:10.1039/C1CS15237H.

14. Mantri, Y.; Jokerst, J.V. Engineering Plasmonic Nanoparticles for Enhanced Photoacoustic Imaging. *ACS Nano* **2020**, *14*, 9408–9422, doi:10.1021/acsnano.0c05215.

15. Wu, Y.; Ali, M.R.K.; Chen, K.; Fang, N.; El-Sayed, M.A. Gold nanoparticles in biological optical imaging. *Nano Today* **2019**, *24*, 120–140, doi:10.1016/j.nantod.2018.12.006.

16. Sharifi, M.; Attar, F.; Saboury, A.A.; Akhtari, K.; Hooshmand, N.; Hasan, A.; El-Sayed, M.A.; Falahati, M. Plasmonic gold nanoparticles: Optical manipulation, imaging, drug delivery and therapy. *J. Control. Release* **2019**, *311-312*, 170–189, doi:10.1016/j.jconrel.2019.08.032.

17. Riehemann, K.; Schneider, S.W.; Luger, T.A.; Godin, B.; Ferrari, M.; Fuchs, H. Nanomedicine--challenge and perspectives. *Angew. Chem. Int. Ed Engl.* **2009**, *48*, 872–897, doi:10.1002/anie.200802585.

18. Mitchell, M.J.; Billingsley, M.M.; Haley, R.M.; Wechsler, M.E.; Peppas, N.A.; Langer, R. Engineering precision nanoparticles for drug delivery. *Nat. Rev. Drug Discov.* **2021**, *20*, 101–124, doi:10.1038/s41573-020-0090-8.

19. Yoo, J.; Park, C.; Yi, G.; Lee, D.; Koo, H. Active Targeting Strategies Using Biological Ligands for Nanoparticle Drug Delivery Systems. *Cancers (Basel)* **2019**, *11*, doi:10.3390/cancers11050640.

20. Rizvi, S.A.A.; Saleh, A.M. Applications of nanoparticle systems in drug delivery technology. *Saudi Pharm. J.* **2018**, *26*, 64–70, doi:10.1016/j.jsps.2017.10.012.

21. Hui, Y.; Yi, X.; Hou, F.; Wibowo, D.; Zhang, F.; Zhao, D.; Gao, H.; Zhao, C.-X. Role of Nanoparticle Mechanical Properties in Cancer Drug Delivery. *ACS Nano* **2019**, *13*, 7410–7424, doi:10.1021/acsnano.9b03924.

22. Han, X.; Xu, K.; Taratula, O.; Farsad, K. Applications of nanoparticles in biomedical imaging. *Nanoscale* **2019**, *11*, 799–819, doi:10.1039/c8nr07769j.

23. Kim, D.; Kim, J.; Park, Y.I.; Lee, N.; Hyeon, T. Recent Development of Inorganic Nanoparticles for Biomedical Imaging. *ACS Cent. Sci.* **2018**, *4*, 324–336, doi:10.1021/acscentsci.7b00574.

24. Creech, C.B.; Walker, S.C.; Samuels, R.J. SARS-CoV-2 Vaccines. *JAMA* **2021**, *325*, 1318–1320, doi:10.1001/jama.2021.3199.

25. Marcandalli, J.; Fiala, B.; Ols, S.; Perotti, M.; van der Schueren, W. de; Snijder, J.; Hodge, E.; Benhaim, M.; Ravichandran, R.; Carter, L.; et al. Induction of Potent Neutralizing Antibody Responses by a Designed Protein Nanoparticle Vaccine for Respiratory Syncytial Virus. *Cell* **2019**, *176*, 1420-1431.e17, doi:10.1016/j.cell.2019.01.046.

26. Brouwer, P.J.M.; Brinkkemper, M.; Maisonnasse, P.; Dereuddre-Bosquet, N.; Grobben, M.; Claireaux, M.; Gast, M. de; Marlin, R.; Chesnais, V.; Diry, S.; et al. Two-component spike nanoparticle vaccine protects macaques from SARS-CoV-2 infection. *Cell* **2021**, *184*, 1188-1200.e19, doi:10.1016/j.cell.2021.01.035.

27. Jain, K.K. Nanodiagnostics: application of nanotechnology in molecular diagnostics. *Expert Rev. Mol. Diagn.* **2003**, *3*, 153–161, doi:10.1586/14737159.3.2.153.

28. Rudramurthy, G.R.; Swamy, M.K.; Sinniah, U.R.; Ghasemzadeh, A. Nanoparticles: Alternatives Against Drug-Resistant Pathogenic Microbes. *Molecules* **2016**, *21*, doi:10.3390/molecules21070836.

29. Okada, M.; Matsumoto, T. Synthesis and modification of apatite nanoparticles for use in dental and medical applications. *Japanese Dental Science Review* **2015**, *51*, 85–95, doi:10.1016/j.jdsr.2015.03.004.

30. Mosayebi, J.; Kiyasatfar, M.; Laurent, S. Synthesis, Functionalization, and Design of Magnetic Nanoparticles for Theranostic Applications. *Adv. Healthc. Mater.* **2017**, *6*, doi:10.1002/adhm.201700306.

31. Bleul, R. *Herstellung, Charakterisierung und Funktionalisierung polymerer Nanopartikel und Untersuchung der Wechselwirkungen mit biologischen Systemen*, 2014.

32. Dadfar, S.M.; Roemhild, K.; Drude, N.I.; Stillfried, S. von; Knüchel, R.; Kiessling, F.; Lammers, T. Iron oxide nanoparticles: Diagnostic, therapeutic and theranostic applications. *Advanced Drug Delivery Reviews* **2019**, *138*, 302–325, doi:10.1016/j.addr.2019.01.005.

33. Wu, Y.; Lu, Z.; Li, Y.; Yang, J.; Zhang, X. Surface Modification of Iron Oxide-Based Magnetic Nanoparticles for Cerebral Theranostics: Application and Prospection. *Nanomaterials (Basel)* **2020**, *10*, doi:10.3390/nano10081441.

34. Amani, A.; Begdelo, J.M.; Yaghoubi, H.; Motallebinia, S. Multifunctional magnetic nanoparticles for controlled release of anticancer drug, breast cancer cell targeting, MRI/fluorescence imaging, and anticancer drug delivery. *Journal of Drug Delivery Science and Technology* **2019**, *49*, 534–546, doi:10.1016/j.jddst.2018.12.034.

35. World health otganization. Available online: https://www.who.int (accessed on 28 November 2021).

36. Choi, K.Y.; Liu, G.; Lee, S.; Chen, X. Theranostic nanoplatforms for simultaneous cancer imaging and therapy: current approaches and future perspectives. *Nanoscale* **2012**, *4*, 330–342, doi:10.1039/c1nr11277e.

37. Hauser, A.K.; Mitov, M.I.; Daley, E.F.; McGarry, R.C.; Anderson, K.W.; Hilt, J.Z. Targeted iron oxide nanoparticles for the enhancement of radiation therapy. *Biomaterials* **2016**, *105*, 127–135, doi:10.1016/j.biomaterials.2016.07.032.

38. Lu, M.; Cohen, M.H.; Rieves, D.; Pazdur, R. FDA report: Ferumoxytol for intravenous iron therapy in adult patients with chronic kidney disease. *Am. J. Hematol.* **2010**, *85*, 315–319, doi:10.1002/ajh.21656.

39. Veisi, H.; Pirhayati, M.; Kakanejadifard, A.; Mohammadi, P.; Abdi, M.R.; Gholami, J.; Hemmati, S. In Situ Green Synthesis of Pd Nanoparticles on Tannic Acid-Modified Magnetite Nanoparticles as a Green Reductant and Stabilizer Agent: Its Application as a Recyclable Nanocatalyst (Fe 3 O 4 @TA/Pd) for Reduction of 4-Nitrophenol and Suzuki Reactions. *ChemistrySelect* **2018**, *3*, 1820–1826, doi:10.1002/slct.201702869.

40. Rane, A.V.; Kanny, K.; Abitha, V.K.; Thomas, S. Methods for Synthesis of Nanoparticles and Fabrication of Nanocomposites, *6*, 121–139, doi:10.1016/B978-0-08-101975-7.00005-1.

41. Jesus, A.C.B.; Jesus, J.R.; Lima, R.J.S.; Moura, K.O.; Almeida, J.M.A.; Duque, J.G.S.; Meneses, C.T. Synthesis and magnetic interaction on concentrated Fe3O4 nanoparticles obtained by the co-precipitation and hydrothermal chemical methods. *Ceramics International* **2020**, *46*, 11149–11153, doi:10.1016/j.ceramint.2020.01.135.

42. Fernandes, M.T.C.; Garcia, R.B.R.; Leite, C.A.P.; Kawachi, E.Y. The competing effect of ammonia in the synthesis of iron oxide/silica nanoparticles in microemulsion/sol–gel system. *Colloids and Surfaces A: Physicochemical and Engineering Aspects* **2013**, *422*, 136–142, doi:10.1016/j.colsurfa.2013.01.025.

43. Sundar, S.; Venkatachalam, G.; Kwon, S. Sol-Gel Mediated Greener Synthesis of γ-Fe2O3 Nanostructures for the Selective and Sensitive Determination of Uric Acid and Dopamine. *Catalysts* **2018**, *8*, 512, doi:10.3390/catal8110512.

44. Okoli, C.; Sanchez-Dominguez, M.; Boutonnet, M.; Järås, S.; Civera, C.; Solans, C.; Kuttuva, G.R. Comparison and functionalization study of microemulsion-prepared magnetic iron oxide nanoparticles. *Langmuir* **2012**, *28*, 8479–8485, doi:10.1021/la300599q.

45. Malik, M.A.; Wani, M.Y.; Hashim, M.A. Microemulsion method: A novel route to synthesize organic and inorganic nanomaterials. *Arabian Journal of Chemistry* **2012**, *5*, 397–417, doi:10.1016/j.arabjc.2010.09.027.

46. Unni, M.; Uhl, A.M.; Savliwala, S.; Savitzky, B.H.; Dhavalikar, R.; Garraud, N.; Arnold, D.P.; Kourkoutis, L.F.; Andrew, J.S.; Rinaldi, C. Thermal Decomposition Synthesis of Iron Oxide Nanoparticles with Diminished Magnetic Dead Layer by Controlled Addition of Oxygen. *ACS Nano* **2017**, *11*, 2284–2303, doi:10.1021/acsnano.7b00609.

47. Hufschmid, R.; Teeman, E.; Mehdi, B.L.; Krishnan, K.M.; Browning, N.D. Observing the colloidal stability of iron oxide nanoparticles in situ. *Nanoscale* **2019**, *11*, 13098–13107, doi:10.1039/c9nr03709h.

48. Gutierrez, L.; Gomez, L.; Irusta, S.; Arruebo, M.; Santamaria, J. Comparative study of the synthesis of silica nanoparticles in micromixer–microreactor and batch reactor systems. *Chemical Engineering Journal* **2011**, *171*, 674–683, doi:10.1016/j.cej.2011.05.019.

49. Ma, J.; Lee, S.M.-Y.; Yi, C.; Li, C.-W. Controllable synthesis of functional nanoparticles by microfluidic platforms for biomedical applications - a review. *Lab Chip* **2017**, *17*, 209–226, doi:10.1039/c6lc01049k.

50. Mathew, D.S.; Juang, R.-S. An overview of the structure and magnetism of spinel ferrite nanoparticles and their synthesis in microemulsions. *Chemical Engineering Journal* **2007**, *129*, 51–65, doi:10.1016/j.cej.2006.11.001.

51. Wu, K.; Su, D.; Liu, J.; Saha, R.; Wang, J.-P. Magnetic nanoparticles in nanomedicine: a review of recent advances. *Nanotechnology* **2019**, *30*, 502003, doi:10.1088/1361-6528/ab4241.

52. Rosensweig, R.E. Heating magnetic fluid with alternating magnetic field. *Journal of Magnetism and Magnetic Materials* **2002**, *252*, 370–374, doi:10.1016/S0304-8853(02)00706-0.

53. Cornell, R.M.; Schwertmann, U. *The Iron Oxides;* Wiley, 2003.

54. Ahrens, T.J. *Rock Physics & Phase Relations;* American Geophysical Union: Washington, D. C., 1995, ISBN 9781118668108.

55. Odenbach, S. *Handbook of Magnetic Materials*, 16th ed.; Elsevier: Amsterdam, 2006.

56. Hoehn, M.; Wiedermann, D.; Justicia, C.; Ramos-Cabrer, P.; Kruttwig, K.; Farr, T.; Himmelreich, U. Cell tracking using magnetic resonance imaging. *J. Physiol.* **2007**, *584*, 25–30, doi:10.1113/jphysiol.2007.139451.

57. Bulte, J.W.M.; Arbab, A.S.; Douglas, T.; Frank, J.A. Preparation of Magnetically Labeled Cells for Cell Tracking by Magnetic Resonance Imaging, *386*, 275–299, doi:10.1016/S0076-6879(04)86013-0.

58. Becker, C.; Hodenius, M.; Blendinger, G.; Sechi, A.; Hieronymus, T.; Müller-Schulte, D.; Schmitz-Rode, T.; Zenke, M. Uptake of magnetic nanoparticles into cells for cell tracking. *Journal of Magnetism and Magnetic Materials* **2007**, *311*, 234–237, doi:10.1016/j.jmmm.2006.11.203.

59. Dobson, J. Magnetic nanoparticles for drug delivery. *Drug Dev. Res.* **2006**, *67*, 55–60, doi:10.1002/ddr.20067.

60. Wu, M.; Huang, S. Magnetic nanoparticles in cancer diagnosis, drug delivery and treatment. *Mol. Clin. Oncol.* **2017**, *7*, 738–746, doi:10.3892/mco.2017.1399.

61. Patitsa, M.; Karathanou, K.; Kanaki, Z.; Tzioga, L.; Pippa, N.; Demetzos, C.; Verganelakis, D.A.; Cournia, Z.; Klinakis, A. Magnetic nanoparticles coated with

polyarabic acid demonstrate enhanced drug delivery and imaging properties for cancer theranostic applications. *Sci. Rep.* **2017**, *7*, 775, doi:10.1038/s41598-017-00836-y.

62. Mu, X.; Li, J.; Yan, S.; Zhang, H.; Zhang, W.; Zhang, F.; Jiang, J. siRNA Delivery with Stem Cell Membrane-Coated Magnetic Nanoparticles for Imaging-Guided Photothermal Therapy and Gene Therapy. *ACS Biomater. Sci. Eng.* **2018**, *4*, 3895–3905, doi:10.1021/acsbiomaterials.8b00858.
63. Dowaidar, M.; Nasser Abdelhamid, H.; Hällbrink, M.; Langel, Ü.; Zou, X. Chitosan enhances gene delivery of oligonucleotide complexes with magnetic nanoparticles-cell-penetrating peptide. *J. Biomater. Appl.* **2018**, *33*, 392–401, doi:10.1177/0885328218796623.
64. Shaterabadi, Z.; Nabiyouni, G.; Soleymani, M. Physics responsible for heating efficiency and self-controlled temperature rise of magnetic nanoparticles in magnetic hyperthermia therapy. *Prog. Biophys. Mol. Biol.* **2018**, *133*, 9–19, doi:10.1016/j.pbiomolbio.2017.10.001.
65. Iglesias, G.R.; Jabalera, Y.; Peigneux, A.; Checa Fernández, B.L.; Delgado, Á.V.; Jimenez-Lopez, C. Enhancement of Magnetic Hyperthermia by Mixing Synthetic Inorganic and Biomimetic Magnetic Nanoparticles. *Pharmaceutics* **2019**, *11*, doi:10.3390/pharmaceutics11060273.
66. Jose, J.; Kumar, R.; Harilal, S.; Mathew, G.E.; Della Parambi, G.T.; Prabhu, A.; Uddin, M.S.; Aleya, L.; Kim, H.; Mathew, B. Magnetic nanoparticles for hyperthermia in cancer treatment: an emerging tool. *Environ. Sci. Pollut. Res. Int.* **2020**, *27*, 19214–19225, doi:10.1007/s11356-019-07231-2.
67. Nosrati, H.; Salehiabar, M.; Kheiri Manjili, H.; Davaran, S.; Danafar, H. Theranostic nanoparticles based on magnetic nanoparticles: design, preparation, characterization, and evaluation as novel anticancer drug carrier and MRI contrast agent. *Drug Dev. Ind. Pharm.* **2018**, *44*, 1668–1678, doi:10.1080/03639045.2018.1483398.

68. Arsalani, S.; Guidelli, E.J.; Silveira, M.A.; Salmon, C.E.G.; Araujo, J.F.D.F.; Bruno, A.C.; Baffa, O. Magnetic Fe3O4 nanoparticles coated by natural rubber latex as MRI contrast agent. *Journal of Magnetism and Magnetic Materials* **2019**, *475*, 458–464, doi:10.1016/j.jmmm.2018.11.132.

69. Jeon, M.; Halbert, M.V.; Stephen, Z.R.; Zhang, M. Iron Oxide Nanoparticles as T1 Contrast Agents for Magnetic Resonance Imaging: Fundamentals, Challenges, Applications, and Prospectives. *Adv. Mater.* **2021**, *33*, e1906539, doi:10.1002/adma.201906539.

70. Salehipour, M.; Rezaei, S.; Mosafer, J.; Pakdin-Parizi, Z.; Motaharian, A.; Mogharabi-Manzari, M. Recent advances in polymer-coated iron oxide nanoparticles as magnetic resonance imaging contrast agents. *J Nanopart Res* **2021**, *23*, 1467, doi:10.1007/s11051-021-05156-x.

71. Vazquez-Prada, K.X.; Lam, J.; Kamato, D.; Xu, Z.P.; Little, P.J.; Ta, H.T. Targeted Molecular Imaging of Cardiovascular Diseases by Iron Oxide Nanoparticles. *Arterioscler. Thromb. Vasc. Biol.* **2021**, *41*, 601–613, doi:10.1161/ATVBAHA.120.315404.

72. Koleoso, M.; Feng, X.; Xue, Y.; Li, Q.; Munshi, T.; Chen, X. Micro/nanoscale magnetic robots for biomedical applications. *Mater. Today Bio* **2020**, *8*, 100085, doi:10.1016/j.mtbio.2020.100085.

73. Yan, X.; Zhou, Q.; Vincent, M.; Deng, Y.; Yu, J.; Xu, J.; Xu, T.; Tang, T.; Bian, L.; Wang, Y.-X.J.; et al. Multifunctional biohybrid magnetite microrobots for imaging-guided therapy. *Sci. Robot.* **2017**, *2*, doi:10.1126/scirobotics.aaq1155.

74. Alapan, Y.; Yasa, O.; Schauer, O.; Giltinan, J.; Tabak, A.F.; Sourjik, V.; Sitti, M. Soft erythrocyte-based bacterial microswimmers for cargo delivery. *Sci. Robot.* **2018**, *3*, doi:10.1126/scirobotics.aar4423.

75. Saygin, Z.M.; Kliemann, D.; Iglesias, J.E.; van der Kouwe, A.J.W.; Boyd, E.; Reuter, M.; Stevens, A.; van Leemput, K.; McKee, A.; Frosch, M.P.; et al. High-resolution magnetic resonance imaging reveals nuclei of the human amygdala:

manual segmentation to automatic atlas. *Neuroimage* **2017**, *155*, 370–382, doi:10.1016/j.neuroimage.2017.04.046.

76. Zhang, H.; Li, L.; Liu, X.L.; Jiao, J.; Ng, C.-T.; Yi, J.B.; Luo, Y.E.; Bay, B.-H.; Zhao, L.Y.; Peng, M.L.; et al. Ultrasmall Ferrite Nanoparticles Synthesized via Dynamic Simultaneous Thermal Decomposition for High-Performance and Multifunctional T1 Magnetic Resonance Imaging Contrast Agent. *ACS Nano* **2017**, *11*, 3614–3631, doi:10.1021/acsnano.6b07684.

77. Ni, D.; Bu, W.; Ehlerding, E.B.; Cai, W.; Shi, J. Engineering of inorganic nanoparticles as magnetic resonance imaging contrast agents. *Chem. Soc. Rev.* **2017**, *46*, 7438–7468, doi:10.1039/c7cs00316a.

78. Yurt, A.; Kazancı, N. Investigation of magnetic properties of various complexes prepared as contrast agents for MRI. *Journal of Molecular Structure* **2008**, *892*, 392–397, doi:10.1016/j.molstruc.2008.06.024.

79. Shokrollahi, H. Contrast agents for MRI. *Mater. Sci. Eng. C Mater. Biol. Appl.* **2013**, *33*, 4485–4497, doi:10.1016/j.msec.2013.07.012.

80. Aime, S.; Caravan, P. Biodistribution of gadolinium-based contrast agents, including gadolinium deposition. *J. Magn. Reson. Imaging* **2009**, *30*, 1259–1267, doi:10.1002/jmri.21969.

81. Gleich, B.; Weizenecker, J. Tomographic imaging using the nonlinear response of magnetic particles. *Nature* **2005**, *435*, 1214–1217, doi:10.1038/nature03808.

82. Weizenecker, J.; Gleich, B.; Rahmer, J.; Dahnke, H.; Borgert, J. Three-dimensional real-time in vivo magnetic particle imaging. *Phys. Med. Biol.* **2009**, *54*, L1-L10, doi:10.1088/0031-9155/54/5/L01.

83. Buzug, T.M.; Bringout, G.; Erbe, M.; Gräfe, K.; Graeser, M.; Grüttner, M.; Halkola, A.; Sattel, T.F.; Tenner, W.; Wojtczyk, H.; et al. Magnetic particle imaging: introduction to imaging and hardware realization. *Z. Med. Phys.* **2012**, *22*, 323–334, doi:10.1016/j.zemedi.2012.07.004.

84. Teeman, E.; Shasha, C.; Evans, J.E.; Krishnan, K.M. Intracellular dynamics of superparamagnetic iron oxide nanoparticles for magnetic particle imaging. *Nanoscale* **2019**, *11*, 7771–7780, doi:10.1039/c9nr01395d.

85. Borgert, J.; Schmidt, J.D.; Schmale, I.; Rahmer, J.; Bontus, C.; Gleich, B.; David, B.; Eckart, R.; Woywode, O.; Weizenecker, J.; et al. Fundamentals and applications of magnetic particle imaging. *J. Cardiovasc. Comput. Tomogr.* **2012**, *6*, 149–153, doi:10.1016/j.jcct.2012.04.007.

86. Kaul, M.G.; Weber, O.; Heinen, U.; Reitmeier, A.; Mummert, T.; Jung, C.; Raabe, N.; Knopp, T.; Ittrich, H.; Adam, G. Combined Preclinical Magnetic Particle Imaging and Magnetic Resonance Imaging: Initial Results in Mice. *Rofo* **2015**, *187*, 347–352, doi:10.1055/s-0034-1399344.

87. Gas, P. Essential Facts on the History of Hyperthermia and their Connections with Electromedicine. *Electrotechnical Review*, *R. 87, nr 12b*.

88. Jordan, A.; Wust, P.; Scholz, R.; Tesche, B.; Fähling, H.; Mitrovics, T.; Vogl, T.; Cervós-Navarro, J.; Felix, R. Cellular uptake of magnetic fluid particles and their effects on human adenocarcinoma cells exposed to AC magnetic fields in vitro. *Int. J. Hyperthermia* **1996**, *12*, 705–722, doi:10.3109/02656739609027678.

89. Jordan, A.; Scholz, R.; Wust, P.; Fähling, H.; Felix, R. Magnetic fluid hyperthermia (MFH): Cancer treatment with AC magnetic field induced excitation of biocompatible superparamagnetic nanoparticles. *Journal of Magnetism and Magnetic Materials* **1999**, *201*, 413–419.

90. Nielsen, O.S.; Horsman, M.; Overgaard, J. A future for hyperthermia in cancer treatment? *European Journal of Cancer* **2001**, *37*, 1587–1589, doi:10.1016/S0959-8049(01)00193-9.

91. Bohara, R.A.; Thorat, N.D.; Pawar, S.H. Role of functionalization: strategies to explore potential nano-bio applications of magnetic nanoparticles. *RSC Adv.* **2016**, *6*, 43989–44012, doi:10.1039/C6RA02129H.

92. Thorat, N.D.; Shinde, K.P.; Pawar, S.H.; Barick, K.C.; Betty, C.A.; Ningthoujam, R.S. Polyvinyl alcohol: an efficient fuel for synthesis of superparamagnetic LSMO nanoparticles for biomedical application. *Dalton Trans.* **2012**, *41*, 3060–3071, doi:10.1039/c2dt11835a.

93. Grüttner, C.; Müller, K.; Teller, J.; Westphal, F. Synthesis and functionalisation of magnetic nanoparticles for hyperthermia applications. *Int. J. Hyperthermia* **2013**, *29*, 777–789, doi:10.3109/02656736.2013.835876.

94. Bohara, R.A.; Yadav, H.M.; Thorat, N.D.; Mali, S.S.; Hong, C.K.; Nanaware, S.G.; Pawar, S.H. Synthesis of functionalized Co 0.5 Zn 0.5 Fe 2 O 4 nanoparticles for biomedical applications. *Journal of Magnetism and Magnetic Materials* **2015**, *378*, 397–401, doi:10.1016/j.jmmm.2014.11.063.

95. Bordelon, D.E.; Cornejo, C.; Grüttner, C.; Westphal, F.; DeWeese, T.L.; Ivkov, R. Magnetic nanoparticle heating efficiency reveals magneto-structural differences when characterized with wide ranging and high amplitude alternating magnetic fields. *Journal of Applied Physics* **2011**, *109*, 124904, doi:10.1063/1.3597820.

96. Cabrera, D.; Coene, A.; Leliaert, J.; Artés-Ibáñez, E.J.; Dupré, L.; Telling, N.D.; Teran, F.J. Dynamical Magnetic Response of Iron Oxide Nanoparticles Inside Live Cells. *ACS Nano* **2018**, *12*, 2741–2752, doi:10.1021/acsnano.7b08995.

97. Wang, Y.; He, J.; Liu, C.; Chong, W.H.; Chen, H. Thermodynamik und Kinetik in der Nanosynthese. *Angew. Chem.* **2015**, *127*, 2046–2079, doi:10.1002/ange.201402986.

98. Arbain, R.; Othman, M.; Palaniandy, S. Preparation of iron oxide nanoparticles by mechanical milling. *Minerals Engineering* **2011**, *24*, 1–9, doi:10.1016/j.mineng.2010.08.025.

99. Hudson, R.; Feng, Y.; Varma, R.S.; Moores, A. Bare magnetic nanoparticles: sustainable synthesis and applications in catalytic organic transformations. *Green Chem* **2014**, *16*, 4493–4505, doi:10.1039/C4GC00418C.

100. Andrade, R.G.D.; Veloso, S.R.S.; Castanheira, E.M.S. Shape Anisotropic Iron Oxide-Based Magnetic Nanoparticles: Synthesis and Biomedical Applications. *Int. J. Mol. Sci.* **2020**, *21*, doi:10.3390/ijms21072455.

101. Laurent, S.; Forge, D.; Port, M.; Roch, A.; Robic, C.; Vander Elst, L.; Muller, R.N. Magnetic iron oxide nanoparticles: synthesis, stabilization, vectorization, physicochemical characterizations, and biological applications. *Chem. Rev.* **2008**, *108*, 2064–2110, doi:10.1021/cr068445e.

102. Faraji, M.; Yamini, Y.; Rezaee, M. Magnetic nanoparticles: Synthesis, stabilization, functionalization, characterization, and applications. *JICS* **2010**, *7*, 1–37, doi:10.1007/BF03245856.

103. Gupta, A.K.; Gupta, M. Synthesis and surface engineering of iron oxide nanoparticles for biomedical applications. *J. Phys. D: Appl. Phys.* **2005**, *26*, 3995–4021, doi:10.1016/j.biomaterials.2004.10.012.

104. Teja, A.S.; Koh, P.-Y. Synthesis, properties, and applications of magnetic iron oxide nanoparticles. *Progress in Crystal Growth and Characterization of Materials* **2009**, *55*, 22–45, doi:10.1016/j.pcrysgrow.2008.08.003.

105. Majidi, S.; Sehrig, F.Z.; Farkhani, S.M.; Goloujeh, M.S.; Akbarzadeh, A. Current methods for synthesis of magnetic nanoparticles. *Artif. Cells Nanomed. Biotechnol.* **2016**, *44*, 722–734, doi:10.3109/21691401.2014.982802.

106. Cheera, P.; Karlapudi, S.; Sellola, G.; Ponneri, V. A facile green synthesis of spherical Fe3O4 magnetic nanoparticles and their effect on degradation of methylene blue in aqueous solution. *Journal of Molecular Liquids* **2016**, *221*, 993–998, doi:10.1016/j.molliq.2016.06.006.

107. Menchaca-Nal, S.; Londoño-Calderón, C.L.; Cerrutti, P.; Foresti, M.L.; Pampillo, L.; Bilovol, V.; Candal, R.; Martínez-García, R. Facile synthesis of cobalt ferrite nanotubes using bacterial nanocellulose as template. *Carbohydr. Polym.* **2016**, *137*, 726–731, doi:10.1016/j.carbpol.2015.10.068.

108. Xi, G.; Wang, C.; Wang, X. The Oriented Self-Assembly of Magnetic Fe 3 O 4 Nanoparticles into Monodisperse Microspheres and Their Use as Substrates in the Formation of Fe 3 O 4 Nanorods. *Eur. J. Inorg. Chem.* **2008**, *2008*, 425–431, doi:10.1002/ejic.200700863.

109. Ding, Y.; Liu, F.; Jiang, Q.; Du, B.; Sun, H. 12-Hydrothermal Synthesis and Characterization of Fe3O4 Nanorods. *J Inorg Organomet Polym* **2013**, *23*, 379–384, doi:10.1007/s10904-012-9789-2.

110. HAN, C.; MA, J.; WU, H.; YAOWEI; HU, K. A LOW-COST AND HIGH-YIELD PRODUCTION OF MAGNETITE NANORODS WITH HIGH SATURATION MAGNETIZATION. *J. Chil. Chem. Soc.* **2015**, *60*, 2799–2802, doi:10.4067/S0717-97072015000100005.

111. Huang, Z.; Zhang, Y.; Tang, F. Solution-phase synthesis of single-crystalline magnetic nanowires with high aspect ratio and uniformity. *Chem. Commun.* **2005**, 342–344, doi:10.1039/b410463c.

112. Cui, H.-J.; Shi, J.-W.; Yuan, B.; Fu, M.-L. Synthesis of porous magnetic ferrite nanowires containing Mn and their application in water treatment. *J. Mater. Chem. A* **2013**, *1*, 5902, doi:10.1039/c3ta01692g.

113. Guo, C.; Xia, F.; Wang, Z.; Zhang, L.; Xi, L.; Zuo, Y. Flowerlike iron oxide nanostructures and their application in microwave absorption. *Journal of Alloys and Compounds* **2015**, *631*, 183–191, doi:10.1016/j.jallcom.2015.01.087.

114. Wang, D.; Yang, P.; Huang, B. Three-dimensional flowerlike iron oxide nanostructures: Morphology, composition and metal ion removal capability. *Materials Research Bulletin* **2016**, *73*, 56–64, doi:10.1016/j.materresbull.2015.08.008.

115. Guardia, P.; Di Corato, R.; Lartigue, L.; Wilhelm, C.; Espinosa, A.; Garcia-Hernandez, M.; Gazeau, F.; Manna, L.; Pellegrino, T. Water-soluble iron oxide nanocubes with high values of specific absorption rate for cancer cell hyperthermia treatment. *ACS Nano* **2012**, *6*, 3080–3091, doi:10.1021/nn2048137.

116. Wortmann, L.; Ilyas, S.; Niznansky, D.; Valldor, M.; Arroub, K.; Berger, N.; Rahme, K.; Holmes, J.; Mathur, S. Bioconjugated iron oxide nanocubes: synthesis, functionalization, and vectorization. *ACS Appl. Mater. Interfaces* **2014**, *6*, 16631–16642, doi:10.1021/am503068r.

117. LaMer, V.K.; Dinegar, R.H. Theory, Production and Mechanism of Formation of Monodispersed Hydrosols. *J. Am. Chem. Soc.* **1950**, *72*, 4847–4854, doi:10.1021/ja01167a001.

118. Ostwald, W. Studien über die Bildung und Umwandlung fester Körper. *Zeitschrift für Physikalische Chemie* **1897**, 289–330.

119. Schlenoff, J.B.; Li, M.; Ly, H. Stability and Self-Exchange in Alkanethiol Monolayers. *J. Am. Chem. Soc.* **1995**, *117*, 12528–12536, doi:10.1021/ja00155a016.

120. Polarz, S. Shape Matters: Anisotropy of the Morphology of Inorganic Colloidal Particles - Synthesis and Function. *Adv. Funct. Mater.* **2011**, *21*, 3214–3230, doi:10.1002/adfm.201101205.

121. Herring, C. Some Theorems on the Free Energies of Crystal Surfaces. *Phys. Rev.* **1951**, *82*, 87–93, doi:10.1103/PhysRev.82.87.

122. Li, H.; Xin, H.L.; Muller, D.A.; Estroff, L.A. Visualizing the 3D internal structure of calcite single crystals grown in agarose hydrogels. *Science* **2009**, *326*, 1244–1247, doi:10.1126/science.1178583.

123. Feng, Y.; Wang, Y.; Wang, H.; Chen, T.; Tay, Y.Y.; Yao, L.; Yan, Q.; Li, S.; Chen, H. Engineering "hot" nanoparticles for surface-enhanced Raman scattering by embedding reporter molecules in metal layers. *Small* **2012**, *8*, 246–251, doi:10.1002/smll.201102215.

124. Lu, G.; Li, S.; Guo, Z.; Farha, O.K.; Hauser, B.G.; Qi, X.; Wang, Y.; Wang, X.; Han, S.; Liu, X.; et al. Imparting functionality to a metal–organic framework material by controlled nanoparticle encapsulation. *Nature Chem* **2012**, *4*, 310–316, doi:10.1038/nchem.1272.

125. Sindoro, M.; Feng, Y.; Xing, S.; Li, H.; Xu, J.; Hu, H.; Liu, C.; Wang, Y.; Zhang, H.; Shen, Z.; et al. Triple-layer (au@perylene)@polyaniline nanocomposite: unconventional growth of faceted organic nanocrystals on polycrystalline Au. *Angew. Chem. Int. Ed Engl.* **2011**, *50*, 9898–9902, doi:10.1002/anie.201102994.

126. ZHAO, Y.; QIU, Z.; HUANG, J. Preparation and Analysis of Fe3O4 Magnetic Nanoparticles Used as Targeted-drug Carriers. *Chinese Journal of Chemical Engineering* **2008**, *16*, 451–455, doi:10.1016/S1004-9541(08)60104-4.

127. Massart, R. Preparation of aqueous magnetic liquids in alkaline and acidic media. *IEEE Trans. Magn.* **1981**, *17*, 1247–1248, doi:10.1109/TMAG.1981.1061188.

128. Wu, W.; He, Q.; Jiang, C. Magnetic iron oxide nanoparticles: synthesis and surface functionalization strategies. *Nanoscale Res. Lett.* **2008**, *3*, 397–415, doi:10.1007/s11671-008-9174-9.

129. Babes; Denizot; Tanguy; Le Jeune, J.J.; Jallet. Synthesis of Iron Oxide Nanoparticles Used as MRI Contrast Agents: A Parametric Study. *Journal of Colloid and Interface Science* **1999**, *212*, 474–482, doi:10.1006/jcis.1998.6053.

130. Tominaga, M.; Matsumoto, M.; Soejima, K.; Taniguchi, I. Size control for two-dimensional iron oxide nanodots derived from biological molecules. *Journal of Colloid and Interface Science* **2006**, *299*, 761–765, doi:10.1016/j.jcis.2006.02.022.

131. Sjøgren, C.E.; Briley-Saebø, K.; Hanson, M.; Johansson, C. Magnetic characterization of iron oxides for magnetic resonance imaging. *Magn. Reson. Med.* **1994**, *31*, 268–272, doi:10.1002/mrm.1910310305.

132. Itoh, H.; Sugimoto, T. Systematic control of size, shape, structure, and magnetic properties of uniform magnetite and maghemite particles. *Journal of Colloid and Interface Science* **2003**, *265*, 283–295, doi:10.1016/S0021-9797(03)00511-3.

133. Pardoe, H.; Chua-anusorn, W.; St. Pierre, T.G.; Dobson, J. Structural and magnetic properties of nanoscale iron oxide particles synthesized in the presence

of dextran or polyvinyl alcohol. *Journal of Magnetism and Magnetic Materials* **2001**, *225*, 41–46, doi:10.1016/S0304-8853(00)01226-9.

134. Khalafalla, S.; Reimers, G. Preparation of dilution-stable aqueous magnetic fluids. *IEEE Trans. Magn.* **1980**, *16*, 178–183, doi:10.1109/TMAG.1980.1060578.

135. Thapa, D.; Palkar, V.R.; Kurup, M.B.; Malik, S.K. *Properties of magnetite nanoparticles synthesized through a novel chemical route*, 2004. Available online: https://arxiv.org/pdf/cond-mat/0406184.

136. Sugimoto, T.; Matijević, E. Formation of uniform spherical magnetite particles by crystallization from ferrous hydroxide gels. *Journal of Colloid and Interface Science* **1980**, *74*, 227–243, doi:10.1016/0021-9797(80)90187-3.

137. Li, Z.; Tan, B.; Allix, M.; Cooper, A.I.; Rosseinsky, M.J. Direct coprecipitation route to monodisperse dual-functionalized magnetic iron oxide nanocrystals without size selection. *Small* **2008**, *4*, 231–239, doi:10.1002/smll.200700575.

138. Anik, M.I.; Hossain, M.K.; Hossain, I.; Mahfuz, A.M.U.B.; Rahman, M.T.; Ahmed, I. Recent progress of magnetic nanoparticles in biomedical applications: A review. *Nano Select* **2021**, *2*, 1146–1186, doi:10.1002/nano.202000162.

139. Liu, J.; Su, D.; Wu, K.; Wang, J.-P. High-moment magnetic nanoparticles. *J Nanopart Res* **2020**, *22*, 1–16, doi:10.1007/s11051-020-4758-0.

140. Hyeon, T.; Lee, S.S.; Park, J.; Chung, Y.; Na, H.B. Synthesis of highly crystalline and monodisperse maghemite nanocrystallites without a size-selection process. *J. Am. Chem. Soc.* **2001**, *123*, 12798–12801, doi:10.1021/ja016812s.

141. Yin, Y.; Alivisatos, A.P. Colloidal nanocrystal synthesis and the organic-inorganic interface. *Nature* **2005**, *437*, 664–670, doi:10.1038/nature04165.

142. Daw, R.; Finkelstein, J. Lab on a chip. *Nature* **2006**, *442*, 367, doi:10.1038/442367a.

143. Sackmann, E.K.; Fulton, A.L.; Beebe, D.J. The present and future role of microfluidics in biomedical research. *Nature* **2014**, *507*, 181–189, doi:10.1038/nature13118.

144. Shang, L.; Cheng, Y.; Zhao, Y. Emerging Droplet Microfluidics. *Chem. Rev.* **2017**, *117*, 7964–8040, doi:10.1021/acs.chemrev.6b00848.

145. Yu, Y.; Shang, L.; Guo, J.; Wang, J.; Zhao, Y. Design of capillary microfluidics for spinning cell-laden microfibers. *Nat. Protoc.* **2018**, *13*, 2557–2579, doi:10.1038/s41596-018-0051-4.

146. Zou, M.; Wang, J.; Yu, Y.; Sun, L.; Wang, H.; Xu, H.; Zhao, Y. Composite Multifunctional Micromotors from Droplet Microfluidics. *ACS Appl. Mater. Interfaces* **2018**, *10*, 34618–34624, doi:10.1021/acsami.8b11976.

147. Shrimal, P.; Jadeja, G.; Patel, S. A review on novel methodologies for drug nanoparticle preparation: Microfluidic approach. *Chemical Engineering Research and Design* **2020**, *153*, 728–756, doi:10.1016/j.cherd.2019.11.031.

148. Sengupta, P.; Khanra, K.; Chowdhury, A.R.; Datta, P. Lab-on-a-chip sensing devices for biomedical applications, *21*, 47–95, doi:10.1016/B978-0-08-102420-1.00004-2.

149. Zhao, C.-X.; He, L.; Qiao, S.Z.; Middelberg, A.P.J. Nanoparticle synthesis in microreactors. *Chemical Engineering Science* **2011**, *66*, 1463–1479, doi:10.1016/j.ces.2010.08.039.

150. Wang, J.; Song, Y. Microfluidic Synthesis of Nanohybrids. *Small* **2017**, *13*, doi:10.1002/smll.201604084.

151. Watt, J.; Hance, B.G.; Anderson, R.S.; Huber, D.L. Effect of Seed Age on Gold Nanorod Formation: A Microfluidic, Real-Time Investigation. *Chem. Mater.* **2015**, *27*, 6442–6449, doi:10.1021/acs.chemmater.5b02675.

152. Hong, T.; Lu, A.; Liu, W.; Chen, C. Microdroplet Synthesis of Silver Nanoparticles with Controlled Sizes. *Micromachines (Basel)* **2019**, *10*, doi:10.3390/mi10040274.

153. Jähnisch, K.; Baerns, M.; Hessel, V.; Ehrfeld, W.; Haverkamp, V.; Löwe, H.; Wille, C.; Guber, A. Direct fluorination of toluene using elemental fluorine in gas/liquid microreactors. *Journal of fluorine chemistry* **2000**, *105*, 117–128.

154. Yube, K.; Mae, K. Efficient Oxidation of Aromatics with Peroxides under Severe Conditions Using a Microreaction System. *Chem. Eng. Technol.* **2005**, *28*, 331–336, doi:10.1002/ceat.200407114.

155. Yu, B.; Lee, R.J.; Lee, L.J. Microfluidic Methods for Production of Liposomes. In *Liposomes,* 1. ed.; Düzgüneş, N., Ed.; Elsevier: Amsterdam, 2009; pp 129–141, ISBN 9780123813794.

156. Girod, M.; Vogel, S.; Szczerba, W.; Thünemann, A.F. How temperature determines formation of maghemite nanoparticles. *Journal of Magnetism and Magnetic Materials* **2015**, *380*, 163–167, doi:10.1016/j.jmmm.2014.09.057.

157. Panariello, L.; Wu, G.; Besenhard, M.O.; Loizou, K.; Storozhuk, L.; Thanh, N.T.K.; Gavriilidis, A. A Modular Millifluidic Platform for the Synthesis of Iron Oxide Nanoparticles with Control over Dissolved Gas and Flow Configuration. *Materials (Basel)* **2020**, *13*, doi:10.3390/ma13041019.

158. Suryawanshi, P.L.; Sonawane, S.H.; Bhanvase, B.A.; Ashokkumar, M.; Pimplapure, M.S.; Gogate, P.R. Synthesis of iron oxide nanoparticles in a continuous flow spiral microreactor and Corning® advanced flow™ reactor. *Green Processing and Synthesis* **2018**, *7*, 1–11, doi:10.1515/gps-2016-0138.

159. Simmons, M.; Wiles, C.; Rocher, V.; Francesconi, M.G.; Watts, P. The Preparation of Magnetic Iron Oxide Nanoparticles in Microreactors. *Journal of Flow Chemistry* **2013**, *3*, 7–10, doi:10.1556/JFC-D-12-00024.

160. Abou Hassan, A.; Sandre, O.; Cabuil, V.; Tabeling, P. Synthesis of iron oxide nanoparticles in a microfluidic device: preliminary results in a coaxial flow millichannel. *Chem. Commun.* **2008**, 1783–1785, doi:10.1039/b719550h.

161. Norfolk, L.; Rawlings, A.E.; Bramble, J.P.; Ward, K.; Francis, N.; Waller, R.; Bailey, A.; Staniland, S.S. Macrofluidic Coaxial Flow Platforms to Produce Tunable Magnetite Nanoparticles: A Study of the Effect of Reaction Conditions and Biomineralisation Protein Mms6. *Nanomaterials (Basel)* **2019**, *9*, doi:10.3390/nano9121729.

162. Shepherd, S.J.; Issadore, D.; Mitchell, M.J. Microfluidic formulation of nanoparticles for biomedical applications. *Biomaterials* **2021**, *274*, 120826, doi:10.1016/j.biomaterials.2021.120826.

163. Werner, B.; Hessel, V.; Löb, P. Mischer mit mikrostrukturierten Folien für chemische Produktionsaufgaben. *Chemie Ingenieur Technik* **2004**, *76*, 567–574, doi:10.1002/cite.200406168.

164. Hessel, V.; Löwe, H.; Stange, T. Micro chemical processing at IMM--from pioneering work to customer-specific services; 14N-21N.

165. Schönfeld, F.; Hessel, V.; Hofmann, C. An optimised split-and-recombine micro-mixer with uniform chaotic mixing. *Lab Chip* **2004**, *4*, 65–69, doi:10.1039/b310802c.

166. Ziegenbalg, D.; Kompter, C.; Schönfeld, F.; Kralisch, D. Evaluation of different micromixers by CFD simulations for the anionic polymerisation of styrene. *Green Processing and Synthesis* **2012**, *1*, doi:10.1515/gps-2012-0004.

167. Carrier, O.; Funfschilling, D.; Debas, H.; Poncin, S.; Löb, P.; Li, H.-Z. Pressure drop in a split-and-recombine caterpillar micromixer in case of newtonian and non-newtonian fluids. *AIChE J.* **2013**, *59*, 2679–2685, doi:10.1002/aic.14035.

168. Wu, K.; Su, D.; Saha, R.; Liu, J.; Wang, J.-P. Investigating the effect of magnetic dipole–dipole interaction on magnetic particle spectroscopy: implications for magnetic nanoparticle-based bioassays and magnetic particle imaging. *J. Phys. D: Appl. Phys.* **2019**, *52*, 335002, doi:10.1088/1361-6463/ab2580.

169. Hierrezuelo, J.; Sadeghpour, A.; Szilagyi, I.; Vaccaro, A.; Borkovec, M. Electrostatic stabilization of charged colloidal particles with adsorbed polyelectrolytes of opposite charge. *Langmuir* **2010**, *26*, 15109–15111, doi:10.1021/la102912u.

170. Mao, Y.; Cates, M.E.; Lekkerkerker, H.N.W. Depletion force in colloidal systems. *Physica A: Statistical Mechanics and its Applications* **1995**, *222*, 10–24, doi:10.1016/0378-4371(95)00206-5.

171. Gómez-Lopera, S.A.; Plaza, R.C.; Delgado, A.V. Synthesis and Characterization of Spherical Magnetite/Biodegradable Polymer Composite Particles. *Journal of Colloid and Interface Science* **2001**, *240*, 40–47, doi:10.1006/jcis.2001.7579.

172. Kumar, M.N.V.R.; Muzzarelli, R.A.A.; Muzzarelli, C.; Sashiwa, H.; Domb, A.J. Chitosan Chemistry and Pharmaceutical Perspectives. *Chem. Rev.* **2004**, *104*, 6017–6084, doi:10.1021/cr030441b.

173. Lu, A.-H.; Salabas, E.L.; Schüth, F. Magnetische Nanopartikel: Synthese, Stabilisierung, Funktionalisierung und Anwendung; pp 1242–1266.

174. Lellouche, J.-P.; Perlman, N.; Joseph, A.; Govindaraji, S.; Buzhansky, L.; Yakir, A.; Bruce, I. New magnetically responsive polydicarbazole-magnetite nanoparticles. *Chem. Commun.* **2004**, 560–561, doi:10.1039/b309375a.

175. Sanchez, L.M.; Martin, D.A.; Alvarez, V.A.; Gonzalez, J.S. Polyacrylic acid-coated iron oxide magnetic nanoparticles: The polymer molecular weight influence. *Colloids and Surfaces A: Physicochemical and Engineering Aspects* **2018**, *543*, 28–37, doi:10.1016/j.colsurfa.2018.01.050.

176. Srinivasan, K.; Samuel, E.J.J. Evaluation of Radiation Shielding Properties of the Polyvinyl Alcohol/Iron Oxide Polymer Composite. *J. Med. Phys.* **2017**, *42*, 273–278, doi:10.4103/jmp.JMP_54_17.

177. Xue, W.; Liu, Y.; Zhang, N.; Yao, Y.; Ma, P.; Wen, H.; Huang, S.; Luo, Y.; Fan, H. Effects of core size and PEG coating layer of iron oxide nanoparticles on the

distribution and metabolism in mice. *Int. J. Nanomedicine* **2018**, *13*, 5719–5731, doi:10.2147/IJN.S165451.

178. Bangs, L.B. New developments in particle-based immunoassays: Introduction. *Pure and Applied Chemistry* **1996**, *68*, 1873–1879, doi:10.1351/pac199668101873.

179. *Bio/Technology;* Rye, P.D., Ed., 14, 155, 1996.

180. Tomczak, N.; Liu, R.; Vancso, J.G. Polymer-coated quantum dots. *Nanoscale* **2013**, *5*, 12018, doi:10.1039/c3nr03949h.

181. Stamm, M. *Polymer Surfaces and Interfaces*: *Characterization, Modification and Applications;* Springer Berlin / Heidelberg: Berlin, Heidelberg, 2008, ISBN 9783540738657.

182. Berry, C.C.; Curtis, A.S.G. Functionalisation of magnetic nanoparticles for applications in biomedicine; R198-R206.

183. Bagtash, M.; Yamini, Y.; Tahmasebi, E.; Zolgharnein, J.; Dalirnasab, Z. Magnetite nanoparticles coated with tannic acid as a viable sorbent for solid-phase extraction of Cd2+, Co2+ and Cr3+. *Microchim Acta* **2016**, *183*, 449–456, doi:10.1007/s00604-015-1667-5.

184. Larsen, M.T.; Kuhlmann, M.; Hvam, M.L.; Howard, K.A. Albumin-based drug delivery: harnessing nature to cure disease. *Mol. Cell. Ther.* **2016**, *4*, 3, doi:10.1186/s40591-016-0048-8.

185. Vismara, E.; Bongio, C.; Coletti, A.; Edelman, R.; Serafini, A.; Mauri, M.; Simonutti, R.; Bertini, S.; Urso, E.; Assaraf, Y.; et al. Albumin and Hyaluronic Acid-Coated Superparamagnetic Iron Oxide Nanoparticles Loaded with Paclitaxel for Biomedical Applications. *Molecules* **2017**, *22*, 1030, doi:10.3390/molecules22071030.

186. Li, H.; Yan, K.; Shang, Y.; Shrestha, L.; Liao, R.; Liu, F.; Li, P.; Xu, H.; Xu, Z.; Chu, P.K. Folate-bovine serum albumin functionalized polymeric micelles loaded with superparamagnetic iron oxide nanoparticles for tumor targeting and magnetic

resonance imaging. *Acta Biomater.* **2015**, *15*, 117–126, doi:10.1016/j.actbio.2015.01.006.

187. Kalidasan, V.; Liu, X.L.; Herng, T.S.; Yang, Y.; Ding, J. Bovine Serum Albumin-Conjugated Ferrimagnetic Iron Oxide Nanoparticles to Enhance the Biocompatibility and Magnetic Hyperthermia Performance. *Nanomicro. Lett.* **2016**, *8*, 80–93, doi:10.1007/s40820-015-0065-1.

188. Vogel, H. *Gerthsen Physik*, 20., aktualisierte Auflage; Springer Berlin Heidelberg: Berlin, Heidelberg, s.l., 1999, ISBN 9783662074640.

189. *Bioanalytik;* Lottspeich, F.; Engels, J.W., Eds., 3. Auflage; Springer Spektrum: Berlin, Heidelberg, 2012, ISBN 3827429420.

190. Walter, J.; Thajudeen, T.; Süss, S.; Segets, D.; Peukert, W. New possibilities of accurate particle characterisation by applying direct boundary models to analytical centrifugation.

191. Fischer, H.; Polikarpov, I.; Craievich, A.F. Average protein density is a molecular-weight-dependent function. *Protein Sci.* **2004**, *13*, 2825–2828, doi:10.1110/ps.04688204.

192. Jachimska, B.; Wasilewska, M.; Adamczyk, Z. Characterization of globular protein solutions by dynamic light scattering, electrophoretic mobility, and viscosity measurements. *Langmuir* **2008**, *24*, 6866–6872, doi:10.1021/la800548p.

193. Hawe, A.; Hulse, W.L.; Jiskoot, W.; Forbes, R.T. Taylor dispersion analysis compared to dynamic light scattering for the size analysis of therapeutic peptides and proteins and their aggregates. *Pharm. Res.* **2011**, *28*, 2302–2310, doi:10.1007/s11095-011-0460-3.

194. CPS instrument. CPS-Scheibenzentrifugen. Available online: https://www.cpsinstruments.eu (accessed on 26 November 2021).

195. Stanjek, H.; Häusler, W. Basics of X-ray Diffraction. *Hyperfine Interactions* **2004**, *154*, 107–119, doi:10.1023/B:HYPE.0000032028.60546.38.

196. Bunaciu, A.A.; Udriştioiu, E.G.; Aboul-Enein, H.Y. X-ray diffraction: instrumentation and applications. *Crit. Rev. Anal. Chem.* **2015**, *45*, 289–299, doi:10.1080/10408347.2014.949616.

197. Otto, M. *Analytische Chemie*, 5. Auflage; Wiley-VCH: Weinheim, 2019, ISBN 9783527814879.

198. Wu, K.; Su, D.; Saha, R.; Liu, J.; Chugh, V.K.; Wang, J.-P. Magnetic Particle Spectroscopy: A Short Review of Applications Using Magnetic Nanoparticles. *ACS Appl. Nano Mater.* **2020**, *3*, 4972–4989, doi:10.1021/acsanm.0c00890.

199. Löwa, N.; Seidel, M.; Radon, P.; Wiekhorst, F. Magnetic nanoparticles in different biological environments analyzed by magnetic particle spectroscopy. *Journal of Magnetism and Magnetic Materials* **2017**, *427*, 133–138, doi:10.1016/j.jmmm.2016.10.096.

200. Loewa, N.; Wiekhorst, F.; Gemeinhardt, I.; Ebert, M.; Schnorr, J.; Wagner, S.; Taupitz, M.; Trahms, L. Cellular Uptake of Magnetic Nanoparticles Quantified by Magnetic Particle Spectroscopy. *IEEE Trans. Magn.* **2013**, *49*, 275–278, doi:10.1109/TMAG.2012.2218223.

201. Poller, W.C.; Löwa, N.; Wiekhorst, F.; Taupitz, M.; Wagner, S.; Möller, K.; Baumann, G.; Stangl, V.; Trahms, L.; Ludwig, A. Magnetic Particle Spectroscopy Reveals Dynamic Changes in the Magnetic Behavior of Very Small Superparamagnetic Iron Oxide Nanoparticles During Cellular Uptake and Enables Determination of Cell-Labeling Efficacy. *J. Biomed. Nanotechnol.* **2016**, *12*, 337–346, doi:10.1166/jbn.2016.2204.

202. Löwa, N.; Gutkelch, D.; Welge, E.-A.; Welz, R.; Meier, F.; Baki, A.; Bleul, R.; Klein, T.; Wiekhorst, F. Novel Benchtop Magnetic Particle Spectrometer for Process Monitoring of Magnetic Nanoparticle Synthesis. *Nanomaterials (Basel)* **2020**, *10*, doi:10.3390/nano10112277.

203. Ludwig, F.; Balceris, C.; Jonasson, C.; Johansson, C. Analysis of AC Susceptibility Spectra for the Characterization of Magnetic Nanoparticles. *IEEE Trans. Magn.* **2017**, *53*, 1–4, doi:10.1109/TMAG.2017.2693420.

204. Bałanda, M. AC Susceptibility Studies of Phase Transitions and Magnetic Relaxation: Conventional, Molecular and Low-Dimensional Magnets. *Acta Phys. Pol. A* **2013**, *124*, 964–976, doi:10.12693/APhysPolA.124.964.

205. Technische Universität Braunschweig. AC-S. Available online: https://www.emg.tu-bs.de (accessed on 28 November 2021).

206. Holz, M. *Magnetic Resonance in Chemistry*, 31st ed., 1993.

207. Di Marco, M.; Sadun, C.; Port, M.; Guilbert, I.; Couvreur, P.; Dubernet, C. Physicochemical characterization of ultrasmall superparamagnetic iron oxide particles (USPIO) for biomedical application as MRI contrast agents. *Int. J. Nanomedicine* **20**, *2*, 609–622.

208. Meiboom, S.; Gill, D. Modified Spin-Echo Method for Measuring Nuclear Relaxation Times. *Review of Scientific Instruments* **1958**, *29*, 688–691, doi:10.1063/1.1716296.